HZDR-085

Wissenschaftlich-Technische Berichte
HZDR-085 2018 · ISSN 2191-8708

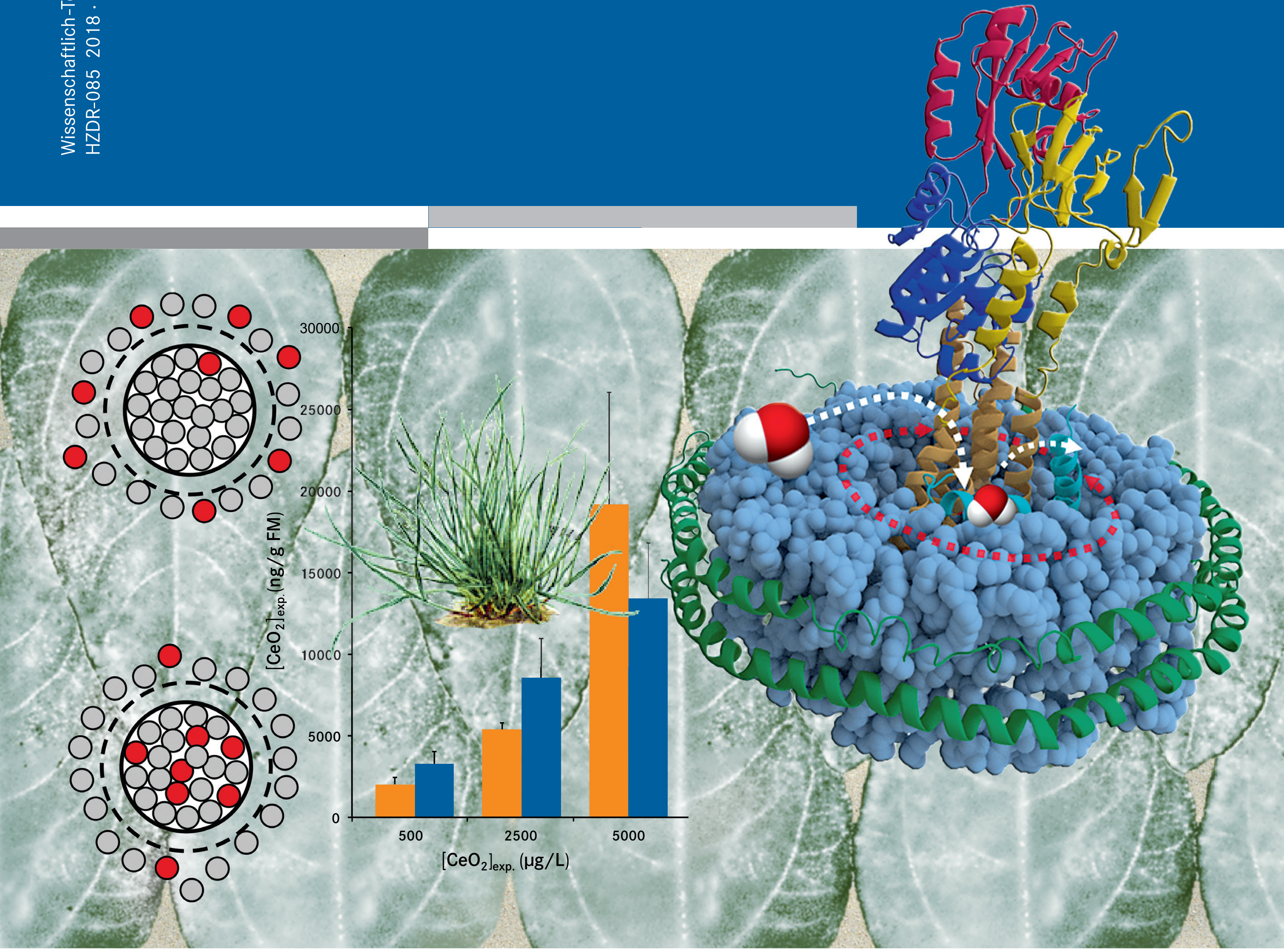

ANNUAL REPORT 2017

INSTITUTE OF RESOURCE ECOLOGY

HZDR
HELMHOLTZ
ZENTRUM DRESDEN
ROSSENDORF

Wissenschaftlich-Technische Berichte
HZDR-085

Annual Report 2017

Institute of Resource Ecology

Editorial board:

Prof. Dr. Thorsten Stumpf
Dr. Harald Foerstendorf
Dr. Frank Bok
Dr. Anke Richter

HZDR

HELMHOLTZ
ZENTRUM DRESDEN
ROSSENDORF

Impressum

Print edition: ISSN 2191-8708
Electronic edition: ISSN 2191-8716

https://www.hzdr.de/publications/Publ-27092
urn:nbn:de:bsz:d120-qucosa-233253

Published by Helmholtz-Zentrum Dresden–Rossendorf e.V.

Contact

Helmholtz-Zentrum Dresden–Rossendorf e.V.
Institute of Resource Ecology
Bautzner Landstraße 400
D-01328 Dresden
Germany

Phone: +49 (0) 351 260 3210
Fax: +49 (0) 351 260 3553
e-mail: contact.resourceecology@hzdr.de
http://www.hzdr.de/fwo

This report is also available at http://www.hzdr.de/fwo

Cover picture

The Institute of Resource Ecology successfully increased its publication activities during the past years. This can be seen not only from the number of publications but also from the progression of the average impact factor (see Preface). Exemplarily for outstanding publications in 2017, the cover picture of this report depicts two articles published in the high-ranked Journal "*Angewandte Chemie – International Edition*":

- Fischermeier, E.; Pospíšil, P.; Sayed, A.; Hof, M.; Solioz, M.; Fahmy, K. (2017) Dipolar Relaxation Dynamics at the Active Site of an ATPase Regulated by Membrane Lateral Pressure. *Angewandte Chemie – International Edition* **56**, 1269–1272.
- Schymura, S.; Fricke, T.; Hildebrand, H.; Franke, K. (2017) Elucidating the role of dissolution in CeO_2 nanoparticle plant uptake by smart radiolabeling. *Angewandte Chemie – International Edition* **56**, 7411–7414.

Preface

THE INSTITUTE OF RESOURCE ECOLOGY (IRE) IS ONE of the eight institutes of the Helmholtz-Zentrum Dresden – Rossendorf (HZDR). The research activities are mainly integrated into the program "Nuclear Waste Management, Safety and Radiation Research (NUSAFE)" of the Helmholtz Association (HGF) and focused on the topics "Nuclear Waste Management" and "Reactor Safety". Additionally, further activities investigate chemical and environmental aspects of processing and recycling of strategic metals, namely rare earth elements. These activities are located in the HGF program "Energy Efficiency, Materials and Resources (EMR)". Both programs, and therefore all work which is done at IRE, belong to the research field "Energy" of the HGF.

The research objectives are the protection of humans and the environment from hazards caused by pollutants resulting from technical processes that produce energy and raw materials. Treating technology and ecology as a unity is the major scientific challenge in assuring the safety of technical processes and gaining their public acceptance. We investigate the ecological risks exerted by radioactive and non-radioactive metals in the context of nuclear waste disposal, the production of energy in nuclear power plants and in processes along the value chain of metalliferous raw materials. A common goal is to generate better understanding of the essential processes controlling metal mobilization and immobilization at the molecular level by using advanced spectroscopic methods. This in turn enables us to improve models, codes and data for predictive calculations, extending the assessment of the transport and distribution of these contaminants in the environment to a macroscopic scale.

The extraordinary broadness of research topics and activities is illustrated below by some selected highlights: The IRE made substantial progress in 2017 with the upgrade of the Rossendorf Beamline at the European Synchrotron Radiation Facility (ESRF) in Grenoble. The prototype spectrometer was replaced by the final 5-crystal spectrometer and is now available for HR-XANES, XES and RIXS measurements (→ pp. 12–13). The peak investment was the purchase of a Pilatus 2D detector, which has been commissioned and successfully used for first diffraction experiments. And finally, EXAFS measurements of large sample series became much more comfortable by the installation of a new glovebox housing automated multisample changers both under room temperature and cryogenic (10 K) conditions. All of these installations were done in parallel to running 42 successful experiments by user groups from HZDR, Germany, the European Community, and Russia.

Nanostructured oxide dispersion strengthened steels are supposed to exhibit excellent irradiation resistance but suffer from minor fracture toughness. We have observed that oxide particles as small as a few nm combined with grain sizes in the sub-µm range give rise to superior irradiation resistance (→ p. 60). The avoidance of coarse inclusions was found to be crucial for sufficiently high fracture toughness (→ p. 59). Favorable combinations of irradiation resistance and fracture toughness for nuclear applications are now realistic.

A statistical approach was used to analyze the early phase of a hypothetical station blackout accident for a generic German pressurized water reactor with the severe accidents code ATHLET-CD (→ p. 67). The novel method was proved to provide more detailed information for the analysis of the safety of reactors compared with today typically applied deterministic approaches.

For computer simulations, we often worry about GIGO (garbage in, garbage out). In our reactive transport modeling (RTM) applications, two examples (→ pp. 28 and 30) highlight the use of measured fluid flow velocities as critical input parameters to reactive transport simulations. Most RTM approaches rely on calculated flow fields only. Having this mind, we compare the results of both approaches. The results critically underscore the importance of direct insight into flow field data as a sound background for improved predictive concepts.

Scientists of the institute of resource ecology demonstrated that microcalorimetry provides a sensitive real-time monitor of U(VI) toxicity in a plant cell model of Brassica napus, which is particularly suited for radioecological studies. The calorimetric descriptor "metabolic capacity" was introduced and showed that it correlates with the enzymatically determined cell viability. The combination with TRLFS and thermodynamic modelling indicated that the cell metabolism is affected predominantly by U(VI) hydroxo species.

Metal transport across cell membranes forms the interface between the Geo- and Biosphere. Ion hydration and rehydration are key mechanistic steps during transport. We have shown at molecular resolution how the cell membrane regulates the hydration of the ion binding site in a conserved class of heavy metal-transporting membrane proteins (see Cover picture).

The IRE established in 2017 local experimental capabilities for synthetic chemistry of actinides (including transuranium elements) as well as computational capabilities. The activities were focused primarily on actual research on the fundamental chemistry of f-elements including the successful synthesis and characterization of an exotic uranium compound (→ p. 22) and computational characterization of Tc compounds (→ p. 23).

The siting process for a suitable repository for highly active nuclear waste is still at an early stage in Germany. As a direct consequence, the current licensing of the intermediate storage facilitates has to be expanded from 40 years to much longer time frames. Thus, possible corrosion routes during the intermediate storage of the zircalloy cladding material surrounding nuclear fuel rods have gained increased attention. One very significant corrosion product formed on the cladding surface is Zirconium(IV) oxide. Therefore, the structural incorporation of trivalent actinides and their analogs into ZrO_2 was investigated. The combination of powder X-ray diffraction and laser luminescence spectroscopy allowed characterizations of both the bulk and local structure of Eu^{3+}-doped zirconia phases, respectively. It could be shown that the local sites differ significantly from the bulk crystal phase due to large disorder around the Eu^{3+} dopant (→ p. 41).

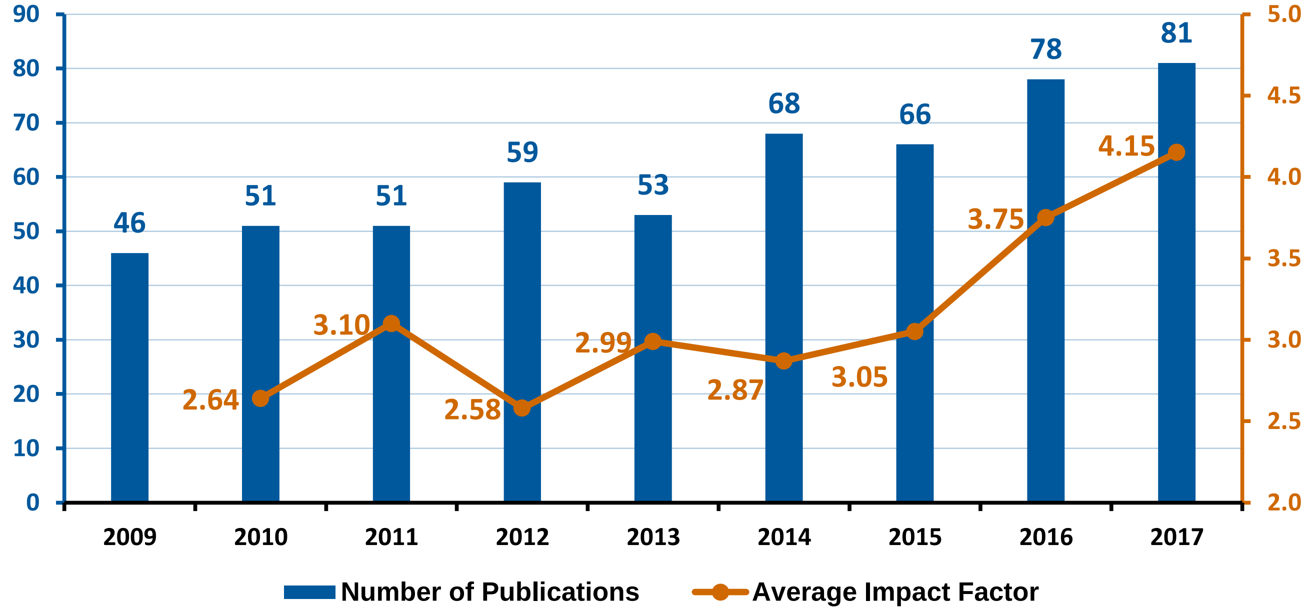

Statistics on the peer-reviewed articles published by the Institute of Resource Ecology as responsible or contributing institution during the past years.

Besides these highlights, we obtained many other new scientific results in the past year, which are presented in this annual report. Furthermore, 81 original papers were published in peer-reviewed international scientific journals. In 2017, we increased the average impact factor to a value of 4.15.

In January 2017, a research unit from the Institute of Ion Beam Physics at HZDR joined the IRE as the eighth department of Structural Materials. This administrative operation pools the activities in the topic "Reactor Safety" at HZDR under one roof. Hence, more than 130 scientists, technicians, and students working on their Ph.D., diploma, master, or bachelor thesis, were employed at the Institute of Resource Ecology. Thereof, 38 Ph.D. students worked at the institute in 2017. Support of young scientists is an important tool to ensure the competence and further scientific excellence in future times. Therefore, we are pleased that Björn Drobot got the Ph.D. awards of the German Chemical Society (GDCh Fachgruppe Nuklearchemie) as well as of the HZDR in 2017. Furthermore, Kristina Kvashnina applied successfully for an ERC starting grant. She started her work as a group leader in Grenoble at the ESRF in January 2018.

For his excellent scientific work and several years of teaching Vinzenz Brendler, who is the head of the Department of Surface Processes and vice director of the institute, became a honorary professor at the University of Applied Sciences in Dresden (Hochschule für Technik und Wirtschaft Dresden) in October 2017.

After more than 43 years working in Rossendorf, Gerhard Geipel retired in 2017. The institute organized a ceremonial act with several international speakers in November to take Gerhard Geipel's leave. In the future Johannes Raff will be responsible for the Department of Biogeochemistry which was headed by Gerhard Geipel for 14 years. Furthermore, Johanna Lippmann-Pipke left the institute and went to the Federal Institute for Geosciences and Natural Resources (Bundesanstalt für Geowissenschaften und Rohstoffe). Cornelius Fischer took over her position as the head of the Department of Reactive Transport in September 2017.

In retrospect of a successful year 2017 I would like to thank the visitors, German and international ones, for their interest in our research and for their participation in the institute seminars. We would also like to thank our scientific collaborators and the visiting scientists for coming to Dresden/Rossendorf in 2017 to share their knowledge and experience with us. We will continue to strongly encourage the collaborations and visits by scientists in the future. Special thanks are due to the executive board of the HZDR, the Ministry of Science and Arts of the Free State Saxony (SMWK), the Federal Ministry of Education and Research (BMBF), the Federal Ministry of Economics and Energy (BMWi), the Deutsche Forschungsgemeinschaft (DFG), the European Commission, and other organizations for their support.

Thorsten Stumpf

Prof. Dr. Thorsten Stumpf
Director of the
Institute of Resource Ecology

Contents

SCIENTIFIC CONTRIBUTIONS

PART I: THE CHEMISTRY OF LONG-LIVED RADIONUCLIDES

PART II: LONG-LIVED RADIONUCLIDES & TRANSPORT PHENOMENA IN GEOLOGICAL SYSTEMS

PART III: LONG-LIVED RADIONUCLIDES IN BIOLOGICAL SYSTEMS

PART IV: NUCLEAR REACTOR SAFETY RESEARCH

PUBLICATIONS

SCIENTIFIC ACTIVITIES

SCIENTIFIC CONTRIBUTIONS (PART I)

The Chemistry of
LONG-LIVED RADIONUCLIDES

Temperature dependency of the uranium(IV) fluorescence

T. Zimmermann, R. Steudtner, S. Lehmann, V. Brendler

Luminescence spectroscopy is a powerful tool to study the chemistry of f-elements in trace concentration. Manifold operating mode, *e.g.* steady-state, time-resolved, laser-induced, site-selective, cryogenic, etc. can be used to investigate the environmental behavior of An/Ln in various geological and biological systems. For U(IV), first experimental results suggest that time-resolved laser-induced fluorescence spectroscopy (TRLFS) is able to provide information about the speciation in aqueous solutions. This requires a detailed knowledge on the basic luminescence characteristic of the chosen fluorophore. Namely band positions and lifetimes are strongly temperature dependent.[1] Therefore, we investigated the temperature dependence of the luminescence behavior of the excited U(IV) ion in a temperature range from 274–333 K.

EXPERIMENTAL. First, a U(IV) stock solution was prepared by reduction of U(VI) using an electrochemical cell. The reduction was monitored by UV-vis spectroscopy, the residual content was analyzed by TRLFS and confirmed to be less than 1 % U(VI). For fluorometry, we used concentrations of 10 mM U(IV) and measured the fluorescence intensity at temperatures between 274 and 333 K. The samples used for TRLFS contained concentrations of about 100 µM U(IV). We could determine fluorescence lifetimes for room and liquid nitrogen temperature (77 K). For cryo-TRLFS, the samples were placed into NMR-tubes, which were put in a cold-finger Dewar filled with liquid nitrogen. At temperatures above 273 K the samples were measured in 1 cm quartz cuvettes. The excitation wavelength was $\lambda_{exc.}$ = 245 nm.

RESULTS. The luminescence spectra as function of temperature measured by fluorometry are shown in Fig. 1. We detected the typical luminescence characteristics of the free U(IV) ion in aqueous solution under acidic conditions. The emission maxima are determined at 321, 410 and 523 nm and are independent from the temperature in the aqueous phase. In Fig. 2, the intensities at 410 nm are plotted against the reciprocal temperature. For the luminescence intensity, we observed an unusual non-linear decrease with increasing temperature. This effect was observed for all three main emission bands. In comparison, the temperature dependence of the luminescence intensity for the free U(VI) can be described by linear correlation between intensity and temperature.[2]

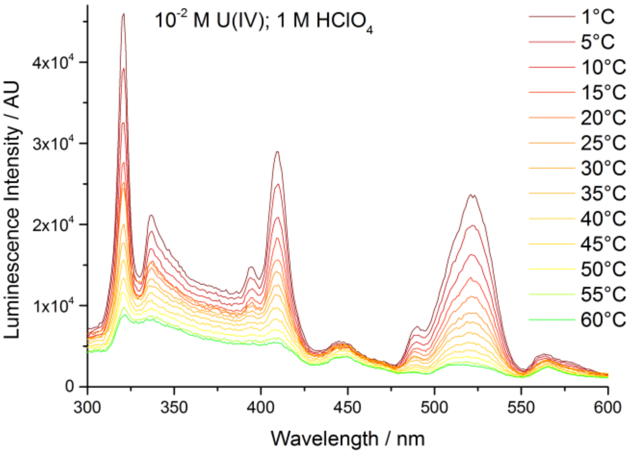

Fig. 1: Temperature dependency of the fluorescence of U(IV) in 1 M $HClO_4$ from 274 to 333 K (from top to below).

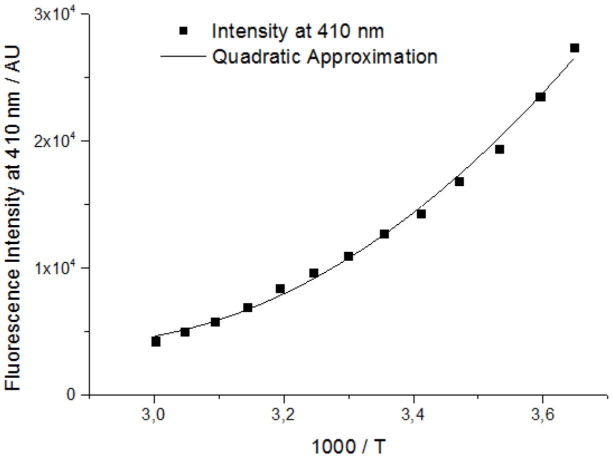

Fig. 2: Fluorescence intensities of U(IV) in 1 M $HClO_4$ at 410 nm at temperatures between 274 and 333 K.

Under cryogenic conditions, we observed changes in the spectrum (Fig. 3). The emission band at 410 nm shows a band splitting to 410 and 416 nm. The fluorescence decay time is 145 ± 10 ns. The lifetimes are in good agreement with the literature and other in-house publications.[3]

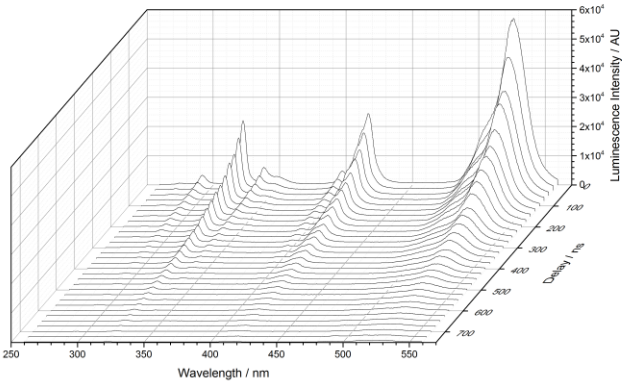

Fig. 3: Time-resolved fluorescence spectra of 100 µM Uranium(IV) in 1 M $HClO_4$ at a temperature of 77 K.

ACKNOWLEDGEMENTS. The authors kindly acknowledge funding by the German Ministry of Economic Affairs and Energy under the grant 02E11334B.

---

[1] Lakowicz, J. R. (2006) *Principles of fluorescence spectroscopy*, Springer, New York
[2] Steudtner, R., *et al.* (2007) *FZD-Report 459*, p. 16.
[3] Lehmann, S., *et al.* (2009) *Spectrochim. Acta* **73**, 902–908.

Evolution of the uranium chemical state in mixed-valence oxides

G. Leinders,[1] R. Bes,[2] J. Pakarinen,[1] K. O. Kvashnina, M. Verwerft[1]

[1]Belgian Nuclear Research Centre (SCK·CEN), Institute for Nuclear Materials Science, Mol, Belgium; [2]Department of Applied Physics, Aalto University, Aalto, Finland

The chemical states of uranium in the binary oxides UO_2, U_4O_9, U_3O_7, U_3O_8, and UO_3 are a fundamental yet hitherto unresolved question, which we solve here by using High Energy Resolution Fluorescence Detection X-ray Absorption Near Edge Spectroscopy (HERFD-XANES) at the uranium M_4 edge. In the mixed-valence oxides U_4O_9, U_3O_7, and U_3O_8 we were able to resolve the distribution of formal oxidation states. Moreover, we clearly identify a pivot from U(IV)−U(V) to U(V)−U(VI) charge compensation, corresponding to the transition from a fluorite-type structure (U_3O_7) to a layered structure (U_3O_8).[1] Such physicochemical properties are of interest to a broad audience of researchers and engineers active in domains ranging from fundamental physics to nuclear industry and environmental science.

The worldwide research effort to study binary uranium oxide compounds stems not only from their relevance in the frame of safety and economic performance of nuclear power plants or sustainable nuclear waste management, but also from a fundamental point of view.[2] The uranium atom contains outer-shell electrons ($5f^3$, $6d^1$, and $7s^2$) located in dispersive and hybridized bands near the Fermi level. Such electronic configuration can give rise to diverse chemical interactions, including the formation of both ionic and covalent bonds.

EXPERIMENTAL. In this study, we use HERFD-XANES[3] at the uranium M_4 edge (*i.e.*, excitation of the $3d_{3/2}$ core electrons) to unambiguously identify formal oxidation states present in monovalent and mixed-valence uranium compounds by probing the 5f-electron shell configuration. Results on a systematic series of binary uranium oxides are reported, including data measured for the first time on U_3O_7. The stable binary uranium oxides do not present a pure U(V) compound, hence KUO_3 was included in the present assessment as well.

RESULTS. An overview of the data is shown in Fig. 1. The monovalent uranium compounds (UO_2, KUO_3, β-UO_3) clearly display a shift in the position of the absorption maxima. Compared to U(IV), the maximum of the U(V) absorption line is shifted to higher energies by 1.2 eV and for U(VI) by 1.6 eV. The mixed-valence compounds U_4O_9 and U_3O_7 display more complex absorption spectra. In both solids, two distinct maxima are distinguished, and the position of both features corresponds exactly to the absorption maxima of the monovalent compounds UO_2 and KUO_3. A quantitative evaluation of the uranium valence state distribution in the mixed-valence compounds (Tab. 1) was performed, utilizing the accurate HERFD-XANES data measured at the U M_4 edge analyzed by iterative transformation factor analysis (ITFA).[4] Results reported in Tab. 1 are in excellent agreement with values expected from stoichiometric considerations. Our results allow an unambiguous assignment of U(IV) and U(V) valence states as major components in U_4O_9 and U_3O_7 and also confirm the increasing U(V) contribution at the expense of U(IV) as the degree of oxidation increases (U_4O_9 → U_3O_7). A significant U(VI) contribution can be excluded in these fluorite-type oxides, while a transition to the U(V)−U(VI) charge compensation mechanism occurs upon further oxidation (U_3O_7 → U_3O_8). These results finally elucidate the evolution of the uranium chemical state in the binary oxide system and provide input for further structural and theoretic al research on this important class of actinide materials.

Tab. 1: Distribution of uranium oxidation states in mixed-valence uranium compounds, quantified using ITT on the measured HERFD-XANES U M_4 edge spectra, and comparison of the average U valence derived from the experimental analysis and theory.

Compound	U(IV)*	U(VI)*	U(VI)*	Average U valence	
				Exp.	Theor.
U_4O_9	51	49	0	4.49	4.50
U_3O_7	36	64	0	4.64	4.67
U_3O_8	0	65	35	5.35	5.33

*: relative abundance of valence states (%), ± 3 %.

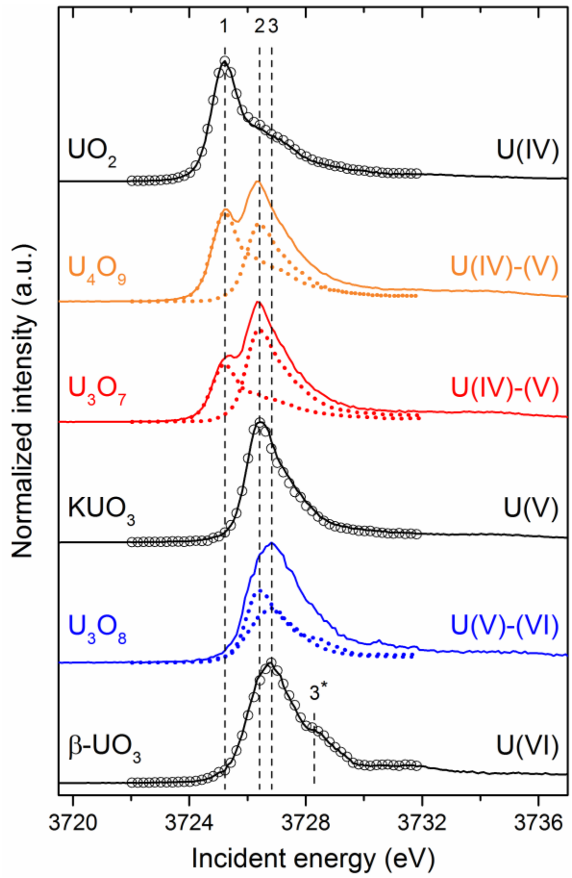

Fig. 1: HERFD-XANES spectra around the uranium M_4 edge in various uranium oxide compounds (solid lines). The spectral features denoted by 1−2−3(3*) relate to the formal valence states U(IV)−U(V)−U(VI), respectively. Individual component spectra reproduced from the iterative target test (dotted lines and open circles), see also Tab. 1.

---

[1] Leinders, G. *et al.* (2017) *Inorg. Chem.* **56**, 6784−6787.
[2] Kvashnina, K. O. *et al.* (2013) *Phys. Rev. Lett.* **111**, 253002.
[3] Kvashnina, K. O. *et al.* (2016) *J. Synchrotron Radiat.* **23**, 836−841.
[4] Rossberg, A. *et al.* (2009) *Environ. Sci. Technol.* **43**, 1400−1406.

Electronic structure study of Th systems using $L_{3\,\alpha}$ HERFD, RIXS and computational methods

J. Galanzew, K. O. Kvashnina

Our understanding of actinide chemistry lags behind that of the remainder of the periodic table. There are some knowledge gaps in fields controlling the chemical reactivity and bonding mechanisms between Th and ligands in complex actinide systems. Here, we report the results of HERFD and RIXS experiment at the Th L_3 edge for different Th systems, performed at Rossendorf Beamline (BM20) of ESRF.[1]

The content of thorium (Th) in the Earth's crust is three to four times higher than that of uranium, so the idea of using thorium as the main component of nuclear fuel is currently developing.[2]

In recent years, High Energy Resolution Fluorescence Detected (HERFD) and Resonant Inelastic X-ray Scattering (RIXS) were shown to be a highly valuable tool for investigation of the electronic structure of actinides.[3–5] Also codes for *ab initio* calculations like FEFF9.6 underwent drastical improvement, especially for the *f*-element systems.[6]

EXPERIMENTAL. Th $L_{3\alpha}$ HERFD spectra and RIXS maps of $[Th_2(\mu_2\text{-}OH)_2Cl_2(OH)_2(H_2O)_{10}]Cl_2$, ThO_2, and $Th(NO_3)_4 \cdot 5\,H_2O$ were measured at ROBL beamline (BM20) of ESRF in a HERFD setup (0.5 m radius) with one Si (8 8 0) stripped analyzer crystal (0.5 m bending radius). For the incident beam a Si (1 1 1) double crystal monochromator and a vertical slit of 100 µm were used.

Th 4f XPS spectra of ThO_2 and $Th(NO_3)_4 \cdot 5\,H_2O$ were measured using the monochromatic Al K_α line with a ULVAC-PHI VersaProbe II spectrometer.

Ab initio calculations for Th L_3 XANES were performed using the FEFF 9.6 code with tabulated crystal structures.

RESULTS. FEFF9.6 calculations[6] suggest a different crystal field splitting of the 6*d* states (ranging over few eV) for several thorium compounds (cf. Fig. 1).

HERFD spectra show a broader absorption edge for ThO_2 compared to $Th(NO_3)_4$ in agreement to the simulated spectra. Evaluation of the RIXS maps (cf. Fig 2) however showed an increased absorption broadening for ThO_2 compared to $Th(NO_3)_4$ (9.6 eV *vs.* 5.8 eV, respectively); the difference of 3.8 eV is most probably the result of two superimposed structures from the 6*d* state splitting.

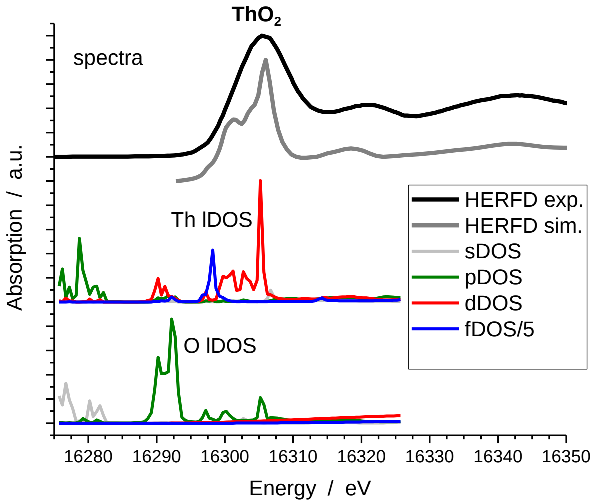

Fig. 1: Experimental and simulated Th L_3 HERFD spectrum of ThO_2.

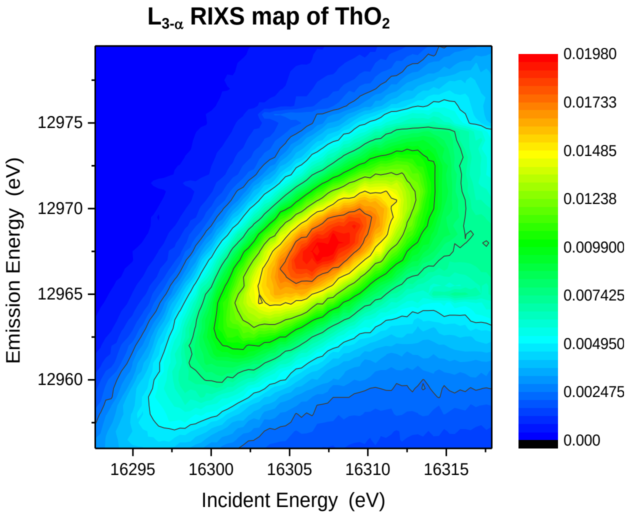

Fig. 2: RIXS intensities displayed as a contour map with axes corresponding to incident and emission energies over the Th L_3 absorption edge and Th La_1 emission line of ThO_2.

A surprising result was obtained during further evaluation of the RIXS maps (cf. Fig. 2). An emission broadening of ThO_2 (6.4 eV) compared to $Th(NO_3)_4$ (5.0 eV) was observed. The resonant emission depends on the 3d core states. Most probable explanation is a multiplet splitting of the excited states.

Th 4f XPS spectra show a shift of 1.4 eV to lower binding energy for ThO_2 compared to $Th(NO_3)_4$. The shake-up satellite for the leading edge in ThO_2 shows a much lower intensity than the same signal in $Th(NO_3)_4$.

XPS results indicate a covalent contribution to bond formation in ThO_2, a covalent contribution could interact with one electron in the resonant excited state and explain the result obtained from investigation of RIXS maps. The possibility to use RIXS maps as a tool to investigate covalence will be an interesting field for future study.

---

[1] Kvashnina, K. O. *et al.* (2016) *J. Synchrotron Rad.* **23**, 836–841.
[2] International Atomic Energy Agency (2005) *Thorium fuel cycle. Potential benefits and challenges.* International Atomic Energy Agency, Vienna.
[3] Butorin, S. M. *et al.* (2016) *Chem. Eur. J.* **22**, 9693–9698.
[4] Butorin, S. M. *et al.* (2016) *J. Phys. Chem. C* **113**, 8093–8097.
[5] Butorin, S. M. *et al.* (2016) *PNAS* **22**, 9693–9698.
[6] Rehr, J. J. *et al.* (2010) *Phys. Chem. Chem. Phys.* **12**, 5503–5513.

Bonding analysis of tetravalent actinide complexes with salen

R. Kloditz, T. Radoske, M. Patzschke, T. Stumpf

With real-space bonding analysis tools, the bonding character of [An(IV)Cl$_2$(thf)$_2$(salen)] (An = Th and U) was investigated. In the formed complex, the U^{4+} atom with its two f-electrons shows a more covalent bond character to the electron-donating partners of N and O of the ligand than the Th^{4+} atom possessing no f-electrons.

Mixed N- and O-donor ligands, such as salen, are some of the promising agents for the separation of tetravalent actinides in high-level radioactive liquid wastes. To obtain a deeper understanding on the efficacy and selectivity of these promising agents, the nature of chemical bonding of the resulting complexes must be investigated. To this end, we herein provide the plots of density differences and non-covalent interactions (NCI) for the [An(IV)Cl$_2$(thf)$_2$(salen)] complexes (An = Th and U) (Fig. 1) to visualize the chemical bonding in these complexes.

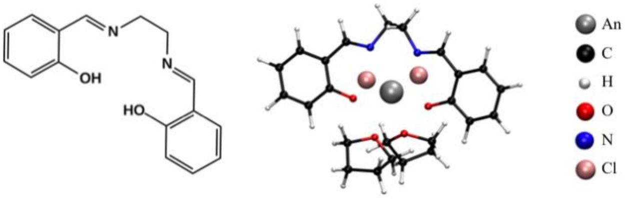

Fig. 1: Structure of the H$_2$(salen) ligand and the optimised structure of the [An(IV)Cl$_2$(thf)$_2$(salen)] complex. Salen = Bis(salicylidene)-ethylenediamine, thf = tetrahydrofurane.

COMPUTATIONAL DETAILS. All structures were optimized using the quantum chemical program suite Turbomole, ver. 7.2.[1] The DFT calculations were done using def2-TZVPP as basis set for all atoms and the PBE functional. For the Th and U atom, a respective 60-electron RECP was used. Dispersion effects were considered by the empirical approximation of S. Grimme and COSMO was used for solvent effects. The density differences were obtained using DGrid 4.6 and the NCI were calculated with NCIPlot, ver. 3.0.

RESULTS. Density differences are obtained by subtracting the electron densities of the fragments of the complex from the density of the whole complex. The fragments are composed of the actinide ion, two chloride ions, two thf molecules and the salen ligand. The resultant density difference plots are shown in Fig. 2.

The Th complex shows a significant increase in electron density between Th and the O atoms of the ligand. This indicates an orbital overlap and thus a covalent bond. In contrast, no such overlap is found for the Th-N interaction and only a weak bond is detected between Th and Cl. The U complex shows a more complicated picture. This is mainly due to the contribution of the two f-electrons of U^{4+}. The biggest difference in the electron density between the Th and U complexes derives from a polarization of the f-orbitals during the formation of the complex, showing no direct influence on the bonding situation. The density difference between U and O is comparable to that in the Th complex and, thus, can be explained as a covalent U–O bond. However, in contrast to the Th complex, the f-electrons in the U complex induce a visible overlap between U and N as well as a higher charge concentration between U and Cl. Thus, these bonds have a stronger covalent bonding character than those in the Th complex.

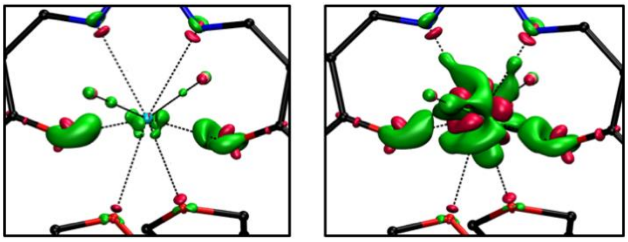

Fig. 2: Density difference plots of [Th(IV)Cl$_2$(thf)$_2$(salen)] (left) and [U(IV)Cl$_2$(thf)$_2$(salen)] (right). Positive differences are shown in green (isovalue = +0.02 a.u.), and negative differences are coloured in red (isovalue = –0.02 a.u.).

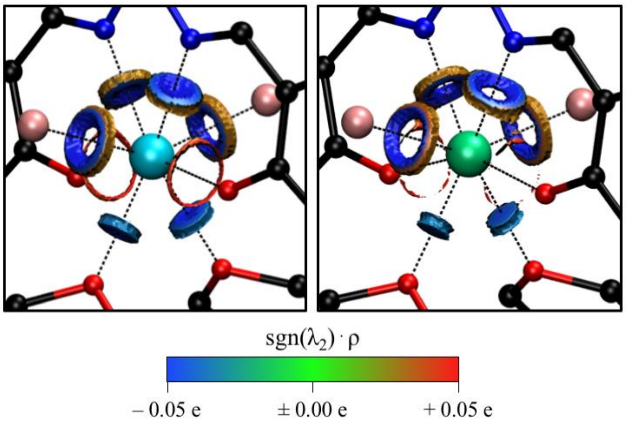

Fig. 3: NCI plots of [Th(IV)Cl$_2$(thf)$_2$(salen)] (left) and [U(IV)Cl$_2$(thf)$_2$(salen)] (right). s = 0.55, 0.03 a.u. ≤ ρ ≤ 0.05 a.u.

Another powerful tool for visualization of a bond character by means of real space bonding analysis is the NCI-plots developed by Contreras-Garcia et.al., depending on the electron density ρ(r) and its reduced gradient s(r).[2] This method reveals the areas with weak interactions characterised by $\rho(r) \leq 0.05$ a.u. and small s(r). A further distinction is made with λ_2, the second of the eigenvalues of the diagonalised Hessian ordered by size. A blue colour stands for an attractive interaction (*e.g.* ionic or H-bonding), whilst red is characteristic for repulsion (*e.g.* steric effects).

The NCI plots for the Th and U complexes are shown in Fig. 3, where van-der-Waals interactions ($\rho(r) < 0.03$ a.u.) are neglected. The weakest bond is found between An and O$_{\mathrm{thf}}$, indicating the role of thf as only compensation of the coordination sphere of Th and U. The ring shapes found in the An–Cl and An–O$_{\mathrm{salen}}$ interactions are characteristic of weak covalent bonds, indicating that the density between the metal centre and the bonding partners is bigger than 0.05 a.u. Similar structures can be observed for higher density ranges for C–N or C–C bonds. The bonding situation in the Th and U complexes is quite similar with the exception that the (covalent) interactions for U–N, U–Cl and U–O$_{\mathrm{salen}}$ are stronger in the U complex. The U–N interaction shows a ring and the density between U and O$_{\mathrm{salen}}$ is so big that the red ring almost disappears.

---

[1] Ahlrichs, R. *et al.* (1989) *Chem. Phys. Lett.* **162**, 165–169.
[2] Contreras-Garcia, J. *et al.* (2011) *J. Chem. Theory Comput.* **7**, 625–632.

Comparison of diamagnetic contributions of *f*-element containing compounds to NMR chemical shifts

T. Radoske, S. Schöne, M. Patzschke, J. März, P. Kaden

Interpretation of NMR data of paramagnetic compounds needs to be referred to the data of an isostructural diamagnetic compound to enable the interpretation of solely paramagnetic contributions and thus allow the interpretation of the bonding situation around the paramagnetic center. Comparison between the two different *f*-element series, however, is often hampered by the limited availability of diamagnetic reference compounds. Investigations of complexes of tetravalent lanthanides and actinides (Ce(IV) vs. Th(IV) complexes) allow the direct comparison between these 4*f*- and 5*f*-element series, revealing small but significant differences. This also underpins the necessity of a diamagnetic reference in each individual *f*-element series.

NMR spectroscopy on coordination compounds containing *f*-element metal ions often features additional chemical shifts that are due to unpaired electron density at the metal center. Mechanisms of propagating the influence of the metal center through the whole coordinating ligand molecule have been used already for a long time to describe the bonding situation in these kinds of metal-organic complexes. However, this evaluation of paramagnetic influences relies on the separation of diamagnetic and paramagnetic shift contributions. By subtracting the chemical shifts of a diamagnetic isostructural compound, only the paramagnetic contributions are left. However, even for the most studied *f*-element complexes, namely the trivalent lanthanides, scientists argue about which reference is the most suitable (i.e. La(III) vs. Lu(III)). When comparing data from the trivalent actinide series, however, there is no diamagnetic reference in the actinide series, as neither Ac(III) nor Lr(III) is available in NMR-relevant quantities.

To compare the effects of diamagnetic metal centers on the chemical shifts of coordinating ligands, a different oxidation state has thus to be chosen. In the series of tetravalent actinides and lanthanides, both series have a diamagnetic metal ion (Ce(IV) and Th(IV)) which allows the comparison and investigation of potential differences introduced by an extra electron shell in the case of the actinides.

An appropriate ligand system to study these effects has to provide stable and preferably symmetric complexes in solution, ideally featuring both hard- and soft donor coordination sites in one molecule. In this study, the ligand salen (*N*,*N′*-ethylenebis(salicylimine)) was chosen as it is well known for efficient complexation with metal ions, forming stable complexes in organic solvents, and filling the coordination sphere of tetravalent metal ions completely while compensating the charge of the tetravalent metal ion with their four deprotonated oxygen donor sites (Fig. 1). Additionally, the metal ion is coordinated to the four nitrogen donor atoms to form stable and symmetric 1 : 2 complexes.

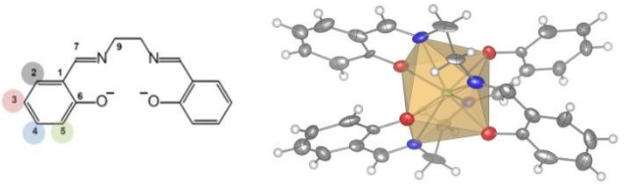

Fig. 1: Chemical structure of salen (left) and the molecular structure of [M(salen)$_2$] (M = Ce(IV) and Th(IV)) (right).

EXPERIMENTAL. To synthesize the Ce(IV) and Th(IV) complexes with salen, one equivalent of the metal salt, two equivalents of the protonated ligand (H_2salen) and four equivalents of sodium methanolate were dissolved in methanol separately and mixed subsequently. Upon addition of the base, the complex was immediately precipitated as fine yellowish powder. The powder was washed twice with methanol, subsequently washed twice with pentane, and dried. The dried product was then dissolved in THF-d8. NMR spectra were recorded on a Varian Inova 400 spectrometer equipped with a PFG direct probe operating at 399.89 MHz. Solvents and tubes were bought at Deutero GmbH and used as received.

RESULTS. A comparison of the spectra acquired for pure salen ligand, Th-salen complex and Ce-salen complex is presented in Fig. 2. Upon the complexation with the metals, the signals of the salen ligand are shifted significantly. This is probably due to the change in the electronic environment of the nuclei under investigation. Upon the complexation, oxygen and nitrogen donors are interacting with the metal ions, forming a certain type of chemical bond. The direct driving force of the complexation is the charge compensation of the tetravalent metal ion with four deprotonated and thus charged phenyl hydroxyl groups. The chemical shifts of the two resulting diamagnetic complexes are different but showing mainly the same trend in the direction of shift. This is most likely due to a similar interaction that is modified just by the size of the metal ion (Ce(IV) = 0.97 Å and Th(IV) = 1.05 Å for CN = 8).[1] However, the signal of the proton next to the nitrogen and the phenyl ring (H7) does not show the same net shift. This could point to a different influence present in the Th(IV) complexes as compared to the Ce(IV) complex. Even as the differences between the two *f*-element complexes are observed to be small, it is apparent that a diamagnetic reference in the same *f*-group series should be chosen for a reliable compensation of diamagnetic components for the evaluation of bond properties via paramagnetic NMR.

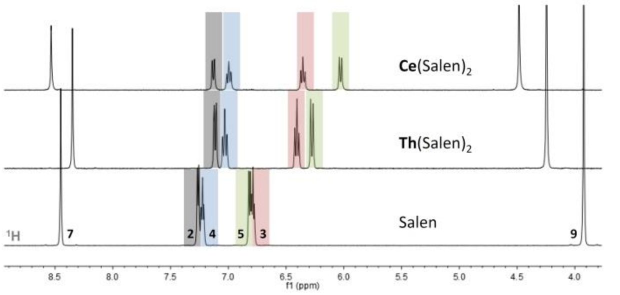

Fig. 2: Proton NMR spectra of salen, and its respective 2 : 1 M(IV) complexes of Ce(IV) and Th(IV) in THF-d8.

---

[1] Shannon, R. (1976). *Acta Cryst.* **32**, 751−767.

Polynuclear solution species and crystal structure of Zr(IV) acetate

C. Hennig, S. Weiss, W. Kraus,[1] J. Kretzschmar, A. C. Scheinost
[a]BAM Federal Institute for Materials Research and Testing, Berlin, Germany

Complex formation and coordination of zirconium with acetic acid were investigated with Zr K-edge EXAFS spectroscopy and single crystal diffraction. The EXAFS spectra show that a stepwise increase of acetic acid in aqueous solution with 0.1 M Zr(IV) leads to a structural rearrangement from initial tetranuclear hydrolysis species $[Zr_4(OH)_8(OH_2)_{16}]^{8+}$ to a hexanuclear acetate species $Zr_6(O)_4(OH)_4(CH_3COO)_{12}$. The solution species $Zr_6(O)_4(OH)_4(CH_3COO)_{12}$ was preserved in crystals by evaporation of the aqueous solution. Single crystal diffraction reveals an uncharged hexanuclear cluster in the crystalline compound $Zr_6(\mu_3\text{-}O)_4(\mu_3\text{-}OH)_4(CH_3COO)_{12}\cdot 8.5H_2O$. EXAFS measurements show that the structure of the hexanuclear zirconium acetate cluster in solution and solid state are identical.[1]

The presence of a tetranuclear Zr(IV) hydrolysis complex in aqueous solution has been described by several authors (Fig. 1).[2] The extraordinary stability of this complex makes it likely that acetate replace only the terminal water molecules, whereas the tetranuclear core remains preserved, as suggested by Tosan *et al.*[3] The aim of this study is to identify the molecular structure of this complex in solution and solid state.

EXPERIMENTAL. Two concentrated stock solutions were prepared (*i*) 1.0 M $ZrOCl_2\cdot 8H_2O$ (Sigma Aldrich, p.a.), (*ii*) 2.0 M CH_3COOH (VWR, p.a.). A sample series of 0.1 M Zr(IV) with different molar ratios of acetic acid/Zr(IV) was prepared by addition of stock solution (*i*) to an appropriate amount of solution (*ii*). The crystalline compound $Zr_6(\mu_3\text{-}O)_4(\mu_3\text{-}OH)_4(CH_3COO)_{12}\cdot 8.5H_2O$ was obtained from a mixture of 5 mL 1.0 M $ZrOCl_2$ with 5 mL of 1 M CH_3COOH. The initial pH of 0.30 increased to 1.77 by adding 2 M ammonium acetate solution. The clear solution was slowly evaporated at room temperature.

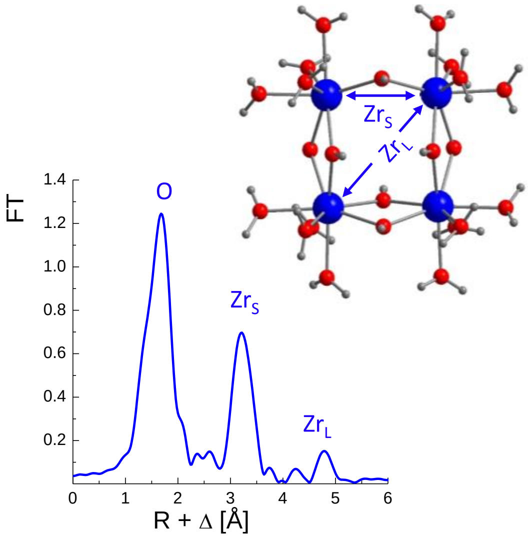

Fig. 1: Fourier transform of Zr K-edge k^3-weighted EXAFS data of the Zr(IV) species $[Zr_4(OH)_8(OH_2)_{16}]^{8+}$. The spectrum reveals Zr backscattering peaks at short (Zr_S) and long (Zr_L) distance, as indicated in the molecule drawing on top.

RESULTS. First, we identified the Zr(IV) hydrolysis species of the initial solution before the complexation with acetate. The Fourier transform in Fig. 1 shows three peaks labelled with the symbol of the related backscattering atoms of the tetranuclear hydrolysis complex $[Zr_4(OH)_8(H_2O)_{16}]^{8+}$. The successive complex formation of 0.1 M Zr(IV) with CH_3COOH at pH 1.5 with increasing molar ratios of acetic acid/Zr(IV) reveals a significant change of the spectral features.[1] The limiting Zr(IV) acetate species is shown in Fig. 2. The first peak undergoes a splitting, compared with the spectrum of the initial species $[Zr_4(OH)_8(H_2O)_{16}]^{8+}$. The second peak, Zr_S, increases in intensity compared with the initial species, which was fitted with 3.8(3) Zr atoms at a Zr–Zr_S distance of 3.521(2) Å. The third peak, Zr_L reveals 1.3(2) Zr neighbors at a Zr–Zr_L distance of 4.984(9) Å. The limiting solution species of Zr acetate was preserved in a crystal in order to elucidate the full complex structure by single crystal diffraction. The success of this procedure was verified by comparing the EXAFS spectrum of the limiting zirconium acetate solution species with the EXAFS spectrum of the crystalline material.[1]

Figure 2 shows on top the molecular configuration of Zr(IV) acetate. The complex consists of a hexanuclear cluster whose faces form a nearly regular octahedron bridged by 8 μ_3-oxygen atoms and 12 bidentate *syn*-*syn* bridging acetate ligands. Each Zr(IV) has a coordination number 8, caused by 4 μ_3-oxygen atoms and 4 μ-O atoms of carboxylate bridges. This structure is observed for the first time and differ completely from the structure predicted by Tosan *et al.*[3]

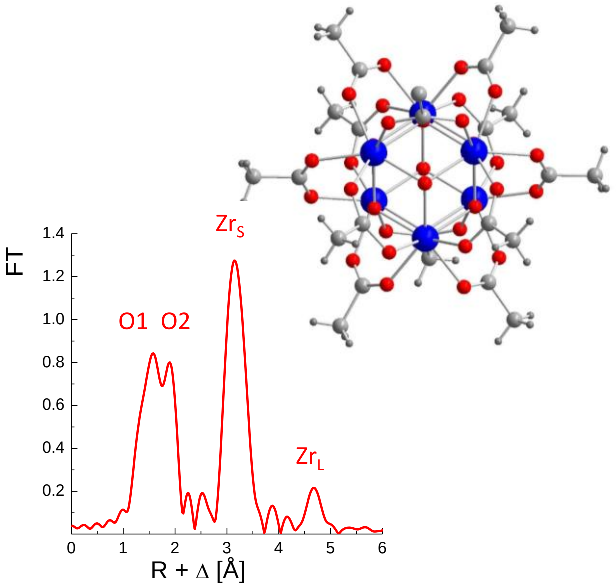

Fig. 2: Fourier transform of Zr K-edge k^3-weighted EXAFS data of the solution species $Zr_6(O)_4(OH)_4(CH_3COO)_{12}$. Top: the structure of the hexameric Zr cluster obtained from the crystal structure of the solid sample $Zr_6(\mu_3\text{-}O)_4(\mu_3\text{-}OH)_4(CH_3COO)_{12}\cdot 8.5H_2O$.

---

[1] Hennig, C. *et al.* (2017) *Inorg. Chem.* **56**, 2473–2480.
[2] Hagfeldt, C. *et al.* (2004) *Dalton Trans.* 2142–2151.
[3] Tosan, J. L. *et al.* (1994) *J. Non-Cryst. Solids* **168**, 23–32.

Elucidation of americium(III) malate complexation by EXAFS, MD and chemometrics

A. Rossberg, F. Taube,[1] M. Trumm[2]

[1]Technische Universität Dresden, Dresden, Germany; [2]Institute for Nuclear Waste Disposal, KIT, Karlsruhe, Germany

Concrete serves as an engineering barrier in nuclear waste repositories. Organic additives are commonly used for enhancing physico-chemical and mechanical properties of fresh concrete, but may interfere through their strongly complexing functional groups with radionuclides, potentially leading to an enhanced Am(III) release in case of water intrusion. Here we present a refined aqueous speciation of Am(III) with malic acid (Mal) as representative for organic additives, by combining EXAFS data analyzed by chemometrics with molecular dynamics calculations.

EXPERIMENTAL. Am-L_{III} EXAFS spectra from 10 samples of a pH series (pH 0.9–8.0) with [Am(III)] = 1.2×10^{-3} mol/L and [Mal] = 1.9×10^{-2} mol/L were recorded with a 13-element Ge detector at room temperature. The fluorescence data were dead-time corrected. Speciation calculations were performed by using complex stability constants for the 1 : 1 and 1 : 2 Am-Mal complex obtained by isothermal titration calorimetry (ITC). *Ab-initio* molecular dynamic (MD) calculations were carried out with TURBOMOLE on Nd(III)-Mal complexes as structural analogues for the corresponding Am(III) complexes and three hydration shells were implemented.[1] BP86 functional and DZVP basis sets were used, while the MD trajectories were calculated by application of 300 K Nosé-Hoover dynamics with a time-step of 1 fs. To ensure equilibration after 0.5 ps the trajectories were collected up to 4.5 ps. With iterative target transform factor analysis (ITFA), the 10 EXAFS spectral mixtures were decomposed into fractions and spectra of the structural components.[2]

RESULTS. Based on the stability constants, the aqueous speciation changes from 100 % Am(III)-hydrate at pH 0.9 to 14 % 1 : 1 and 86 % 1 : 2 complex at pH 8.0. This causes a spectral change in the k^3-weighted EXAFS spectra of only 16 %, rendering the structural analysis of the complexes by common shell fitting procedures impossible. Therefore, we employed additional structural information from MD to extract the spectra of the single components with ITFA. The MD calculations indicate for both Am(III)-Mal complexes an asymmetric coordination of the two carboxylic groups of Mal (Fig. 1). The Am–O1 distance is similar to the average Am–O_{water} distances (both denoted as O_{long}), while the Am–O2 distance is significantly shorter (Fig. 1). Moreover, since the signal of O1 is similar to that of O_{water} both signals can be attributed to one spectral component (comp 1), while all remaining contributions originating from Mal (except of O1), belong to a second spectral component (comp 2). Independently, but in line with these considerations, ITFA applied to the spectral mixtures yielded two statistically significant components. According to MD calculations the total coordination number (CN_{tot}) is 9 for Am(III)-hydrate, and 8 for both the 1 : 1 and the 1 : 2 complexes. By using CN_{tot} and the pH-speciation, for each pH the theoretical coordination number (CN_{theo}) of comp 1 and comp 2 is calculated. By introducing CN_{theo} for pH 0.9 and 8.0 ITFA calculates all remaining CN_{ITFA} and the spectra of the components (Fig. 2). CN_{theo} and CN_{ITFA} agree within only 0.3 atoms. The shell fit of comp 1 and comp 2 resulted in 1 x O_{long}@2.48 Å, 1 x O2@2.42 Å and 1.7 x C1/2@3.35 Å, respectively (Fig. 2). The EXAFS signals of these components together with the pH-speciation and the CN_{tot} well reproduce the experimental EXAFS spectra within the experimental error. This binding motive of a monodentate coordination of the carboxylic group is in line with the previously elucidated Am(III)-formate (Form) system, where we observed O_{water}@2.48 Å, O_{Form}@2.41 Å and C_{Form}@3.40 Å).[3] In conclusion, the unique combination of a calorimetry-determined speciation, MD calculations and *state-of-the-art* numerical data analyzation allowed a spectroscopic confirmation of the pH-speciation and to define a prevailing monodentate coordination of both carboxylic groups, hence the formation of a 7-membered ring within the Am-malate system for the first time.

Fig. 1: Snapshot of MD calculated structure of the 1 : 1 complex. Average radial distances are: Am–O1 = 2.37 Å, Am–O2 = 2.45 Å, Am–O_{water} = 2.48 Å, Am–C1/2 = 3.51 Å.

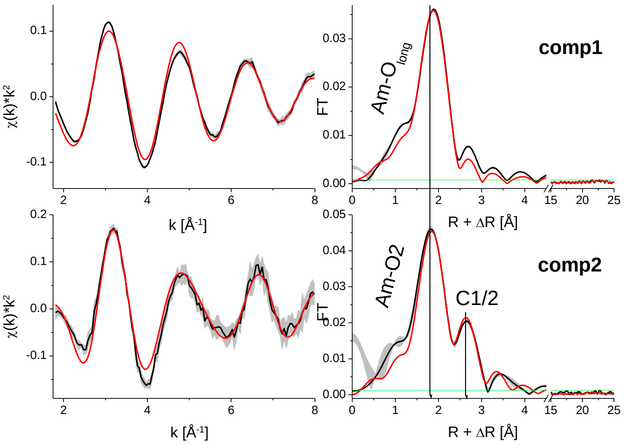

Fig. 2: ITFA isolated (black line) EXAFS contributions (left) and related Fourier Transforms (right) of component comp1 (top) and comp2 (bottom) with shell fit (red line). Confidence interval at the 95 % confidence level (gray). The noise level (green) is estimated by using the R-range 15–25 Å.

---

[1] TURBOMOLE V7 (2016) A development of University of Karlsruhe and Forschungszentrum Karlsruhe GmbH, 1989–2017.

[2] Rossberg, A. *et al.* (2003) *Anal. Bioanal. Chem.* **376**, 631–638.

[3] Froehlich, A. *et al.* (2017) *Inorg. Chem.* **56**, 6820–6829.

Uranium(VI)-complexation with inorganic ligands in the temperature range 275−313 K

H. Lösch, T. Stumpf, N. Huittinen

The complexation of uranium(VI) with silicate in the aqueous system was investigated using TRLFS as a function of pH, silicate concentration and temperature. Based on the recorded emission spectra a peak deconvolution was performed to obtain the free component spectra and calculate the complexation constant. To extract thermodynamic data and to compare the constant with estimation methods the experiment was also conducted at different temperatures.

EXPERIMENTAL. For the investigation of the U(VI) complexation with silicate, tetramethyl orthosilicate (TMOS) or a Si-ICP-standard was used as silicate sources. To avoid the formation of colloidal silicate species, the silicate concentration was below the solubility limit of silicic acid in the range between 3×10^{-4} to 2×10^{-3} M. The U(VI) concentration and ionic strength were kept constant at 5×10^{-5} M and 0.2 M using $NaClO_4$, respectively, in all experiments. The TRLFS measurements were performed with a Nd:YAG-laser ($\lambda_{exc.}$ = 266 nm) in the temperature range between 275−313 K, using a cooled/heated cuvette housing.

RESULTS. First, the luminescence behavior of U(VI) in the absence and presence of silicates was investigated. Figure 1 shows the emission spectra of samples without silicates (left) and with a silicate concentration of 8×10^{-4} M (right) as a function of pH.

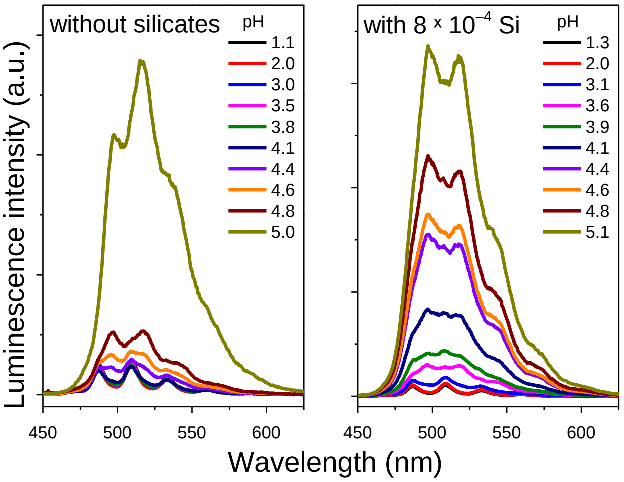

Fig. 1: Comparison of emission spectra of 5×10^{-6} M U(VI) samples without silicates (left) and with constant [Si] = 8×10^{-4} M (right) at different pH at 298 K.

The spectra without silicates clearly show the existence of the free uranyl cation and the 1 : 1 uranium hydroxo species until pH 4.4. At higher pH, the strong luminescence signal of the 3 : 5 hydroxo species dominates the spectra.[1] In the samples with a constant silicate concentration of 8×10^{-4} M, the spectra are dominated by the aquo ion signal until pH 3.6. Thereafter, a large increase in the luminescence intensity is observed, pointing toward U(VI) interaction with the silicates. Such a large increase of the luminescence intensity upon complexation was not expected from a previous study by Moll *et al.*[2] and serves as a first indication for the formation of polynuclear or colloidal U(VI)-silicate species.

The use of different silicates (TMOS and a Si-ICP-standard) show no influence on the U(VI) luminescence spectra, implying that the same species form independently from the silicon source (data not shown).

In the temperature dependent measurements a constant pH of 4.3 was used (Fig. 2). The emission spectra at low temperatures (275, 283, 288 K) show changes in the peak shapes with increasing silicate concentration, but no significant increase in luminescence intensity (Fig. 2, left). The contrary behavior is observed for the spectral data at 313 K (Fig. 2, right). This implies that different reactions between U(VI) and silicate occur depending on the temperature. Upon comparison with previous data,[2] the dominant species at temperatures below 298 K is the $UO_2–OSi(OH)_3^+$ complex. Upon increasing temperature, the speciation changes, presumably due to the formation of polynuclear or colloidal U(VI)-silicate species.

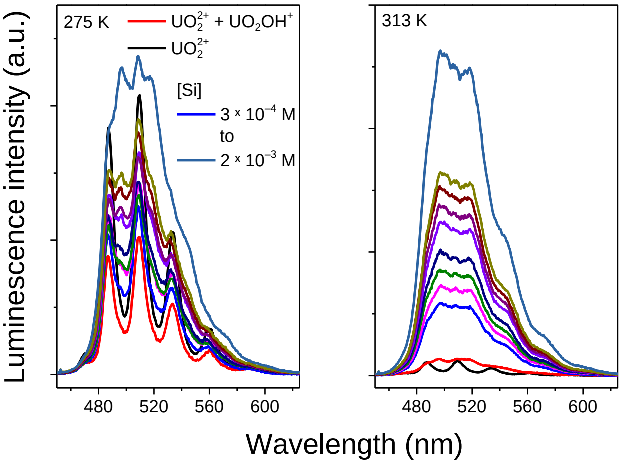

Fig. 2: Emission spectra of 5×10^{-6} M U(VI) at different silicate concentrations at 275 K (left) and 313 K (right).

The nature of the formed polynuclear or colloidal uranium-silicate species will require further attention. However, conditional constants for the assumed $UO_2–OSi(OH)_3^+$ complex in the low temperature regime could be calculated based on derived species distributions from the recorded luminescence spectra. The constants are summarized in Tab. 1.

Tab. 1: Conditional complexation constants for the $UO_2–OSi(OH)_3^+$ complex.

Temperature (K)	log K^*(T)
275	−2.18
283	−2.13
288	−2.42

ACKNOWLEDGEMENTS. The authors kindly acknowledge funding from the BMBF (02NUK039B). N. Jordan and R. Steudtner are thanked for valuable help throughout the course of the project.

---

[1] Drobot, B. *et al.* (2015) *Chem. Sci.* **6**, 964−972.
[2] Moll, H. *et al.* (1998) *J. Alloys Compd.* **271-273**, 765−768.

Impact of elevated temperature on the complexation of Cm(III) with aqueous phosphates

N. Jordan, M. Demnitz,[1] H. Lösch, N. Huittinen
[1]Technische Universität Dresden, Dresden, Germany

The impact of elevated temperature (25 to 80 °C) on the complexation of Cm(III) by phosphate was investigated by time-resolved laser induced fluorescence spectroscopy (TRLFS). Using the specific ion interaction theory (SIT), the complexation constants at infinite dilution (log $\beta°$) were obtained. Finally, using the van't Hoff equation, positive enthalpy of reaction ($\Delta_R H°$) and entropy of reaction ($\Delta_R S°$) were derived.

Future monazite ($LnPO_4$) applications may involve their use as immobilization matrices for specific High Level Waste (HLW) streams, which may generate elevated concentrations of aqueous phosphates in the environment. Currently, very little data is available for actinide complexation with the inorganic phosphate ligands ($H_2PO_4^-$, HPO_4^{2-}, and PO_4^{3-}). In addition, no studies investigating actinide complexation reactions with phosphates at elevated temperatures, which are of relevance in the proximity of heat-generating HLW repositories, can be found. Thus, the general purpose of this study was to establish reliable complexation constants for the Cm(III)/phosphate system (Cm(III) representing the trivalent actinides present in HLW streams), based on an independent spectroscopic validation of the stoichiometry of the derived complexes.

EXPERIMENTAL. At first, the *in situ* solution speciation of Cm(III) in the presence of phosphates was investigated with TRLFS (λ_{ex} = 396.6 nm) at 25 °C. The concentration of ^{248}Cm(III) was ranging from 3×10^{-7} to 5×10^{-7} mol·L^{-1}. The proton concentration was kept constant at 0.1 mol·L^{-1} and the ionic strength, imposed by $NaClO_4$, was ranging from 0.6 to 2.1 mol·L^{-1}. The total phosphate concentration was not exceeding a maximum of 10 % of the total ionic strength, in order to keep all activity coefficients reasonably constant. Finally, the impact of elevated temperature (25 to 80 °C) was studied at an ionic strength of 1.1 mol·L^{-1}.

RESULTS. At 25 °C, the increasing phosphate concentration induced a red shift of the Cm(III) emission spectra (Fig. 1). The spectral deconvolution led to two single components, *i.e.* the Cm^{3+} aquo ion and the $CmH_2PO_4^{2+}$ complex, as well as their species distribution. Slope analysis was performed in the molal scale to obtain the respective conditional log $\beta(I)$ constants at 25 °C, based on the following equilibrium:

$$Cm^{3+} + H_3PO_4 \rightleftharpoons CmH_2PO_4^{2+} + H^+ \qquad (1)$$

The molality of free $H_3PO_{4(aq)}$ was calculated with PHREEQC using the Thermochimie SIT database.[1, 2] By plotting $\log_{10}\beta - \Delta z^2 D$ ($\Delta z^2 = -4$) (as a function of the ionic strength,[3] a linear regression provided the log $\beta°$ (intercept with the y-axis) and $-\Delta\varepsilon$ (slope) parameters (Fig. 2). The ion interaction coefficient $\varepsilon(H^+;ClO_4^-)$ was taken from Lemire *et al.*, while $\varepsilon(Cm^{3+};ClO_4^-)$ was assumed to be equal to $\varepsilon(Am^{3+};ClO_4^-) = 0.49 \pm 0.03$ kg·mol^{-1}.[3] Following the SIT formalism, the ion interaction coefficient of the uncharged species H_3PO_4 was set to zero.[3] The complexation constant at infinite dilution log β^o and the ion interaction coefficient $\varepsilon(CmH_2PO_4^{2+};ClO_4^-)$ were found to be 0.34 ± 0.12 and 0.10 ± 0.09 kg·mol^{-1}, respectively.

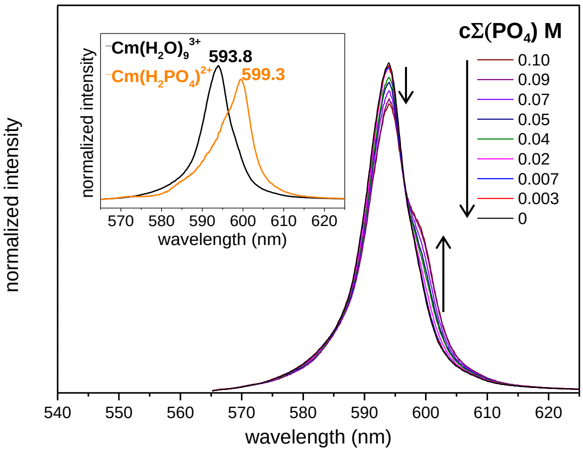

Fig. 1: Emission spectra of Cm(III) for varying phosphate concentrations, at 25 °C (I = 1.1 mol·L^{-1}). Inset: single components after peak deconvolution.

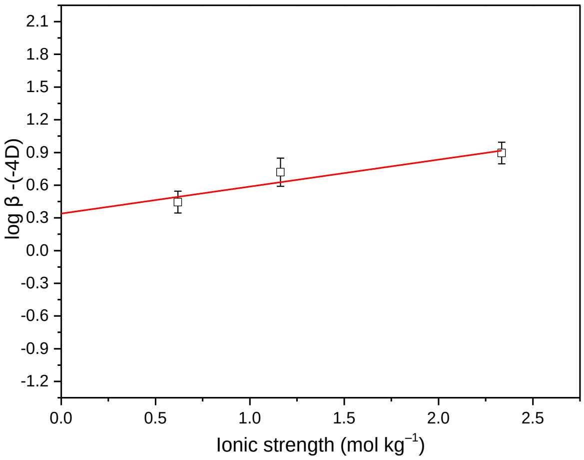

Fig. 2: Linear SIT regression plot for the $CmH_2PO_4^{2+}$ complex at 25 °C.

Upon increasing the temperature, the equilibrium (1) was found to shift towards the product side (data not shown). The extrapolation at infinite dilution was also performed using the SIT equation, by assuming constant the interaction coefficients in the temperature range from 25 to 80 °C.[3] Using the van't Hoff equation, the enthalpy $\Delta_R H°$ (assumed constant between 25 to 80 °C) and entropy $\Delta_R S°$ of reaction (1) were determined to be 10.2 kJ·mol^{-1} and 41.4 J·mol^{-1}·K^{-1}, respectively, revealing an endothermic and entropy driven complexation reaction.

ACKNOWLEDGEMENTS. The German Federal Ministry of Education and Research (BMBF) is acknowledged for funding the SEM^2 (033R127D) and ThermAc (02NUK039B) projects.

---

[1] Parkhurst, D. L. *et al.* (1999) User's guide to PHREEQC (version 2).
[2] Giffaut, E. *et al.* (2014) *Appl. Geochem.* **49**, 225–236.
[3] Lemire, R. J. *et al.* (2013) *Chemical Thermodynamics of Iron: Part I*, OECD Publications, Paris.

Implementation of spectro-electrochemical setup for *in situ* investigation of actinide redox reactions in aqueous solution

R. Husar, R. Steudtner

We report the implementation of a novel spectro-electrochemical setup and introduce its multiple applications, *e.g.* to the preparation of pure oxidation states of redox species or to investigate transient redox species as a venue for investigation into the fundamental structure-redox reactivity relationship.

Aqueous redox chemistry of actinides (An) is complex and intriguing because of their close orbital energy (*e.g.* $5f^6\ 7s^2$ for Pu) as well as practical difficulty to prepare their pure redox species. For instance, for plutonium (Pu) species under acidic conditions, similar redox potentials for the oxidation states (III)/(IV)/(V)/(VI) render their co-existence of these four different valences, the chemical behavior of which shows significant differences for each oxidation state.[1] To avoid the coexistence of different redox species of An, electrochemical techniques are essential. We herein report the implementation of a spectro-electrochemical setup in our controlled area to simultaneously provide the following capabilities;

I. preparation of pure oxidation states of An species,
II. investigation into the electronic structures of different An ions (*i.e.* AnO_2^{2+}, AnO_2^{+}, An^{4+} and An^{3+}) under highly coherent experimental conditions,
III. stabilization of redox sensitive redox species without using chemical oxidants/reductants, and
IV. an *in situ* spectroscopic approach to investigate transient redox species (TRS).

Knowledge about TRS is of importance particularly for the elucidation of redox reaction mechanisms, as their potential occurrence is considered to interfere redox reactions and eventually to affect thermodynamic and kinetic turnover of chemical reactions.[2] We aim to provide a novel setup as a venue for studying the fundamental relationship between structure and redox reactivity.

EXPERIMENTAL DESIGN. A UV-vis/NIR absorption spectroscopy cell with quartz optical windows for time-resolved laser-induced fluorescence spectroscopy (TRLFS) was coupled with an optical mini-setup and a mobile potentio-galvanostat. The setup shown in Fig. 1 consists of two compartments, the reaction compartment with optical paths for UV-vis/NIR and TRLFS and the cell cap with electrode materials for redox potential manipulation. It was designed for the usage both in- and outside a glovebox. The specifically designed electrodes are separated *via* a ceramic diaphragm to avoid side redox reactions. Electrode materials are optimally arranged not to interfere the optical paths and analytic windows of the reaction compartment. Diffusion of redox couples and mixing of sample solution are achieved by magnetic stirring. Various potentiostatic-galvanostatic modes can be applied to investigate redox-active species under environmentally relevant conditions with diluted metal ion concentration or under conditions to prepare pure redox species with a high heavy metal ion concentration.

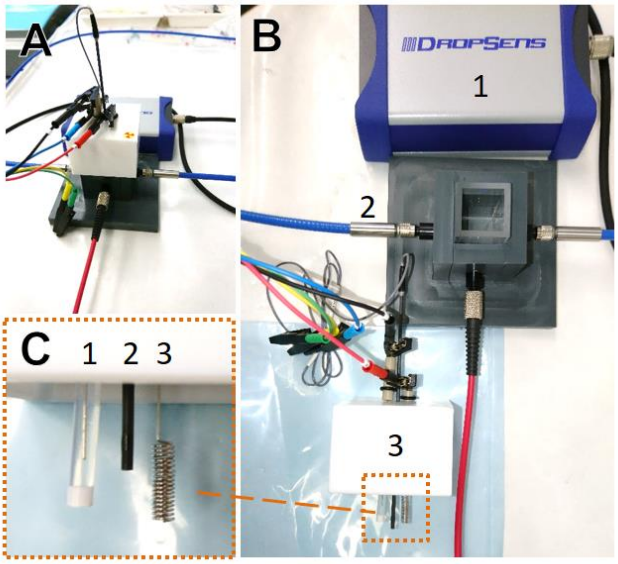

Fig. 1: Images of spectro-electrochemical cell (A) and their compartments (B and C): a mobile potentiostat with Bluetooth connection (B1), an optical cell with UV-vis/NIR and TRLFS paths – top-side view (B2), an electrodes cell cap – side view (B3) and assembly of electrode materials – side view (C) with auxiliary (C1), reference (C2) and working electrodes (C3).

---

[1] Katz, J. J. *et al.* (1986) *The Chemistry of the Actinide Elements*. Chapman and Hall, London.
[2] Fukuzumi, S. *et al.* (2015) *Chem. Eur. J.* **21**, 17548–17559.

New insights into the interaction of α-isosaccharinic acid with uranium(VI): UV-vis spectroscopy combined with factor analysis

H. Brinkmann, A. Rossberg, H. Moll, T. Stumpf

Isosaccharinic acid (ISA) is the main product of the alkaline degradation of cellulosic materials, which are expected to be present in low and intermediate level waste in considerable amounts.[1] The complexation of radionuclides (RN) with ISA affects their sorption behavior and solubility adversely.[2] Hence, it is necessary to characterize the formed RN-ISA complexes in terms of metal to ligand ratio, stability, and structure. Since the knowledge about the interaction of ISA with uranium(VI) is weak, the objective of this study is to determine single component absorption spectra of formed UO_2^{2+}-ISA complexes, which serve as reference data for further U-ISA investigations. The changes of the absorption spectra of several test-series, which were caused by pH-changes and ligand concentrations, were measured. The overall 62 UV-vis spectra were evaluated with iterative transformation factor analysis (ITFA), which is a powerful mathematical tool to interpret spectroscopic measurements of an unknown system.[3]

EXPERIMENTAL. $Ca(ISA)_2$ was prepared as described by Vercammen *et al.* and the purity was proofed with powder XRD and ^{1}H-NMR.[4] The NaISA stock solution was prepared, using a cation exchange resin.[1] The amount of Na and Ca was finally determined by ICP-MS. Test solutions for UV-vis measurements were prepared with the NaISA stock solution and a uranyl-perchlorate stock solution. Five test series with the metal to ligand ratios of 2 : 1, 1 : 1, 1 : 2, 1 : 6, and 1 : 16 were prepared. The ionic strength was adjusted to 1 M with $NaClO_4$ and the pH was adjusted with NaOH or rather $HClO_4$. For the UV-vis measurements a 1 cm cuvette and a TIDAS100 spectrometer were used.

RESULTS. The recorded UV-vis spectra of all test series were baseline corrected and evaluated with ITFA. The measured spectra (dotted lines) of the test series with metal to ligand ratios of 1 : 2 and 1 : 16 as well as the four calculated single component spectra (solid lines) were depicted in Fig. 1. Table 1 provides an overview of the absorption maxima and the related extinction coefficients of the four occurring species.

Species 1, which shows an absorption maximum at 414 nm, can unambiguously be assigned to the free uranyl ion.[5] Species 2, 3, and 4 are therefore different UO_2^{2+}-ISA complexes. Interestingly, species 2 occurs at very low pH values, which is indicative for the complex formation with the protonated form of ISA, $[UO_2(HISA)]^{2+}$. This is contrary to other less complex organic ligands.

Species 3 and 4 were successively formed with increasing pH, which in turn is indicative for the complex formation with the deprotonated ISA. Since species 4 was not formed if an excess of UO_2^{2+} was present, species 3 and 4 can consequently be assigned to the 1 : 1 and the 1 : 2 complexes, $[UO_2(ISA)]^+$ and $[UO_2(ISA)_2]$.

The flexible backbone of the ligand as well as the existence of four alcoholic groups might be responsible for the formation of the $[UO_2(HISA)]^{2+}$ complex. To verify this and to determine the binding motives in the complexes it is necessary to use additional methods. For this purpose ATR-FTIR and EXAFS spectroscopy will be applied. This study represents the basis for these investigations, since UV-vis spectroscopy can be used as reference method. The speciation in the samples can be determined, based on the now known single component absorption spectra, which will facilitate the data evaluation dramatically.

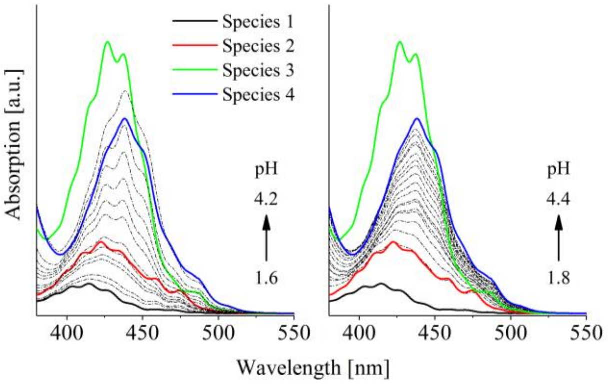

Fig. 1: Measured UV-vis spectra of uranyl-ISA solutions (dotted lines) and calculated single component spectra of species 1 to 4 (solid lines). Metal to ligand ratios: 1 : 2 (left) and 1 : 16 (right); $[UO_2^{2+}]$ = 15 mM.

Tab. 1: Absorption maxima and extinction coefficients.

Species	1	2	3	4
Absorption maximum (nm)	414.0	422.3	426.1	438.1
Extinction coefficient ($L \cdot mol^{-1} \cdot cm^{-1}$)	8.9	21.7	82.2	59.0

ACKNOWLEDGEMENTS. This project has received funding from the Euratom research and training programme 2014-2018 under Grant Agreement no. 61880.

---

[1] Glaus, M. A. *et al.* (1999) *Anal. Chim. Acta* **398**, 111–122.
[2] Van Loon, L. R. *et al.* (1999) *Radiochim. Acta* **86**, 183–189.
[3] Roßberg, A. *et al.* (2003) *Anal. Bioanal. Chem.* **376**, 631–638.
[4] Vercammen, K. *et al.* (1999) *Acta Chem. Scand.* **53**, 241–246.
[5] Bell, J. and Biggers, R. (1965) *J. Mol. Spectrosc.* **18**, 247–275.

Bending the uranyl unit – Synthesis and characterization of $[UO_2Cl_2(phen)_2]$ (phen = 1,10-phenanthroline)

S. Schöne, T. Radoske, J. März, T. Stumpf, M. Patzschke, A. Ikeda-Ohno

The simple U(VI) complex of $[UO_2Cl_2(phen)_2]$ (1) has been synthesized from $UO_2Cl_2{\cdot}nH_2O$ and 1,10-phenanthroline, showing a significant bending of the linear uranyl unit in a unique dodecadeltahedral coordination geometry. An extensive π-stacking network between the phen ligands and the hydrogen bonding interactions between the uranyl oxygens and the hydrogens of the adjacent phen molecules are playing a major role in the formation of 1. These interactions have been further proven by quantum chemical calculations.

The chemistry of uranium is primarily dominated by the oxidation states +4 and +6, where tetravalent uranium (U(IV)) forms a spherical cation, whilst hexavalent one (U(VI)) occurs as a trans-dioxo divalent cation (uranyl unit: UO_2^{2+}) in natural systems. The uranyl unit is remarkably stable and generally shows a linear arrangement in solid state compounds.[1] The coordination chemistry of uranium(VI) is therefore limited to the equatorial plane of the uranyl unit. In most cases, dipyramidal coordination polyhedra are formed with organic- and inorganic ligands. There are only a limited number of examples of different coordination geometries, such as a rhombohedron in the complex $[UO_2(phen)_3][OTf]$ (OTf = O_3SCF_3).[2] Here, we report another example of a uranyl(VI) complex showing a unique dodecadeltahedral geometry with a significantly bent uranyl unit.

EXPERIMENTAL. The synthesis of complex **1** was performed in N_2-filled inert glove boxes. $UO_2Cl_2{\cdot}nH_2O$ ($n = 1$ or 3) was prepared from $UO_3{\cdot}mH_2O$.[3] 1,10-Phenanthroline was used as received. Complex **1** was obtained as yellow precipitate by the addition of a solution of phen in acetone to a solution of $UO_2Cl_2{\cdot}nH_2O$ in acetone, and was recrystallized from hot acetone.

RESULTS. The molecular structure of $[UO_2Cl_2(phen)_2]$ is shown in Fig. 1. The uranium center is eightfold coordinated by two "yl" oxygens (O_{yl}), two chlorines (Cl) and four nitrogens (N) of two phen molecules, forming a unique dodecadeltahedral coordination geometry.

The two coordinating phen molecules are arranged nearly perpendicularly to each other (87.1°). Distinct interactions between the "yl" oxygens/chlorines and the adjacent hydrogens of the phen molecules (dotted lines in Fig. 1) are stabilizing the complex structure. The O–U–O angle in complex **1** is 161.8(1)°, which is one of the smallest uranyl angles reported thus far.[4] In the crystal structure, the $[UO_2Cl_2(phen)_2]$ molecules are connected *via* two distinct π-stacking networks formed by the phen ligands of adjacent molecules.[5] The electronic structure of complex **1** was further investigated by quantum chemical calculations. The DFT-optimized structure with a plot of weak interactions is shown in Fig. 2. The quantum theory of atoms in molecules (QTAIM) analysis on the complex indicates the delocalization index (DI) value of 0.06 between the uranyl oxygen and the adjacent hydrogen as well as 0.1 between the chlorine and the adjacent hydrogen atoms, revealing a weak but distinct interaction between these atoms. These weak interactions between the uranyl oxygens/chlorines and the adjacent hydrogens of phen molecules encourage to compress the volume of complex **1** in the crystal structure, causing the significant bending of the uranyl unit. In fact, the bending of the uranyl unit in the crystal structure involves an energy gain of 29.8 kJ/mol. Hence, the observed bending of the uranyl unit is energetically favorable in the crystal structure of **1**.

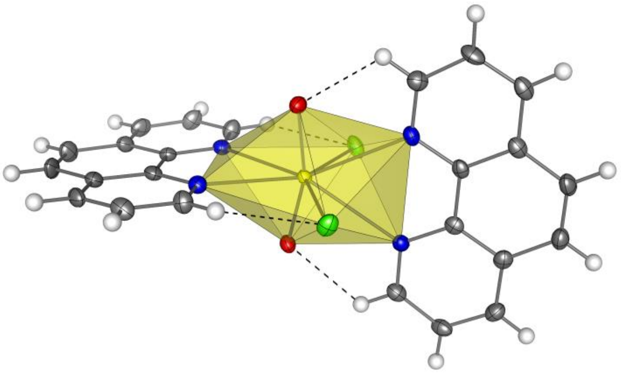

Fig. 1: Molecular structure of $[UO_2Cl_2(phen)_2]$ with dodecadeltahedral coordination geometry around the uranium center. Colour code: carbon (C, gray), hydrogen (H,white), chlorine (Cl, green), nitrogen (N, blue), oxygen (O, red), and uranium (U, yellow).

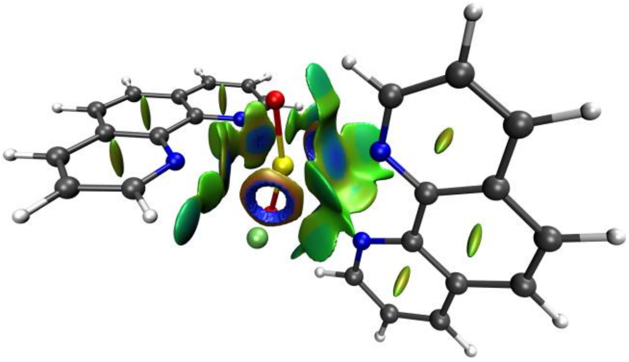

Fig. 2: Plot of weak interactions in the DFT-optimized structure of complex **1**. The degree of the interactions is illustrated by the colour-gradation from blue (strong non-covalent interaction) *via* green (very weak interactions) to red (strong non-bonded orbital overlapping). Colour code: carbon (C, gray), hydrogen (H,white), chlorine (Cl, green), nitrogen (N, blue), oxygen (O, red), and uranium (U, yellow).

ACKNOWLEDGEMENTS. This work was supported by the German Federal Ministry of Education and Research (BMBF) funding under the project number 01176176/1 (FENABIUM).

---

[1] Burns, P. C. (2005) *Can. Mineral.* **43**, 1839−1894.
[2] Berthet, J.-C. *et al.* (2003) *Chem. Commun.*, 1660−1661.
[3] Wilkerson, M. P. *et al.* (2004) in: *Inorganic Syntheses Vol. 34*, pp. 93-95, John Wiley & Sons, Inc., Hoboken, NJ, U.S.A.
[4] Pedrick, E. A. *et al.* (2016) *Inorg. Chem.* **55**, 5693−5701.
[5] Schöne, S. *et al.* (2017) *Chem Eur. J.* **23**, 13574−13578.

Technetium complexes with arylselenolato and aryltellurolato ligands

B. Noschang Cabral,[1] L. Kirsten,[2] A. Hagenbach,[2] P. C. Piquini,[1] M. Patzschke, E. Schulz Lang,[1] U. Abram[2]
[1]Universidade Federal de Santa Maria, Santa Maria, Brazil; [2]Freie Universität Berlin, Berlin, Germany

Technetium is an important fission product in nuclear waste. Its chemistry is different from the lighter and heavier homologous elements. Herein, new compounds forming direct bonds between Tc and M (M = Se, Te) are reported and the bonding situation is analyzed by quantum chemical calculations.[1]

Technetium complexes have been studied for a long time. Many examples of Tc complexes with O and S donor ligands are known, whilst only very few Tc-Se and Tc-Te complexes have been synthesized so far. These examples are cluster compounds. Here we present the synthesis and bonding analysis for the first Tc(V) and Tc(III) complexes with arylselenato or aryltellurolato ligand.

EXPERIMENTAL. Detailed procedures for the preparation of $(NBu_4)[TcOCl_4]$, $[TcCl_3(PPh_3)_2(CH_3CN)]$ and $(ArE)_2$ (see reaction scheme in Fig. 1) were reported in our recent publication.[1] The final products were characterized by means of IR, NMR and X-ray diffraction. Calculations were performed using the PBE and CAM-B3LYP, employing basis sets of triple-zeta quality and using an ECP for Te. All calculations were performed using the Turbomole and Gaussian software packages.

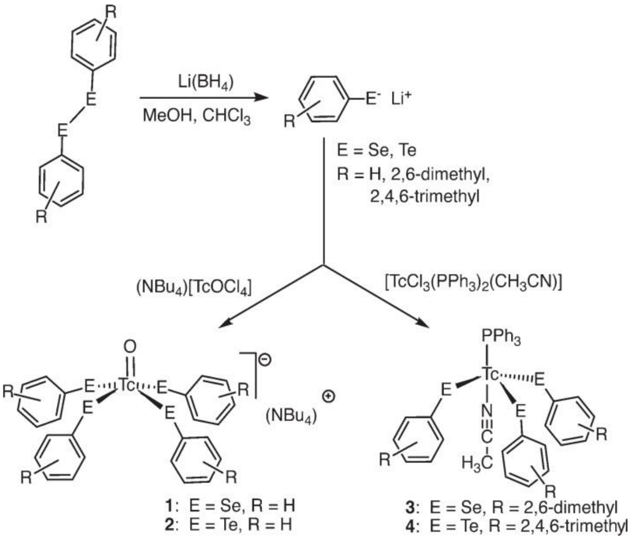

Fig. 1: Synthetic routes to the complexes presented in this study.

RESULTS. In order to obtain the final compounds shown in Fig. 1, special care had to be taken in the choice of reducing agent for the first step. A solution of 2 M $LiBH_4$ in THF was used. This solution cleaves the diaryl-diselenides/ tellurides quantitatively. An excess of reducing agent has to be avoided as the Tc(V) core is otherwise readily reduced.

In Tab. 1, the Tc–Se and Tc–Te distances in the obtained complexes are given. The geometric parameters not involving Se and Te do not change much between species **1** and **2** (Tc(V))**,** and between species **3** and **4** (Tc(III)). The bond distance for the Tc(V) species is in excellent agreement with the single-bond radii published by Pyykkö.[2] Interestingly, the Tc(III) bond distances in species **3** and **4** are between single and double bond radii, a first sign of a stronger interaction in the case of Tc(III). This is supported by the calculated Mayer bond orders of 1.0 for complex **2** (Tc(V)–Te) and 1.3 for complex **4** (Tc(III)–Te).

Tab. 1: Tc–Se and Tc–Te bond lengths for complexes **1**, **2**, **3** and **4.**

Species	Tc–Se (pm)	Tc–Te (pm)
1, **2** (Tc^{V})	247	266
3, **4** (Tc^{III})	238	256

Another useful tool for bond analysis are charges and populations derived from natural bond orbitals (NBO). The charges for Tc are −0.68 in **4** and +0.01 in **2**. This is surprisingly low and hints at an electron donating effect from Te. The slightly positive charge for **2** is due to the interaction with oxygen. When looking at the charges for Te, we find +0.18 for **2** and +0.38 for **4**. This would support the picture of the electron-donating Te. When looking at the d-population of Tc, one finds 6.43 for **2** and 7.17 for **4**. This should be compared to a formal d occupation for Tc(V) of 2 and for Tc(III) of 4, showing a substantial increase in the d-orbital population of Tc upon the formation of both complexes. The picture is very similar for the Se complexes **1** and **3**. This is surprising, as the electronegativity of Se (2.55) and Te (2.1) is somewhat higher than for Tc (1.9). The electron localization function (ELF) in Fig. 2 further supports this picture. The Te attached to Tc(III) is more distorted, a sign of stronger directional bonding. The Tc(III) is also more distorted with higher values of the ELF in the corners of a square, this is a sign of p → d π donation towards Tc.

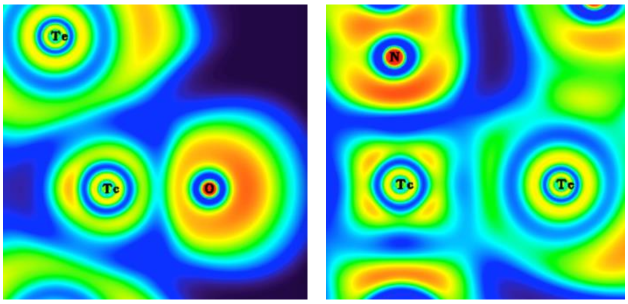

Fig. 2: ELF plot for the Tc–Te bonds in **2** (left) and **4** (right).

CONCLUSIONS. The first instances of heavy chalcogenid-Tc complexes are presented. They show an interesting bonding situation between Tc and Se/Te, where Tc is the electronegative end.

---

[1] Noschang Cabral, B. *et al.* (2017) *Dalton Trans.* **46**, 9280−9286.
[2] Pyykkö, P. *et al.* (2008) *Chem. Eur. J.* **15**, 186−197.

Polynuclear lanthanide complexes based on 8-Hydroxyquinoline-calix[4]arene-scaffold: crystal structures and magnetic properties

A. Jäschke, M. Patzschke, R. Steudtner, S. Schöne, B. Kersting[1]

[1]Institute of Inorganic Chemistry, Leipzig University, Leipzig, Germany.

The Calix[4]arene-based ligand shows a strong affinity towards trivalent lanthanides. We investigated the magnetic properties of the formed tetranuclear complexes in solid state using super conducting quantum interference device (SQUID).

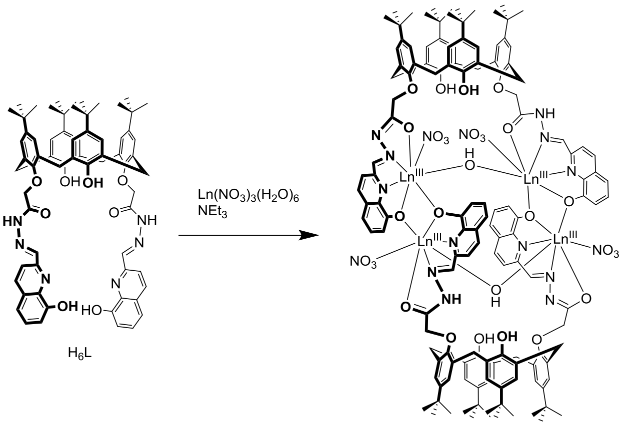

Fig. 1: Synthesis of tetranuclear lanthanide complexes. Ln^{III} = Tb, Dy, Yb .

Under basic conditions, the reaction of H_6L with a variety of lanthanide(III) nitrates generates tetranuclear complexes $[Ln_4(H_3L)_2(OH)_2(NO_3)_4(MeCN)_2]$ (Ln = Tb (**1**), Dy (**2**), Yb (**3**))(Fig. 1).[1] The Ln(III) ions are coordinated by four tetradentate 8-hydroxyquinoline-hydrazone-carbonyl units in a distorted dodecahedral geometry (Fig. 2).

EXPERIMENTAL. Direct current and alternating current analyses were performed on polycrystalline samples. Temperature-dependent (330 K – 2 K) dc magnetic susceptibility measurements were conducted on a MPMS 7XL SQUID (QUANTUM DESIGN) in an external magnetic field of 5 kOe. The magnetic dynamics were explored by ac magnetic susceptibilities (H_{ac} = 2 kOe) under zero and external (H_{dc} = 2 – 3 kOe) dc fields. Diamagnetic corrections were applied for the sample holder (gelatine capsule) and the core diamagnetism from the sample (estimate with pascal constants).

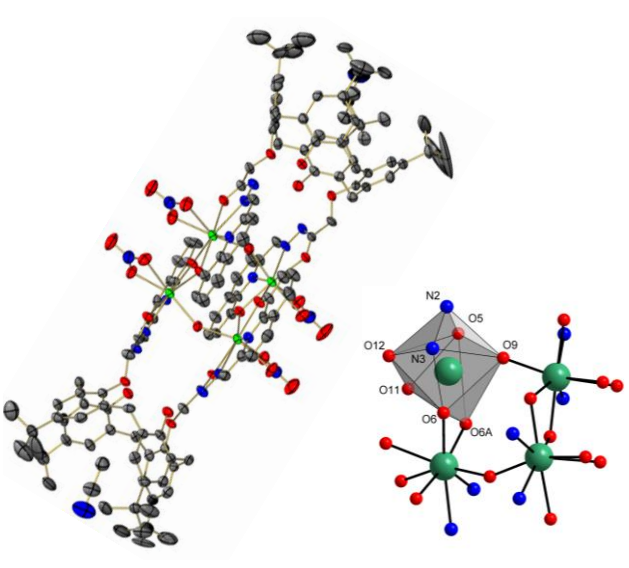

Fig. 2: Molecular structure of $[Ln_4(H_3L)_2(OH)_2(NO_3)_4(MeCN)_2]$ and distorted octahedral coordination polyhedron of the central Ln_4-core.

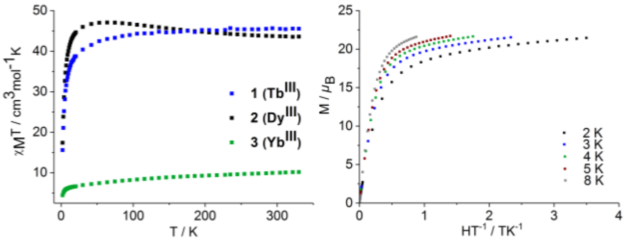

Fig. 3: Temperature dependence of $\chi_M T$ of **1**–**3** (left) and M *vs.* H/T plots below 10 K for **1** (right).

RESULTS. Magnetic susceptibility measurements of complexes **1**–**3** (H_{dc} = 5 kOe, 2 – 330 K) show a strong temperature dependence. The $\chi_M T$ values at room temperature for the Tb(III) (**1**) as well as Yb(III) (**3**) complex are 45.66 and 9.99 cm^3 mol^{-1} K, respectively, which are close to the expected values of 47.28 and 10.28 cm^3 mol^{-1} K for four isolated Tb(III)/Yb(III) ions (Tb: $^7F_6$, g = 3/2; Yb: $^2F_{7/2}$, g = 8/7).[2] With decreasing temperature, the $\chi_M T$ products remain almost constant down to 100 K, but they start to decrease (**3** smoothly decreases), eventually approaching a value of 15.59 for **1** and 4.43 cm^3 mol^{-1} K for **3** at 2 K. Fitting the data for **1** and **3** between 2 and 300 K to the Curie-Weiss law provides a Curie constant (C) of 46.03 and 10.11 cm^3 mol^{-1} K, respectively, and Weiss constants (θ) of −3.75 as well as −11.52 K. The decrease of the $\chi_M T$ products is attributed to the mean different crystal fields around the Ln(III) ions in complexes **1** and **3** due to the progressive depopulation of the excited M_J Stark sublevels.[3] This was also confirmed by the non-superimposition of isothermal curves in the M *vs.* H/T plots below 10 K (Fig. 3). As the coupling between 4f electrons is usually weak due to the core orbital nature of lanthanide ions, the strong magnetic anisotropy and the thermal population of low-lying excited states generally tend to mask these additional possible weak interactions. For the Dy(III) complex **2** the observed room temperature $\chi_M T$ product is 43.68 cm^3 mol^{-1} K, which is considerably lower than the theoretical value of 56.68 cm^3 mol^{-1} K for four uncoupled Dy(III) ions ($^6H_{15/2}$, g = 4/3). This is due to an impurity of the crystalline sample with a binuclear complex species.[1]

In the future, luminescence measurements of the solid samples are planned in order to determine the crystal field splitting of the ground state of the trivalent lanthanides.

---

[1] Jäschke, A. (2017) PhD thesis, Leipzig University.

[2] Orchard, A. F. (2007) *Magnetochemistry*, Oxford University Press, Oxford.

[3] Ren, M. *et al.* (2016) *Dalton Trans.* **45**, 690–695.

Long-Lived Radionuclides & Transport Phenomena in GEOLOGICAL SYSTEMS

Variability in crystal surface reactivity: A critical constraint for reactive transport analysis and modeling

C. Fischer, A. Lüttge[1]

[1]MARUM & Faculty of Geosciences, Universität Bremen, Bremen, Germany

Reactive transport modeling of fluid-solid interactions relies on (*i*) contrasts in fluid flow velocity and (*ii*) variability of surface reactivity. The first point is based on data from, *e.g.*, combined PET and µCT techniques. The second point, however, is usually addressed by simple reaction rate data only. Thus, it neglects information about the intrinsic variability of crystal surface reactivity that often results in a rate range of 2–3 orders of magnitude.[1] Such variability is however an important constraint for the evolution of surface roughness and porosity pattern in crystalline matter. Here, we highlight important sources of the intrinsic variability of crystal surface reactivity and their impact on surface reaction rates. Rate maps and rate spectra provide critical information about the spatial and temporal variability of surface reactivity that is required to predict the evolution of porosity pattern in crystalline matter (Fig. 1).[2]

EXPERIMENTAL AND ANALYTICAL. Experimental settings similar to those in many calcite dissolution studies in literature were used in order to provide comparable results.[1] After each reaction step, the surface topography was analyzed using vertical scanning interferometry (VSI). Using the inert surface section as a height reference, a height difference map was calculated. The height difference (dz) per reaction time (dt) of each (x, y) map point contains information about the height retreat velocity (dz/dt). The material flux map was used to calculate the rate map by dividing each (dz/dt) value by the molar volume. Comparisons to mean reaction rates were calculated by using the mean height retreat of all dz (x, y) values.

RESULTS AND DISCUSSION. The measurable heterogeneity of surface reaction rates is key to mapping concurrently acting reaction mechanisms, which are the kinetic signature of processes at the atomic scale. The analysis of spatially-resolved measured dissolution or precipitation flux maps describes the overall range of reactivity and the spatial heterogeneity of surface reactivity (Fig. 1A). The statistical analysis of flux map data in the frequency domain, using the spectral distributions of rate contributors, allows us to understand how reaction rates vary in time and space (Fig. 1B). Consequently, this information has been integrated in the concept of “rate spectra”. We apply the quantitative information from the experimental results about rate spectra modes and amplitudes (Fig. 1) to calibrate kinetic Monte Carlo (kMC) simulations. Variations in the type and spatial density of crystal defects were implemented. More specifically, the difference in the observed contrast in material flux of experimental *vs.* kMC results was minimized. The experimental determinations of surface roughness and topography results revealed the predominance of particular defect types as controlling factors of the observed rate variability (Fig. 1A, sections 1–3). This information was used as the first input, and the material flux results were then optimized by varying the defect density in the kMC model.

An important constraint for model parameterization is the amount of surface normal retreat. Using this constraint and the parameter variations discussed above, unambiguous parameterization leads to modeling results that show strong similarities to the experimental results of rate mapping. The grains 1 and 2 contain contrasting screw dislocation densities, *i.e.*, 30 *vs.* 1000 defects per grain. Grain 3 contains point defects only.

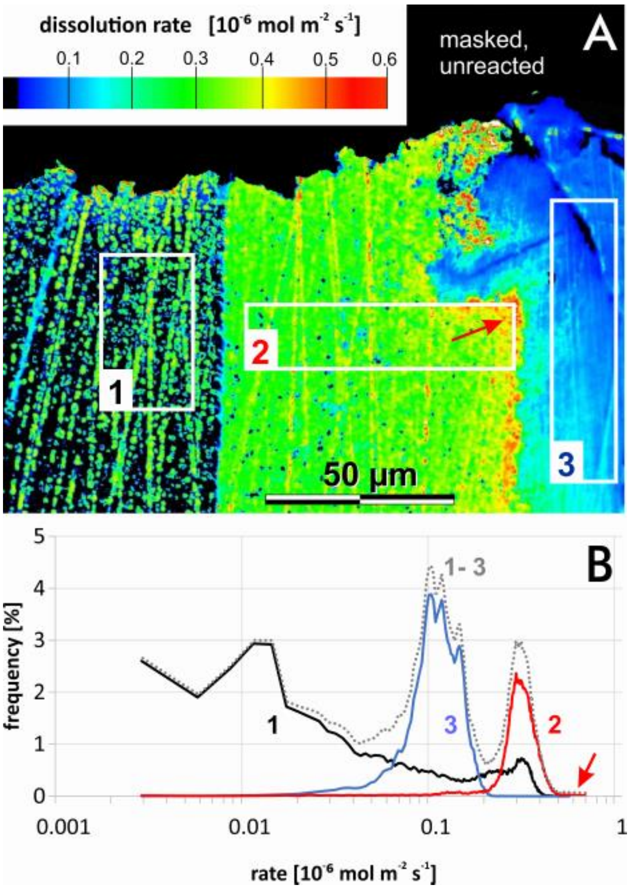

Fig. 1: Dissolution rate heterogeneity of polycrystalline calcite analyzed using (A) rate map visualization based on interferometry data and (B) rate spectra, based on three subsections of (A), each area is 1600 µm^2. The arrow indicates the highest reactivity at the grain boundary in-between grains 2 and 3.

The results suggest that a meaningful modeling of spatial patterns of both surface reactivity and porosity is realizable by the specification of defect type and density in kMC simulation calculations.[2] Further investigation into and the resulting quantitative information on such parameters are required for a multitude of geomaterials. We further conclude that the combination of experimental and modeled rate spectra results with reactive transport models has the potential for upscaling reaction rates that allow for a reliable prediction of material fluxes in reacting fluid–solid systems.

ACKNOWLEDGEMENTS. This work was funded by the German Research Foundation (DFG) grant # Fi1212/7 to CF (at U Bremen).

---

[1] Arvidson, R. S. *et al.* (2003) *Geochim. Cosmochim. Acta* **67**, 1623–1634.
[2] Fischer, C. *et al.* (2017) *Earth Planet. Sci Lett.* **457**, 100–105.

3D reactive transport modeling of leaching a single-fractured rock core. Part I: The fluid flow model

L. Karimzadeh, J. Kulenkampff, S. Schymura, J. Lippmann-Pipke[1]

[1]Federal Institute for Geosciences and Natural Resources (BGR), Hannover, Germany

In the framework of the EU-funded research project BIOMOre,[1] we focus on (*i*) leaching experiments on the lab scale and (*ii*) the related reactive transport modeling. A critical challenge of our tasks is the implementation of the feedback in-between the alteration of porosity due to calciferous copper ore dissolution and related modifications of the hydrodynamics of the reacting fluid. Here, we present simulation results of the lixiviant flow in an induced single-fractured rock core sample. The second part (this volume) focuses on the mineral leaching and solute transport in the core.

EXPERIMENTAL. A mechanically induced fracture (Fig. 1a) was obtained by a geomechanical shear test on a sandstone drill core (D = 6 cm, L = 10 cm) sampled from the Permian Kupferschiefer ore formation (Rudna mine, Poland). The fractured sample was encased in Plexiglas column using silicon and epoxy resins to seal the column wall prior to taking a µCT-scan (Fig. 1b). Column leaching experiments using the core sample were carried out at constant injecting flow rate of 1 mL/h.

MODELING. For modeling, the fractured core sample was conceptualized as one half of a cylinder, with a horizontal fracture with 0.5 mm aperture with a randomly distributed heterogeneous porosity (Fig. 2a) with 1.5 mL of total pore volume as measured by conservative tracer experiment. The rock core matrix was assigned a homogeneous porosity of 10 % as indicated by measurements.
Fluid flow in the fracture is simulated by the Navier-Stokes equations, while the flow in the matrix is described by the Brinkman equations. The coupling of fracture and matrix flow in the model is achieved by using the Brinkman-Forchheimer equations.[2] Due to a very low matrix *vs.* fracture permeability, advection in the porous matrix set to zero. Here, only diffusion takes place.

RESULTS. The governing equations for fluid flow and conservative tracer transport are solved within the finite element code COMSOL Multiphysics®. The experimental breakthrough curve (BTC) from the conservative tracer experiment were used to parameterize the solute transport in the model on the basis of the best fit under the assumption that matrix diffusion is a fading mechanism and advection dominates tracer transport through the fracture. Thus, the model is capable of utilizing effective porosity and effective velocity field v_i (v_{ix},v_{iy},v_{iz}) data, extracted from GeoPET transport process visualization on a 1.15 mm³ grid.[3] On that scale, the model will later be complemented with a complete set of geochemical reactions simulating dissolution, precipitation, and solute transport.

ACKNOWLEDGEMENTS. We gratefully acknowledge financial support by the European Commission Horizon 2020 research and innovation program, project grant agreement No. 642456. We thank KGHM Polska Miedź S. A., Poland, for providing sample material, and the Institute of Geotechnics, Technical University Bergakademie Freiberg, Germany, for inducing a well-defined fracture to the sample. We also thank Stefan Gruhne for sample preparation.

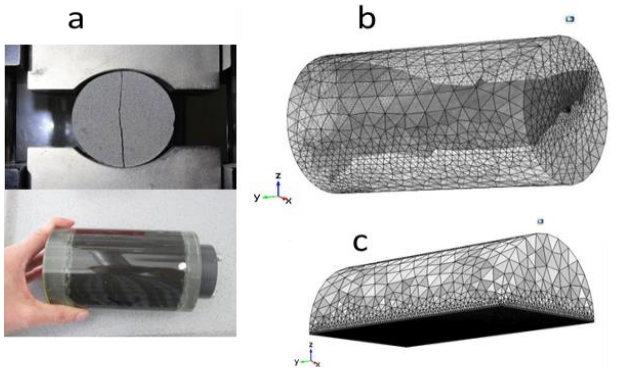

Fig. 1: (a) Induced single fracture and sample preparation, (b) overlay of the fracture geometry obtained from µCT scans and finite element meshes of the core (b), and (c) finite element meshes of the simplified geometry used in the current model.

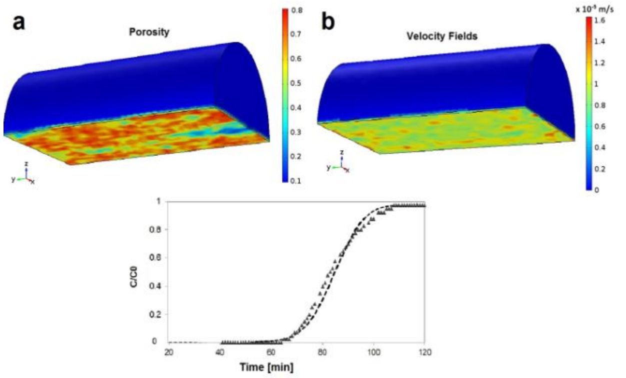

Fig. 2: (a) Porosity, (b) calculated velocity fields in flow direction (v_{iy}), and (c) normalized tracer transport breakthrough curve (BTC) obtained from experiments (triangles) and modelling (dotted line).

---

[1] http://www.biomore.info/home (as of: 18/02/13).
[2] COMSOL Multiphysics Reference Manual, V5.3, COMSOL, Inc., www.comsol.com.
[3] Kulenkampff, J. *et al.* (2016) *Solid Earth* **7**, 1217−1231.

3D reactive transport modeling of leaching a single-fractured rock core.
Part II: The reactive solute transport model

L. Karimzadeh, S. Schymura, J. Kulenkampff, R. Möckel, J. Lippmann-Pipke[1]

[1]Federal Institute for Geosciences and Natural Resources (BGR), Hannover, Germany

Mineral dissolution and the transport of reactive and nonreactive solutes in a rock core sample with an induced single fracture were studied. A combination of column leaching experiments and three-dimensional modeling was applied to investigate coupled mineral dissolution and precipitation reactions and to study the solute transport through the core sample.

EXPERIMENTAL. The experimental setup is described elsewhere.[1] The fluids were injected into the sample at a constant flow rate of 1 mL/h in three stages: (1) a moderately hard synthetic fresh water (pH = 8.5, 22 days) to remove salt minerals, (2) an acidic solution with pH 1.5 (H_2SO_4, 23 days) to reduce the carbonate content, (3) 0.17 mol/L concentrated ferric iron added to the acidic solution (pH 1.5, H_2SO_4, 20 days) in order to dissolve the Cu-sulfid minerals and increase the copper recovery from the sample.

MODELING. Geochemical modeling was conducted by means of the COMSOL-PHREEQC interface iCP. The core matrix consist of a homogenous mineral composition according to XRD measurements (not shown here). The chemical processes considered in the model are kinetically controlled mineral dissolution and precipitation in the porous media simulated by means of PHREEQC,[3] using a BRGM database, and advective-dispersive transport in the fracture and matrix diffusion in the rock mass calculated by COMSOL Multiphysics.[1]

The porosity evolution resulting from mineral dissolution and precipitation processes for each cell is calculated *via* the changes of the mineral volume fraction occurring between two successive time steps.

RESULTS. Adjustment of the reactive mineral surface area was used to match the variation of the aqueous concentrations with time (Fig. 1). The simulated change in calcite and gypsum content and the porosity change after 20 days of washing with sulfuric acid are shown in Fig. 2. At this first stage, the calcite dissolution rate is relatively low. The acid fluid during stage 2 of the experiment causes a rapid increase of the calcite dissolution rate in the fracture and, with a considerable lower rate, in the matrix (Fig. 2a). This difference of the magnitudes of the calcite dissolution rates is directly related to the advective transport in the fracture and the diffusive transport within the rock matrix. Secondary gypsum forms in the sample with the intrusion of sulfuric acid into the sample (Fig. 2b). The gypsum precipitation rate is controlled by both, Ca^{2+} from calcite dissolution in the matrix and SO_4^{2-} supplied from the injected solution.

ACKNOWLEDGEMENTS. We gratefully acknowledge financial support by the European Commission, Horizon 2020, research and innovation program, project grant agreement No. 642456.We also thank P. Blanc, BRGM, France, for providing the thermodynamic data sets, M. Schlegel, GEOS Freiberg, for mineral composition data, and M. Eckart, DMT, Germany for discussions. We also thank C. Schößler for her support related to laboratory works.

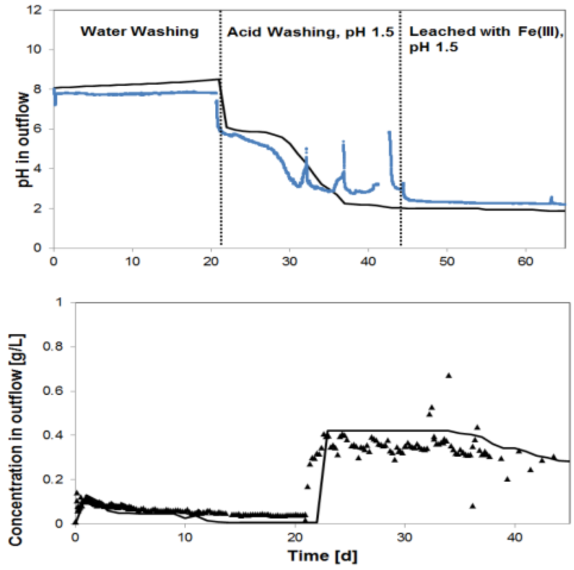

Fig. 1: Measured (symbols) and modelled (lines) pH (upper) and Ca^{2+} concentrations after leaching with water, sulfuric acid, and Fe(III).

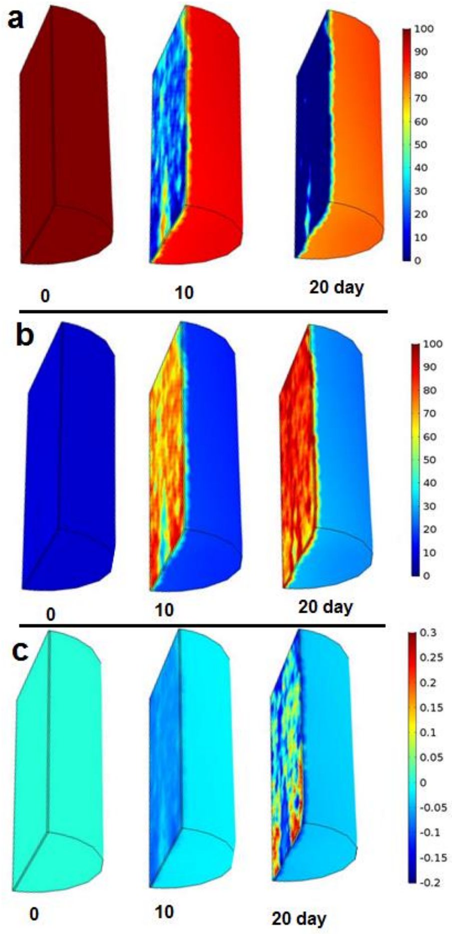

Fig. 2: (a) Calcite concentration (normalized to its initial value of 25.3 g/L_{rock}), (b) secondary gypsum concentration (normalized to its maximum concentration (21.78 g/L_{rock}), and (c) porosity change in % in the sample after 0, 10 and 20 days of washing with sulfuric acid (experimental step 2).

---

[1] Karimzadeh, L. (2018) this report, p. 28.

[2] Nardi, A. *et al.* (2014) *Comput. Geosci.* **69**, 10–21.

[3] Parkhurst, L. D. *et al.* (1999) *User's guide to PHREEQC U.S.G.S.*, Denver, p. 326.

Heterogeneous flow and its influence on breakthrough curves: evidence and reactive transport modeling

H. Lippold, L. Karimzadeh, J. Kulenkampff, L. Wissmeier,[1] C. Stuhlfauth,[2] J. Lippmann-Pipke[3]

[1]AF-Consult Switzerland AG, Baden, Switzerland; [2]Johannes Gutenberg University, Mainz, Germany; [3]Federal Institute of Geosciences and Natural Resources (BGR), Hannover, Germany

Interaction constants obtained from batch studies often fail to describe the retention of solutes in column experiments. This is commonly ascribed to non-equilibrium conditions. The present study shows that inconsistencies between static and dynamic systems can be caused by heterogeneous fluid flow as well; evidenced by Positron Emission Tomography (PET) and quantitatively demonstrated by 2D reactive transport modeling. The results underscore that predictions of contaminant transport need thorough consideration of realistic flow fields.

EXPERIMENTAL. $^{18}F^{-}$ as a PET tracer was produced at the in-house cyclotron “CYCLONE 18/9” (IBA). 5 mL of 10 mM KF in 1 mM $NaNO_3$ was added as a carrier. This solution was injected into a column (10 cm × 4 cm ID) packed with goethite-coated sand (1 wt-% goethite), run with 1 mM $NaNO_3$ (0.1 mL min^{-1}) upright in the field of view of the PET scanner “ClearPET” (Elysia-Raytest). A breakthrough curve for the herbicide MCPA (2-methyl-4-chlorophenoxyacetic acid) was recorded as described in a previous report.[1] Adsorption as a function of pH was determined in batch experiments with 1000 g L^{-1} sand-goethite material in order to calibrate the applied surface complexation model.

RESULTS. PET imaging of the $[^{18}F]F^{-}$ distribution after pulse injection (Fig. 1a) revealed preferential flow in the periphery of the column, with accelerated transport and significant dilution in spite of careful packing.

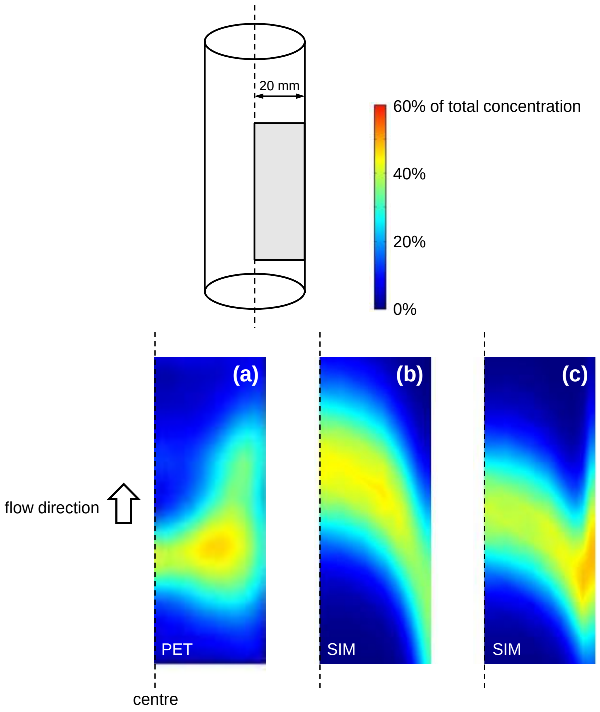

Fig. 1: Half longitudinal section view of a $[^{18}F]F^{-}$ injection pulse in a sand-goethite column. PET image (a), 2D simulation assuming a homogeneous distribution of porosity and permeability (b), 2D simulation assuming increased porosity and permeability in a 1-mm peripheral zone (right-hand edge) (c).

The flow pattern to be expected for this geometry (Fig. 1b) was calculated using the finite element method software COMSOL Multiphysics®, based on the advection-dispersion-reaction equation with flow velocities controlled by the pressure gradient field according to Darcy’s law. In Fig. 1c, this modeling was performed assuming a 1-mm peripheral zone where porosity and permeability exceed the bulk values by a factor of 2 and 4, respectively. With this heterogeneous model, the main characteristics of the observed flow pattern can be roughly reproduced.

Fig. 2 shows a breakthrough curve for MCPA along with results of reactive transport modeling. Chemical interaction between MCPA and goethite is described by the CD-MUSIC surface complexation model with parameters adjusted to adsorption in batch systems, partly taken from Kersten *et al.*[2] The 1D calculation was carried out using the speciation program PHREEQC with hydrodynamic parameter values obtained from a fit to the breakthrough of $[^{3}H]H_2O$ as a conservative tracer. In the 2D calculations, the CD-MUSIC model was combined with the flow models applied in Fig. 1b (homogeneous) and Fig. 1c (heterogeneous), using the Java interface iCP, which couples the codes PHREEQC and COMSOL Multiphysics®.[3]

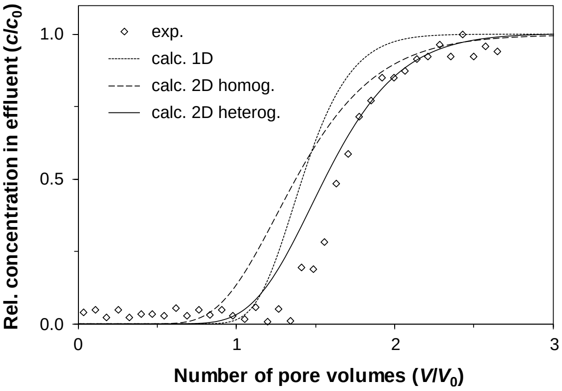

Fig. 2: Experimental and modeled breakthrough curves for MCPA (pH 3.5). The 1D simulation considers longitudinal dispersion only. The homogeneous and heterogeneous 2D simulations are based on the flow models applied in Figs. 1b and 1c, respectively.

With a homogeneous distribution of porosity and permeability, retardation is underestimated as with the 1D model. However, if the peripheral flow effect is considered, the calculated breakthrough is significantly shifted towards higher retention times, and almost coincides with the experimental data.

These results demonstrate that heterogeneous flow needs to be adequately considered in predictive transport models. Disregarding this effect impairs the meaningfulness of interaction constants.

ACKNOWLEDGEMENTS. This work was funded by the German Research Foundation (DFG), support code LI872/5, within the priority program SPP 1315.

---

[1] Lippold, H. *et al.* (2015) *Report HZDR-067*, p. 36.
[2] Kersten, M. *et al.* (2014) *Environ. Sci. Technol.* **48**, 11803−11810.
[3] Nardi, A. *et al.* (2014) *Comput. Geosci.* **69**, 10−21.

Quantitative visualization of ^{22}Na$^+$-cation transport at a salt-cement contact

J. Kulenkampff, K. Jantschik,[1] H. C. Moog[1]
[1]Gesellschaft für Anlagen- und Reaktorsicherheit (GRS) gGmbH, Brunswick, Germany

Transport of ions at the in the vicinity of the interface between the geological and the engineered barrier is a heterogeneous process with strong spatial variability. We successfully applied positron emission tomography (GeoPET) for quantitative visualization of migration of a ^{22}Na radiotracer at the salt-cement interface of a well-defined sample of drill core size.

The host-rock – cement interface is a closely folded heterogeneous volume. First, its structure is caused by the roughness of both material surfaces, with thin interstitial voids. Second, the host-rock near the interface is disturbed by excavation damage. Third, the cement is composed of a heterogeneous mixture of different components. This causes strong spatial variability of transport and exchange processes. Such heterogeneity is no specific characteristic of a particular type of host rock. It is a current topic of research in clay rock (EU-project CEBAMA) and salt (this study).[1] Here, we utilize GeoPET to study transport of ^{22}Na$^+$-cations in the vicinity of such interfaces and to elucidate local variations, which are missed by conventional investigation methods.[2]

EXPERIMENTAL. An aged salt cement plug (diameter 35 mm) was inserted into an axial drill hole through a cylindrical halite drill core (diameter 70 mm, length 100 mm). This compound sample was flushed with concentrated salt brine until it became impermeable by salt deposition. Afterwards it was cast with resin (Araldite) into an acryl glass cylinder. A µCT image of the complete sample is shown in Fig. 1.

The complete sample was covered with end caps, leaving a small head space of 0.6 mL between sample and end caps that serves as tracer reservoir. Salt brine was labelled with 3.16 MBq of ^{22}Na and injected into this head space.

A total of 23 PET-frames were recorded with a frame length of 30 min and increasing time lag over a period of 71 days. The PET-data were corrected and reconstructed according to our standard procedure.[2]

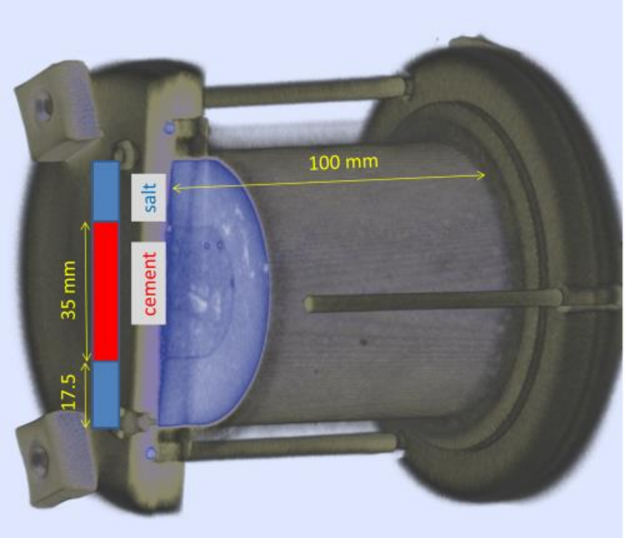

Fig. 1: µCT-image of the sample with cut at the injection port. The joint between salt and cement, as well as the head space, are detectable, but below image resolution of 30 µm.

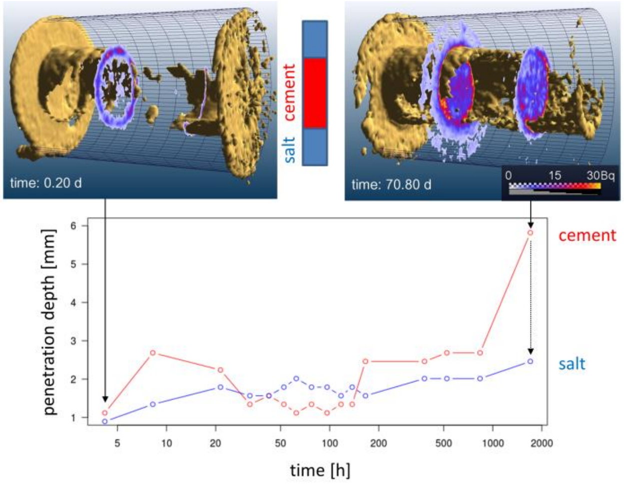

Fig. 2: Top: first and last (71 days) PET-frame. Light brown: isosurface of the maximum tracer activity (seam); blue-red color coded: two transaxial slices of the tracer activity. Bottom: mean radial diffusion depth of the tracer (interquartile range of the mean radial concentration profile).

RESULTS. An initial PET-image shows the penetration of the tracer into the contact zone immediately after injection (Fig. 2: t = 0.2 d). The tracer distribution shows a narrow and spatially fluctuating pattern. Obviously, the sealing of the joint was not perfect, and tracer was sucked into the void space of the joint immediately after tracer injection into the head space. This process – although undesirable in the real repository – is a proper example for demonstrating the suitability of the method of quantitative tracking of liquid leakage.

This heterogeneous pattern (Fig. 2: t = 0.2 d) is the source for subsequent diffusion of ^{22}Na$^+$ into the adjacent material. Figure 2 (t = 70.8 d) shows the last PET-frame. It shows the preferred propagation of the activity into the cement volume.

We computed the mean radial concentration profile, averaging over all slices and all azimuth direction angles. As robust statistical measure of the diffusional penetration depth, we defined the interquartile range from the position of the contact in outward direction (salt) and inward direction (cement). Within the experimental period we did not observe significant propagation into the salt (Fig. 2 bottom, blue line), but observable diffusion into the cement volume (red line). More sophisticated algorithms, applying inverse modelling, have been developed for computing the diffusion coefficient quantitatively.[3]

ACKNOWLEDGEMENTS. The research leading to these results has received funding from the European Union's Horizon 2020 Research and Training Programme of the European Atomic Energy Community (EURATOM) (H2020-NFRP-2014/2015) under grant agreement n° 662147 (CEBAMA).

---

[1] Kulenkampff, J. *et al.* (2017) *KIT Scientific Report* **7734**, 113−119.
[2] Kulenkampff, J. *et al.* (2016) *Solid Earth* **7**, 1217−1231.
[3] Kulenkampff, J. *et al.* (2016) *Solid Earth* **7**, 1207−1215.

Visualizing concentration distributions in macroscopic samples during ore leaching

J. Kulenkampff, L. Karimzadeh, S. Schymura, R. Barthen, M. Gründig, H. Lippold, J. Lippmann-Pipke[1]
[1]Federal Institute for Geosciences and Natural Resources (BGR), Hanover, Germany

In-situ leaching of ores is a complex reactive transport process that is largely controlled by the chemical and hydrological heterogeneity of the material and the respective transport process. We applied the combination of our two imaging tools: positron emission process tomography for imaging both fluid flow and dissolution, coupled with the new µCT for determining the internal structure of the material.

EXPERIMENTAL. In our showcase experiment we leached copper from pebbles that have been artificially coated with [^{64}Cu]CuS (covellite). The PET-experiment consists of two stages:

(1) Quartz pebbles were coated with [^{64}Cu]covellite that was synthesized by microwave assisted chemical bath deposition.[1] The depletion of the ^{64}Cu activity concentration in the surface layer during leaching with glutamic acid was imaged with positron emission tomography (GeoPET).[2,3] We determined the local covellite leaching rates from the decay-corrected ^{64}Cu activity decrease in each voxel (Fig. 1).

(2) After decay of the ^{64}Cu-radionuclide, we conducted a conservative flow experiment with synthetic pore water, labelled with ^{18}F, to visualize the major transport pathways (Fig. 2).

The internal structure and geometry of the pebble pack was obtained with our new µCT-imaging facility (Nikon XT H 225). The geometry was used for proper attenuation and scatter correction of the GeoPET, and the internal structure will be used as well in pore scale reactive transport simulations.

RESULTS. The image overlay of GeoPET with µCT results is a powerful tool considerably improving the process understanding of reactive and conservative solute transport in porous media. Our first results show the strong localization of the flow pathways, along which we assume the leaching process to be more effective than off the beaten track. This is an explanation of the reported discrepancy between low global column leaching rates and higher batch leaching rates, because a smaller portion of the reactive surface is affected by the flow field.

ACKNOWLEDGEMENTS. We gratefully acknowledge financial support by the German Federal Ministry of Education and Research (BMBF), project ref. no. 033RF001, and by the Agence Nationale de la Recherche (ANR), France.

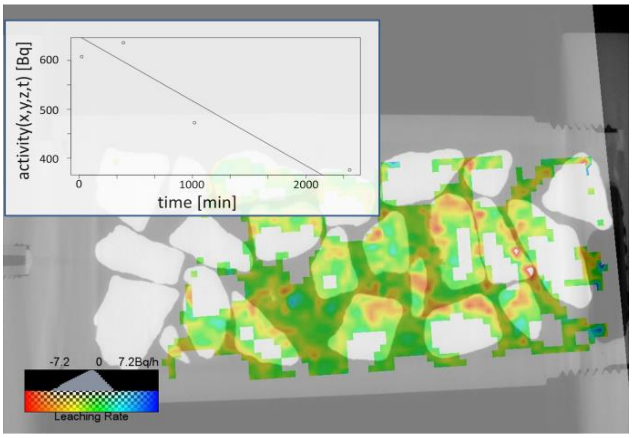

Fig. 1: Overlay of a µCT-slice of the pebble column (grayscale image) combined with the linear approximation of local leaching rates, computed from the [^{64}Cu]covellite –PET frames during leaching with glutamic acid. Colour scale: maximum leaching rate −7.2 Bq/h (red), neutral (green), positive values (blue) would imply deposition of ^{64}Cu. Inset: exemplary activity-time curve at one single representative voxel.

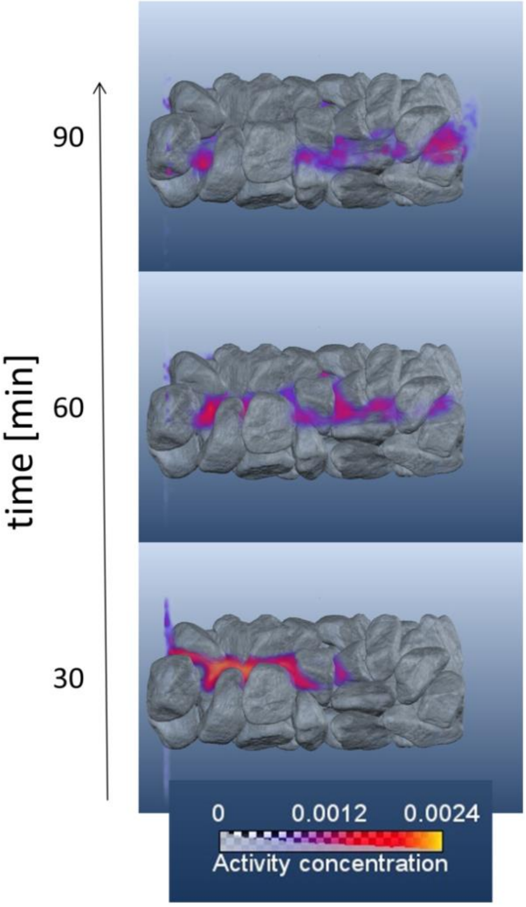

Fig. 2: Three frames out of the suite of PET-frames (integration time 2 min each), overlain by the µCT-image that was applied for attenuation and scatter correction illustrating the fluid transport.

---

[1] Xin, M. et al. (2009) *Appl. Surf. Sci.* **256**, 1436−1442.
[2] Barthen, R. *et al.* (2018) *Chemosphere* **196**, 368−376.
[3] Kulenkampff, J. *et al.* (2016) *Solid Earth* **7**, 1217−1231.

Radiosynthesis of dual-labeled [^{75}Se]CdSe/[^{65}Zn]ZnS quantum dots

S. Schymura, L. Eckert, R. Steudtner, R. Hübner,[1] K. Franke
[1]HZDR, Institute of Ion Beam Physics, Dresden, Germany

Dual-labeled core-shell [^{75}Se]CdSe/[^{65}Zn]ZnS nanoparticles were synthesized. The dual label allows the independent tracking of the nanoparticulate core and the potentially dissolving shell.

Environmental transformations of nanoparticles (NPs) such as dissolution can have a major impact on the risk assessment of manufactured nanomaterials. Smart radiolabeling approaches have been shown to be a helpful tool in tracking dissolution phenomena of CeO_2 NPs in such complex media as plants.[1] In the same vein, we developed a radiosynthesis route for dual-labeled quantum dots (QDs) with core-shell structure allowing for the independent tracking of the nanoparticulate core and the potentially dissolving shell.

EXPERIMENTAL. The synthesis route consisted of two steps. In the first step a precursor solution of [^{75}Se]Se in octadecene was injected into a cadmium precursor solution of CdO in octadecene and oleyic acid at 225 °C to form CdSe nanocrystallites.[2] After a certain reaction time the solution was allowed to cool down and unreacted precursors were removed by multiple methanol extractions. In the second step sulfur and [^{65}Zn]ZnO precursors in octadecene were injected simultaneously into CdSe QD solutions at 225 °C and reacted for 30 min to form a ZnS shell.[3] Reaction yields were monitored by UV-vis spectroscopy and the resulting QDs were characterized by UV-vis, fluorescence spectroscopy, STEM and DLS.

RESULTS. Once the Se precursor solution is injected the reaction yield quickly rises above 90 % within 15-30 min as the initially formed CdSe nanocrystallites grow to sizes between 2 and 4 nm depending on reaction time (Fig. 1). Due to their nature as quantum dots absorption and fluorescence peaks show a distinct redshift with increasing size (Tab. 1).[4]

In the second step the formation of a ZnS shell is confirmed by STEM-EDXS (Fig. 2) and absorption and fluorescence peaks of the CdSe core are largely retained.

The synthesized QDs can be transferred into aqueous solution by a ligand exchange with hydrophilic mercaptopropionic acid.

ACKNOWLEDGEMENTS. We gratefully acknowledge funding by the BMBF within the NanoNature program (FKZ: 03X0144A).

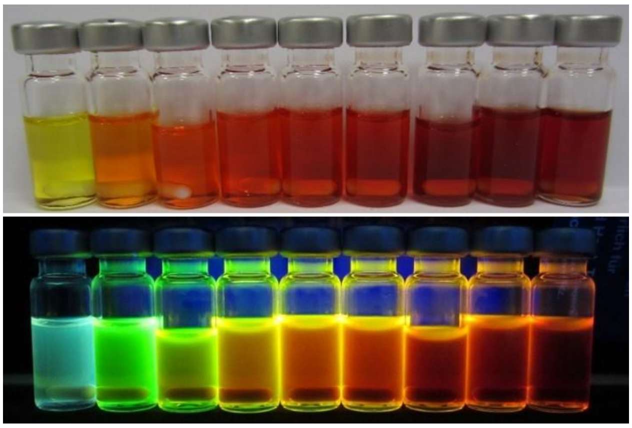

Fig. 1: Colloidal suspensions of CdSe quantum dots of increasing size from left (approximately 2.3 nm diameter) to right (approximately 4.0 nm diameter). Top: Samples viewed in ambient light vary in color from green–yellow to orange–red. Bottom: The same samples viewed under long-wave ultraviolet illumination vary in color from blue to orange-red.

Tab. 1: Absorption E_p and F_p fluorescence peaks, sizes and yields for CdSe quantum dot synthesis for different reaction times.

Reaction time (min)	E_p (nm)	F_p (nm)	Size (nm)*	Yield (%)*
0	488	473	2.30	9.6
1	521	510	2.70	20.5
2.5	542	534	3.04	39.2
5	556	548	3.32	55.3
7.5	562	552	3.46	66.5
10	567	557	3.58	77.8
15	573	561	3.74	92.9
20	577	568	3.85	95.0
30	580	568	3.94	101.3

*: calculated from UV-vis data.[5]

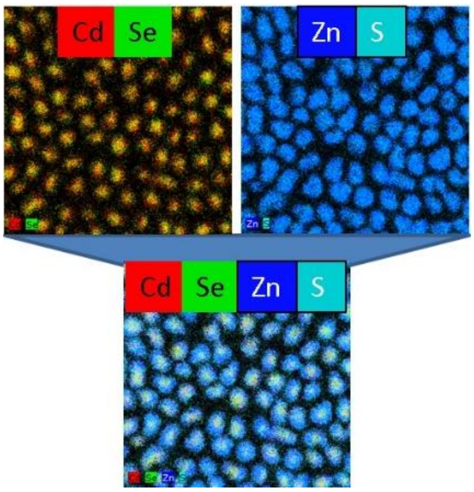

Fig. 2: STEM-EDXS element maps of CdSe/ZnS quantum dots with distributions of Cd and Se, Zn and S and the overlay, respectively.

---

[1] Schymura, S. *et al.* (2017) *Angew. Chem. Int. Ed.* **56**, 7411−7414.
[2] Nordell, K. *et al.* (2005) *J. Chem. Educ.* **82**, 1697−1699.
[3] Xie, R. *et al.* (2005) *J. Am. Chem. Soc.* **127**, 7480−7488.
[4] Kippeny, T. *et al.* (2002) *J. Chem. Educ.* **79**, 1094−1100.
[5] Jasieniak, J. *et al.* (2009) *J. Phys. Chem C.* **113**, 19468−19474.

Uranium(VI) sorption onto hematite: The benefit of using chemically evident surface species in surface complexation modeling

F. Bok

Numerous experimental raw data on the protolysis of hematite and sorption of uranium(VI) onto this mineral are available in literature. Using these data, a thermodynamic sorption data set could be created based on a realistic surface chemistry. It requires only one species for both: inert and carbonate containing systems.

Hematite (α-Fe_2O_3) is one of the iron(III) mineral phases ubiquitous in nature and one of the main corrosion products of container material for radioactive waste. Thus, its interaction with radionuclides (*e.g.* uranium) is a major retardation processes to confine the distribution of uranium in groundwater and thus the biosphere. Quality assured and consistent thermodynamic data are necessary for the description of uranium sorption onto hematite, *e.g.*, in safety case calculations.

CALCULATION. The literature indicates surface site density (SSD) values from 0.12 to 22 nm^{-2}. Both limits are obviously unrealistic. Also, some measurement methods (*e.g.* tritium replacement) are not likely to be suitable for determining the SSD for larger sorbing ligands (*e.g.* uranium). Thus, SSD was calculated from crystallographic data using the software package 'Mercury CSD'.[1, 2] In contrast to many other minerals, hematite does not have a dominant crystal form. There are well over 40 different morphologies known for α-Fe_2O_3. Therefore, the 16 most frequently occurring morphology planes were selected for the SSD determination. For each plane, the number of surface oxygen atoms per square nanometer, which can be assigned to one octahedron only, was determined and assigned to a ≡FeOH site. Subsequently, the obtained single planes SSD values were averaged to a total SSD value.

For the thermodynamic data necessary for surface complexation modeling, already published experimental data were critically examined. The experimental data points were redigitized using the software package 'Engauge-Digitizer'.[3] For the fitting procedure the parameter estimation software 'UCODE2014' was coupled with the geochemical speciation code 'PhreeqC' using the aqueous speciation and mineral solubility data based on the 'PSI/Nagra Chemical Thermodynamic Database 12/7'.[4–6] The Diffuse Double Layer model has been used to describe the sorption process. First, the obtained titration data points yielded the protolysis constants (p$K_{a1/2}$) using a 2pK approach:

$$\equiv FeOH_2^+ \leftrightarrow \equiv FeOH + H^+$$
$$\equiv FeOH \leftrightarrow \equiv FeO^- + H^+$$

SELECTION OF SURFACE SPECIES. In the literature, many different surface species have been postulated for the sorption of uranium(VI) to hematite: mono- and bidentate species, hydrolysed uranium species and also ternary uranyl carbonato surface complexes. EXFAFS investigations indicate a bidentate surface complex on the goethite minerals surface.[7] The chemical similarity of the surfaces of both iron minerals (octahedrons from Fe^{3+} and O^{2-}) leads to the assumption that a comparable surface complex will also be present on hematite:

Tab. 1: Surface complexation data set for the sorption of uranium(VI) onto hematite.

Model parameter	Value
Site density	5.7 nm^{-2}
Protolysis constant 1 (pK_{a1}°)	6.50 ± 0.03
Protolysis constant 2 (pK_{a2}°)	10.07 ± 0.08
Formation constant for surface complex ($\log_{10}K$°)	−3.82 ± 0.08

$$2 \equiv FeOH + UO_2^{2+} + 3\ H_2O \leftrightarrow (\equiv FeO)_2UO_2(H_2O)_3^0 + 2\ H^+$$

The surface complex formation constant ($\log_{10}K$) was fitted to the experimental sorption data points using the previously obtained SSD and p$K_{a1/2}$ values.[8–11]

RESULTS. The model parameters are listed in Tab. 1. The use of one binary bidentate surface complex is sufficient to fully describe the sorption of uranium to hematite (Fig. 1). This includes ternary systems containing carbonate. No further ternary surface species is necessary for the description of all U(VI)-CO_2-Fe_2O_3 systems where experimental data points from sorption experiments are available that have passed the critical evaluation (see Fig. 2).[12, 13] In combination with 'PSI/Nagra Chemical Thermodynamic Database 12/7', this robust and chemically evident model can be extrapolated over a wider range of environmental conditions.

ACKNOWLEDGEMENTS. Thanks to Madlen Stockmann and Juliane März for discussions on usage of several software packages.

---

[1] Blake, R. L. *et al.* (1966) *Am. Mineral.*, **51**, 121–129.
[2] Mercury CSD 3.9 software package, http://www.ccdc.cam.ac.uk/mercury (2017-03-23).
[3] Mitchell M. (2014) Engauge Digitizer, https://github.com/markummitchell/engauge-digitizer (2017-09-12).
[4] Poeter, E. P. *et al.* (2005) *IGWMC Report number GWMI 2014-02.*
[5] Parkhurst, D. L. *et al.* (2013) *U.S. Geological Survey Techniques and Methods, Vol. book 6-A43.*
[6] Thoenen, T. *et al.* (2014) *PSI Report No. 14-04.*
[7] Sherman D. *et al.* (2008) *Geochim. Cosmochim. Acta*, **72**, 298–310.
[8] Liger, E. *et al.* (1999) *Geochim. Cosmochim. Acta*, **63**, 2939–2955.
[9] Romanchuck, A. Y. *et al.* (2014), *Radiochim. Acta*, **102**, 303–310.
[10] Viani, B. E. *et al.* (1998) *Lawrence Livermore National Laboratory Report number UCRL-ID-129848*, p. 15.
[11] Zeng, H. *et al.* (2009) *Environ. Sci. Technol.* **43**, 1373–1378.
[12] Ho, C. H. *et al.* (1986) *J. Colloid Interface Sci.* **110**, 165–171.
[13] Lenhart, J. J. *et al.* (1999), *Geochim. Cosmochim. Acta* **63**, 2891–2901.

See next page for figures 1 and 2.

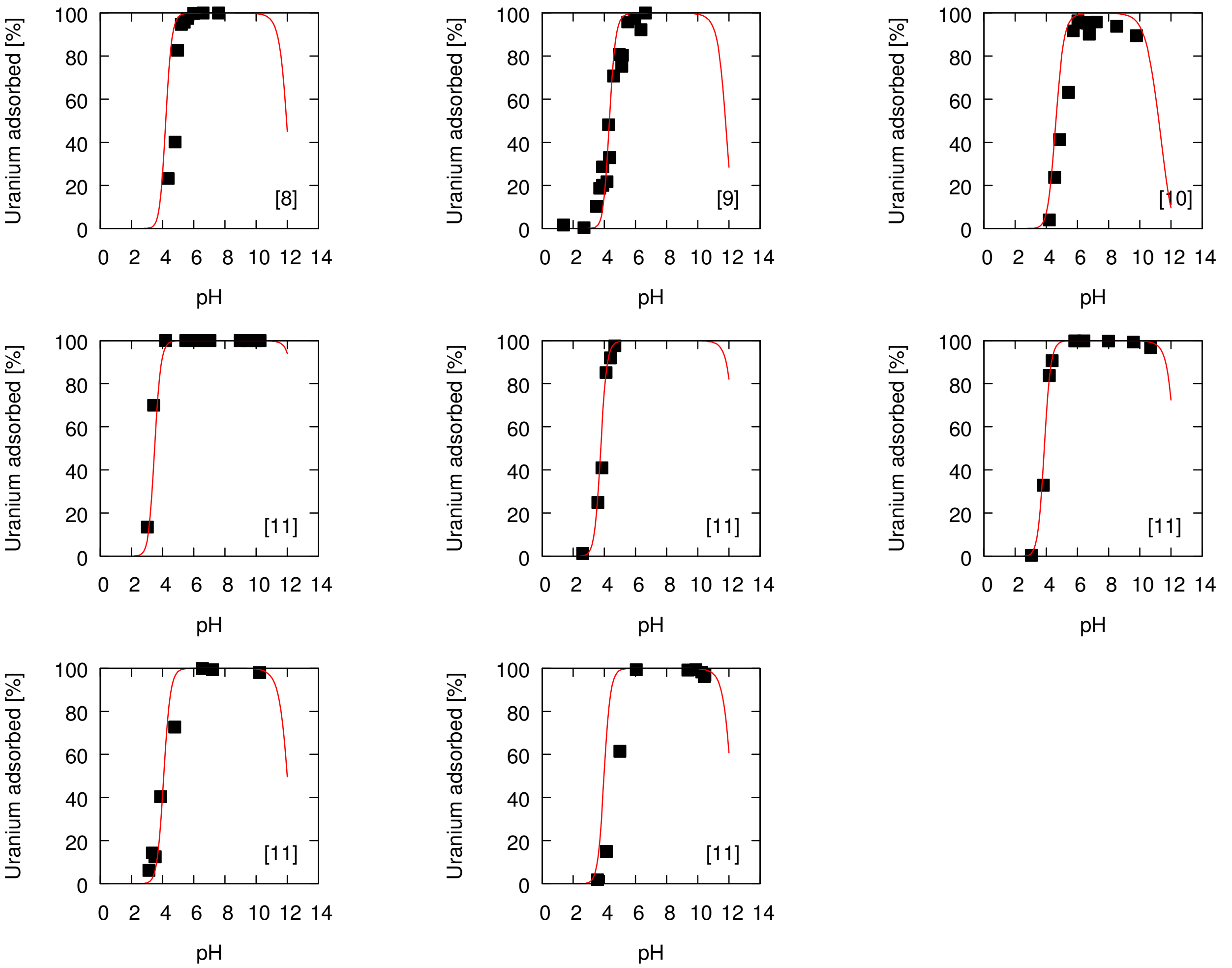

Fig. 1: Experimental data points (■) and calculations (—) of the sorption of uranium(VI) onto hematite under CO_2-free atmosphere. Top-left: 5×10^{-7} M U, 0.53 g/L, 109 m^2/g, top-center: 7.9×10^{-8} M U, 0.3 g/L, 35 m^2/g, top-left: 2×10^{-6} M U, 1 g/L, 1.5 m^2/g, medium-left: 1×10^{-6} M U, 1 g/L, 239.1 m^2/g, medium-center: 1×10^{-6} M U, 1 g/L, 62.6 m^2/g, medium-right: 1×10^{-6} M U, 1 g/L, 35.8 m^2/g, bottom-left: 1×10^{-6} M U, 1 g/L, 13.5 m^2/g, bottom-center: 1×10^{-6} M U, 1 g/L, 21.2 m^2/g.

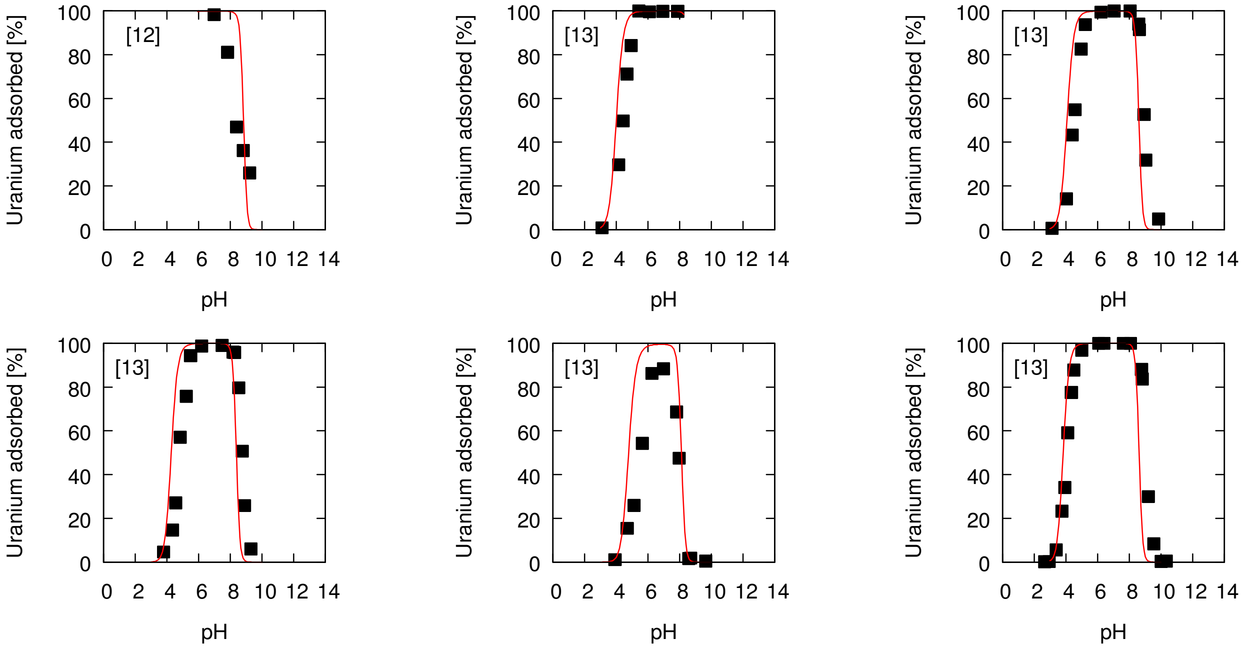

Fig. 2: Experimental data points (■) and calculations (—) of the sorption of uranium(VI) onto hematite under CO_2-containing atmosphere. Top-left: 5×10^{-6} M U, 0.2 g/L, 34 m^2/g, top-center: 1×10^{-6} M U, 0.9 g/L, 17.4 m^2/g, top-left: 1×10^{-6} M U, 0.9 g/L, 17.4 m^2/g, bottom-left: 1×10^{-6} M U, 0.9 g/L, 17.4 m^2/g, bottom-center: 1×10^{-6} M U, 0.09 g/L, 17.4 m^2/g, bottom-right: 1×10^{-6} M U, 9 g/L, 17.4 m^2/g.

Sorption of Se(IV) onto γ-alumina – Part I: An IR study of the impact of aqueous CO_2

H. Foerstendorf, N. Mayordomo, J. Lützenkirchen,[1] K. Heim, S. Weiss, U. Alonso,[2] T. Missana,[2] K. Schmeide, N. Jordan

[1]Institute for Nuclear Waste Disposal, Karlsruhe Institute of Technology, Karlsruhe, Germany; [2]CIEMAT, Department of Environment, Madrid, Spain

The impact of added carbonate (to achieve atmospherically equivalent concentrations) on the sorption of Se(IV) on γ-alumina was investigated by *in situ* IR spectroscopy. The formation of a predominant inner-sphere Se(IV) surface species with a higher affinity to the solid phase than the carbonate ions was observed.

The retention of fission products such as Se-79 is of major concern for a nuclear waste repository in deep geological formations. For a reliable risk assessment, the molecular processes occurring at the mineral-water interfaces have to be understood in detail. γ-alumina can serve as a model oxide for spectroscopic investigations of the sorption processes of dissolved fission products. In continuation of our previous report,[1] we investigated the impact of carbonate ions on the sorption processes of Se(IV)-oxoanions on the γ-alumina surface.[2]

EXPERIMENTAL. The set-up and the performance of the *in situ* experiments have been described elsewhere.[3,4] All experiments – unless noted otherwise – were carried out in D_2O to overcome the strong background absorption properties of bulk water in the frequency range below 900 cm^{-1}.[4] The ionic strength was fixed at 0.1 M NaCl.

RESULTS. The spectrum obtained upon Se(IV) sorption under inert gas conditions (Fig. 1, black trace) showed bands at 844 and 756 cm^{-1} representing stretching modes of the SeO_3^{2-} moiety.[5] These band maxima revealed significantly different frequencies compared to the spectrum of the aqueous species (Fig. 1, grey solid trace) reflecting the formation of surface species at the alumina surface. An evaluation of the spectrum by spectral decomposition and fitting with two bands suggested that only one single surface species was formed (Fig. 1, dotted lines) corroborating results from previous EXAFS investigations.[6]

The formation of inner-sphere species was further corroborated by subsequently flushing the alumina with a solution containing only background electrolyte, which resulted in poor reversibility of the sorption reaction. Additionally, the performance of the spectroscopic experiments at different ionic strengths showed no impact on the sorption behavior supporting the inner-sphere character of the Se(IV) surface species.[2] For the study of the impact of dissolved inorganic carbonate (DIC) on Se(IV) sorption, the Se(IV) sorption experiment was performed after the solid phase was equilibrated with DIC. The reduced intensity of the spectrum obtained indicated that carbonate ions hamper the accessibility of binding sites at the alumina surface (Fig. 2). However, the *in situ* sorption experiment where Se(IV) and carbonate ions were simultaneously exposed to the alumina surface equilibrated under inert gas conditions clearly showed that Se(IV) suppressed the sorption of carbonate ions (Fig. 3), which in turn demonstrates the higher affinity of selenite anions to the alumina surface.

These qualitative spectroscopic findings constitute a prerequisite for the comprehensive description of the sorption system Se(IV)/γ-Al_2O_3 studied by batch sorption experiments and thermodynamic modeling.[2,7]

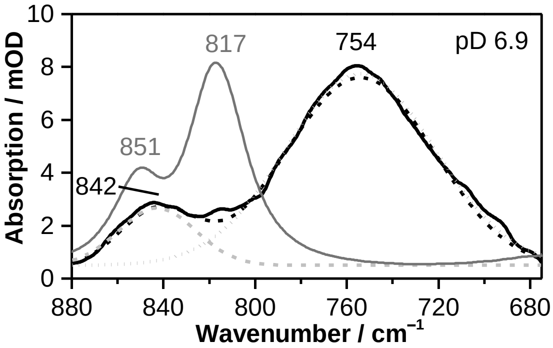

Fig. 1: IR spectra of Se(IV). Spectra of the aqueous HSeO$_3^-$ species recorded in H_2O (grey solid trace) and of the Se(IV) surface species on γ-alumina (black solid trace, under N_2(g)). The spectral components of the latter spectrum obtained after decomposition and the fitting result (residual: 0.00019) are shown as grey and black dotted traces, respectively.

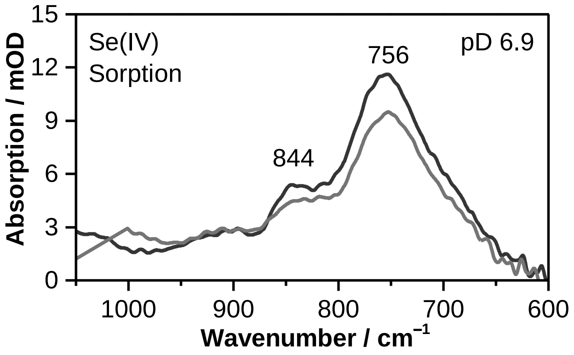

Fig. 2: IR spectra of the Se(IV) sorption complex on γ-alumina in the absence (black trace, under N_2(g)) and presence (grey trace) of DIC.

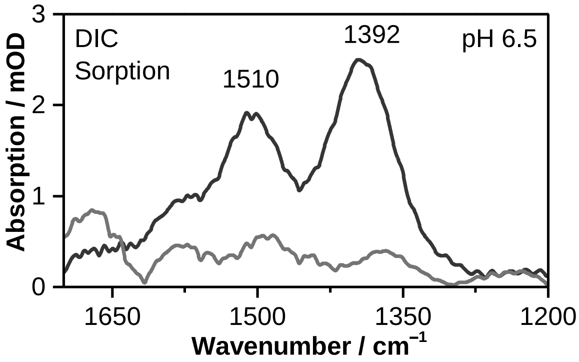

Fig. 3: IR spectrum showing the CO_3^{2-} modes of sorbed species on γ-alumina obtained in the absence (black trace) of Se(IV), whereas the spectrum recorded in presence of Se(IV) demonstrates the suppression of carbonate sorption (grey trace). Spectra recorded in H_2O.

ACKNOWLEDGEMENTS. N. Mayordomo acknowledges the MINECO stay abroad grant EEBB-I-15-09446.

[1] Mayordomo, N. *et al.* (2016) *Report HZDR-067*, p. 33.
[2] Mayordomo, N. *et al.* (2018) *Environ. Sci. Technol.* **52**, 581–588.
[3] Foerstendorf, H. *et al.* (2012) *J. Colloid Interface Sci.* **377**, 299–306.
[4] Jordan, N. *et al.* (2013) *Geochim. Cosmochim. Acta* **103**, 63–75.
[5] Kretzschmar, J. *et al.* (2015) *Dalton Trans.* **44**, 10508–10515.
[6] Elzinga, E. J. *et al.* (2009) *J. Colloid Interface Sci.* **340**, 153–159.
[7] Jordan, N. *et al.* (2018) this report, p. 37.

Sorption of Se(IV) onto γ-alumina – Part II: Surface Complexation Modeling

N. Jordan, N. Mayordomo, H. Foerstendorf, J. Lützenkirchen,[1] K. Heim, S. Weiss, U. Alonso,[2] T. Missana,[2] K. Schmeide

[1]Institute for Nuclear Waste Disposal, Karlsruhe Institute of Technology, Karlsruhe, Germany; [2]CIEMAT, Department of Environment, Madrid, Spain

The sorption of Se(IV) on γ-alumina was studied by batch experiments. The surface properties of the neat alumina surface were in a first step modeled with a three-plane surface complexation model, involving singly coordinated hydroxyl groups. Based on spectroscopic evidence, the Se(IV) sorption envelopes were described considering one bidentate surface complex.

Complementary to the investigations of the previous report,[1] the adsorption of Se(IV) anionic species on γ-alumina was described by surface complexation modeling (SCM), involving batch and spectroscopic studies. Indeed, accurate knowledge about the occurring surface processes is mandatory for a robust thermodynamic description based on SCM, to constrain the number of surface species and their stoichiometry.

EXPERIMENTAL. Alumina suspensions (20 g/L) at different ionic strengths of NaCl were titrated from pH 5 to pH 11 by NaOH addition under N_2 flux (Fig. 1). Se(IV) sorption experiments on alumina were carried out at two initial Se(IV) concentrations and at two ionic strengths in terms of NaCl content (Fig. 2). After three days of equilibration, the remaining Se(IV) concentration in solution was determined by ICP-MS, after phase separation. SCM was performed using a 1-pK CD-MUSIC model,[2] and a surface site density of 7 sites/nm^2.[3] The aqueous Se(IV) protonation constants were taken from Olin *et al.*[4]

RESULTS. A satisfactory description of the titration data is obtained with the proposed model (Fig. 1). The reactions used and the corresponding parameters are summarized in Table 1. Se(IV) retention on alumina increases with decreasing pH, and is independent of ionic strength (Fig. 2). Se(IV) inner sphere complexation is supported by the shift of the isoelectric point of alumina towards lower pH values in the presence of selenite (data not shown) and the infrared results.[3,5] SCM was performed considering one bidentate surface species, based on spectroscopic findings.[1,3,5] The model used to calculate the lines in Fig. 2, involving the $[\{(\equiv AlO)(\equiv AlOH)\}SeO]^0$ species (Tab. 1), was the one that yielded the best fit among all the variations tested. These results can be implemented in reactive transport models to improve the prediction of the environmental fate of selenium.

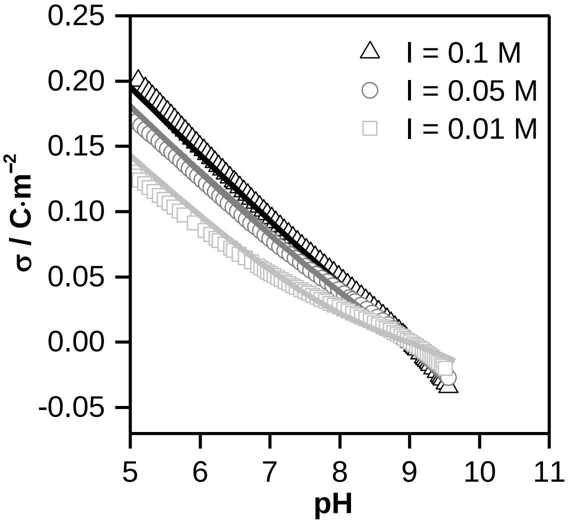

Fig. 1: Surface charge of alumina as a function of pH in (△) 0.1 M, (○) 0.05 M and (□) 0.01 M NaCl (m/v = 20 g/L, under N_2). Lines represent the fits.

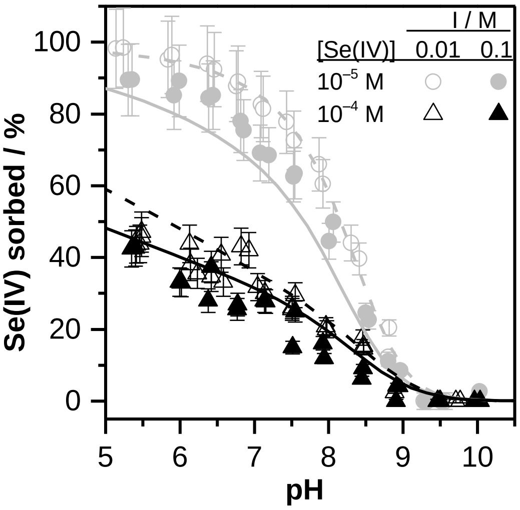

Fig. 2: Se(IV) sorbed (%) on alumina as a function of pH in (empty symbols) 0.01 M and (full symbols) 0.1 M NaCl, under different [Se(IV)]: (grey) 10^{-5} M and (black) 10^{-4} M (m/v = 0.25 g/L, under N_2). Lines are the model fits.

Tab. 1: Alumina surface properties and thermodynamic parameters.

Species	Reaction	log *K*
$\equiv AlOH^{-0.5}$		0
$\equiv AlOH_2^{+0.5}$	$\equiv AlOH^{-0.5} + H^+$	9.0
$\equiv AlOH^{-0.5}\cdots Na^+$	$\equiv AlOH^{-0.5} + Na^+$	−0.096
$\equiv AlOH_2^{+0.5}\cdots Cl^-$	$\equiv AlOH_2^{+0.5} + H^+ + Cl^-$	−0.176
$[(\equiv AlO)(\equiv AlOH)SeO]$	$2(\equiv AlOH^{-0.5}) + 3H^+ + SeO_3^{2-}$	30.0

ACKNOWLEDGEMENTS. N. Mayordomo acknowledges the MINECO stay abroad grant EEBB-I-15-09446.

---

[1] Foerstendorf, H. *et al.* (2018), this report, p. 36.
[2] Hiemstra, T. *et al.* (1989) *J. Colloid Interface Sci.* **133**, 91–104.
[3] Mayordomo, N. *et al.* (2018) *Environ. Sci. Technol.* **52**, 581–588.
[4] Olin, A. *et al.* (2005) *Chemical Thermodynamics of Selenium*, Elsevier, Amsterdam.
[5] Elzinga, E. J. *et al.* (2009) *J. Colloid Interface Sci.* **340**, 153–159.

Influence of carbonate, calcium and ionic strength on the U(VI) retention by Ca-bentonite and Na-montmorillonite at (hyper)alkaline conditions

T. Philipp, K. Schmeide

The retention of U(VI) by Ca-bentonite and Na-montmorillonite was studied in (hyper)alkaline solutions as a function of pH at different carbonate and calcium concentrations as well as at different ionic strengths. Batch sorption experiments and luminescence spectroscopy showed that the formation of uranyl carbonate complexes reduces the U(VI) retention only up to a certain pH (9.5–11, depending on the carbonate concentration). Above that pH, hydrolysed U(VI) complexes dominate the aquatic speciation, leading to increased retention. Calcium concentration and ionic strength seem to have only a minor effect on the overall sorption behavior in the pH range 8–13.

Montmorillonite-rich clays, such as bentonite, are considered as buffer and backfill material within the geo-technical barrier of deep geological repositories for radioactive waste.[1] Therefore, profound understanding of the radionuclide retention processes in these materials under environmentally relevant conditions is essential for a long-term safety assessment. Such conditions can involve high ionic strengths and high pH, as North German Clay formations feature highly saline pore waters,[2] promoting the evolution of hyperalkaline cement pore waters from corroding concrete within a repository. In contrast to the neutral pH-range, the U(VI) sorption behavior under alkaline conditions is largely unknown. Therefore, batch experiments were combined with spectroscopic investigations in order to also gain insight into the underlying processes on the molecular level.

EXPERIMENTAL. pH dependent batch sorption experiments (pH 8–13) were performed with Ca-bentonite (Calcigel®) in a diluted Gipshut solution (2.5 M NaCl, 0.02 M $CaCl_2$, 0.02 M Na_2SO_4, 0.0051 M KCl) and with Na-montmorillonite in NaCl (2.5 M, 0.1 M) at low (~5×10^{-4} M) as well as at high carbonate concentrations (0.001–0.1 M). The aqueous U(VI) speciation in the diluted Gipshut solution was investigated with cryo-TRLFS (−120 °C) using a pulsed Nd:YAG laser (0.3 mJ, 266 nm).

RESULTS AND DISCUSSION. At low carbonate concentrations, U(VI) retention by Ca-bentonite is low up to pH 9.5 (Fig. 1) due to the dominating presence of (calcium) uranyl carbonate complexes (Fig. 2a), which hardly sorb. Above pH 10, an abrupt change in speciation to negatively charged uranyl hydroxide complexes can be observed. At high carbonate concentrations, U(VI) retention remains at a low level up to pH 11.5. TRLFS verifies that uranyl carbonate complexes prevail up to elevated pH. Here, at pH 11.5 an abrupt change in speciation occurs (Fig. 2b). The complexes formed at higher pH show luminescence properties comparable neither to hydroxide nor to carbonate complexes. These spectra are assumed to represent mononuclear mixed uranyl hydroxo carbonate complexes that might form under such extreme conditions. In both cases, the change in speciation at elevated pH leads to an increased U(VI) retention (at low carbonate concentration from pH 10 to 12, at high carbonate concentrations with a local maximum around pH 12). Mechanisms that are responsible for this very strong retention (surface complexation / surface precipitation) are not yet fully understood, but will be clarified by direct spectroscopic investigation of the sorbed complexes (EXAFS, TRLFS, *in situ* ATR FT-IR).

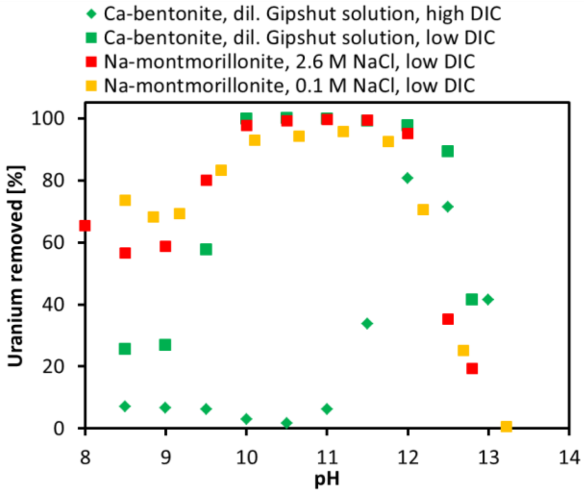

Fig. 1: pH dependent U(VI) retention ([U] = 1×10^{-6} M) by Ca-bentonite in dil. Gipshut solution and by Na-montmorillonite in NaCl at different carbonate concentrations and ionic strengths.

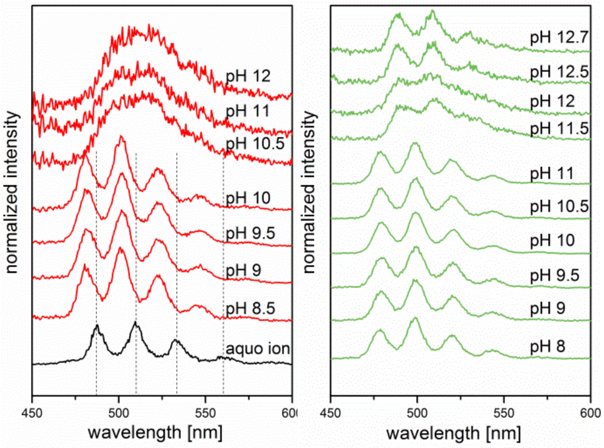

Fig. 2: Luminescence spectra of U(VI) ([U] = 1×10^{-6} M) in diluted Gipshut solution at low (left) and high (right) carbonate content.

The experiments with Na-montmorillonite and NaCl (*i.e.* without Ca) show that calcium influences the U(VI) sorption only at pH ≤ 9.5 by the formation of ternary calcium uranyl carbonate complexes, that are characterized by an even lower sorption affinity compared to the uranyl tricarbonate complex. Experiments with 0.1 M NaCl exhibit that the ionic strength has very limited impact on the U(VI) sorption at high pH. Furthermore, all investigated parameters (carbonate, calcium and ionic strength) seem to have minor effects on the U(VI) retention above pH 12.

ACKNOWLEDGEMENT. This work was funded by the BMWi (No. 02 E 11415B).

---

[1] Lommerzheim, A. *et al.* (2014) *Report DBETEC 08-2014-Z.*
[2] Wolfgramm, M. *et al.* (2011) *Z. geol. Wiss.* **39**, 173–193.

Site-selective TRLFS study of the influence of saline carbonate-containing solutions on the retention of Cm(III) by CSH phases

J.-M. Wolter, N. Huittinen, K. Schmeide

The retention of Cm(III) by calcium silicate hydrate (CSH) phases in saline carbonate-containing solutions representative of North German claystone formations was studied. For this, Cm(III) loaded CSH phases with two different calcium to silicon ratios (C/S: 1.0, 2.0) were synthesized. Their stability in brines containing 2.5 M NaCl/0.02 M $NaHCO_3$ or 0.02 M $NaHCO_3$ was monitored for 60 days. Before and after leaching, the Cm(III) loaded CSH phases were characterized by site-selective time-resolved laser-induced fluorescence spectroscopy (TRLFS) to detect changes of the Cm(III)-CSH binding mode and the formation of secondary phases. Results indicated that at a low C/S ratio Cm(III) is not mobilized by carbonate but incorporated into newly formed secondary phases like calcite and vaterite. At a high C/S ratio, the Cm(III) stays inside the CSH phase and is not incorporated into formed secondary phases like calcite.

Neutron capture reactions of isotopes present in nuclear fuel lead to the formation of various minor actinide isotopes like ^{241,243}Am or $^{242\text{-}247}$Cm.[1] The mass contributed by minor actinides in spent nuclear fuel is rather small but their high radiotoxicity over a long time period makes their safe storage in a deep geological repository mandatory.[2,3] Cementitious material, used for sealing constructions in deep geological repositories for intermediate and high level nuclear waste, consists mainly of hardened cement paste (HCP) and possesses a high immobilization potential for Am(III)/Cm(III).[4] HCP is a mixture of mineral phases like CSH, portlandite, calcium aluminate hydrates, AF_t or AF_m phases in dependence on additives.[5] Previous studies of the Cm(III)/HCP system showed an incorporation of Cm(III) mainly into the CSH phase.[4,6] The present study focuses on the influence of saline carbonate solutions on Cm(III) incorporation in CSH phases.

EXPERIMENTAL. All experiments were performed under inert gas conditions (N_2 atmosphere, CO_2 and $O_2 < 2$ ppm). CSH phases were prepared in alkaline water (0.294 M NaOH, pH 13.3) in the presence of 2.8×10^{-6} M Cm(III), starting from fumed silica and carbonate-free CaO, at a solid-to-liquid (S/L) ratio of 24 g/L. The CSH phases with C/S ratios of 1.0 and 2.0 showed Cm loadings of 28 ppm. TRLFS measurements were performed at 4 K using wavelengths between 600 and 625 nm for a selective excitation of the Cm(III) species. For leaching experiments, the CSH phases were equilibrated in 2.5 M NaCl/0.02 M $NaHCO_3$ or 0.02 M $NaHCO_3$ (S/L = 10 g/L) over a time period of 60 d.

RESULTS. The incorporation of Cm(III) in synthetic CSH phases was confirmed by site-selective TRLFS (Fig. 1). Tits *et al.* identified two Cm(III) species in CSH phases, either Cm(III) substituted Ca^{2+} in the CSH interlayer or Cm(III) was incorporated in the CaO complex layer of CSH phases.[6] However, the current site-selective excitations of the Cm(III) species in the CSH phases revealed a fluent transition between both sites (cf. Fig. 1).

The leaching of Cm(III)-doped CSH phases in 2.5 M NaCl/0.02 M $NaHCO_3$ or 0.02 M $NaHCO_3$ did not lead to a Cm(III) release into the supernatant solution. However, site-selective TRLFS investigations of the leached CSH phase with the low C/S ratio (1.0) showed that the Cm(III) was partially incorporated in calcite and vaterite formed as secondary minerals due to contact with the carbonate-containing solutions. In contrast, the CSH phase with a high C/S ratio (2.0), that contains additionally portlandite, showed no changes of the Cm(III) speciation upon leaching. That verifies that Cm(III) was still incorporated in the CSH phase.

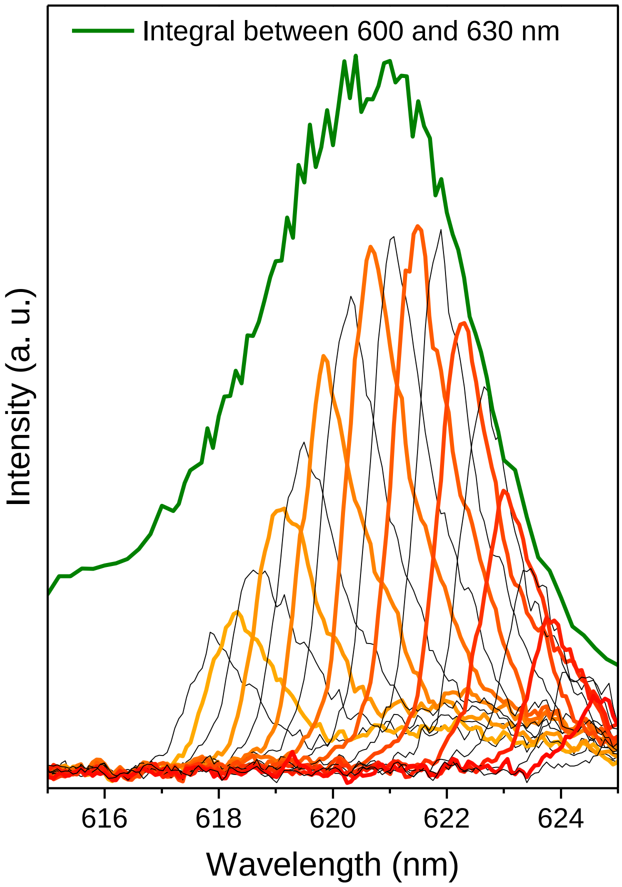

Fig. 1: Section of the wavelength dependent luminescence emission of Cm(III) incorporated into CSH phases with a C/S ratio of 1.0. Emission lines were recorded between 600 and 630 nm in 0.2 nm steps and are displayed between 615 and 625 nm in 0.4 nm steps and coloured in yellow to red alternating with black for a better discriminability.

ACKNOWLEDGEMENT. This work was funded by the BMWi (No. 02 E 11415B).

---

[1] Radulescu, G. *et al.* (2010) *SCALE 5.1 Predictions of PWR Spent Nuclear Fuel Isotopic Compositions.*
[2] Bruno, J. *et al.* (2006) *Elements* **2**, 343–349.
[3] Buck, E. C. *et al.* (2004) *Special Publications* **236**, 65–88, Geological Society, London.
[4] Stumpf, T. *et al.* (2004) *J. Colloid Interface Sci.* **276**, 118–124.
[5] Lothenbach, B. *et al.* (2016) *A Practical Guide to Microstructural Analysis of Cementitious Materials*, p. 191–192.
[6] Tits, J. *et al.* (2003) *Environ. Sci. Technol.* **37**, 3568–3573.

µTRLFS: Spatially-resolved sorption studies of Eu(III) on Eibenstock granite with time-resolved laser induced fluorescence spectroscopy

K. Molodtsov, J. Rothe,[1] K. Dardenne,[1] M. Schmidt

[1]Institute for Nuclear Waste Disposal, Karlsruhe Institute of Technology, Karlsruhe, Germany

The sorption behavior of Eu^{3+} on whole natural granite from Eibenstock, Germany was investigated by a new method called µTRLFS – a spatially resolved upgrade of time-resolved laser induced fluorescence spectroscopy (TRLFS). With mappings of the emission intensity (F_1+F_2), the peak ratio (F_2/F_1) and selected lifetime measurements, it could be determined that not only different mineral phases interact differently with Eu^{3+}, but the sorption behavior also varies within one mineral grain, especially at grain boundaries.

Granite is one of the potential host rock formations for radioactive waste repositories. Previous spatially-resolved studies showed that the sorption behavior of granite is not homogeneous on each mineral phase.[1, 2] However, these studies only investigate the quantitative distribution of Eu^{3+}, while its speciation is neglected. µTRLFS fills this gap by providing spatially-resolved speciation mappings.

EXPERIMENTAL. Thin-sections with a thickness of 150 µm were prepared for the µTRLFS experiments. The sample was contacted with a solution containing 5×10^{-5} M Eu^{3+} and 0.1 M NaCl (pH 8) in a flow cell for 1 day at a flow rate of 30 mL/h. The elemental composition ($Z \geq 19$) of the sample was mapped by µXRF at the INE-Beamline, Karlsruhe with a resolution of 10 µm. The mineral phase distribution was determined by a combination of the µXRF data and thin-section microscopy. µTRLFS measurements were performed with a Nd:YAG pumped dye laser setup at 394 nm. The laser was focused to approximately 20 µm in diameter, and the sample was scanned by a XYZ-Stage in a 20 µm grid. Full spectra were collected for each data point, and mappings were calculated automatically based upon the total fluorescence intensity of the F_1+F_2 bands and peak ratio of F_2/F_1.

RESULTS. The mineral phase identification reveals that the surface of the region of interest (ROI) is mainly composed of quartz, biotite and alkali feldspar (Fig. 1). The Qz* region is a thin quartz layer over alkali feldspar, while at Bt* a thin biotite layer is located over quartz.

µTRLFS mappings of the fluorescence intensity can be correlated to the sorption capacity of the sample and mappings of the peak ratio to the complexation strength, which can be understood as a speciation mapping (Fig. 2). The sorption capacity mapping shows that more Eu^{3+} is sorbed on alkali feldspar than on quartz. Most of the biotite regions show nearly no fluorescence. This is most likely due to biotite's high iron content, which quenches Eu^{3+} fluorescence. At the grain boundary between quartz and biotite the sorption capacity is partially strongly increased in comparison to quartz (A). In one place on the biotite grain the surface seems to differ (B) regarding the fluorescence intensity and the F_2/F_1 ratio, which is most likely due to the quartz layer being on top of the biotite grain at this location.

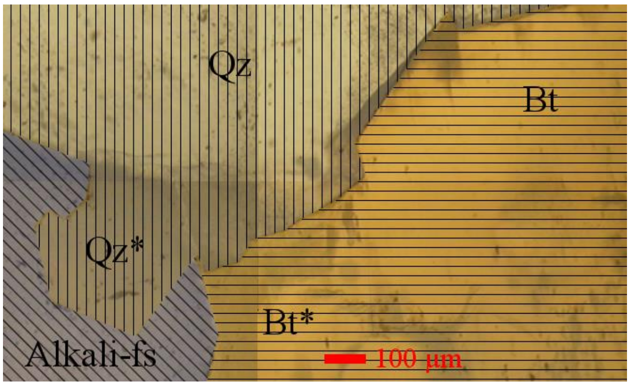

Fig. 1: Mineral phase distribution on the surface of the granite sample with biotite (horizontal lines), quartz (vertical lines) and alkali feldspar (diagonal lines).

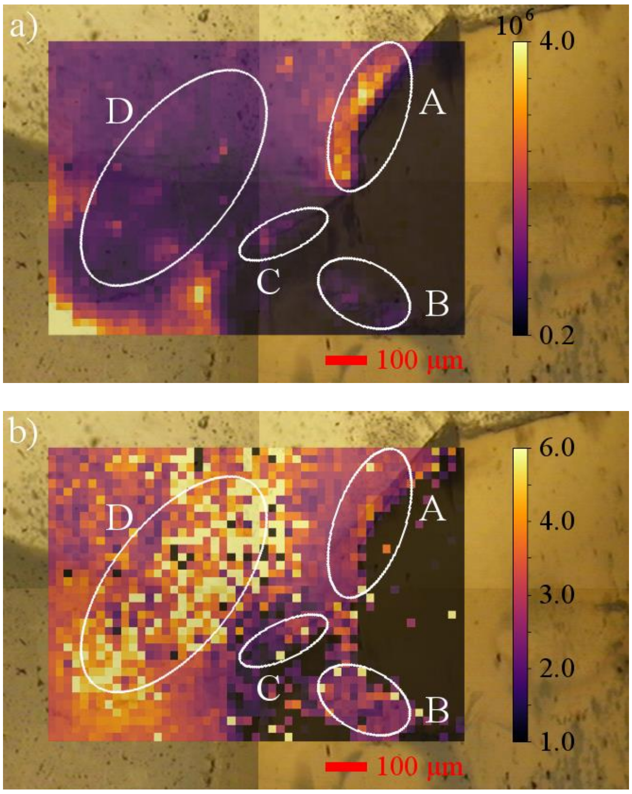

Fig. 2: a) Fluorescence intensity of F_1+F_2, b) Peak ratio of F_2/F_1.

When comparing the peak ratios at the other sites of the ROI it becomes obvious that parts of quartz and its boundary to biotite exhibits lower F_2/F_1 ratios (B, C) than others (A, D) and alkali feldspar. This indicates a stronger complexation of Eu^{3+} in the two latter cases. For example, this could point to inner sphere sorption on alkali feldspar and parts of the quartz (A, D) and predominantly outer sphere sorption on the rest of the quartz regions (B, C).

This proves that Eu^{3+} species are not homogeneously spread over mineral grains, but speciation varies, especially on grain boundaries, indicating the necessity to investigate the sorption behavior on complex rocks by imaging techniques to fully understand the retention mechanisms.

---

[1] Ishida, K. *et al.* (2009) *Environ. Sci. Technol.* **43**, 1744–1749.
[2] Fukushi, K. *et al.* (2013) *Environ. Sci. Technol.* **47**, 12811–12818.

Eu^{3+} incorporation into zirconia bearing phases

M. Eibl, C. Hennig, T. Stumpf, N. Huittinen

With the combination of powder X-ray diffraction (PXRD) and laser luminescence spectroscopy the bulk and the local structure of Eu^{3+} doped zirconia was investigated. It could be shown that the local sites differ significantly from the bulk crystal phase due to large disorder around the Eu^{3+} dopant. The intensity ratio of the Eu^{3+} $^7F_2/^7F_1$ emission transition intensities reveals changes in the local symmetry, which is not visible in the bulk investigations. These symmetry variations can be explained by changes in the homogeneity of the zirconia structure.

Zirconium(IV) oxide is a corrosion product of the zircalloy cladding material surrounding nuclear fuel rods.[1] Therefore, studies involving interactions such as structural incorporation of actinides into ZrO_2 are necessary to enable predictions about the long term safety of final repositories for nuclear waste.

EXPERIMENTAL. For the incorporation studies $ZrOCl_2$ was dissolved in dilute HCl together with varying amounts of $EuCl_3$. The solutions were added dropwise to an alkaline solution of NaCl (0.5 M, pH 12) resulting in instantaneous formation of a white precipitate of Eu^{3+}-doped hydrous zirconia. The precipitate was separated by centrifugation at a relative centrifugal force of 6800 g and washed with water. The wet paste was dried in an oven and calcined at 1000 °C for 5 h. The solid was grinded and analyzed with PXRD using a Rigaku MiniFlex 300. Laser luminescence data was obtained with a pulsed Nd:YAG (Continuum Surelite II) pump laser and a solid-state optical parametric oscillator (OPO, PANTHER EX OPO, Continuum). The excitation of Eu^{3+} was carried out at 394 nm.

RESULTS. The incorporation of actinides or their lanthanide analogues into zirconia results in a structural change from the monoclinic phase to high temperature tetragonal or cubic phases. When preparing samples of different percentages of Eu^{3+} doping, a decrease of the monoclinic structure with an increasing fraction of the tetragonal phase is observed until a doping percentage of 10 mol-%, where the tetragonal phase reaches its maximum percentage (Fig. 1). Upon further increased doping fractions, the cubic phase becomes predominant. From 18 mol-% a single phase cubic structure can be seen only.

The luminescence properties of Eu^{3+} can give information on its local environment. Surprisingly, the emission behavior of the tetragonal and the cubic phase is very similar and shows a splitting pattern corresponding to a low symmetry site (Fig. 2, left).

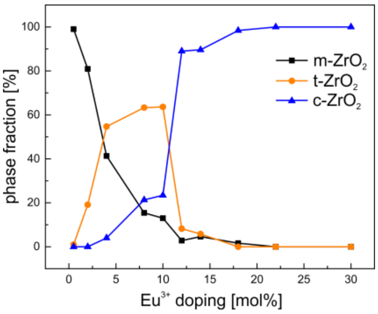

Fig. 1: Fraction of monoclinic, tetragonal and cubic phase in dependence on the europium content.

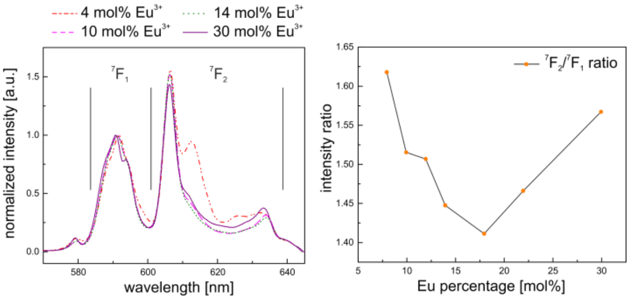

Fig. 2: Luminescence emission spectra of zirconia, doped with various percentages of Eu^{3+} (left) and the corresponding $^7F_2/^7F_1$ emission band intensity ratios (right).

The probable reason for that is that the charge compensation, necessary to account for the lower charge of Eu^{3+} in comparison to the host Zr^{4+}, takes place by introducing oxygen vacancies into the lattice. This leads to a strong distortion and a lowering of the coordination number compared to a fluorite type cubic phase.

Only slight changes can be observed in the ratio of the integrated intensity of the $^7F_2$ and $^7F_1$ transition (Fig. 2, right). With increasing Eu^{3+} content a decreasing intensity ratio can be seen until a fraction of 18 mol-%, which is an indication for increasing local symmetry.[2] This can be explained with the decreasing fraction of the monoclinic phase and a higher homogeneity of the Eu^{3+} distribution. At higher doping percentages the intensity ratio is increasing again. This might be due to a higher proximity of the Eu^{3+} ions in the lattice, leading to the existence of differing europium sites, i.e. Eu^{3+} ions affected by neighbor Eu^{3+} ions and unaffected Eu^{3+} ions.

Although neither the host cation (Zr^{4+}) nor the dopant ion (Eu^{3+}) exists in a cubic symmetry in this system, the bulk is indistinguishable from a cubic fluorite type structure in PXRD (Fig. 3).[3] Thus, it can be concluded, that the local structure around the lattice sites in defect lattices cannot be represented by the bulk structure.

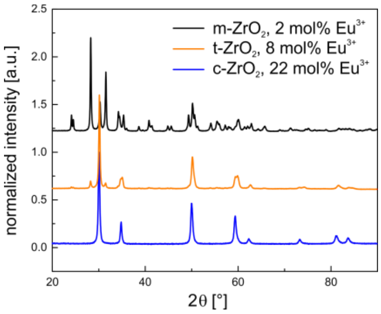

Fig. 3: X-ray diffraction pattern of Eu^{3+}-doped monoclinic, tetragonal and cubic zirconia stabilized at varying Eu^{3+} concentrations:

---

[1] Cox, B. (2004) *J. Nucl. Mater.* **336**, 331–368.
[2] Binnemans, K. (2015) *Coord. Chem. Rev.* **295**, 1–45.
[3] Li, P. *et al.* (1993) *Phys. Rev. B* **48**, 10063–10073.

Aliovalent cation substitution in UO_2: Electronic and local structures of $U_{1-y}La_yO_{2\pm x}$ solid solutions

D. Prieur, L. Martel,[1] J.-F. Vigier,[1] A. C. Scheinost, K. O. Kvashnina, J. Somers,[1] P. M. Martin[2]

[1]European Commission, Joint Research Centre (JRC), Karlsruhe, Germany; [2]CEA, Nuclear Energy Division, Research Department on Mining and Fuel Recycling Processes, SFMA, Bagnols-sur-Cèze, France

We provide here by using U L_{III} EXAFS and U M_{IV} HERFD-XANES spectroscopies the experimental proof that La(III) for U(IV) substitution in UO_2 proceeds not through the creation of O vacancies (as has often been assumed), but by the oxidation of U(IV) to U(V) in proportions equimolar to the substituted trivalent lanthanum.[1]

The substitution of uranium in UO_2 by aliovalent atoms, like most of the lanthanides and some of the actinides, can lead under specific conditions to the formation of $U_{1-y}M_yO_{2\pm x}$ solid solutions. The substitution of U by another cation, of lower valence, implies either the formation of oxygen vacancies or an increase of the U oxidation state. Both charge compensating mechanisms modify the overall oxygen to metal ratio (O/M), which ultimately effects phase stability, defect chemistry and the chemical potential of oxygen of the material.[2] An accurate determination of the oxygen stoichiometry of mixed oxides $U_{1-y}M_yO_{2\pm x}$ is hence crucial, along with a detailed understanding of the nature of the charge compensating defects and their effects on the local structure. In this context, the purpose of this work is to investigate by XAS the electronic and local environments of the U, M and O elements in $U_{1-y}M_yO_{2\pm x}$ solid solutions.

EXPERIMENTAL. $U_{1-y}La_yO_{2\pm x}$ (y = 0.06; 0.11; 0.22) samples have been prepared at Joint Research Centre (JRC Karlsruhe) by gel-supported precipitation, also referred to as sol–gel external gelation.[3] The resulting beads were washed, dried, calcined and then sintered for 4 hours at 1923 K under Ar/H_2. XAS data was recorded at the European Synchrotron Radiation Facility (ESRF, France).
The U L_{III} XAS spectra were recorded at room temperature in transmission mode at the Rossendorf Beamline (BM20) dedicated to actinide elements.[4] The U M_{IV} and La L_{III} HERFD-XANES (High Energy Resolved Fluorescence Detection) spectra were recorded at the ESRF beamline ID26.

RESULTS. The Fourier transforms (FTs) of the U L_{III} EXAFS spectra are presented in Fig. 1. The U M_{IV} XANES spectra have been analysed by Iterative Transformation Factor Analysis (ITFA) in order to derive the molar fraction of U(IV), U(V) and U(VI) (cf. Fig. 2).[5] We found that the incorporation of La(III) in the UO_2 lattice is associated to the formation of a quasi-equimolar fraction of U(V). Despite the cationic substitution, ideal solid solutions are obtained and the fluorite structure is maintained. However, the local structure is slightly affected compared to pure UO_2 with the interatomic distances decreasing with U(V) content.

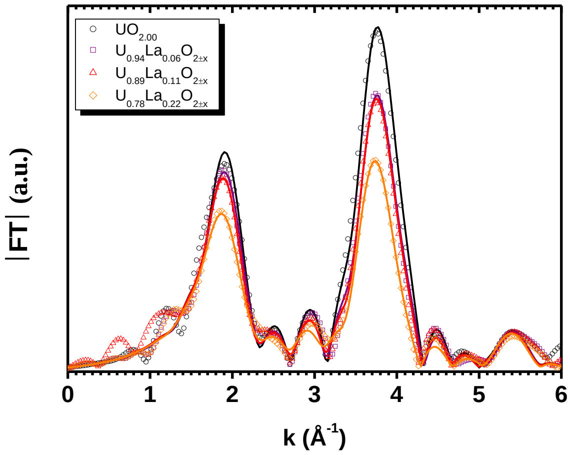

Fig. 3: Experimental and fitted U L_{III} EXAFS spectra of $U_{1-y}La_yO_{2\pm x}$.

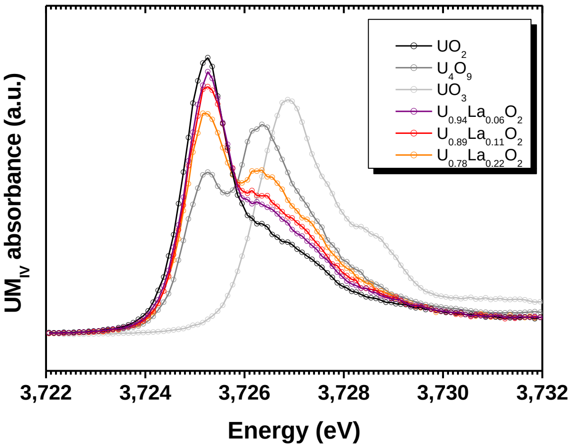

Fig. 2: Experimental (—) and fitted (o) U M_{IV} HERFD-XANES derived from IFTA.

In the literature, it is often assumed, and sometimes claimed without experimental proof, that the incorporation of La(III) in UO_2 is accommodated through the formation of O vacancies leading then to the formation of hypostoichiometric solid solution. Our result shows that this assumption is wrong and that the oxygen stoichiometry ratio cannot be stated without experimental proof. This statement can be also extended to other $U_{1-y}M_yO_{2\pm x}$ solid solutions.

ACKNOWLEDGEMENTS. The authors acknowledge Co Boshoven, Daniel Bouexière, Sébastien Gardeur, Antony Guiot, Patrick Lajarge, Chris Selfslag, and Sarah Nourry for their help during the sample synthesis and characterization at JRC Karlsruhe.

---

[1] Prieur, D. *et al.* (2018) *Inorg. Chem.* **57**, 1535–1544.
[2] Prieur, D. *et al.* (2011) *Inorg. Chem.* **50**, 12437–12445.
[3] Martel, L. *et al.* (2014) *J. Phys. Chem. C* **118**, 27640–27647.
[4] Matz, W. *et al.* (1999) *J. Synchrotron Radiat.* **6**, 1076–1085.
[5] Roßberg, A. *et al.* (2003) *Anal. Bioanal. Chem.* **376**, 631–638.

Incorporation of europium(III) into scheelite-related host matrices ABO_4 (A = Ca^{2+}, Sr^{2+}, Ba^{2+}; B = W^{6+}, Mo^{6+}): Role of A- and B-sites on the dopant site-distribution and photo-luminescence

B. Xiao, M. Schmidt

A comprehensive spectroscopic study is conducted by means of polarization-dependent site-selective time resolved laser-induced fluorescence spectroscopy (p-TRLFS), to delineate the influence of the host phase cations on the local coordination sphere of the dopant for a series of scheelite- and powellite-type matrices doped with Eu(III).[1]

Scheelite and powellite related materials doped with trivalent lanthanides or actinides have been the subject of extensive research due to their important role in mineralogical, technological and environmental implications. Their solid-solutions, formed by disordered structural substitution, have received wide attention in the context of the immobilization of highly radiotoxic nuclear wastes.[2] However, the structural details behind such disordered substitution are difficult to characterize by crystallography, especially when the dopant is present at trace concentration levels. This work aims to clarify the impact of A- and B- sites on the local symmetry distortion from the bulk crystallographic site symmetry in scheelite-type ABO_4 (A = Ca^{2+}, Sr^{2+}, Ba^{2+}; B = W^{6+}, Mo^{6+}) single crystals.

EXPERIMENTAL. Bulk single crystals, up to 10 mm in size, with smooth facets were grown by a high-temperature flux method. The optical axis (crystallographic *c*-axis) of the grown crystals was determined by X-ray diffraction (Rigaku MiniFlex diffractometer) in order to make the polarization-dependent spectra. To examine the details of site distributions, low temperature (< 10 K) fluorescence spectra were recorded. TRLFS was performed using a Nd:YAG laser system (Continuum) pumped dye laser (Radiant Dyes NarrowScan K). Rhodamine 6G was used as a dye for direct excitation of Eu^{3+} ions from the ground $^7F_0$ state to the emitting $^5D_0$ state.

RESULTS. The p-TRLFS results with Eu^{3+} as a structural probe reveal that the speciation of the incorporated Eu^{3+} is much more complicated than expected. Significant fluorescent polarization dependence could be clearly seen from some of the ABO_4 members, such as $CaWO_4$ (Fig. 1), but not others, e.g. $CaMoO_4$.

The specific distortion of the lattice depends on both the A and B cations. With the increase of the A^{2+} host cation radius and A-O bond distance from Ca^{2+} to Ba^{2+}, we observe a line-broadening trend across the ABO_4 family, which arises from multiple similar cationic environments introduced by the coupled substitution. This broadening feature is most pronounced in the endmember $NaEu(MoO_4)_2$ due to the extremely heterogeneous coordination environments surrounding the Eu^{3+} ions. Second, the position of high wavelength excitation peaks shows a remarkable linear dependence upon host cation radius. The fact that the $^5D_0 \leftarrow {}^7F_0$ band shift to higher energy (blue shift) with the increase of the host cation radius indicates a weaker metal-ligand interaction, showing that the oxygen atoms within the lattice do not deviate strongly from their crystallographic positions and Eu–O bond distances are mostly governed by the bond distance of A to oxygen in the structure. The linear correlation between the excitation energy of the $^5D_0 \leftarrow {}^7F_0$ transition and the average Eu–O bond distance could be used to calculate average bond distances for the $NaEu(MoO_4)_2$ and the compound that is not readily available in the literature. We find value of 2.537 Å for $NaEu(MoO_4)_2$ (see Fig. 2), which fall in between the values of the Ca^{2+} and Sr^{2+} compounds, and is significantly larger than the value previously reported for $NaEu(MoO_4)_2$.[3]

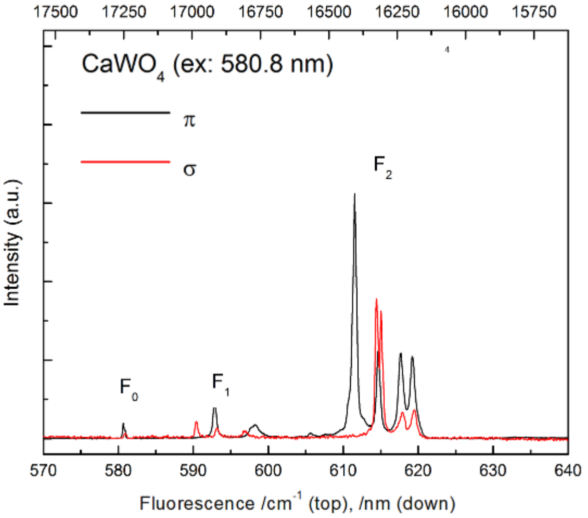

Fig. 1: Fluorescence emission of Eu^{3+} doped $CaWO_4$ excited at 580.8 nm (17,218 cm^{-1}). Legend: π spectrum is determined with the ***E*** vector parallel to the *c*-axis, whereas σ spectrum is defined by ***E*** perpendicular to the *c*-axis.

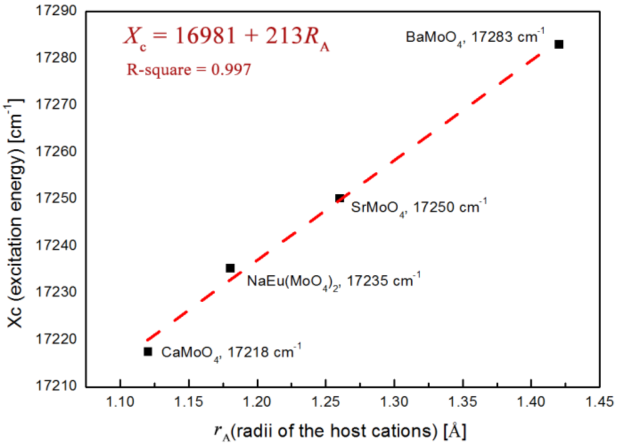

Fig. 2: The linear trend of the excitation energy X_c (cm^{-1}) changes as a function of the host cation radius *r* (Å).

---

[1] Xiao, B. et al. (2018) *Inorg Chem.*, accepted.
[2] Bosbach, D. et al. (2004) *Radiochim. Acta* **92**, 639–643.
[3] Arakcheeva, A. et al. (2012) *Chem. Sci.* **3**, 384–390.

SCIENTIFIC CONTRIBUTIONS (PART III)

Long-Lived Radionuclides in

BIOLOGICAL SYSTEMS

Uranium biomineralization by the fungus *Penicillium simplicissimum* isolated from a former uranium mine

S. Schäfer, U. Gerber, E. Krawczyk-Bärsch, M. L. Merroun[1]

[1]University of Granada, Department of Microbiology, Granada, Spain

The aim of this study was to investigate the interaction of the fungus *Penicillium simplicissimum* with uranium (U) for bioremediation purposes. Therefore, the U removal was quantified by ICP-MS, and the interaction mechanisms were analyzed using STEM/HAADF coupled with EDX. The results reveal a U removal capacity of 100 mg U/g dry biomass after two days. The obtained results from this study could demonstrate active interaction mechanisms between the isolated strain and U, since extracellular biomineralization and intracellular bioaccumulation were observed.

The former U mine in Königstein (Germany) is currently remediated by partial flooding of the underground. The flooding water is pumped above ground and treated by a costly waste water treatment plant. After more than 15 years of continuous remediation, the flooding water still contains elevated concentrations of U (8 mg/L) and other heavy metals. Due to the effortful waste water treatment, alternative strategies are of great interest. The use of microorganisms for (bio-)remediation could be an effective alternative. Fungi, like *Penicillium*, are widely known for their heavy metal-tolerance and their capability of adapting to extreme environmental conditions.[1] Therefore, they are possible candidates for bioremediation applications. However, the interaction mechanisms, like biosorption and biomineralization, are not completely understood and need to be further investigated.[2, 3]

EXPERIMENTAL. The fungus *P. simplicissimum* was cultured in SDA-medium for 4 days at 30 °C.[4] Afterwards, the cells were washed twice with sterile tap water pH 5.0. The cells were diluted in sterile tap water to a dry biomass (DBM) concentration of 0.15 g/L. $UO_2(NO_3)_2$ was added to a final concentration of 0.1 mM. All experiments were performed in triplicates. For the determination of the U removal capacity, the cells were incubated for 52 h at 30 °C with constant shaking (150 rpm). Regularly, 0.5 mL samples were taken and sterile-filtered for ICP-MS measurement. For STEM/HAADF measurement, after 48 h the cells were centrifuged (10,000 rpm, 4 °C) and the obtained cell pellet was immediately processed at Centro de Instrumentación Científica (University of Granada, Spain).

RESULTS. During the incubation of *P. simplicissimum* over 52 h at an initial U concentration of 0.1 mM, the fungus removed over 100 mg U/g DBM from solution (Fig. 1). With decreasing initial biomass concentration, the absolute U removal increased significantly to over 500 mg U/g DBM (investigated down to a DBM of 0.001 g/L, data not shown). Interestingly, the U removal capacity rises logarithmically. After 24 h the slope decreases clearly, and the U removal capacity approaches its equilibrium. The decreasing slope could be explained by less active cells, possibly caused by stress, *e.g.* the influence of unavailable carbon sources. The obtained results show that the fungal cells probably interact with U *via* a biphasic process: 1) a rapid and passive U biosorption phase; followed by 2) a metabolically active and slow process which could be governed by biomineralization and intracellular accumulation.

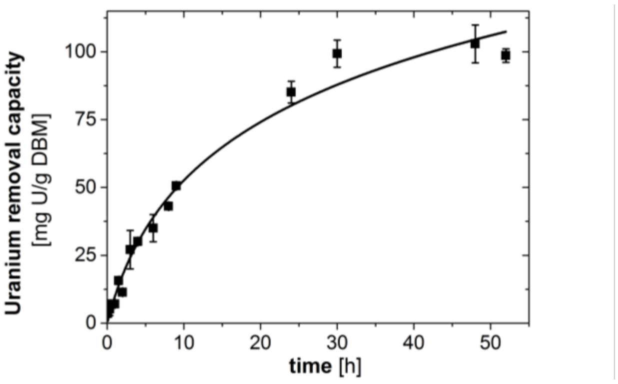

Fig. 1: Uranium removal capacity of *P. simplicissimum* over 52 h at 30 °C. Initial uranium concentration: 0.1 mM, background tap water pH 5.0. DBM stands for dry biomass.

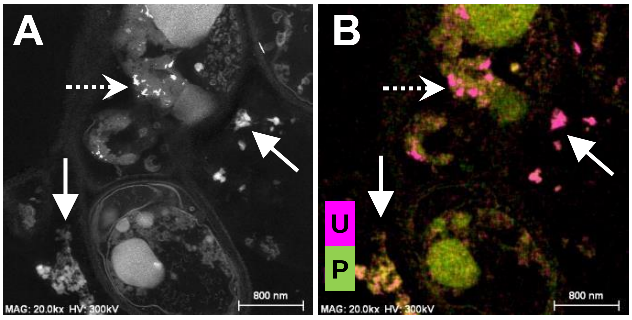

Fig. 2: STEM/HADDF (A) and elemental mapping (B) of uranium (magenta) and phosphorus (green); indicating an intracellular (dotted arrow) and extracellular (standard arrows) occurrence of both in *P. simplicissimum*.

The STEM/HAADF results (Fig. 2) confirm this assumption. After 48 h incubation, we could observe extracellular amounts of U, which indicate active biomineralization. Furthermore, some minor intracellular amounts of U were detected. In both cases U is associated with phosphorous.

OUTLOOK. The results emphasize the potential of the fungus *P. simplicissimum* for possible bioremediation approaches. Nevertheless, the interaction mechanisms with U and other heavy metals have to be investigated in more detail. Therefore, further studies investigating the effects of temperature and cell viability on the U removal should be performed.

ACKNOWLEDGEMENTS. The research leading to these results has received funding from Verbundprojekt Strahlung und Umwelt III: „Transfer von Radionukliden in aquatischen Ökosystemen" (TransAqua) under grant agreement number 02NUK030F. The authors thank S. Gurlit for ICP-MS measurements. S. Schäfer acknowledges the University of Granada for Internship Grant and STEM/HAADF measurements.

---

[1] Siddiquee, S. (2015) *J. Microb. Biochem. Technol.* **7**, 384–393.
[2] Fomina, M. *et al.* (2014) *Bioresour. Technol.* **160**, 3–14.
[3] Verma, N. *et al.* (2017) *Recent Pat. Biotechnol.* **11**, 171–187.
[4] Odds, F. C. (1991) *J. Med. Vet. Mycol.* **29**, 355–359.

Spectroscopic characterization of U(VI) sequestration by *Acidovorax facilis*

E. Krawczyk-Bärsch, U. Gerber, K. Müller, R. Steudtner

In kinetic batch experiments, cells of *A. facilis* were contacted for 5 min to 24 h with 0.1 mM U(VI). In TRLFS studies it was shown that the local coordination of U species associated with the cells depends upon time. U is bound mainly to phosphoryl groups of lipopolysaccharide (LPS) at the outer membrane within the first hour. Thus, both phosphoryl and carboxyl functionality groups of LPS and peptidoglycan (PGN) of *A. facilis* cells may effectuate the removal of high U amounts from solution at 16 – 24 h of incubation.

EXPERIMENTAL. For the studies cells of *A. facilis* were grown in nutrient broth medium (NB) (Peptone 5.0 g/L and Beef Extract 3.0 g/L, pH 7.0 ± 0.2, Sifin, Berlin, Germany) at 30 °C and 120 rpm on a rotary shaker overnight until reaching the stationary phase. Subsequently, the cells were washed and diluted to an $OD_{600\,nm}$ of 1.0 (12.0 ± 1.0 mg dry weight/mL) with sterilized tap water at pH 5.0 and used for each experimental method. A stock solution of $UO_2(NO_3)_2$ was added to adjust a U(VI) concentration of 0.1 mM in the cell suspension. The experiments were performed at pH 5, under aerobic conditions and at 30 °C on a rotary shaker at 1,116 × g. After 5 min, 1 h, 16 h, and 24 h, samples were taken and centrifuged for 5 min at 13,200 rpm. The supernatants were used for the determination of U concentration by means of inductively coupled plasma spectrometry (ICP-MS). The pellets were re-suspended in sterilized tap water (pH 5) and used for TRLFS studies. The U(VI) luminescence was measured at 153 K after excitation with laser pulses at 266 nm and an average pulse energy of 300 µJ. The emission of the samples was recorded using an iHR550 spectrograph and an ICCD camera in the 370.0 – 670.0 nm wavelength ranges by averaging 100 laser pulses and using a gate time of 2000 µs.

RESULTS. The U removal capacity of *A. facilis* cells at 0.1 mM U was determined in mg U per g dry biomass (DBM) and it was found, that 21 mg U was removed during the first 5 minutes of the experiments. After an incubation time of 1 h, the cells removed about 30 mg U/g DBM. After 24 h, the equilibrium was reached and the bacterial cells displayed a total U removal capacity of 58 mg U/g DBM. The measured TRLFS emission spectra of the U complexes formed by the cells of *A. facilis* at 0.1 mM U concentration and incubation time of 5 min, 1 h, 16 h and 24 h are characterized by five emission bands. As shown in the luminescence spectrum (Fig. 1A), the luminescence intensities increase with incubation time, which is correlated with the time-dependent removal of U(VI) by *A. facilis* cells. The TRLFS spectra of the samples which were incubated with U for 5 min and 1 h are characterized by similar peak maxima (Fig. 1A). Compared to the band positions of the uranyl-lipopolysaccharide-complex ($R\text{-}O\text{-}PO_3\text{-}UO_2$) luminescence spectrum at pH 4, there is a good agreement with only small deviations (Tab. 1).[1] It seems that UO_2^{2+} is bound on LPS at the beginning of the incubation. The spectra of the samples, which were measured after 16 and 24 h of incubation time with U, are characterized by uranyl(VI) band positions, which are shifted to lower wavelengths (Fig. 1A). The peak maxima show similarities to reference spectra of the 1 : 2 uranyl carboxyl complex ($[R\text{-}COO]_2\text{–}UO_2$) of uranyl-peptidoglycan at pH 5.6 as shown in Tab. 1 and Fig. 1B.[2]

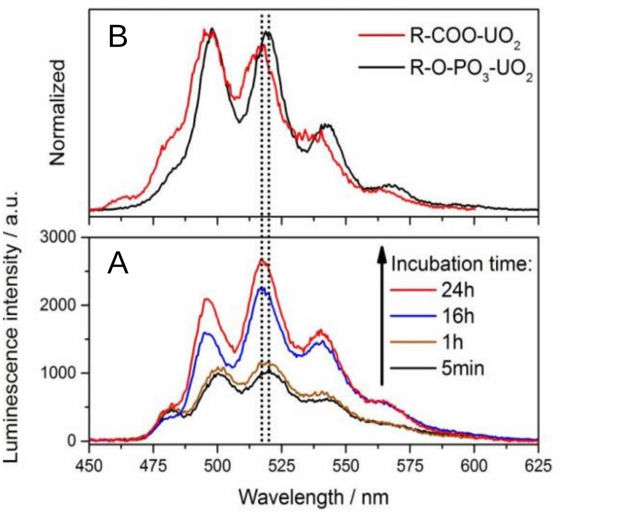

Fig. 1: Luminescence spectra of *A. facilis* cells exposed to 0.1 mM U after different incubation times (Fig. 1A) at 30 °C. The spectra are compared to reference spectra of uranyl-LPS-complex and uranyl-PGN-complex (Fig. 1B).[1, 2]

Tab. 1: Luminescence band positions of *A. facilis* cells exposed to 0.1 mM U compared to band positions of reference spectra of uranyl-lipopolysaccharide-complex and uranyl-peptidoglycan-complex.[1, 2]

Samples	h	Luminescence emission bands (nm)			
A. facilis pH 5.0	0.01	480.7	499.7	520.1	545.1
A. facilis pH 5.0	24	479.3	495.5	517.3	541.4
$LPS\text{–}R\text{–}OPO_3\text{–}UO_2$ pH 4.0 [1]	24	481.5	498.1	519.6	542.9
$PGN\text{–}(R\text{–}COO)_2\text{–}UO_2$ pH 5.6 [2]	24	481.6	498.1	518.0	539.0

The luminescence spectra obtained by TRLFS in our studies after 16 h and 24 h of incubation with U are indicating that UO_2^{2+} was bound on carboxyl functionality groups of the PGN. However, the determined spectra and luminescence characteristics definitely refer to the formation of more than one uranyl-species. It has to be taken into account that a uranyl phosphoryl coordination is additionally formed which could be consisted of a uranyl-LPS-complex.[3]

ACKNOWLEDGEMENTS. The research leading to these results has received funding from Verbundprojekt Strahlung und Umwelt III: „Transfer von Radionukliden in aquatischen Ökosystemen" (TransAqua) under grant agreement number 02NUK030F.

---

[1] Barkleit, A. *et al.* (2008) *Dalton Trans.*, 2879 – 2886.
[2] Barkleit, A. *et al.* (2009) *Dalton Trans.*, 5379 – 5385.
[3] Krawczyk-Bärsch, E. *et al.* (2018) *J. Hazard. Mater.* **347**, 233 – 241.

Sorption of trivalent f-elements by biomaterials of marine origin – A TRLFS and solid-state NMR Study

K. Kammerlander,[1] N. Huittinen, M. Patzschke, S. Paasch,[1] E. Brunner,[1] T. Stumpf

[1]Institute of Bioanalytical Chemistry, Technische Universität Dresden, Dresden, Germany

To evaluate the suitability of biomaterials of marine origin to effectively scavenge trivalent f-elements, we investigated Eu^{3+} and Cm^{3+} uptake by chitin using TRLFS and solid-state NMR spectroscopy.

Chitin, a biopolymer consisting of N-acetylglucosamine monomer units connected by β-(1,4)-glycosidic bonds (Fig. 1) is the second most abundant biopolymer on earth after cellulose. It is well-known for its ability to sorb a wide range of transition metal ions, such as copper, chromium and mercury.[1–3] However, the interactions between chitin and f-element ions have not been studied as extensively, with the exception of uranium ions.[4]

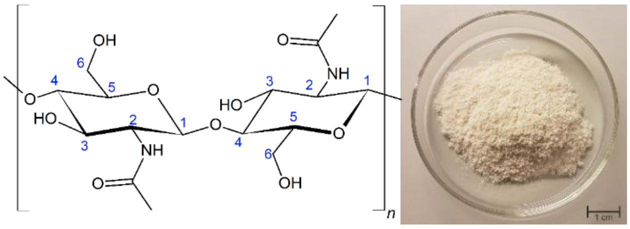

Fig. 1: Molecular structure of chitin (left), α-chitin raw material used for sorption experiments (right).

A study by Ozaki *et al.* has provided some insight into the possible interactions of Am^{3+}, Cm^{3+} and Eu^{3+} with chitin, chitosan and cellulose using TRLFS.[5] However, in the present study, we employed two complimentary spectroscopic methods, solid-state NMR and time-resolved laser fluorescence spectroscopy (TRLFS) to investigate both the organic chitin matrix and the trivalent f-element (Cm^{3+} and Eu^{3+}) interactions with the material.

EXPERIMENTAL. Suspensions of α-chitin in aqueous solutions containing Eu^{3+} or Cm^{3+} (glovebox, N_2) in 1 mM $NaClO_4$ we prepared with varying initial metal ion concentrations (Eu^{3+}: 10^{-6}–10^{-3} M; Cm^{3+}: 3×10^{-7}–10^{-6} M) and pH values (Eu^{3+}: 4–7; Cm^{3+}: 7–8) and equilibrated for 7 days under constant stirring. After centrifugation, wet pastes were recovered and subsequently analyzed. TRLFS measurements were conducted both using non-selective excitation in the UV-range (λ_{ex} = 394 nm for Eu^{3+} and 396.6 nm for Cm^{3+}) and selective excitation at 10 K in the wavelength region 575–580 nm (Eu^{3+}) and 595–610 nm (Cm^{3+}). ^{1}H-, ^{13}C-CP- and ^{15}N-CP-NMR spectra were acquired using a Bruker Ascend 800 MHz spectrometer with an H/C/N EFREE MAS probe head and rotation frequencies of 10–15 kHz (Eu^{3+} doped samples only). Additionally, the Cm^{3+} sorption capacity was analyzed using liquid scintillation counting (Tri-Carb 3100 TR, Perkin Elmer) and the Eu^{3+} sorption capacity was measured after ashing and dissolving the samples with ICP-MS (Elan 9000, Perkin Elmer).

RESULTS. At lower ion concentrations at pH 7, Eu^{3+} ions are almost completely sorbed and retained by chitin. Upon increasing the concentration and at lower pH values, the sorption capacity decreases. Since the concentrations of the Cm^{3+} doped samples are lower compared to the range of europium concentrations, almost complete sorption (> 95 %) could be achieved. Using TRLFS, the formation of inner-sphere complexes is indicated by the significant red shift in the Cm^{3+} spectra compared to the Cm^{3+} aquo ion (Fig. 2) and the $^7F_2/^7F_1$ emission band intensity ratio in the Eu^{3+} spectra. However, the natural occurrence of iron and manganese ions as trace elements in the chitin raw material interferes with the spectroscopic measurements by distorting the evaluation of the luminescence lifetimes through the introduction of an additional non-radiative quenching mechanism (Fe) and masking the Cm^{3+} signal due to transitions at similar energy levels (Mn). Similarly, no significant differences in the solid-state ^{13}C-CP- and ^{15}N-CP-NMR spectra could be detected, regardless of ion concentration or pH value due to the low Eu^{3+} to monomer unit ratio, and the line broadening caused by the prevalence of paramagnetic ions.
Despite these drawbacks, two interaction mechanisms between the trivalent metal cations and the chitin solid were tentatively identified: 1) incorporation into the chitin backbone resulting in an almost complete removal of the hydration water around the metal cations, and 2) surface sorption onto the chitin molecule.

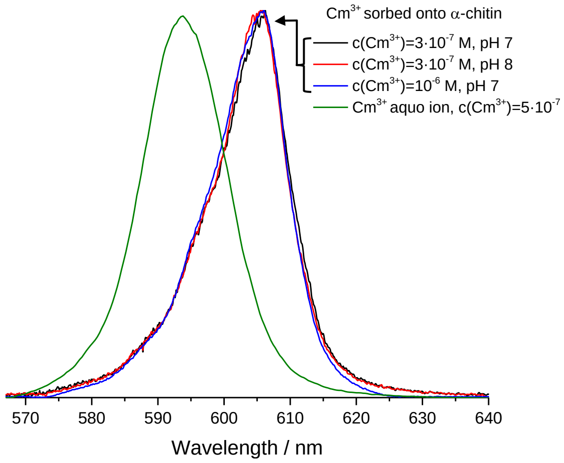

Fig. 2: TRLFS emission spectra of the Cm^{3+} aquo ion and Cm^{3+} ions sorbed onto chitin.

In the future, we will further explore the interactions between the trivalent f-element cations and the chitin monomers, glucosamine and N-acetylglucosamine and support the spectroscopic data with theoretical calculations to elucidate the Eu^{3+} and Cm^{3+} speciation. Other biomaterials produced by marine species such as diatoms or marine sponges are also interesting candidates for the application as natural sorbents for remediation and decontamination purposes.

ACKNOWLEDGEMENTS. This work has been funded by the BMBF - Germany (Federal Ministry of Education and Research) within the research activity project FENABIUM (02NUK046A).

---

[1] Gonzalez-Davila, M. *et al.* (1990) *Geochim. Cosmochim. Acta* **54**, 761–768.
[2] Singh, P. *et al.* (2016) *Appl. Water Sci.* **6**, 199–204.
[3] Miretzky, P. *et al.* (2009) *J. Hazard. Mater.* **167**, 10–23.
[4] Schleuter, D. *et al.* (2013) *Carbohydr. Polym.* **92**, 712–718.
[5] Ozaki, T. *et al.* (2006) *J. Environ. Toxicol. Chem.* **25**, 2051–2058.

U(VI) toxicity onto *Brassica napus* cells: correlation of calorimetric data with oxidoreductase activity and U(VI) speciation

S. Sachs, K. Fahmy, J. Oertel, G. Geipel, F. Bok

We demonstrated microcalorimetry as a sensitive real-time monitor of U(VI) toxicity in a plant cell model. The calorimetric descriptor "metabolic capacity" was introduced, which correlates with the enzymatically determined cell viability. The combination with TRLFS and thermodynamic modeling indicated that the cell metabolism is affected predominantly by U(VI) hydroxo species.

The transfer of radionuclides into the food chain is a central concern in the safety assessment of both nuclear waste repositories and remediation strategies in radioactively contaminated areas. The interaction of radionuclides with plants is mostly described by transfer factors without knowing the underlying processes. However, previous studies showed, for instance, a speciation-dependent influence of radionuclide uptake and translocation in plants. We studied the interaction of U(VI) with canola cells (*Brassica napus*) focusing on the concentration-dependent impact of U(VI) on the cell metabolism.[1]

EXPERIMENTAL. Starting from a callus cell culture, suspension cultures of *Brassica napus* cells were grown in medium R (pH 5.8).[2] Isothermal microcalorimetry was performed with a TAMIII instrument (Waters) to monitor the metabolic heat flow produced by the cells in the absence or presence of 2×10^{-5}–2×10^{-4} M U(VI) in medium R with a reduced phosphate concentration of 1×10^{-5} M (medium R_{red}). After microcalorimetric measurements, the cell viability (oxidoreductase activity) was determined by MTT test, which detects the activity of mitochondrial and cytosolic dehydrogenases.[3] The U(VI) speciation in medium R_{red} at pH 5.8 was studied by time-resolved laser-induced fluorescence spectroscopy (TRLFS) and thermodynamic modeling. All experiments are explained in detail by Sachs *et al.*[1]

RESULTS. *Brassica napus* cells showed a temporal decrease in metabolic thermal power and a general reduction of heat production with increasing U(VI) concentration. So far, metabolic calorimetry suffered from the lack of models describing metabolic decline.[4] To overcome this, the model-independent descriptor "metabolic capacity" that allows the evaluation of calorimetric data of declining metabolic phases was introduced in this work. The "metabolic capacity" M represents the product of the time-dependent heat flow P (overall "enzyme activity") and the integrated dissipated heat H (overall "substrate depletion") relative to a time zero (t_0):

$$M(t) = P(t) \cdot H(t), with\ H(t) \int_{t0}^{t} P(t)dt \qquad (1)$$

The normalization of the maximal "metabolic capacity" with respect to the initial heat flow $P(t_0)$ of each cell culture results in the "characteristic metabolic capacity" M_c. The evaluation of individual thermograms was described in detail.[1] Here, M_c and the normalized cell viability are, to a very good approximation, linearly related at U(VI) concentrations up to 200 µM as shown in Fig. 1. In the case of the *Brassica napus* cells, the M_c values reveal a half-maximal inhibitory concentration (IC_{50}) of 160 µM U(VI), which agrees with the MTT viability test due to the almost ideal correlation.

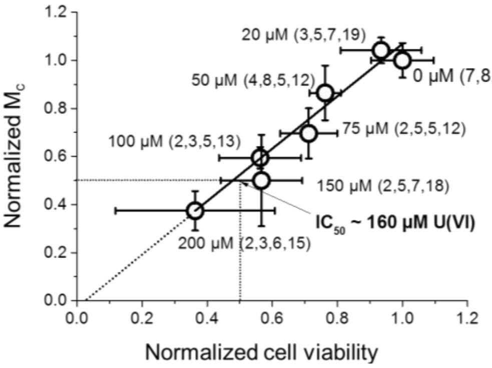

Fig. 1: Correlation of oxidoreductase activity (viability) with "characteristic metabolic capacity" M_c normalized to control samples without U(VI). The first and second number in brackets indicates how many cell cultures and thermograms contributed to each microcalorimetric data point, respectively. The third and fourth numbers give the corresponding information on cell cultures and individual MTT tests.

The effects of U(VI) on the cell metabolism may depend on its speciation in the medium (pH after experiment: 5.5–5.9). At pH 5.8, $UO_2HPO_4(s)$ dominates at 20 µM U(VI) followed by a significant amount of $(UO_2)_3(OH)_5^+$. The latter increases with $[U(VI)_{tot}]$ and is the dominating species at $[U(VI)_{tot}] > 50$ µM. Besides that, $(UO_2)_4(OH)_7^+$, UO_2OH^+, UO_2^{2+}, and $(UO_2)_2(CO_3)(OH)_3^-$ species are formed, whereas the amount of $UO_2HPO_4(s)$ remains constant due to the limited phosphate concentration. The two dominant U(VI) species in medium R_{red} were verified by TRLFS.[1] Figure 2 correlates M_c with $[U(VI)_{tot}]$ and, alternatively, with the sum of $[(UO_2)_3(OH)_5^+]$ and $[(UO_2)_4(OH)_7^+]$ that make more than 50 % of all U(VI) species for $[U(VI)_{tot}] > 20$ µM. The normalized M_c values scale linearly with the U(VI) hydroxo complex concentration. For [U(VI) hydroxo species] = 0 µM, the data intersect the y-axis at the expected value of $M_c = 1$ for control samples without U(VI), which is not met for $[U(VI)_{tot}] = 0$ µM. This indicates that the dissolved species possess the highest bioavailability, whereas $UO_2HPO_4(s)$ contribute to $[U(VI)_{tot}]$ without lowering M_c.[1]

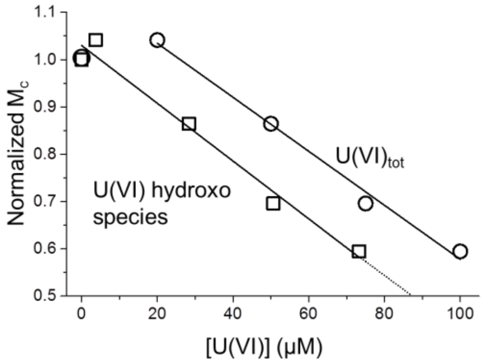

Fig. 2: U(VI) species dependency of M_c. Squares: M_c *vs.* the concentration of the dominant hydroxo species. Circles: M_c *vs.* $[U(VI)_{tot}]$.

ACKNOWLEDGEMENTS. The authors thank M. Obeid, J. Seibt, S. Heller, J. Philipp, and S. Gurlit for experimental support.

---

[1] Sachs, S. *et al.* (2017) *Environ. Sci. Technol.* **51**, 10843–10849.
[2] www.dsmz.de/Fileadmin/downloads/PC/medium/R.pdf.
[3] Mosmann, T. (1983) *J. Immunol. Methods* **65**, 55–63.
[4] Braissant, O. *et al.* (2013) *Thermochim. Acta* **555**, 64–71.

Comparison of the uranium association of fungi in minimal medium and soil extract

A. Wollenberg, A. Günther, J. Raff

Batch experiments and also time-resolved laser-induced fluorescence spectroscopy (TRLFS) experiments were implemented to determine the interactions of the fungi *Leucoagaricus naucinus* and *Schizophyllum commune* with uranium(VI) in soil extract compared to experiments in minimal medium.

EXPERIMENTAL. *L. naucinus* was cultivated in medium 90 (malt extract 30 g/L and soya peptone 3 g/L), and *S. commune* was cultivated in the complex yeast medium with tryptophan (2 g/L tryptone, 2 g/L yeast extract, 0.5 g/L $MgSO_4$, 0.5 g/L KH_2PO_4, 1 g/L K_2HPO_4, 1 g/L tryptophan, 20 g/L glucose). The fungal biomass was harvested by washing with sterile minimal medium (19.5 mg/L $MgSO_4$, 2.4 mg/L $FeCl_3$, 0.9 mg/L K_2HPO_4) and filtration. The soil extract was produced by mixing sterile soil with sterile deionized water in the ratio of 1 : 3 overnight. The supernatant was centrifuged to remove particles. For binding experiments, the minimal medium (MM) with metal (pH = 5, $[U]_0 = 50$ mg/L) or the soil extract (SE) with metal (natural pH 5.7 $[U]_0 = 50$ mg/L) was mixed with fungal biomass (dry biomass of 312 mg/L) and shaken at 100 rpm for 48 h. The U(VI) speciation was determined by TRLFS experiments at −120 °C using a pulsed Nd-YAG laser (Continuum) and a CCD camera (Horiba Jobin Yvon IHR 550) to detect the luminescence.

RESULTS. As can be seen in Fig. 1, *S. commune* and *L. naucinus* can associate up to 50 % of uranium in the MM after 48 h. The results show, that there is no difference in the amount of associated uranium by *S. commune* depending on the initial solution. By comparison, *L. naucinus* is able to associate 10 % more uranium in SE than in the MM. Therefore, it can be assumed that the organic substances, which have been detected by HPLC measurements in the SE (results not shown), improve the bioavailability of U(VI) for *L. naucinus*.

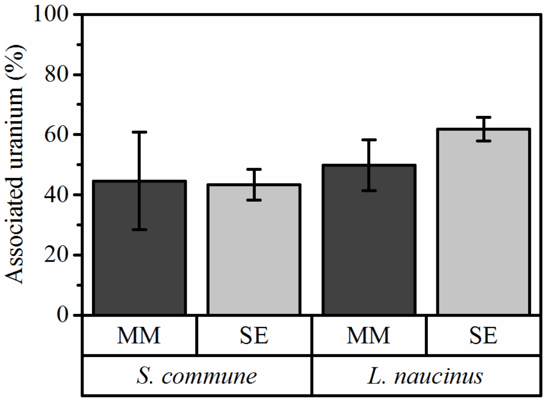

Fig. 1: Associated uranium in % by fungi ($c_{dw} = 312$ mg/L) in MM (pH = 5, $[U]_0 = 50$ mg/L) and SE (pH = 5., $[U]_0 = 50$ mg/L) after 48 h.

The main uranium emission bands of fungal associated species are shifted to higher wavelengths compared to the respective signals in the initial solutions (see Tab. 1). In case of *S. commune*, the position of emissions bands indicate a uranium association to phosphate groups of organic molecules such as fructose-6-phosphate.[1] Additionally, the uranium spectra of *S. commune* in SE and MM are comparable (see Fig. 2). Although the uranyl band positions of *L. naucinus* (from MM and SE) are only slightly shifted compared to the signals of *S. commune*, the shapes of the spectra are significantly different (see Fig. 2). The latter most likely indicates a mixture of carboxyl and phosphoryl groups being involved in the binding of uranium by *L. naucinus.* However, there are also no significant differences between the uranium spectra of *L. naucinus* in MM and in SE.

Tab. 1: Main uranium emission bands of used solutions and fungal biomass.

Sample	Main emission bands (nm)		
MM	491.1	511.3	533.5
S. commune in MM	498.3	520.0	543.0
L. naucinus in MM		520.8	542.0
SE	492.6	513.5	535.4
S. commune in SE	497.8	518.8	541.0
L. naucinus in SE		519.7	541.7

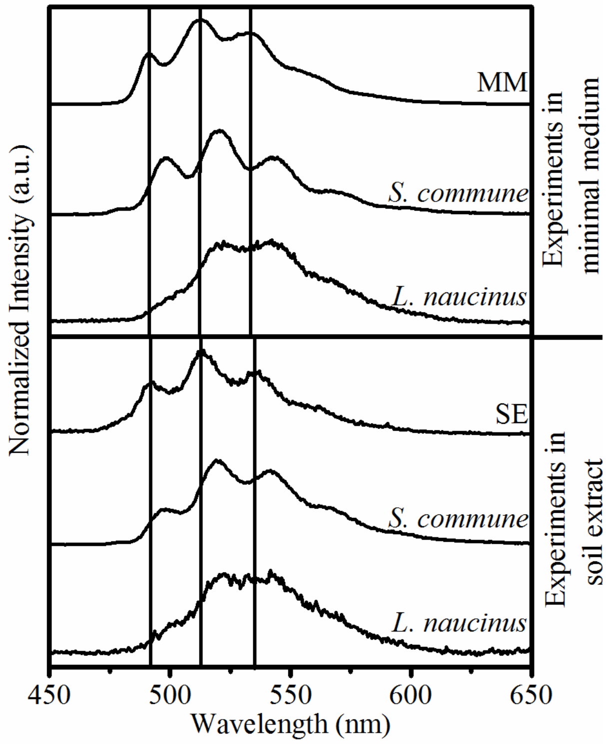

Fig. 2: Uranium TRLF spectra of contaminated fungi and corresponding MM (pH = 5, $[U]_0 = 50$ mg/L) or SE (pH = 5.7, $[U]_0 = 50$ mg/L).

In summary, the results show that the fungal biochemistry and not the surrounding environment determines the speciation of associated uranium.

ACKNOWLEDGEMENTS. The authors kindly acknowledge the funding of the project BioVeStRa by the BMBF under contract No. 15S9276A and thank to Sabrina Gurlit and Aline Chlupka for elemental analyses.

---

[1] Koban, A. *et al.* (2004) *Radiochim. Acta* **92**, 903–908.

Reduction of selenium oxyanions by *Bacillus* sp. JG-B5T

S. Fischer, R. Jain,[1] R. Hübner,[2] N. Jordan

[1]HZDR, Helmholtz Institute Freiberg for Resource Technology, Dresden, Germany; [2]HZDR, Institute of Ion Beam Physics and Materials Research, Dresden, Germany

This study focuses on the interaction of two water soluble selenium oxyanions, selenite and selenate, with the *Bacillus* sp. JG-B5T, isolated from a uranium mining waste pile. The ability of *B.* sp. JG-B5T to reduce Se(IV) oxyanions leading to the formation of less water soluble biogenic selenium(0) nanoparticles (BioSeNPs) was shown.

Selenium can be a toxic element for aquatic organisms and birds in the µg/L range.[1] Thus, understanding the mobility of Se in the environment is important. Microorganisms are known to reduce water soluble selenium oxyanions to colloidal BioSeNPs with a biological corona, leading to a different mobility in water and thus affecting the environmental fate of selenium.[2] In this study, the ability of the rod-shaped strain *B.* sp. JG-B5T to reduce selenium oxyanions was studied. This microorganism was isolated from the uranium mining waste pile Haberland near Johanngeorgenstadt (Saxony, Germany) in 1997.[3] Such piles are heavy-metal-contaminated environments laden with high concentrations of iron, manganese, lead or chromium.[4] In this oxidative environment, it is conceivable that bacteria evolved mechanisms to handle the stress and thus may interact efficiently also with selenium.[5]

EXPERIMENTAL. Samples were prepared by inoculating 2.5 % of *B.* sp. JG-B5T preculture in fresh nutrient broth medium with and without 2.5 mM Na_2SeO_3 and Na_2SeO_4. The cultivation was done at 30 °C on a shaker at 120 rpm for 14 days. At different time intervals, aliquots were taken for analytical analysis. Optical density (OD) at 600 nm was measured against blank medium of the same dilution. Aliquots were centrifuged (15,557 g, 4 °C, 25 min) and the total selenium concentration as well as the Se(IV) content were measured in the supernatant (spiked with HNO_3) by ICP-MS and by HG-AAS, respectively. The surface morphology and the qualitative chemical composition of the BioSeNPs were characterized by scanning electron microscopy (SEM) coupled with energy-dispersive X-ray spectroscopy (EDXS) analysis.

RESULTS. Growth profiles of *B.* sp. JG-B5T with selenate (data not shown) and without selenate addition (Fig. 1A, black line) were very similar. In both cases the maximum OD was measured after 26.5 h of cultivation. No significant decrease of the total selenium concentration as well as no increase of Se(IV) concentration were observed even after 14 days (data not shown). In contrast, the growth profile of *B.* sp. JG-B5T after selenite addition (Fig. 1B, black line) showed a short initial lag phase of 8 h and the maximum OD was reached after 48.5 h. After 14 days of cultivation, 70 % of selenite was reduced (Fig. 1B, red and blue line). The red color of the culture indicated the reduction of selenite to BioSeNPs. SEM imaging showed spherical particles with a diameter between 70 to 200 nm, building larger agglomerates of 300 to 550 nm size (Fig. 2). These BioSeNPs mainly consist of Se, but also Cl, C, O and Na were observed by EDXS analysis.

The present study shows that *B.* sp. JG-B5T reduces only the bacterial toxic selenite to spherical BioSeNPs under aerobic conditions. However, the presence of selenate seems to have no effect on bacterial health for the investigated bacteria strain *B.* sp. JG-B5T.

Therefore, the bacterial selenite reduction affects the selenium oxidation state and its morphology, which impacts the mobility, bioavailability and toxicity of selenium in the environment.

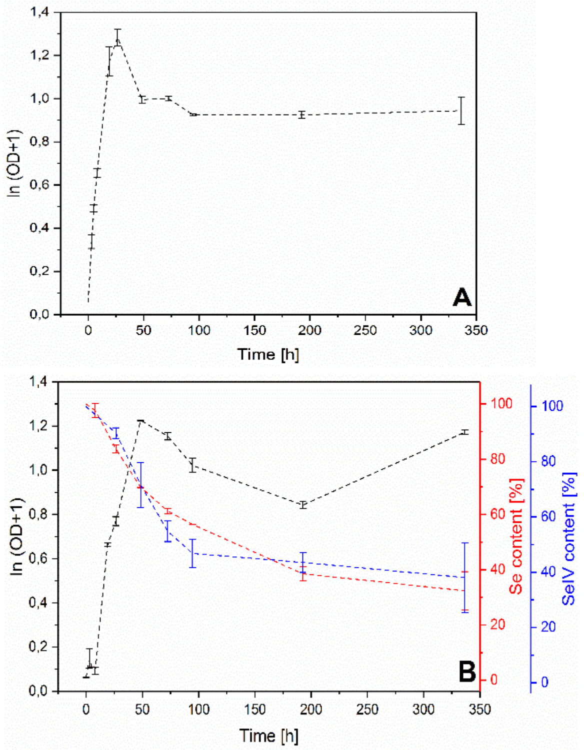

Fig. 1: Growth profile (black line) of *B.*sp. JG-B5T without addition (A) and with selenite addition (B); total selenium content (red line); Se(IV) content (blue line).

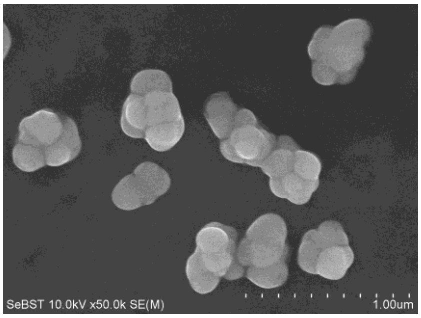

Fig. 2: SEM image of BioSeNPs formed during the reduction of selenite by *B.*sp. JG-B5T.

ACKNOWLEDGEMENTS. We thank S. Gurlit for ICP-MS + HG-AAS, E. Christalle for SEM/EDXS and L. Hohlfeld for assistance in lab work.

---

[1] Lenz, M. *et al.* (2009) *Sci. Total Environ.* **407**, 3620−3633.
[2] Jain, R. *et al.* (2017) *Environ.-Sci. Nano* **4**, 1054−1063.
[3] Panak, H. *et al.* (1998) *J. Alloy Compd.* **271−273**, 262−266.
[4] Selenska-Pobell, S. *et al.* (2001) *Antonie Leeuwenhoek* **79**, 149−161.
[5] Lederer, F. L. *et al.* (2013) *Microbiology* **159**, 1097−1108.

Comparative study of two extremely halophilic *Halobacterium* species from rock salt

M. Bachran, S. Kluge, M. Bader, A. Cherkouk

Two extremely halophilic *Halobacterium* species isolated from rock salt in Germany (*Halobacterium* sp. GP5 1-1) and Austria (*Halobacterium noricense* DSM 15987^T) were compared in terms of their morphology, 16S rRNA gene sequence and protein profile. Both species showed a high similarity (> 99 %) in their 16S rRNA gene sequence. However, the two species showed differences in morphology and protein pattern.

Rock salt, in addition to clay and crystalline rock, is a potential host rock formation for the long-term storage of radioactive waste in a deep geological repository in Germany. Due to the high salinity only adapted microorganisms such as extremely halophilic archaea can survive under these conditions.[1] Up to now, only a few of such archaea could be isolated from different rock salts, as for example different *Halobacterium* species like *H. hubeiense* JI20-1 from a 2000 m deep rock salt in Hubei Province, China, *H. noricense* DSM 15987^T from a salt mine in Austria, and *Halobacterium* sp. WIPP from the WIPP (Waste Isolation Pilot Plant) in Carlsbad, New Mexico, USA.[2−4] In this study, *Halobacterium* sp. GP5 1-1, which was isolated from rock salt from Gorleben, will be compared with *Halobacterium noricense* DSM 15987^T with respect to its morphology, 16S rRNA gene sequence, and protein pattern.

EXPERIMENTAL. The two *Halobacterium* species were cultivated in modified R2A medium (3 M NaCl) at 30 °C in the dark. In the exponential growth phase, the cells were harvested by centrifugation and then washed three times with 3 M NaCl, pC_{H+} 6 (corrected pH due to high ionic strength).[5] Prior to *in situ* polymerase chain reaction (PCR), washed cells were lysed in water to reduce the high content of NaCl. Archaea specific primer (Arch21f and Arch958r) were used to amplify the 16S rRNA gene.[6] The products were purified (MSB® Spin PCRapace, Stratec Molecular) and Sanger sequenced from GATC Biotech AG. The 16S rRNA gene sequences were aligned using ClustalW and the phylogenetic tree was constructed with MEGA7 using the maximum-likelihood algorithm.[7] The sequences obtained from the two *Halobacterium* species were compared with the sequences of the NCBI database by means of BLAST algorithm[8] to get the phylogenetic closest relatives. Additionally, both species were compared on the protein level by SDS-PAGE using a 10 % polyacrylamide separation gel loaded with dry biomass of 0.1 mg.[9] After electrophoresis, the gel was stained with colloidal Coomassie Brilliant Blue.

RESULTS. As shown in Fig. 1, the two species show significant differences in their morphology. The cells of *Halobacterium* sp. GP5 1-1 are of polymorphic shape and those of *H. noricense* DSM 15987^T are uniformly shaped coccus. Rod shaped as well as coccoid and irregular shaped cells were also seen for *H. hubeiense* JI20-1.[2]

16S rRNA gene sequences of the two examined species show a 99.9 % similarity. Only one base is different out of 802 bases. In fact, the 16S rRNA gene sequence of *Halobacterium* sp. GP5 1-1 is identical to the 16S rRNA gene sequence of *H. hubeiense* JI20-1 and *Halobacterium* sp. WIPP (Fig. 2).

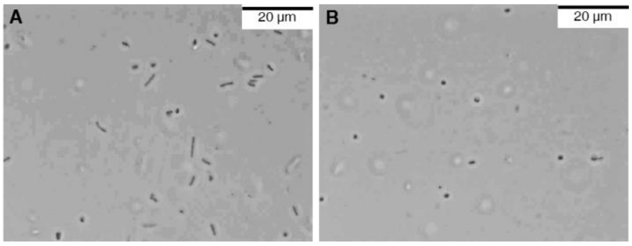

Fig. 1: Light microscopy images of *Halobacterium* sp. GP5 1-1 (A) and *Halobacterium noricense* DSM 15987^T (B) in the exponential growth phase in modified R2A medium.

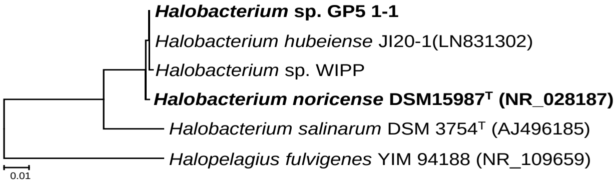

Fig. 2: Phylogenetic dendrogram showing the position of the two examined *Halobacterium* species (bold) based on 16S rRNA gene sequences. Bar: 1 % sequence divergence.

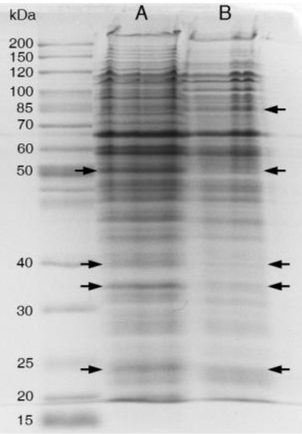

Fig. 3: SDS-PAGE image of whole cell protein patterns of *Halobacterium* sp. GP5 1-1 (A) and *Halobacterium noricense* DSM 15987^T (B).

The whole protein pattern of the both species show also differences between the two species (Fig. 3). Due to the fact that the same amount of biomass was loaded to the gel, a direct comparison is possible. Distinct differences in intensity and size or shifted bands can be recognized (Fig. 3, examples are indicated with black arrows).

The next step will be to carry out uranium bioassociation studies with the extremely halophilic isolate *Halobacterium* sp. GP5 1-1, which can be combined with proteomic analyses.

In conclusion, despite the fact that both investigated species show nearly the same 16S rRNA gene sequence, differences in morphology and protein level exist. It needs to be clarified whether both species thusly behave different under repository relevant conditions, especially regarding their interactions with uranium.

[1] Larue, J. (2010) *Abschlussbericht Projekt VerSi GRS-A-3535/4*, p. 34.
[2] Jaakkola, S. T. *et al.* (2016) *Environ. Microbiol.* **18**, 565−579.
[3] Gruber, C. *et al.* (2004) *Extremophiles* **8**, 431−439.
[4] Swanson, J. S. *et al.* (2012) *Report LA-UR-12-22824*, p. 1.
[5] Borkowski, M. *et al.* (2009) *Report LA-14360*, p. 26−27.
[6] DeLong, E. F. (1992) *Proc. Natl. Acad. Sci.* **89**, 5685−5689.
[7] Kumar, S. *et al.* (2016) *Mol. Biol. Evol.* **33**, 1870−1874.
[8] Altschul, S. F. *et al.* (1990) *J. Mol. Biol.* **215**, 403−410.
[9] Laemmli, U. K. (1970) *Nature* **227**, 680−700.

Evolution of microbial diversity in bentonite-microcosms

N. Matschiavelli, S. Kluge, V. Prause,[1] A. Meleshyn,[1] A. Cherkouk
[1]Gesellschaft für Anlagen- und Reaktorsicherheit (GRS) gGmbH, Braunschweig, Germany

Concerning the deep geological disposal of high-level radioactive waste (HLW), bentonite plays a crucial role by using it as a barrier and buffer material in between the steel-canister, containing the HLW, and the surrounding host rock. Because of its high swelling capacity and the low hydraulic conductivity, bentonite acts as a kind of seal, retarding water to contact the steel-container. Furthermore, it hinders the migration of radionuclides, which can be released due to the corrosion process. Here, we simulated anoxic conditions, which would establish several weeks to month after closure of the repository. For stimulating microbial effects, acetate, lactate and the humin-analogue antraquinone-2,6-disulfonate (AQDS) were added to microcosms. After one year incubation, stimulated batches show the formation of black precipitates and cavities. Mainly sulfate-reducing organisms were identified, showing that microbes evolve under the respective conditions.

EXPERIMENTAL. The set-up of microcosm-experiments was performed by the "Gesellschaft für Anlagen- und Reaktorsicherheit" (GRS). Here, 300 g of processed, industrial Bentonite SD80 were supplied with 600 mL synthetic Opalinus Clay pore water solution (212 mM NaCl, 26 mM $CaCl_2$, 14 mM Na_2SO_4, 1.6 mM KCl, 17 mM $MgCl_2$, 0.51 mM $SrCl_2$ and 0.47 mM $NaHCO_3$) and filled up in glass flasks which were welded after filling. For stimulation of microbial processes 50 mM lactate, 50 mM acetate and 0.1 mM AQDS were added to the pore-water. The well-mixed slurries incubated at 25 °C in the dark, without shaking for one year. Hereafter, glass flasks were opened and approximately 60 g of Bentonite SD80 were removed in a sterile manner, filled up in sterile tubes and stored at −70 °C until use. For extracting the DNA a modified protocol according to Selenska-Pobell (1995) was applied.[1] The 16S rDNA was amplified by using oligonucleotides 515f and 806r and sequenced with MiSeq Illumina by RTL Genomics.[2]

RESULTS AND DISCUSSION. The microbial potential within the processed bentonite SD80 was elucidated in microcosms, which incubated for one year at 25 °C under anaerobic conditions. The microbial diversity changed drastically during incubation time and showed clear differences between the raw-material and the substrate-containing microcosms (Fig. 1B). In contrast to the raw-material, where three soil-organisms have been found (53 % *Stenotrophomonas* spp., 32 % *Ralstonia* spp. and 15 % *Oscillatoria* spp.), substrate-containing microcosms were dominated by sulfate-reducing bacteria (SRB; 50 % *Desulfitobacterium* spp., 8 % *Desulfosporosinus* spp. and 8 % *Desulfotomaculum* spp.). SRBs use sulfate as terminal electron-acceptor, thereby forming hydrogen sulfide for which it is known to promote the corrosion process.[3, 4] Microbial influenced corrosion (MIC) can lead to a mechanical failure of metals, alloys, concrete and clays and, thus, failure of potential materials used in a HLW repository.[5] Additionally, the generated sulfides could react with minerals and ions, thereby changing their properties (*e.g.* solubility, complexation-behavior). Even in our simple experiment, some changes are quite obvious, like the formation of a black layer in between the contact area of bentonite and pore-water solution (Fig. 1A (1)) as well as isolated black spots (Fig. 1A (3)), indicating the formation of insoluble iron sulfides. Additionally, large cavities where formed (Fig. 1A (2)), very likely due to the formation of gases like hydrogen sulfide, hydrogen gas and carbon dioxide – typical metabolites during sulfate respiration. Electrons for the reduction of sulfate can be provided by a broad range of organic substances or hydrogen gas, potentially formed during radiolysis or anaerobic corrosion of the steel container when coming in contact with water. In our study, the electron donor is very likely the supplemented lactate, which can be converted to acetate (incomplete oxidation) and/or to carbon dioxide and water (complete oxidation).[6]

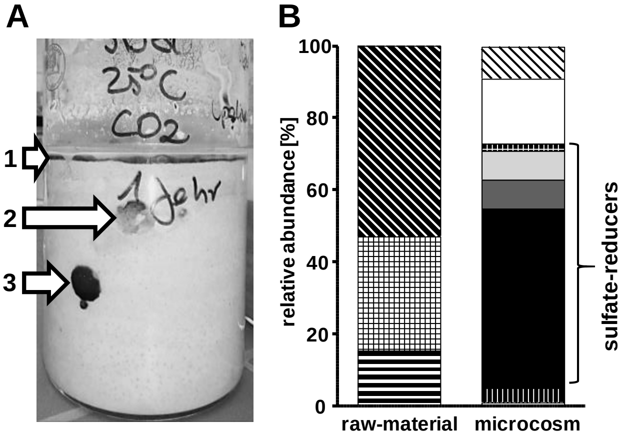

Fig. 1: The microbial diversity in SD80-microcosm after one year incubation at 25 °C. A: SD80-microcosm with Opalinus Clay pore water solution including acetate and lactate. Macroscopic formation of a black layer (1), cavities (2) and black spots (3). B: Microbial diversity in SD80 -raw-material and -microcosm. Every colour/pattern represents a distinct order. After one year, the microcosm is dominated by sulphate-reducing organisms.

Our results emphasize the importance of understanding microbial activity in bentonite and possible interactions with materials used in a HLW repository. Microbial activity could lead to the production of corrosive metabolic byproducts that could have significant influence on the stability of used materials and, thus, on the release of radionuclides. Furthermore, the beneficial properties of the bentonite itself, could be negatively influenced.

ACKNOWLEDGEMENTS. This work was supported by the Federal Ministry for Economic Affairs (No. 02E11344A and 02E11344B).

---

[1] Selenska-Pobell, S. (1995) *MMEM.* **1.5.1.**, 1−17.
[2] Caporaso, J. G. *et al.* (2010) *Proc. Natl. Acad. Sci.* **108**, 4516−4522.
[3] Enning, D. and Garrelfs, J. (2014) *Appl. Environ. Microbiol.* **80**, 1226−1236.
[4] Muyzer G. and Stams, A. J. M. (2008) *Nat. Microbiol.* **6**, 441−454.
[5] Li, K. *et al.* (2013) *Corros. Rev.* **31**, 73−84
[6] Fuchs, G. (2007) in: *Allgemeine Mikrobiologie,* p. 388−395, Georg Thieme Verlag, Stuttgart.

SCIENTIFIC CONTRIBUTIONS (PART IV)

Nuclear Reactor

SAFETY RESEARCH

Estimation of ultimate tensile stress by means of small punch testing

E. Altstadt, M. Houska, S. Holmström[1]

[1]European Commission, Joint Research Centre (JRC), Petten, The Netherlands

A new correlation for the estimation of the ultimate tensile stress from small punch tests was derived by means of finite element simulations with a systematic variation of plasticity parameters. The correlation was shown to be independent of the specific material properties and validated by more than 100 small punch tests of nine different steel heats.

The small punch test (SPT) has been recognized as a supportive means for the development and monitoring of structural materials (Fig. 1). As a screening procedure, the SPT is intended to provide estimations of the material properties with as small amounts of material as possible, allowing for example a quick evaluation of ageing mechanisms such as radiation induced hardening and embrittlement or thermal ageing.[1,2]

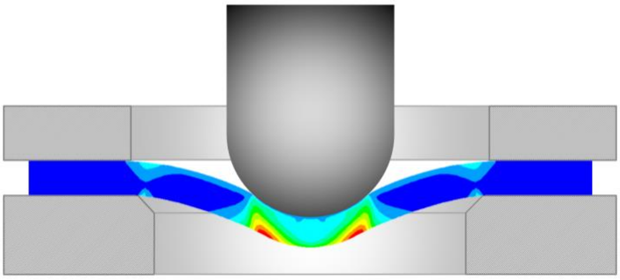

Fig. 1: Schematic of the small punch test. The specimen size is D8 × 0.5 mm.

The following correlation has widely been used for the estimation of the ultimate tensile strength R_m:

$$R_\mathrm{m} = \beta_\mathrm{Rm} \cdot F_\mathrm{m} / (h_0 \cdot v_\mathrm{m}) \,, \tag{1}$$

with F_m being the maximum force and v_m the corresponding punch displacement, h_0 the initial specimen thickness and β_Rm an empirical coefficient. However, this correlation exhibits a limited predictive capability unless adusted for a specific class of materials.[3]

SIMULATION. Finite element simulations were done with a model including contact and friction. Axisymmetric elements with 8 nodes, elastic-plastic material and large deformation and finite strain capability were used for the SP specimen. The element size was 50 µm. The plastic deformation was based on the following constitutive equation:

$$\sigma(\varepsilon^\mathrm{pl}) = \sigma_\mathrm{y0} + r_1 \cdot \left[\alpha \cdot \varepsilon^\mathrm{pl} + 1 - \exp(-n\varepsilon^\mathrm{pl})\right] \,, \tag{2}$$

where σ is the true equivalent stress and ε^pl the true plastic equivalent strain. σ_y0, r_1, α, and n are material parameters. In our simulation we used a generic material behavior with a constant initial flow stress σ_y0 = 570 MPa and a systematic variation of the hardening. In particular, the parameters r_1 and n were varied in such a way that specific values for the ultimate tensile stress (R_m = 650, 700, 800, 900 MPa) and the uniform strain (A_gt = 3 %, 6 %, 10 %, 20 %) were obtained.

EXPERIMENTAL. A number of 131 small punch tests were performed on nine different materials including ferritic-martensitic (f/m) Cr-steels and bainitic reactor pressure vessel steels. The temperature range was −177…+650 °C. By using different materials, and by testing at different temperatures, a wide variation of tensile properties is obtained.

RESULTS. Simulated force-displacement curves for constant R_m and varying A_gt are shown in Fig. 2. The maximum forces F_m are significantly different, while the displacements at maximum force v_m are in a similar range. Moreover, the curves exhibit a common pseudo intersection point. In view of this finding it seems reasonable to use the force F_i at the intersection point instead of F_m for the correlation with the ultimate tensile stress in order to avoid a strong dependence of the correlation factor β_Rm on the tensile properties of the material. The following equation is proposed:

$$R_\mathrm{m} = \beta_\mathrm{Rm} \cdot F_\mathrm{i} / h_0^2 \,, \tag{3}$$

with $F_\mathrm{i} = F(v_\mathrm{i})$, $v_\mathrm{i} = 1.29\, h_0$ and $\beta_\mathrm{Rm} = 0.179$. It could be shown that the intersection point is associated with the onset of plastic instability in the small punch specimen.

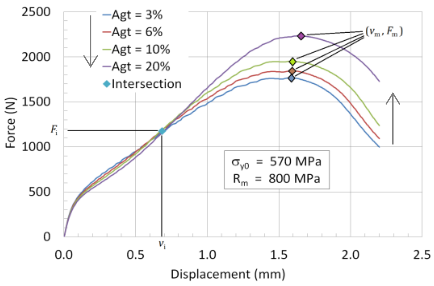

Fig. 2: Simulated force-displacement curves for different uniform strains.

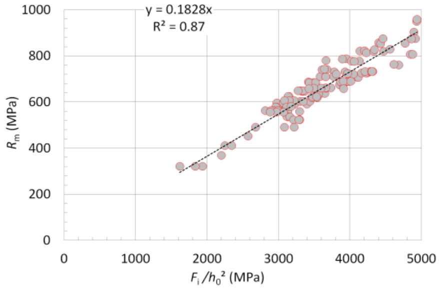

Fig. 3: Correlation between R_m (tensile test) and F_i/h_0^2 (SPT).

The evaluation of the SP experiments is based on the measured force-displacement curves $F(v)$. The characteristic parameters v_m, F_m and F_i were determined for all tests. The correlation between the ultimate tensile stress from the uniaxial tensile tests R_m and F_i/h_0^2 from the SP tests is shown in Fig. 3 and confirms the findings of the FEM simulation with generic material properties. The correlation coefficient β_Rm obtained from the experiments (0.183) agrees very well with the one obtained from the simulations (0.179) even though the tensile properties of the real materials and those of the generic materials are different. This underpins the assumption that the new correlation Eq. (3) is only weakly dependent on the tensile properties of the investigated material.[4]

---

[1] Misawa, T. *et al.* (1991) *J. Nucl. Mater.* **179−181**, 421−424.
[2] Altstadt, E. *et al.* (2016) *J. Nucl. Mater.* **473**, 186−195.
[3] García, T. E. *et al.* (2014) *J. Alloys Compd.* **582**, 708−717.
[4] Altstadt, E. *et al.* (2018) *Int. J. Mech. Sci.* **136**, 85−93.

Prediction of the yield stress of oxide dispersion strengthened (ODS) Fe-Cr alloys based on microstructure observations

F. Bergner, A. Chauhan,[1] C. Heintze, G. Müller, A. Ulbricht
[1]Institute for Applied Materials, Karlsruhe Institute of Technology, Eggenstein-Leopoldshafen, Germany

Although analytic expressions for the yield stress contributions arising from a number of individual hardening mechanisms are well established, the predictive capability for nanostructured oxide dispersion strengthened steels has not yet been comprehensively explored. The present comparison of measured values and microstructure-informed predictions of the yield stress indicates remarkable agreement over a wide range of material parameters.

Nanostructured ODS Fe-Cr alloys currently receive renewed interest because of their excellent creep properties and irradiation damage resistance. This class of materials includes Fe-9 % Cr reduced activation ferritic-martensitic steels such as the European reference steel ODS Eurofer and nanostructured Fe-14 % Cr ferritic steels. A number of different hardening mechanisms give rise to levels of the room temperature yield stress to beyond 1000 MPa. The objective of the present study was the prediction of the room temperature yield stress based on microstructure observations and empirical expressions relating the microstructure parameters with individual hardening contributions. As an additional qualification criterion, the prediction formula should be applicable to non-ODS Fe-Cr alloys and Cr steels thus covering a wide range of yield stress.

EXPERIMENTAL. The set of selected materials covers a ferritic (F) and a martensitic (TM) variant of an Fe-9 % Cr ODS steel,[1] a ferritic Fe-14 % Cr steel,[1] 9 % Cr ODS Eurofer,[2] the ferritic/martensitic steel Eurofer97 [2] and a set of Fe-Cr model alloys,[3] all provided by project partners. The characterization of the microstructure was performed by electron backscatter diffraction (EBSD) to estimate grain size, TEM to estimate dislocation density, and small-angle neutron scattering (SANS) to estimate the size distribution of oxide nanoparticles. The experimental details and results are reported in literature.[1] Standard tensile tests at room temperature were performed to extract the yield stress.

RESULTS. The major hardening mechanisms in metallic materials are lattice friction, solid solution hardening, grain boundary hardening, forest hardening and precipitation hardening. The lattice friction assumes a fixed value for the base-centered cubic Fe-lattice. Solid solution hardening depends on the content of alloying elements in solution, element-specific empirical relations linking atom percent and hardening contribution are available (see [1] and references therein). Grain boundary hardening can be described by the Hall-Petch relationship, Eq. (1). Forest hardening and precipitation hardening refer to the resistance against plastic deformation posed by lattice dislocations, Eq. (2), and precipitates or particles, Eq. (3), respectively.

$$\sigma_{y,g} = k_g d_g^{-1/2} \tag{1}$$

$$\sigma_{y,d} = k_d \rho_d^{-1/2} \tag{2}$$

$$\sigma_{y,p} = k_p (Nd)^{1/2} \tag{3}$$

Best estimates of the pre-factors in Eqs. (1)−(3), which depend on the shear modulus of the material, the Burgers vector of the dislocations and the dimensionless obstacle strength, are reported in [1]. The experimentally obtained values of the grain size d_g, dislocation density ρ_d, number density N and mean diameter d of oxide nanoparticles were introduced to calculate the hardening contributions according to Eqs. (1)−(3).
We have found that the consideration of lattice friction and solid solution hardening give rise to a systematic overestimation of the measured yield stress. These contributions have to be excluded for reasons currently understood only partially.[1] Superposition of grain boundary, forest and precipitation hardening was found to follow a mixed superposition rule according to Eq. (4).

$$\sigma_{y,th} = \sigma_{y,g} + \sqrt{\sigma_{y,d}^2 + \sigma_{y,p}^2} \tag{4}$$

The theoretical yield stress $\sigma_\mathrm{y,th}$ and the measured yield stress $\sigma_\mathrm{y,exp}$ are compared in Fig. 1.

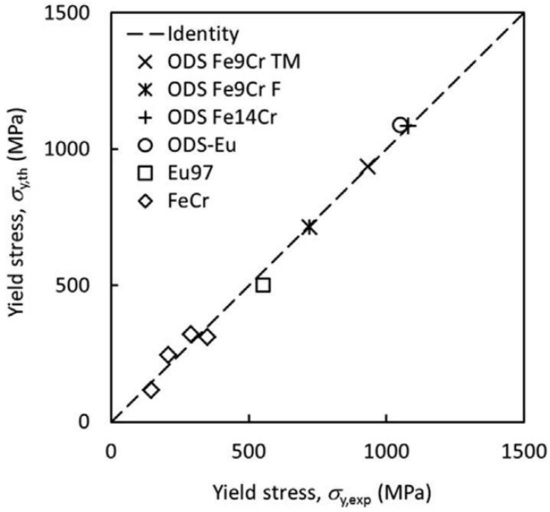

Fig. 1: Comparison of the theoretical yield stress predicted according to Eq. (4) and the measured yield stress.

The comparison indicates remarkable predictive capabilities over a wide range of material parameters. Indeed, the correlation includes ODS alloys and non-ODS counterparts and covers two orders of magnitude in grain size, two orders of magnitude in dislocation density as well as one order of magnitude in yield stress.

ACKNOWLEDGEMENTS. This work was funded within the EU project MatISSE under Grant agreement no. 604862.

---

[1] Chauhan, A. *et al.* (2017) *J. Nucl. Mater.* **495**, 6−19.
[2] Lindau, R. *et al.* (2002) *J. Nucl. Mater.* **307–311**, 769−772.
[3] Matijasevic, M. *et al.* (2008) *J. Nucl. Mater.* **377**, 147−154.

The influence of microstructure on the fracture behaviour of ferritic ODS steels

A. Das, H.-W. Viehrig, E. Altstadt, C. Heintze, F. Bergner, J. Hoffmann[1]

[1]Institute for Applied Materials, Karlsruhe Institute of Technology, Eggenstein-Leopoldshafen, Germany

Oxide dispersion strengthened (ODS) steels are candidate materials for fuel cladding tubes in Gen-IV nuclear fission reactors, and as structural material for fusion devices. ODS steel possess high temperature strength and irradiation resistance but suffer from low fracture toughness, anisotropic fracture behavior and secondary cracking. In the present work, the microstructural factors causing these problems are investigated through fracture toughness testing and basic microstructural analysis. Microstructural factors such as particle-matrix bond strength and grain morphology played a major in influencing fracture toughness and secondary cracking.

ODS steels are foreseen as structural materials in advanced fission reactors and fusion reactors. They have to withstand high temperatures (550 – 650 °C) and high neutron irradiation doses (200 dpa). The powder metallurgical fabrication route typically includes mechanical alloying, consolidation, hot rolling or hot extrusion and a final thermomechanical treatment. Due to the bcc structure, ODS steels exhibit a high irradiation swelling resistance. The Yttrium containing oxide nanoparticles give rise to an enhanced creep resistance by blocking dislocation motion. However, ODS steels exhibit lower fracture toughness as compared to conventional ferritic-martensitic steels. An acceptable limit of fracture toughness for ODS steels (≥ 100 MPa√m) was defined by Byun *et al.*[1] ODS steels often exhibit anisotropic fracture behavior, secondary cracking and low fracture toughness. A microstructure based understanding of the fracture mechanisms can help to tailor ODS steels with better fracture properties.

EXPERIMENTAL. Fracture toughness testing using miniature C(T) specimens were performed using the unloading compliance method on one hot rolled (ODS-KIT HR) and two hot extruded ferritic ODS steels (ODS-KIT HE and ODS-CSM). The samples were broken apart and fractography was performed using SEM. Crack propagation was investigated using electron backscatter diffraction (EBSD). TEM, EBSD, SEM and OM were used to investigate the basic microstructure.

RESULTS. ODS-KIT HR contains 'pan-cake' shaped grains elongated towards the rolling and the short transverse directions while ODS-KIT HE contains 'cigar-shaped' grains elongated towards the extrusion direction. ODS-CSM contains zones of fine and coarse equi-axed grains. All the materials possess a <110> texture parallel to the rolling/extrusion direction. The two materials from KIT contain sub-micron sized Ti enriched particles (avg. size: 60 nm) while ODS-CSM contains Si enriched sub-micron particles (avg. size: 500 nm) in high number density zones aligned parallel to the rolling/extrusion direction. Figure 1 shows the fracture toughness values of the three investigated ODS steels tested at various temperatures. Extremely high fracture toughness is observed for ODS-KIT HE while acceptable fracture toughness is observed for ODS-KIT HR and ODS-CSM in the temperature range of RT to 400 °C. At 600 °C, fracture toughness values of all materials drop below the acceptable limit.

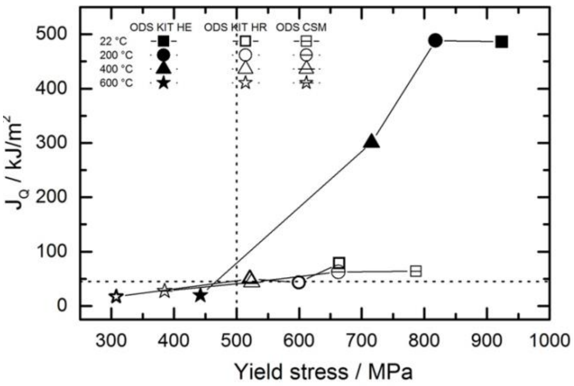

Fig. 1: Fracture toughness (J_Q value) *vs.* yield stress plot at different temperatures for the three ferritic ODS steels in the strongest orientation.

Fracture toughness in different materials is found to be affected predominantly by the particle-matrix bond strength. Fracture toughness is the highest in the L-C / L-T orientation followed by the C-R and C-L / T-L orientations because of the presence or the lack of crack blunting through the elongated coarse grains (Fig. 2). Elongated grain morphology is also the reason for more pronounced secondary cracking in hot rolled material as compared with the hot extruded materials. Secondary cracks are found to stabilize the primary crack and prevent cleavage fracture. They however, form at lower loads than primary cracks and can lead to design problems.[2, 3]

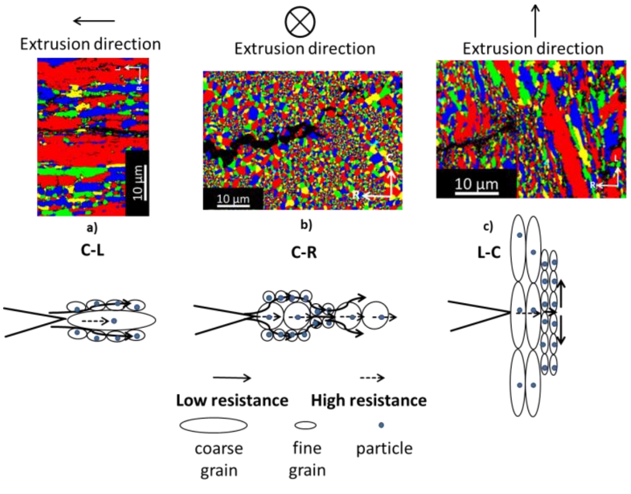

Fig. 2: Schematic showing side view of crack propagation in all the three orientations of hot extruded specimen along with EBSD grain distribution maps supporting them.

ACKNOWLEDGEMENTS. The authors thank Mr. Wolfgang Webersinke, Mr. Mario Houska, Ms. Gudrun Müller and Ms. Michaela Rossner.

---

[1] Byun, T. S. *et al.* (2017) *J. Nucl. Mater.* **484**, 157 – 167.
[2] Das, A. *et al.* (2017) *J. Nucl. Mater.* **491**, 83 – 93.
[3] Das, A. *et al.* (2017) *J. Nucl. Mater.* **497**, 60 – 75.

Influence of microstructure features on the irradiation behavior of ODS Fe-14Cr alloys

I. Hilger, C. Heintze, F. Bergner, A. Ulbricht, T. Weißgärber,[1] B. Kieback[1,2]

[1]Fraunhofer Institute for Manufacturing Technology and Advanced Materials, Branch Lab Dresden, Dresden, Germany; [2]Institut für Werkstoffwissenschaft, Technische Universität Dresden, Dresden, Germany

Several studies revealed oxide-dispersion strengthened (ODS) ferritic steels to be promising candidates for future nuclear applications. In the present work, a novel approach exploiting the bimodal grain size distribution present in the investigated ODS alloys was utilized to separate the effects of the grain size and the oxide particles on the irradiation hardening. Applying single-beam (Fe) and dual-beam (Fe + He) ion irradiations it was shown that the grain size effect is dominant after single-beam irradiation, while after dual-beam irradiation there is a pronounced effect of the oxide particles on irradiation-induced hardening.

Neutron or ion irradiation causes the formation of radiation-induced point defects in displacement cascades. These vacancies and interstitials may mutually recombine or aggregate to form *e.g.* voids and dislocation loops. The high irradiation-induced point defect concentrations exceeding the thermal equilibrium can also give rise to irradiation-enhanced solute atom diffusion promoting precipitation. These nm-scale secondary defects lead to undesired hardening and embrittlement of the material. Certain microstructure features, such as grain boundaries or phase boundaries (*e.g.* particle-matrix interfaces), can act as sinks for irradiation-induced point defects promoting their recombination and thus improving the material's irradiation resistance.[1] The aim of this work was to separately evaluate the impact of grain boundaries and nano-oxides on the irradiation-induced hardening.

EXPERIMENTAL. Fe-14Cr-1W-0.4Ti samples, partially reinforced with 0.6 wt.-% Y_2O_3, were produced by means of mechanical alloying and consolidation *via* spark plasma sintering. Different milling parameters were applied to vary the grain size and oxide particle size.[2] The samples were characterized with respect to the grain size (electron backscatter diffraction) as well as the size (small angle neutron scattering)[3] and spatial distribution of the oxide particles (atom probe tomography + TEM). All ODS samples were found to exhibit a bimodal grain size distribution, which was utilized for the separation of the grain size effect from the particle effect by investigating coarser and ultrafine-grained areas within the same sample. A non-ODS reference and two ODS samples with different particle number densities N were irradiated at room temperature at the Ion Beam Center in single-beam mode with iron (Fe) ions and dual-beam mode with iron and helium (Fe + He) ions prior to the characterization of irradiation-induced hardening by means of nanoindentation.

RESULTS. It was found, that after single-beam (Fe) ion irradiation the ultrafine grained (UFG) regions (d < 0.3 µm) of both ODS samples exhibit a significantly lower irradiation-induced hardening than the non-ODS reference sample (d ≈ 7 µm) and the coarser grained regions of the ODS samples (d ≈ 1.5 µm) (Fig. 1). The observed grain size effect is independent from the number density and spatial distribution of the nano-oxides.

Comparing the coarser grained and UFG areas of both ODS samples after dual-beam (Fe + He) irradiation, a higher number density N and homogeneous oxide particle distribution was shown to induce a significantly lower irradiation-induced hardening at comparable grain size (B_c *vs.* C_c, B_{UFG} *vs.* C_{UFG}, see Fig. 2).

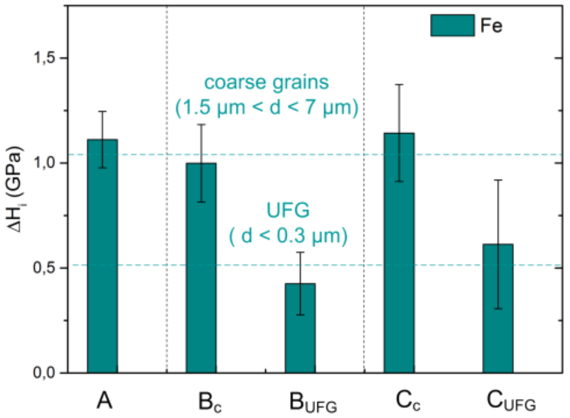

Fig. 1: Irradiation-induced hardening after single-beam (Fe) ion irradiation.

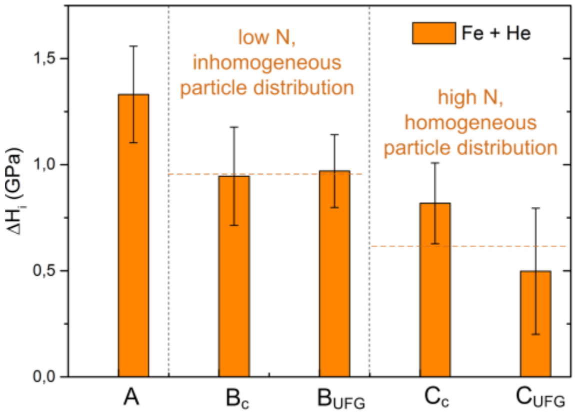

Fig. 2: Irradiation-induced hardening after dual-beam (Fe+He) ion irradiation.

ACKNOWLEDGEMENTS. This work received funding by the European Commission within the MATTER project (Grant Agreement No. 269706) and MATISSE project (Grant Agreement No. 604862).

---

[1] Ackland, G. (2010) *Science* **327**, 1587–1588.
[2] Hilger, I. *et al.* (2015) *J. Nucl. Mater.* **472**, 206–214.
[3] Hilger, I. *et al.* (2016) *J. Alloys Compd.* **685**, 927–935.

Emulation of neutron irradiation damage in Fe-Cr model alloys using ions – a case study

M. Hernández Mayoral,[1] C. Heintze, E. Oñorbe,[1] A. Ulbricht, F. Bergner, C. Pareige[2]

[1]CIEMAT, Division of Structural Materials, Madrid, Spain; [2]Groupe de Physique des Matériaux, Université et INSA de Rouen, Saint Etienne du Rouvray, France

A profound understanding of the mechanisms of neutron damage and of its effect on the mechanical properties is essential for the safe application of structural materials in existing and future nuclear systems. This relies on comprehensive irradiation experiments. The limited availability of suitable neutron irradiation facilities and the duration of neutron irradiations (typically years) give rise to an interest in alternative irradiation sources. Ion irradiation significantly contributed to our current understanding of materials behavior in irradiation environments. Experiments where neutron and ion irradiation of the same alloys and performed with nominally the same parameters are compared directly have the potential to provide new insight into the mechanisms of defect evolution.

EXPERIMENTAL. Fe-Cr binary alloys of industrial purity with Cr contents of 5, 9 and 12 wt.-% were irradiated with neutrons and ions, both at 300 °C up to a dose of about 0.6 dpa. The neutron irradiations were performed at the BR2 reactor, Mol (Belgium). The ion irradiations, using a three-step irradiation with Fe-ions of 0.5, 2 and 5 MeV to obtain an approximately rectangular dpa-profile, were performed at the Ion Beam Centre at HZDR. The microstructural response to irradiation in terms of the irradiation-induced dislocation structure was characterized using transmission electron microscopy applying bright field and weak-beam dark field imaging conditions.

RESULTS. Ion irradiation gave rise to the formation of small dislocation loops in all alloys. Both types of Burgers vectors, a_0<100> and $a_0$1/2<111>, were observed. The loops were distributed homogeneously throughout the matrix (Fig. 1 top). Dislocation loops were also observed after neutron irradiation. However, their spatial distribution was strikingly different. Here, dislocation loops were preferentially formed close to grain boundaries and dislocation lines (Fig. 1 bottom). For all alloys the mean size of loops was higher and the size distribution extended to larger loop sizes in case of the neutron irradiation (Tab. 1). The dominant loop type changed from $a_0$1/2<111> (ions) to a_0<100> (neutrons). A similarly striking difference was observed earlier with respect to irradiation-accelerated precipitation. While the formation of α'-phase was observed after neutron irradiation for Cr contents $\geq$ 9 wt.-% Cr, it was suppressed in case of ion irradiation.[2, 3] The differences are attributed to the three orders of magnitude difference in the damage rate and/or the presence of injected interstitials in case of the ion irradiation promoting the nucleation and growth of visible interstitial loops and suppressing the formation of α'-phase. The present work demonstrates that a direct transfer of ion irradiation results in terms of predicting materials behavior in a neutron irradiation environment should be taken with care.

Tab. 1: Size, number density and type of dislocation loops in Fe-9 wt.-% Cr.[1]

	Ion	Neutron
Mean / maximum size (nm)	3.5 ± 0.1 / 11	5.3 ± 0.2 / 21
Total number density (10^{21} m^{-3})	10 ± 1	2.2 ± 0.8 / 7.9 ± 0.8*
Fraction of loops with b = a_0<100>	32 %	59 %

*: density in loop filled volume.

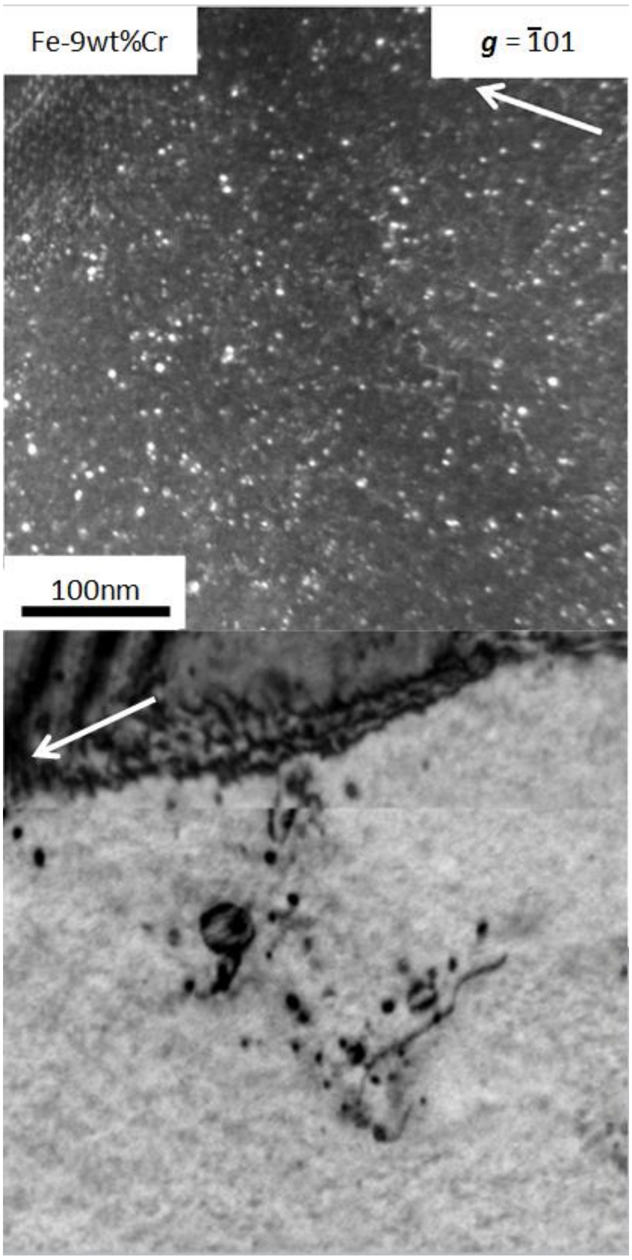

Fig. 1: Microstructure of Fe-9 wt.-% Cr after ion (top) and after neutron (bottom) irradiation at 300 °C up to about 0.6 dpa.[1]

ACKNOWLEDGEMENTS. The ion irradiations were supported by the EC in the framework of SPIRIT, grant no. 227012. This work was also partially supported by the European FP7-Project GETMAT, grant no. 212175.

---

[1] Hernández-Mayoral, M. *et al.* (2016) *J. Nucl. Mater.* **474**, 88−98.
[2] Heintze, C. *et al.* (2011) *J. Nucl. Mater.* **409**, 106−111.
[3] Pareige, C. *et al.* (2015) *J. Nucl. Mater.* **456**, 471−476.

Validation of surveillance concepts and trend curves by the investigation of decommissioned reactor pressure vessels

H.-W. Viehrig, E. Altstadt, M. Houska

The investigation of reactor pressure vessel (RPV) material from the decommissioned Greifswald nuclear power plant representing the first generation of Russian type WWER-440/V-230 reactors offers the opportunity to evaluate the real toughness response. The paper presents test results measured on trepans sampled from the multilayer beltline welding seam SN0.1.4. of the Unit 4 RPV. This unit was shut down after 11 years of operation.

EXPERIMENTAL. Trepans were extracted from different azimuthal locations of the circumferential beltline (located in the region of the reactor core) welding seam SN0.1.4. of the Greifswald Unit 4 RPV. The diameter of the trepan is 119 mm over the whole RPV wall thickness. Table 1 contains the neutron fluence estimated at the inner and outer walls in the axial location of the beltline welding seam. The neutron fluence decreases through the RPV wall by approximately 80 %.

Tab. 1: Accumulated neutron fluence, $\Phi_{E>0.5MeV}$, of the beltline welding seam of the Greifswald Unit 4 RPV.

RPV-material	**$\Phi_{E>0.5MeV}$ (10^{18} n/cm^2)**	
	inner wall	**outer wall**
10 KhMFT, SN0.1.4.	41.13	9.20

The trepans were cut over the thickness into discs of 3 mm and 10 mm thickness using a wire travelling electric discharge machine. From the 3 mm and 10 mm discs, flat tensile and Charpy size SE(B) specimens were machined, respectively. SE(B) and tensile specimens machined from one disc (thickness location) are a set of specimens for the determination of T_0 and the tensile strength values according to ASTM E1921 and ISO 6892, respectively.

RESULTS. Figure 1 shows the macrosection of the Greifswald Unit 4 beltline welding seam and the distribution of the main deleterious elements Cu and P through it. There is a sink of the Cu and P content in the welding root region due to the unalloyed and clean welding wire used there.

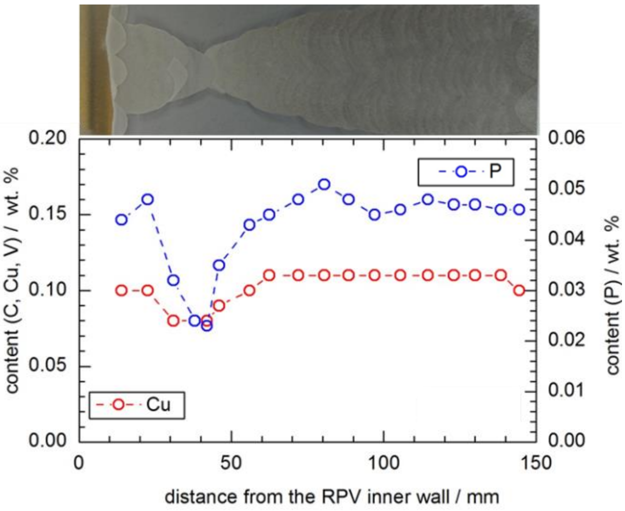

Fig. 1: Metallographic section and P and Cu content through the multilayer welding seam from the cladded Unit 4 RPV.[1]

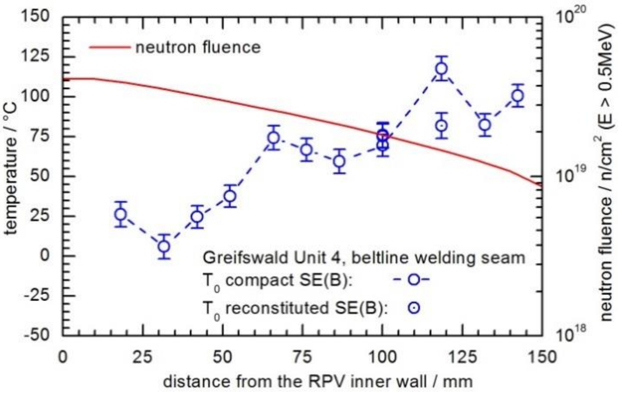

Fig. 2: Progression of the reference temperature, T_0, through the thickness of the Greifswald Unit 4 beltline welding seam SN0.1.4.

The ductile-to-brittle transition (DBT) of ferritic steels can be quantified by a reference temperature, T_0, determined according to the Master Curve approach.[2] Materials with high fracture resistance exhibit a low T_0. Neutron irradiation gives rise to an increase of the reference temperature. Figure 2 shows the progression of T_0 through the Unit 4 multilayer beltline welding seam. The T_0-values vary largely across the welding seam. Beyond the cladding on the inner surface, a T_0 value of 26 °C was measured. The lowest measured T_0-value was 6 °C in the region of the welding root. Beyond the welding root, T_0 increases continuously with a large scatter towards the outer RPV wall. Towards the inner wall the structure is a transition from the welding root to the filling layers and cover layers (Fig. 1). In addition the heat treatment during the welding of the cladding may locally influence the initial toughness. These result in about 55 K lower T_0 compared to the filling layers towards the outer wall in spite of the higher neutron loading. Generally, the progression of the T_0 values through the thickness of the welding seam is not in accordance with the current understanding of what could be expected, a decrease in T_0 with the attenuation of the neutron fluence. The low T_0 values in the welding root region can be explained with the reduced irradiation susceptibility because of the remarkable lower Cu and P content compared to the filling layers (Fig. 1). Metallographic investigations and hardness measurements in the vicinity of the fatigue crack tip indicate that the variation of the T_0-values measured through the filling layers results basically from variation of the intrinsic welding bead structure.[3, 4] Hence, the position of the fatigue crack tip in the multi-layer welding seam is crucial and defines the cleavage fracture toughness. At the thickness location 118 mm T_0 measured with original compact and reconstituted specimen amounts 117 °C and 81 °C, respectively. Hence, for the same neutron loading, a difference in T_0 of 36 K was determined.

---

[1] Valo, M. (2010) *Research Report VTT-R-03746-10*.
[2] Wallin, K. (2010) *Eng. Fract. Mech.* **77**, 285–292.
[3] Viehrig, H. W. *et al.* (2012) *Int. J. Pressure Vessels Pip.* **89**, 129–136.
[4] Viehrig, H. W. *et al.* (2015) *J. Nucl. Mater.* **456**, 334–343.

Effect of neutron flux on radiation damage in reactor pressure vessel (RPV) steels

A. Ulbricht, F. Bergner, A. Wagner, H. Hein,[1] U. Keiderling[2]
[1]AREVA, Erlangen, Germany; [2]Helmholtz-Zentrum Berlin, Germany

The effect of neutron flux on the neutron-irradiation-induced microstructure of RPV base and weld material has been investigated. The approach is based on the selection of pairs of samples of one and the same material irradiated at different flux up to about the same level of neutron fluence. The main methods applied are small-angle neutron scattering (SANS) and positron lifetime spectroscopy (PAS). We have found that the vacancy concentration is higher, and the size of solute clusters is smaller for the high-flux irradiation than for the respective low-flux condition.

The understanding of neutron irradiation damage of reactor pressure vessel (RPV) steels is the basis of a safe and reliable operation of running nuclear power plants during the originally planned life, as well as for envisaged lifetime extensions worldwide. The difficulties associated with the understanding of radiation damage comes from the variety of influencing parameters, such as chemical composition, manufacturing history, temperature, neutron fluence, flux (or dose rate), as well as the small size, about 1 nm, of the irradiation-induced features responsible for deterioration of the mechanical properties. It is now state of the art to underpin empirically established irradiation effects on mechanical properties with both nanostructural observations and mechanistic understanding.[1] However, exhaustive studies of flux effects on the irradiation-induced nanofeatures, mainly defect-solute clusters, nanovoids and dislocation loops, in neutron-irradiated RPV steels are still missing and there are controversial views on the presence of flux effects on mechanical properties. Therefore, one of the key issues of the current EU project SOTERIA is devoted to the flux effect.[2]

EXPERIMENTAL. Two pairs of low Cu RPV steels, a base metal and a weld, representative of Western type RPV material were selected. The preparation of samples was carried out in our hot cell lab. Plan-parallel slices of 1 mm thickness were cut from tested fracture mechanic specimens for microstructural investigation. SANS measurements were performed at the instrument V4 of HZB.[3, 4] Lifetime measurements by means of Gamma-induced PAS were performed with identical samples at the ELBE source of HZDR.[5]

RESULTS. The SANS cross sections of different irradiation conditions of a weld material are shown in Fig. 1(a) and the reconstructed volume-fraction-related size distributions of irradiation-induced clusters in Fig. 1(b). A clear effect was observed, increased intensity at high scattering vectors depending on the neutron flux. The determined mean radii of clusters are summarized in Fig. 1(c) for both weld and base materials. The evolution of the clusters as function of neutron flux can be described by a model based on deterministic growth as opposed to coarsening.[6] The model fit is plotted as dashed line in Fig. 1(c). The measured lifetime (LT) distributions of different conditions of the base material are shown in Fig. 1(d). An increased positron LT was observed for both flux conditions. As compared to the low flux, the high-flux irradiation gives rise to a higher concentration of mono vacancies (V_1) and vacancy clusters consisting of five vacancies on average (V_5).

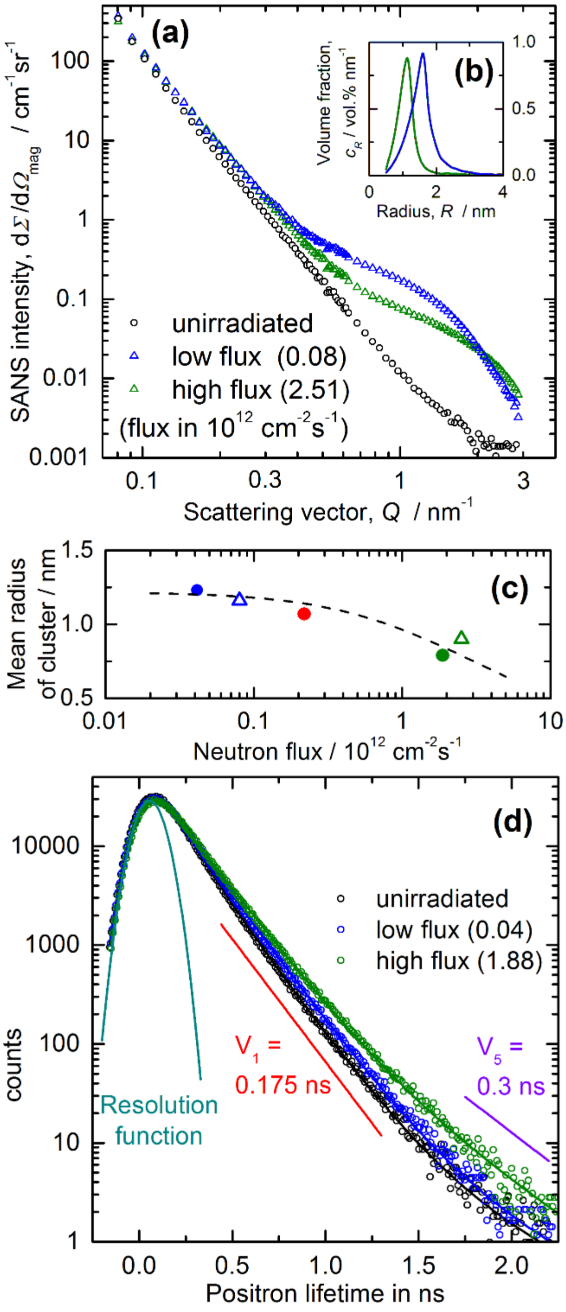

Fig. 1: (a) SANS intensities *vs.* scattering vector (~scattering angle), and (b) derived cluster size distribution of different conditions of weld material; (c) flux dependence of mean cluster size of both weld (triangles) and base materials (circle), and model fit (dashed line) according to [6]; (d) Positron lifetime measurements of different conditions of base material by means of GiPS.[5]

ACKNOWLEDGEMENTS. The work received partial funding from the European Commission within the project SOTERIA under grant agreement number 661913.

---

[1] Zinkle, S. J. *et al.* (2013) *Acta Mater.* **61**, 735–758.
[2] http://soteria-project.eu.
[3] Keiderling, U. *et al.* (1995) *Physica B* **213&214**, 895–897.
[4] Keiderling, U. (2002) *Appl. Phys. A* **74**, S1455–S1457.
[5] Wagner, A. *et al.* (2015) *J. Phys. Conf. Ser.* **618**, 012042.
[6] Wagner, A. *et al.* (2016) *Acta Mater.* **104**, 131–142.

Investigations on passive residual heat removal systems for nuclear power plants

F. Schäfer, M. Sporn,[1] C. Schuster,[1] U. Hampel[2]

[1]Technische Universität Dresden, Dresden, Germany; [2]HZDR, Institute of Fluid Dynamics, Dresden, Germany

In the framework of the German research projects EASY and PANAS investigations on the effectiveness of passive safety systems for accident management in nuclear power plants are carried out. Experimental studies provide detailed information about the physics and the heat removal capabilities of different passive components, needed for model development and code validation. The code system ATHLET-COCOSYS is used to develop new models and methods for a more reliable analysis of the behavior of passive systems in different kind of accident scenarios.[1]

In nuclear power plants, various kinds of active safety systems are installed to control reactor power and to ensure safe and stable core cooling for a wide spectrum of transients and accidents. The safety concept is complemented by inherent safety features and, especially for new reactor designs, by innovative passive safety systems. These systems are based on a change in the thermodynamic equilibrium established at steady-state conditions, enabling them to function without electric power supply. Based on the KERENA™ design, an evolutionary boiling water reactor concept jointly developed by AREVA GmbH and Preussen Elektra GmbH, the function and the interaction of various passive safety systems (*e.g.* emergency condenser, containment cooling condenser, passive core flooding system and passive pressure pulse transmitter) have been experimentally investigated.[2, 3] The integral experiments at the INKA test facility are complemented by more detailed single effect studies on the heat removal mechanisms based on condensation and evaporation at thermodynamic conditions typical for nuclear reactors. Corresponding experiments with application of advanced measurement systems (*e.g.* void fraction and heat transfer probes, X-ray tomography) have been performed at the COSMEA and GENEVA test facilities at HZDR and TU Dresden, respectively.

NUMERICAL INVESTIGATIONS. For the experiments conducted at the INKA test facility a one-dimensional ATHLET model has been developed (Fig. 1). The model consists of three independent fluid-dynamic systems interconnected by heat structures. In an accident the residual heat from the reactor (RPV simulator in the experiment) is removed by heat transfer *via* the emergency condenser (EC) to the flooding pool (FP), and *via* the containment cooling condenser (CCC) to the shielding and storage pool (SSP). Another passive component, the passive pressure pulse transmitter (PPPT), is used as an alternative trigger to activate special functions of the reactor protection system (*e.g.* reactor scram or depressurization of the reactor coolant system). In case of accidents with decreasing reactor water level steam enters the PPPT and due to an increasing heat transfer the rising pressure in the PPPT triggers a pilot valve. The EC and CCC also work in a complete passive manner. Also caused by a decreasing reactor water level steam enters the EC tubes, where it is condensed and the surrounding water in the FP is heated up. When the water in the FP starts to evaporate, or when steam from a leak directly enters the FP or the containment, then at the outer surface of the CCC tubes the steam is condensed and the heat is transferred to the water in the SSP.

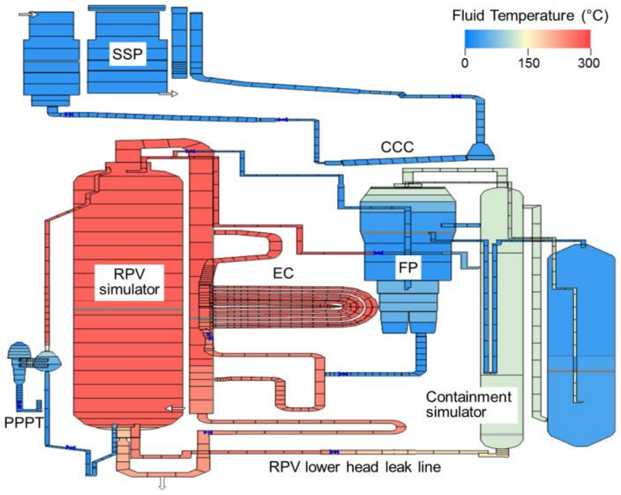

Fig. 1: ATHLET model for the INKA test facility.

The ATHLET model has been applied to simulate different postulated accident sequences as well as to assess the code capabilities in the prediction of the accident progression and the heat removal capabilities of the passive systems. Exemplarily, Fig. 2 shows the EC and CCC heat removal power for a leak at the lower head of the reactor pressure vessel (RPV). In this scenario the mass loss leads to a fast decrease of the reactor water level. Steam generated in the RPV is condensed in the EC tube bundle and the EC power starts to rise. Additionally an automatic depressurization of the reactor is triggered by the PPPT and steam is also condensed in the FP. With the increasing FP temperature also the CCC starts to remove heat from the reactor. The described phenomena are well predicted by ATHLET. For further work a 2D/3D model of the FP and a coupling of the current ATHLET model with COCOSYS will be realized.

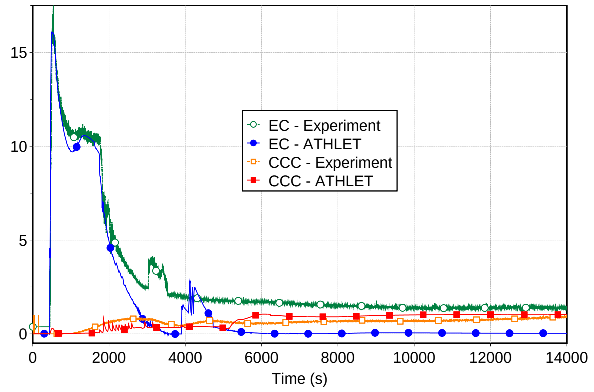

Fig. 2: EC and CCC power for the leak at the lower head of the RPV.

ACKNOWLEDGEMENTS. The work is funded by the German Federal Ministry for Economic Affairs and Energy and the Ministry of Education and Research [grant numbers 1501492D and 02NUK041B].

---

[1] Buchholz, S. *et al.* (2017) *NURETH-17*. Proc.
[2] Wagner, T. *et al.* (2017) *NURETH-17*. Proc.
[3] Leyer, S. *et al.* (2012) *Sci. Technol. Nucl. Install.* **2012**, ID 439374.

Serpent solution of X2 benchmark: fresh core at HZP conditions

Y. Bilodid, E. Fridman

The X2 benchmark, published in AER conference proceedings, describes the first 4 fuel cycles of the Khmelnitsky NPP 2nd unit (KhNPP-2) with VVER-1000 reactor.[1, 2] The benchmark specifications contain description of the reactor core and operational history supplemented by measured operational data. In this work, the HZP experiments conducted in the KhNPP-2 fresh core are modelled with the Serpent-2 Monte Carlo code. The numerical results are validated against the available measured core data.

The X2 benchmark, published in AER conference proceedings, describes first 4 fuel cycles of the power unit with VVER-1000 reactor.

In this work, the hot zero power (HZP) experiments conducted in the KhNPP-2 fresh core are modelled with the Serpent-2 Monte Carlo code. The fresh core HZP critical conditions are practically free from uncertainties associated with fuel burnup and thermal feedbacks, which makes this state very suitable for Monte Carlo code validation. On the other hand, measurements of the power distribution at the HZP state are not provided in the benchmark, so the Monte Carlo solution could be used as a reference for verification of deterministic core simulators.

MODEL. The Serpent model of the VVER-1000 core features a detailed representation of the fuel assemblies, control rods, and the radial reflector. The top and bottom axial reflectors are modeled as homogeneous mixed layers. The materials and geometry parameters of the fuel assembly models correspond to the benchmark specifications. In reality, the active part of fuel assembly includes 13 spacer grids of a 3 cm height each. Since spacer grids and fuel cladding are composed from the same zirconium alloy, the spacer grid is modelled by increasing fuel cladding and guiding tube thickness to preserve total mass of the alloy.

In the Serpent model, black boundary conditions are applied on the inner radius of the reactor pressure vessel and on the outer planes of the axial reflector.

VALIDATION. The Serpent results are compared with measurements in Tab. 1. The full moderator temperature reactivity coefficient was calculated as a difference in reactivity between two static states with different water temperatures. The full SCRAM worth was calculated as a difference in reactivity between two static states with inserted and withdrawn control rods. The critical boric acid concentration, found in Serpent, predicts measured parameters within measurement uncertainties.

The power distribution calculated by this model, illustrated in Fig. 1, could also be used for verification of deterministic codes.

SUMMARY. The X2 VVER-1000 benchmark contains a description of a fresh reactor core and measurements made on hot zero power level, which make it suitable for simulation codes validation, in particular, stand-alone Monte Carlo codes.

The HZP fresh core states were simulated in Serpent 2 Monte Carlo Code applying the ENDF/B-VII isotopic library. The calculated values are in very good agreement with measured data, while the deviations lay within measurement uncertainties. The obtained power distribution will be used as a reference solution for a verification of deterministic codes.

Tab. 1: Comparison of Serpent results *vs.* measurements.

Parameter	Measurement	Serpent
Multiplication factor k_{eff} in critical state	1.0	1.00144
Critical boron concentration (ppm)	1206 ± 26	1219
Temperature reactivity coefficient (pcm/K)	−5.39 ± 0.54	−5.81
Full SCRAM worth (%)	−7.00 ± 0.43	−7.42

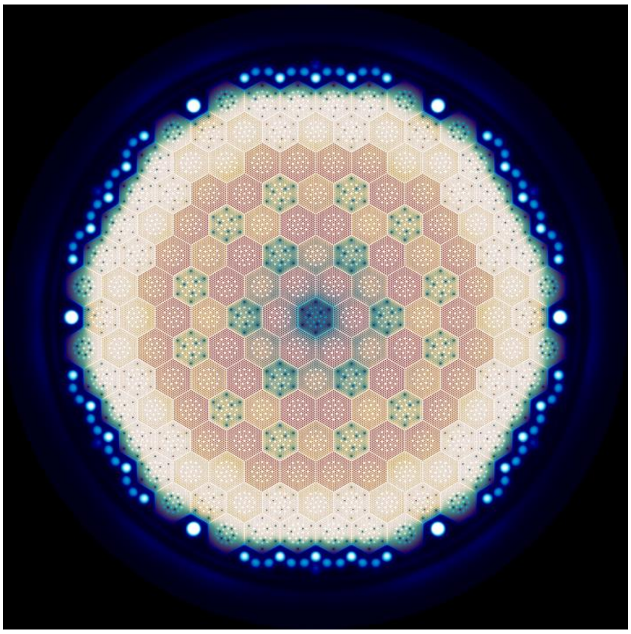

Fig. 1: Serpent result visualization.

The next step will be the generation of homogenized cross sections by Serpent for a nodal diffusion code DYN3D and obtaining a full core solution which could be compared with measurements and Serpent full core reference. The future work will also include the simulation of the full power states and fuel cycle of the X2 benchmark with coupled Monte Carlo – thermohydraulic code system.

---

[1] Lötsch T. *et al.* (2009) *Proc. 19th AER Symp.*, 53−108.

[2] Lötsch T. *et al.* (2010) *Proc. 20th AER Symp.*, 249−335.

[3] Leppänen, J. *et al.* (2013) *Ann. Nucl. Energy* **82**, 142−150.

[4] Rohde, U. *et al.* (2016) *Prog. Nucl. Energy* **89**, 170−190.

Application of ATHLET-CD code for simulation of SBLOCA 50 cm^2 severe accident scenario for a generic German PWR

M. Jobst, P. Wilhelm, Y. Kozmenkov, S. Kliem

The improvement of the safety of nuclear power plants is a continuously on-going process. The analysis of transients and accidents by application of severe accident codes is an important research topic, which significantly contributes to safety enhancements of existing power plants. Despite continuous improvement of the severe accidents codes, the model parameters for late accident phenomena are still subject to significant uncertainties. This parameter study investigates the influence of one of those uncertain parameters in ATHLET-CD, the onset of core melt relocation to the RPV lower head, to the late in-vessel phase of accident progression.[1] The study was performed exemplarily for a small-break loss-of-coolant severe accident with additional late coolant injection to primary circuit.

In the framework of the joint research project WASA-BOSS an ATHLET-CD model for a generic German PWR of type KONVOI was developed.[2–5] The model includes all components, systems and regulations of a generic KONVOI reactor, which are needed to simulate core degradation scenarios in station blackout (SBO) and small and medium break loss-of-coolant accident (SBLOCA/MBLOCA) sequences. Selected results of a SBLOCA scenario are presented here.

NUMERICAL ANALYSES. The ATHLET-CD model developed for a generic KONVOI was used to investigate an SBLOCA scenario with 50 cm^2 leak size. Multiple failures of the emergency core cooling system lead to core uncovery and core heat-up. To prevent further core degradation or to mitigate its consequences, injection to primary circuit by a mobile pump system was investigated by means of numerical analyses with variation of mobile pump activation.

One important aspect of severe accident modelling with ATHLET-CD is investigated in the current analysis: the initiation of core material relocation to the lower head. During core degradation a molten pool is formed in the core surrounded by crust (refrozen material). Due to further material accumulation and heat-up of the molten pool a failure of the crust may occur and the molten material is relocated to the lower head. From that moment on, the ATHLET-CD module AIDA simulates the processes in the lower head including the formation of a lower head molten pool, damage and failure of the RPV.[6, 7] No detailed model of the relocation process is currently available in ATHLET-CD and several possible processes are discussed in the literature.[2, 3] On the one hand one could assume early relocation at relatively low melt masses (*e.g.* directly after the first occurrence of the ceramic melt). On the other hand SBLOCA scenarios are relatively slow scenarios, where the lower head and lower parts of the core are still covered by water, despite that the upper part of the core already might be molten. Therefore the crust and the supporting lower core plate may survive for a longer period of time. This lack of a detailed relocation model leads to additional uncertainty in the late in-vessel phase of the accident sequence.

To investigate the evolution of the transient with the aforementioned mobile pump injection (MPI) and taking into account the described uncertainty about the relocation process, two sets of code simulations were carried out: a 1st set with early relocation at 35 t melt mass, and a 2nd set with the assumption of late relocation at a total melt mass of 100 t. Each set consists of one simulation without MPI and several cases with MPI with varied pump activation criteria.

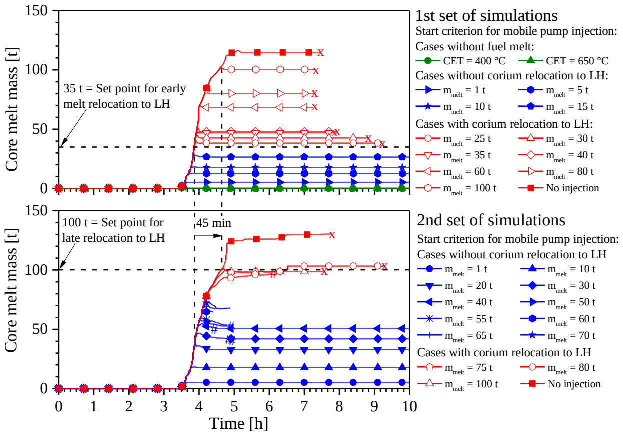

Fig. 1: Mass of molten core material relocated to lower head depending on relocation criterion and on start criterion for mobile pump injection.

RESULTS. In the described scenario, the core starts to heat up with core exit temperatures (CET) above 400 °C at 3 h and start of fuel melting at 3 h 30 min (see Fig. 1 for core melt mass). At 3 h 52 min, the core melt mass reaches 35 t, which is the initiating criterion for melt relocation to the lower head (LH) in the first set. For this scenario, reactor pressure vessel (RPV) failure is predicted at 7 h 25 min (indicated by “x” in Fig. 1). In the 2nd set of simulations, the relocation to LH (100 t melt mass) is reached at 4 h 38 min which is a delay of approximately 45 min compared to the simulation with early relocation (Fig. 1). In additional simulations, MPI was activated at different CET or at already partly molten core. It was shown in the both simulations sets that the RPV can be reflooded, but with some delay of up to 3 hours due to the increase of primary pressure after coolant injection. For the 1st set, it was found that the progression of core melt can be stopped if MPI is activated not later than 3 h 45 min (at 9 % of total core molten). If it is activated later, relocation to the lower head is calculated, followed by RPV failure. In the 2nd set, it was found that the melt progression can be stopped if the mobile pump is activated not later than 4 h 8 min (at 43 % of total core molten). A complete discussion of the results was presented on the ERMSAR 2017 conference.[8]

ACKNOWLEDGEMENTS. Parts of this work were performed within the WASA-BOSS project funded by the German Federal Ministry of Education and Research under project number 02NUK028B. The authors of this publication are responsible for its content.

---

[1] Austregesilo, H. *et al.* (2013) *ATHLET-CD Mod 3.0 Cycle A User's Manual*, Gesellschaft für Anlagen- und Reaktorsicherheit (GRS) mbH.
[2] Tusheva, P. *et al.* (2014) *WASA-BOSS Milestone report M32*.
[3] Tusheva, P. *et al.* (2015) *atw*. **60**, 442–447.
[4] Jobst, M. *et al.* (2016) *WASA-BOSS Milestone report M35*.
[5] Jobst, M. *et al.* (2017) *Report HZDR-080*.
[6] Bals, C. *et al.* (2012) *Report GRS-A-3646*.
[7] Weber, S. *et al.* (2016) *Report GRS-445*.
[8] Jobst, M. *et al.* (2017) *8th European Review Meeting on Severe Accident Research*.

Analysis of the early phase of station blackout accident for PWR with statistical methods

Y. Kozmenkov, M. Jobst, S. Kliem, F. Schäfer, P. Wilhelm

A statistical approach is used to analyse the early phase of station blackout (SBO) accident for generic German pressurized water reactor (PWR). The analysis is mainly focused on the timescale uncertainties of the accident events. 30 input uncertainties related to the simulated physical phenomena/processes are identified and quantified for the plant model. Major contributors to the uncertainties of main events are identified. A linear regression analysis is used for predicting times of events. An accuracy of event predictions is estimated and verified.

ACCIDENT SCENARIO. The accident is initiated by the total loss of AC power supply. All active emergency core cooling systems as well as feedwater supply to steam generators are unavailable. Passive safety systems (hydroaccumulators), systems powered by batteries and the pressurizer relief/safety valves are available. Primary system depressurization is initiated when the maximum coolant temperature at the outlet of the most heated core channel exceeds 400 °C.

RESULTS. A series of 181 SBO calculations with different vectors of quantified uncertainty parameters was performed using the code ATHLET-CD.[1] This number of runs corresponds to the Wilks' formula of the 5th order for 95 %/95 % coverage/confidence level.[2] The timescale uncertainties for the following events are analyzed:

E1 – Start of coolant discharge to containment;
E2 – Initiation of the primary system depressurization;
E3 – Core outlet temperature reaches peak value;
E4 – End of coolant injection from hydroaccumulators;
E5 – Core outlet temperature exceeds 650 °C;
E6 – start of the core melting.

Main results of uncertainty analysis are given in Tab. 1.

Tab. 1: Two-sided tolerance limits and uncertainty intervals for events.

Event	Lower limit (s)	Upper limit (s)	95th percentile interval (s)
E1	3,802	4,862	1,060
E2	6,353	8,063	1,710
E3	7,001	8,695	1,694
E4	7,171	8,938	1,767
E5	12,148	15,554	3,406
E6	12,339	15,793	3,454

A partial correlation coefficient (PCC) with respect to the Spearman's rank correlation was used in the sensitivity analysis as a measure for statistical correlation between input and output parameters. Statistical significances of PCCs were estimated by means of a two-tailed t-test.[2] Eight input uncertainties contribute most of the time uncertainties from Tab. 1. Six of them refer to initial and boundary conditions (reactor power, secondary pressure, primary mass flow rate, etc.). Decay heat was found to be the dominant contributor to the event uncertainties, while 10 of 30 input uncertainties do not correlate with the output uncertainties.

After event observation (*e.g.* E1) the pre-calculated uncertainty intervals for the subsequent event(s) can be replaced by prediction intervals (ε) of linear regression functions:

$$Y = \mu\{Y|X\} = \beta_0 + \beta_1 X \pm \varepsilon \qquad \text{(see Fig. 1)}^{[2]}$$

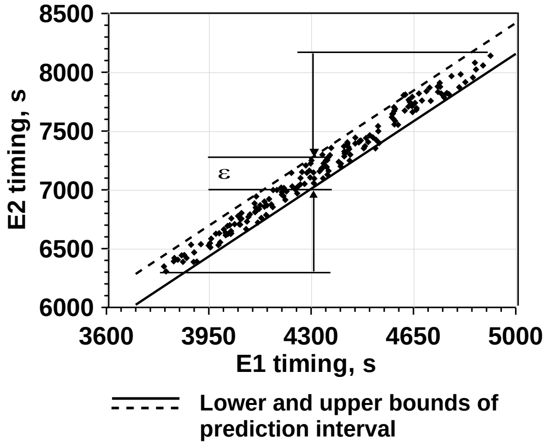

Fig. 1: Reduction of the timescale uncertainty for event E2 after observation of event E1.

The prediction interval is given by the following formula:

$$\varepsilon = t_{n-2,\frac{\alpha}{2}} \cdot \hat{\sigma} \cdot \left(1 + \frac{1}{n} + \frac{(X_i - \bar{X})^2}{(n-1)\cdot\sigma_x^2}\right)^{\frac{1}{2}}, \qquad (1)$$

where

$t_{n-2,\,\alpha/2}$ – critical t-value for significance level α,
$\hat{\sigma}$ – standard error of regression,
n – sample size (the number of calculated variants),
X_i – the value of independent variable,
$\bar{X}$ – average value for independent variable,
σ_x^2 – squared standard deviation for independent variable.

Table 2 summarizes the results of performed regression analysis.

Tab. 2: Linear regression parameters for predictions of SBO events.

Predicted event (Y)	Observed event (X)	β_0	β_1
E2	E1	76.9	1.642
E3	E2	945.5	0.961
E5	E2	1879.6	1.658
E5	E4	−640.8	1.786

In order to check the prediction intervals (like that presented in Fig. 1), an independent (additional) series of 181 calculations was conducted. Each of the four analyzed prediction intervals was confirmed to cover more than 95 % of the test sample cases. Based on the obtained results, specific measures to prevent severe damage of reactor core can be further analyzed.

ACKNOWLEDGEMENTS. This work was performed within the WASA-BOSS project funded by the *German Federal Ministry of Education and Research* under project number 02NUK028B. The authors of this publication are responsible for its content.

---

[1] Austregesilo, H. *et al.* (2014) ATHLET-CD Mod. 3.0 – Cycle B. User's Manual. GRS, Germany.
[2] Kozmenkov, Y. *et al.* (2017) *Nucl. Eng. Des.* **314**, 131–141.

Power imbalance studies at a pressurized water reactor (PWR)

J. Konheiser, S. Müller, M. Seidl[1]
[1]PreussenElektra GmbH, Hannover, Germany

In the course of investigations of asymmetric power distributions in a reactor core, simulations were carried out to calculate the extent to which these power asymmetries can be generated by geometric shifts of the fuel assemblies (FA). For this purpose, a geometric model was created for the Monte-Carlo code MCNP6 that makes it possible to determine the change of the power distributions depending on the displacement gap width between the fuel assemblies.

During the power operation in a German PWR, a stable, azimuthal power imbalance distribution between the theoretical predicted and the measured values was observed. Figure 1 shows the deviation of the activation rates measured with a so-called Aeroball Measuring System (AMS) from the expected reference values and the corresponding extrapolated deviations of the power values. The measuring principle of the AMS is based on the activation of small moveable steel balls with 1.5 wt.-% Vanadium. A detailed description of the AMS can be found in literature.[1] The deviations are plotted over the 15 × 15 grid of the FAs from the reactor. The reference power distributions were calculated with the code SIMULATE-5, a 3D, steady-state, multi-group nodal code for the analysis of both PWRs andy BWRs. In a previous work, the influence of a displacement of the AMS lances in the guide tubes was discussed.[2] This work investigates whether a small shift of the fuel assemblies can cause the differences between measurement and calculation.

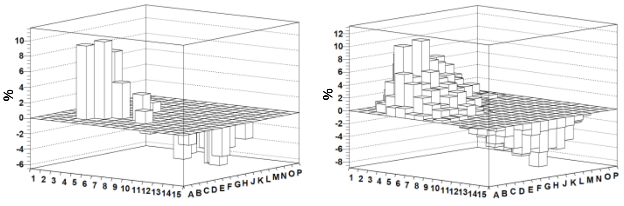

Fig. 1: Left: deviations of measured activations (AMS) to the expected reference values. Right: corresponding extrapolated deviation of the power values.

MONTE-CARLO CALCULATION. The MCNP6 radiation transport code was used for the calculations.[3] This Monte Carlo code is ideally suited for this kind of studies. The geometry can be precisely modeled and also be easily changed. Since small effects are expected, good statistics is required. The geometric model was a 3 × 3 FA matrix. The central FA was equipped with AMS lances at four quasi-independent positions for the calculation. Periodic boundary conditions were assumed. The water gaps between the FA were increased in steps of 0.25 cm up to 1 cm. Figure 2 shows a horizontal cross section through the geometric models at 0, 5 and 10 mm water gap. For the various geometries, calculations with different burnup values and boron concentrations in the cooling water were performed.

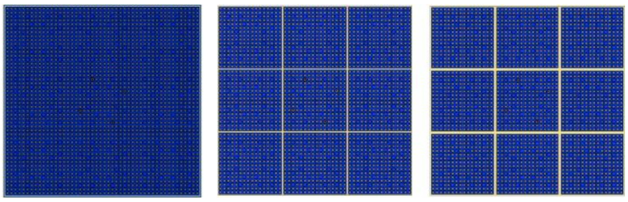
0 mm gap (a) 5 mm gap (b) 10 mm gap (c)

Fig. 2: Geometric model with different water gaps.

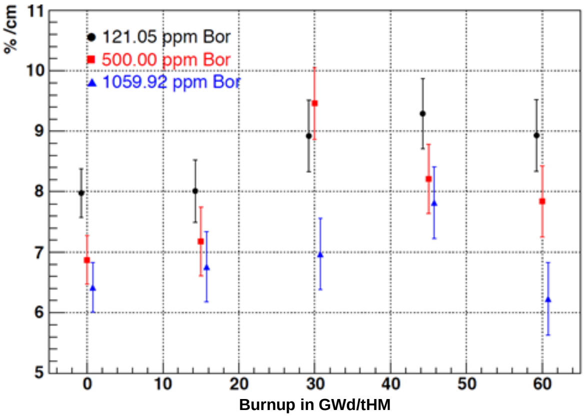

Fig. 3: Deviations of reaction rates in percent depending on burnup and boron concentration when the water gap between FA changes from 0 to 1 cm.

RESULTS. Figure 3 shows the results for various burnup values and boron concentrations. The burnup is given in GWd/tHM (gigawatt-days/ton of heavy metal). Differences in reaction rates between 6 and 9.5 % were calculated by increasing the water gap between the FA from 0 to 1 cm. The maximum differences occur at burnup from 30–40 GWd/tHM. A decrease in the rates of reaction at higher boron concentrations can be observed, except for 30 GWd/tHM. Only here, the value at 550 ppm boron concentration is higher than that at a concentration of 121.05 ppm. However, allowing for the error bars, this effect can be explained with a statistical fluctuation.

CONCLUSION. In the framework of the investigations to imbalance power, calculations with the program MCNP6 were carried out. A geometric model with a 3x3-FA matrix was used. In the central FA four AMS systems were inserted. Increasing the water gap to 1 cm between the FAs resulted in up to 9.5 % higher reaction rates. Dependences on burnup and boron concentration were found. Water gaps between the FA of 1 centimeter and more have to arise to obtain the changes shown in Fig. 1. However, it is not known whether these gaps will emerge. But it is assumed that the studied effect could be one cause for the observed imbalance power.

ACKNOWLEDGEMENTS. This work was supported by PreussenElektra GmbH.

---

[1] AREVA NP, U.S. EPR Nuclear Incore Instrumentation Systems (2006) *Report no. ANP-10271NP Revision 0.*
[2] Konheiser, J. *et al.* (2016) *J. Nucl. Sci. Technol.* **53**, 1715–1722.
[3] Goorley, T. *et al.* (2013) *Supercomputing in Nuclear Applications and Monte Carlo*, Paris.

DYN3D for transient core analysis of Sodium cooled Fast Reactors

E. Nikitin, E. Fridman

The reactor dynamics code DYN3D is being extended for Sodium cooled Fast Reactor (SFR) applications. Recently, new thermal-mechanical models accounting for thermal expansions of the core were implemented. By this means, DYN3D is now able to simulate not only static but also time-dependent scenarios in SFR cores. In order to validate DYN3D for this purpose, a transient case from the Phenix End-of-Life experiments was simulated. The DYN3D solution presents a good agreement with the experimental data indicating the code's feasibility for SFR core analyses.

TEST DESCRIPTION. The unprotected phase of the natural circulation test was selected for validation of DYN3D.[1, 2] The test was initiated by manual dry out of the two steam generators, that caused loss of heat removal from the secondary, and consequently from the primary side. In the first phase, the reactor was operated for 458 seconds, until the manual shutdown was initiated. For the validation, this initial unprotected phase was modeled.

While the total mass flow rate remained constant during the transient, the average core inlet temperature has increased by around 40 K (Fig. 1). As a result, the total power has dropped from 120 to 50 $\mathrm{MW_{th}}$, and the inner core outlet temperature by around 10 K, as shown in Fig. 2. The power reduction driven by the core reactivity was initiated by the thermal expansion of the core diagrid. The further development of the total reactivity (Fig. 2, top) was mainly influenced by the thermal expansion of the diagrid and fuel rods, the Doppler-effect, and the relative CR movement caused by the simultaneous expansion of the core, CR drivelines and vessel.

COMPUTATIONAL METHODOLOGY. The calculation was done in a two-step approach by using the Serpent-DYN3D codes sequence: (1) the necessary nuclear data were generated with Monte Carlo code Serpent, and (2) the time-dependent solution of the test was obtained with DYN3D. The measured inlet temperature evolution was used as time-dependent boundary condition, and the computational results were compared with the measured core reactivity, total power and core outlet coolant temperature curves (Fig. 2).

NUMERICAL RESULTS. The calculated total reactivity, power and core outlet temperature evolutions are presented in Fig. 1 along with the measurements. The power and core outlet temperature curves are completely aligned with experimental data, and remain within measurement uncertainties. In the first ~300 s the calculated reactivity remains in a good agreement with measurements, whereas the DYN3D underestimates the total reactivity, and reaches 7 pcm discrepancy at the end of the transient. The underestimation can be explained with the missing model of vessel expansion. After 300 s, the increasing sodium temperature of the cold pool warms up enough to induce vessel expansion. While the control rods remain in position, the core descends due to vessel expansion. This event acts as a relative control rod withdrawal that increases the core reactivity.

CONCLUSIONS. The DYN3D is capable of simulating transients in SFR cores, when the feedbacks are restricted to the core like the temperature effects and the thermal expansion of the core. Deviations from the measurements are only observed when the vessel expansion starts to influence the control rod position in the core. In order to account for the correct magnitude and time delay of such relative control rod movements, the change in thermal-mechanical conditions of the supporting structures has to be modeled. The development of such models is an ongoing research topic that will be based on the coupling of DYN3D with the thermal-hydraulic system code ATHLET.

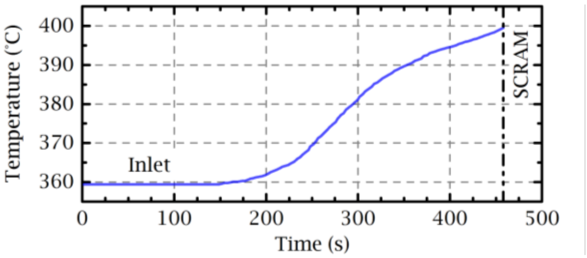

Fig. 1: Coolant temperature evolution at the core inlet (experiment).

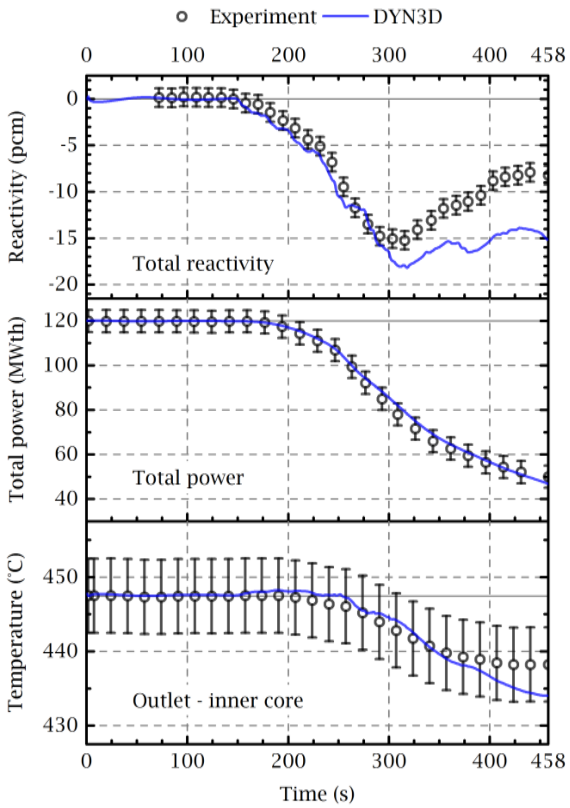

Fig. 2: DYN3D *vs.* Experiment. Top to bottom: total reactivity, total power, average outlet coolant temperature of the inner core.

---

[1] Rohde, U. *et al.* (2016) *Prog. Nucl. Energy.* **89**, 170–190.

[2] IAEA (2013) *Benchmark Analyses on the Natural Circulation Test Performed During the PHENIX End-of-Life Experiments, IAEA-TECDOC-1703*, Vienna.

DYN3D performance improvement by means of code optimization and parallelization

E. Nikitin

The reactor dynamics code DYN3D is under continuous development in order to remain a state-of-the-art simulation tool. Beside the growing functionality, it is necessary to maintain the computational performance of DYN3D. In order to find the hotspots for potential performance improvement, a full profiling of the code was done. The most loaded parts during runtime were found to be in the input data preparation procedures. These procedures were restructured by using optimization and parallelization techniques. The restructuring improved significantly the overall code performance without affecting the numerical results.

BACKGROUND AND MOTIVATION. The DYN3D is a FORTRAN legacy code that is continuously growing with new developments to remain a state-of-the-art reactor simulation tool.[1] As usually, the functionality of the models is the primary objective during implementations, whereas the performance remains a secondary goal. After consecutive implementations done during the last decades, the code can easily become bulky, less readable and less performant.

In close collaboration between the Reactor Safety Division and the Computational Science Group of HZDR, the effort was made to find possible means to improve DYN3D performance without losing functionality.

CODE ANALYSIS. In order to identify the main hotspots in the code structure for potential improvement, code profiling was carried out with the Intel VTune Amplifier tool. The analysis showed that more than 50 % of the overall CPU time is spent in the procedures responsible for the data preparation than in the numerical part of the code. Around 75 % of data preparation time is spent in multi-linear interpolation routines used to obtain the state-dependent nuclear cross section data. Furthermore, the half of this time is used up to compute the interpolated nuclear scattering data.

The reactor model is spatially divided into nodes, and therefore the interpolated data are calculated for each node. Moreover, in time-dependent problems, the interpolation procedures are executed at each time-step multiple times. The analysis demonstrated that the more spatial nodes and time steps are involved, the bigger share these routines have in the execution time.

CONDUCTED WORK. The optimization of the interpolation procedures was based on the following considerations:

- Multi-dimensional arrays are used for containing the parametrized nuclear library. They are frequently accessed in the memory by the interpolation routines. In order to ensure a fast processing of the data, the arrays were reshaped to ensure the most optimal memory access.
- Originally, the interpolation was done in two steps: (1) on the burn-up, and (2) on the rest of the state-variables (*e.g.* fuel and coolant temperature, boron concentration, etc.) in a separate subroutine. In the first step, the data are saved in global arrays that are accessed from the subroutine in the second step. Such procedure creates unnecessary decomposition of the code structure and prohibits parallelization. The usage of global variables was removed, and instead, the necessary parts of the nuclear library are directly passed as arguments to the multi-linear interpolation subroutine. The burn-up interpolation was also included in the subroutine.
- The calculation of state-dependent nuclear data for each spatial node of the reactor model is completely independent, so this task is parallelizable. Therefore, OpenMP directives were introduced to gain additional performance when running on multi-core architectures.[2]
- Along all modifications, the code readability should be maintained. The *go to* statements, that disrupt the top-down flow of the interpolation routines, were replaced with conditional and repetition clauses while preserving the program outcome.

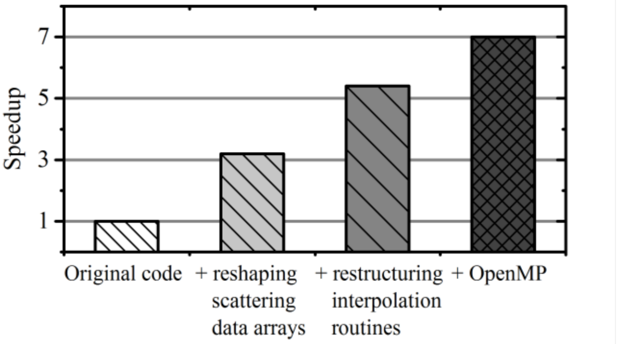

Fig. 1: DYN3D speedup after optimization.

RESULTS. The performance test on the restructured DYN3D was done on one of the real reactor simulation cases from the Phenix End-of-Life experiments.[3] The model contained 17822 spatial nodes with 31 different material types, and 500 time steps were executed. A significant improvement was achieved in terms of calculation speedup, as presented in Fig. 1. The original calculation time of around 8.5 hours was reduced after complete optimization of selected procedures to 1.6 hours, even when the parallelization was inactive. Already the reshaping of the scattering data arrays lead to a threefold acceleration. By using up to 4 threads in parallel execution, the calculation time was further reduced by additional 25 %. In overall, due to restructuring, a speedup factor of 5 to 7 was achieved in DYN3D, while the readability and maintainability was also improved. This code improvement was validated, since the numerical results remained unchanged as compared to the original version, so that the maximal relative difference did not exceed 10^{-9}.

ACKNOWLEDGEMENTS. The work was carried out within the framework of the PhD student exchange program hosted by the Computational Science Group (FWCC). I am most grateful to the whole FWCC group, especially to the group leader Dr. Guido Juckeland for the guidance provided in this project.

---

[1] Rohde, U. *et al.* (2016) *Prog. Nucl. Energy* **89**, 170–190.

[2] OpenMP Architecture Review Board (2015) *OpenMP Application Program Interface, Version 4.5*.

[3] IAEA (2013) *Benchmark Analyses on the Natural Circulation Test Performed During the PHENIX End-of-Life Experiments, IAEA-TECDOC-1703*, Vienna.

- ARTICLES (PEER-REVIEWED)
- ORAL PRESENTATIONS
- APPOINTMENTS
- THESES

ARTICLES (PEER-REVIEWED)

Agrestini, S.; Kuo, C. Y.; Moretti Sala, M.; Hu, Z.; Kasinathan, D.; Ko, K. T.; Glatzel, P.; Rossi, M.; Cafun, J. D.; Kvashnina, K. O.; Matsumoto, A.; Takayama, T.; Takagi, H.; Tjeng, L. H.; Haverkort, M. W.
Long-range interactions in the effective low energy Hamiltonian of Sr_2IrO_4: a core level resonant inelastic x-ray scattering study
Physical Review B 95, 205123 (2017).

Arinicheva, Y.; Popa, K.; Scheinost, A. C.; Rossberg, A.; Dieste-Blanco, O.; Raison, P.; Cambriani, A.; Neumeier, S.; Somers, J.; Bosbach, D.
Structural investigations of (La,Pu)PO_4 monazite solid solutions: XRD and XAFS study
Journal of Solid State Chemistry 493, 404−411 (2017).

Audras, M.; Berthon, L.; Berthon, C.; Guillaumont, D.; Dumas, T.; Illy, M. C.; Martin, N.; Zilbermann, I.; Ben-Eliyahu, Y.; Moissev, Y.; Bettelheim, A.; Camelli, S.; Hennig, C.; Moisy, P.
Structural characterization of Am(III) and Pu(III)-DOTA complexes
Inorganic Chemistry 56, 12248−12259 (2017).

Aupiais, J.; Younes, A.; Moisy, P.; Hennig, C.; Rossberg, A.; Brunel, B.; Kerbaa, M.; Vidaud, C.; Den Auwer, C.
Structural and thermodynamic investigation of An^{IV}LI(O)HOPO
New Journal of Chemistry 41, 11291−11298 (2017).

Bader, M.; Müller, K.; Foerstendorf, H.; Drobot, B.; Schmidt, M.; Musat, N.; Swanson, J. S.; Reed, T. D.; Stumpf, T.; Cherkouk, A.
Multistage bioassociation of uranium onto an extremely halophilic archaeon revealed by a unique combination of spectroscopic and microscopic techniques
Journal of Hazardous Materials 327, 225−232 (2017).

Barkleit, A.; Wilke, C.; Heller, A.; Stumpf, T.; Ikeda-Ohno, A.
Trivalent f-elements in human saliva: A comprehensive speciation study by time-resolved laser-induced fluorescence spectroscopy and thermodynamic calculations
Dalton Transactions 46, 1593−1605 (2017).

Börsig, N.; Scheinost, A. C.; Shaw, S.; Schild, D.; Neumann, T.
Uptake mechanisms of selenium oxyanions during the ferrihydrite-hematite recrystallization
Geochimica et Cosmochimica Acta 206, 236−253 (2017).

Brulfert, F.; Safi, S.; Jeanson, A.; Foerstendorf, H.; Weiss, S.; Berthomieu, C.; Sauge-Merle, S.; Simoni, E.
Enzymatic activity of the CaM-PDE1 system upon addition of actinyl ions
Journal of Inorganic Biochemistry 172, 46−54 (2017).

Brunner, J.; Baburin, I. A.; Sturm, S.; Kvashnina, K.; Rossberg, A.; Pietsch, T.; Andreev, S.; Sturm, E.; Cölfen, H.
Self-Assembled Magnetite Mesocrystalline Films: Towards Structural Evolution from 2D to 3D Superlattices
Advanced Materials Interfaces 4, 1600431 (2017).

Butorin, S. M.; Kvashnina, K. O.; Prieur, D.; Rivenet, M.; Martin, P. M.
Characteristics of chemical bonding of pentavalent uranium in La-doped UO_2
Chemical Communications 53, 115−118 (2017).

Chauhan, A.; Bergner, F.; Etienne, A.; Aktaa, J.; de Carlan, Y.; Heintze, C.; Litvinov, D.; Hernandez-Mayoral, M.; Oñorbe, E.; Radiguet, B.; Ulbricht, A.
Microstructure characterization and strengthening mechanisms of oxide dispersion strengthened (ODS) Fe-9%Cr and Fe-14%Cr extruded bars
Journal of Nuclear Materials 495, 6−19 (2017).

Chave, T.; Le Goff, X.; Scheinost, A. C.; Nikitenko, S. I.
Insights into the structure and thermal stability of uranyl aluminate nanoparticles
New Journal of Chemistry 41, 1160−1167 (2017).

Conradson, S. D.; Andersson, D. A.; Boland, K. S.; Bradley, J. A.; Byler, D. D.; Durakiewicz, T.; Gilbertson, S. M.; Kozimor, S. A.; Kvashnina, K. O.; Nordlund, D.; Rodriguez, G.; Seidler, G. T.; Bagus, P. S.; Butorin, S. M.; Conradson, D. R.; Espinosa-Faller, F. J.; Hess, N. J.; Kas, J. J.; Lezama-Pacheco, J. S.; Martin, P.; Martucci, M. B.; Rehr, J. J.; Valdez, J. A.; Bishop, A. R.; Baldinozzi, G.; Clark, D. L.; Tayal, A.
Closure of the Mott gap and formation of a superthermal metal in the Fröhlich-type nonequilibrium polaron Bose-Einstein condensate in UO_{2+x}
Physical Review B 96, 125114 (2017).

Dalodière, E.; Virot, M.; Morosini, V.; Chave, T.; Dumas, T.; Hennig, C.; Wiss, T.; Blanco, O. D.; Shuh, D. K.; Tyliszczak, T.; Venault, L.; Moisy, P.; Nikitenko, S. I.
Insights into the sonochemical synthesis and properties of salt-free intrinsic plutonium colloids
Scientific Reports 7, 43514 (2017).

Das, A.; Viehrig, H. W.; Altstadt, E.; Heintze, C.; Hoffmann, J.
On the influence of microstructure on fracture behaviour of hot extruded ferritic ODS steels
Journal of Nuclear Materials 497, 60−75 (2017).

Das, A.; Viehrig, H. W.; Bergner, F.; Heintze, C.; Altstadt, E.; Hoffmann, J.
Effect of microstructural anisotropy on fracture toughness of hot rolled 13Cr ODS steel – the role of primary and secondary cracking
Journal of Nuclear Materials 491, 83−93 (2017).

Di Pietro, R.; Erdmann, T.; Carpenter, J. H.; Wang, N.; Shivhare, R. R.; Formanek, P.; Heintze, C.; Voit, B.; Neher, D.; Ade, H.; Kiriy, A.
Synthesis of High-Crystallinity DPP Polymers with Balanced Electron and Hole Mobility
Chemistry of Materials 29, 10220−10232 (2017).

Duan, B.; Heintze, C.; Bergner, F.; Ulbricht, A.; Akhmadaliev, S.; Oñorbe, E.; de Carlan, Y.; Wang, T.
The effect of the initial microstructure in terms of sink strength on the ion-irradiation-induced hardening of ODS alloys studied by nanoindentation
Journal of Nuclear Materials 495, 118−127 (2017).

Elo, O.; Müller, K.; Ikeda-Ohno, A.; Bok, F.; Scheinost, A.; Hölttä, P.; Huittinen, N.
Batch sorption and spectroscopic speciation studies of neptunium uptake by montmorillonite and corundum
Geochimica et Cosmochimica Acta 198, 168−181 (2017).

Eswayah, A.; Hondow, N.; Scheinost, A. C.; Smith, T.; Gardiner, P.
Microbial Transformations of Selenite by Methane-Oxidizing Bacteria
Applied Microbiology and Biotechnology 101, 6713−6724 (2017).

Feig, M.; Bobnar, M.; Veremchuk, I.; Hennig, C.; Burkhardt, U.; Starke, R.; Kundys, B.; Leithe-Jasper, A.; Gumeniuk, R.
Two-gap superconductivity in Ag_{1-x} Mo_6S_8 Chevrel phase
Journal of Physics: Condensed Matter 29, 495603 (2017).

Fischermeier, E.; Pospíšil, P.; Sayed, A.; Hof, M.; Solioz, M.; Fahmy, K.
Dipolar Relaxation Dynamics at the Active Site of an ATPase Regulated by Membrane Lateral Pressure
Angewandte Chemie – International Edition 56, 1269−1272 (2017).

Fridman, E.; Kochetkov, A.; Krása, A.
Modeling of FREYA Fast Critical Experiments with the Serpent Monte Carlo Code
Annals of Nuclear Energy 108, 239−252 (2017).

Fröhlich, D. R.; Kremleva, A.; Rossberg, A.; Skerencak-Frech, A.; Koke, C.; Krüger, S.; Rösch, N.; Panack, P. J.
A combined EXAFS spectroscopic and quantum chemical study on the complex formation of Am(III) with formate
Inorganic Chemistry 56, 6820−6829 (2017).

Grahn, A.; Gommlich, A.; Kliem, S.; Bilodid, Y.; Kozmenkov, Y.
Simulation of an MSLB scenario using the 3D neutron kinetic core model Dyn3D coupled with the CFD software Trio U
Nuclear Engineering and Design 315, 117−127 (2017).

Gregson, M.; Lu, E.; Mills, D. P.; Tuna, F.; McInnes, E. J. L.; Hennig, C.; Scheinost, A. C.; McMaster, J.; Lewis, W.; Blake, A. J.; Kerridge, A.; Liddle, S. T.
The inverse-trans-influence as a general principle of f-block chemistry
Nature Communications 8, 14137 (2017).

Hennig, C.; Weiss, S.; Kraus, W.; Kretzschmar, J.; Scheinost, A.
Solution species and crystal structure of Zr(IV) acetate
Inorganic Chemistry 56, 2473−2480 (2017).

Hirsch, O.; Kvashnina, K.; Willa, C.; Koziej, D.
Hard X-ray Photon-in Photon-out Spectroscopy as a Probe of the Temperature-Induced Delocalization of Electrons in Nanoscale Semiconductors
Chemistry of Materials 29, 1461−1466 (2017).

Hopfe, S.; Flemming, K.; Lehmann, F.; Möckel, R.; Kutschke, S.; Pollmann, K.
Leaching of Rare Earth Elements from fluorescent powder using the tea fungus Kombucha
Waste Management 62, 211−221 (2017).

Huittinen, N.; Arinicheva, Y.; Kowalski, P. M.; Vinograd, V. L.; Neumeier, S.; Bosbach, D.
Probing structural homogeneity of $La_{1-x}Gd_xPO_4$ monazite-type solid solutions by combined spectroscopic and computational studies
Journal of Nuclear Materials 486, 148−157 (2017).

Jäschke, A.; Kischel, M.; Mansel, A.; Kersting, B.
Hydroxyquinoline-Calix[4]arene-Conjugates as Ligands for Polynuclear Lanthanide Complexes: Preparation, Characterization, and Properties of a Dinuclear Eu(III) complex
European Journal of Inorganic Chemistry 2017, 894–901 (2017).

Jain, R.; Cirina, F.; Kaden, P.; Pollmann, K.
Investigation of the Ga Complexation Behaviour of the Siderophore Desferrioxamine B
Solid State Phenomena 262(2017), 643−646.

Jain, R.; Jordan, N.; Tsushima, S.; Hübner, R.; Weiss, S.; Lens, P.
Shape change of biogenic elemental selenium nanomaterials decreases their colloidal stability
Environmental Science: Nano 4, 1054–1063 (2017).

Joseph, C.; Mibus, J.; Trepte, P.; Müller, C.; Brendler, V.; Park, D. M.; Jiao, Y.; Kersting, A. B.; Zavarin, M.
Long-term diffusion of U(VI) in bentonite: Dependence on density
Science of the Total Environment 575, 207–218 (2017).

Kaplan, U.; Amayri, S.; Drebert, J.; Rossberg, A.; Grolimund, D.; Reich, T.
Geochemical Interactions of Plutonium with Opalinus Clay Studied by Spatially Resolved Synchrotron Radiation Techniques
Environmental Science & Technology 51, 7892–7902 (2017).

Karimzadeh, L.; Barthen, R.; Stockmann, M.; Gruendig, M.; Franke, K.; Lippmann-Pipke, J.
Effect of glutamic acid on copper sorption onto kaolinite – batch experiments and surface complexation modeling
Chemosphere 178, 277–281 (2017).

Karimzadeh, L.; Lippmann-Pipke, J.; Franke, K.; Lippold, H.
Mobility and transport of copper(II) influenced by the microbial siderophore DFOB: Column experiment and modelling
Chemosphere 173, 326–329 (2017).

Kazama, H.; Tsushima, S.; Ikeda, Y.; Takao, K.
Molecular and Crystal Structures of Uranyl Nitrate Coordination Polymers with Double-headed 2-Pyrrolidone Derivatives
Inorganic Chemistry 56, 13530–13534 (2017).

Kliem, S.; Kozmenkov, Y.; Hadek, J.; Perin, Y.; Fouquet, F.; Bernard, F.; Sargeni, A.; Cuervo, D.; Sabater, A.; Sanchez-Cervera, S.; Garcia-Herranz, N.; Zerkak, O.; Ferroukhi, H.; Mala, P.
Testing the NURESIM platform on a PWR main steam line break benchmark
Nuclear Engineering and Design 321, 8–25 (2017).

Konheiser, J.; Brachem, C.; Seidl, M.
Investigation of the effects of a variation of fuel assembly position on the ex-core neutron flux detection in a PWR
Journal of Nuclear Science and Technology 54, 188–195 (2017).

Kovalenko, K. A.; Ruban, N. V.; Adonin, S. A.; Korneev, D. V.; Erenburg, S. B.; Trubina, S. V.; Kvashnina, K.; Sokolov, M. N.; Fedin, V. P.
Bi(III) immobilization inside MIL-101: enhanced photocatalytic performance
New Journal of Chemistry 41, 2255–2260 (2017).

Kozmenkov, Y.; Jobst, M.; Kliem, S.; Schaefer, F.; Wilhelm, P.
Statistical Analysis of the Early Phase of SBO Accident for PWR
Nuclear Engineering and Design 314, 131–141 (2017).

Kvashnina, K. O.; Walker, H. C.; Magnani, N.; Lander, G. H.; Caciuffo, R.
Resonant x-ray spectroscopy of uranium intermetallics at the U $M_{4,5}$ edges
Physical Review B 95, 05245103 (2017).

Lahrouch, F.; Chamayou, A. C.; Creff, G.; Duvail, M.; Hennig, C.; Lozano Rodriguez, M. J.; Den Auwer, C.; Di Giorgio, C.
A Combined Spectroscopic/Molecular Dynamic Study for Investigating a Methyl Carboxylated PEI as a Potential Uranium Decorporation Agent
Inorganic Chemistry 56, 1300–1308 (2017).

Lahrouch, F.; Sofronov, O.; Creff, G.; Rossberg, A.; Hennig, C.; Den Auwer, C.; Di Giorgio, C.
Polyethyleneimine Methylphosphonate : towards the design of a new class of macromolecular actinide chelating agent in case of human exposition
Dalton Transactions 46, 13869–13877 (2017).

Leinders, G.; Bes, R.; Pakarinen, J.; Kvashnina, K.; Verwerft, M.
Evolution of the Uranium Chemical State in Mixed-Valence Oxides
Inorganic Chemistry Communications 56, 6784–6787 (2017).

Lippmann-Pipke, J.; Gerasch, R.; Schikora, J.; Kulenkampff, J.
Benchmarking PET for geoscientific applications: 3D quantitative diffusion coefficient estimation in clay rock
Computers & Geosciences 101, 21–27 (2017).

Lippold, H.; Eidner, S.; Kumke, M. U.; Lippmann-Pipke, J.
Dynamics of metal-humate complexation equilibria as revealed by isotope exchange studies – a matter of concentration and time
Geochimica et Cosmochimica Acta 197, 62–70 (2017).

Liu, J.; Falke, S.; Drobot, B.; Oberthuer, D.; Kikhney, A.; Guenther, T.; Fahmy, K.; Svergun, D.; Betzel, C.; Raff, J.
Analysis of self‑assembly of S‑layer protein slp‑B53 from *Lysinibacillus sphaericus*
European Biophysics Journal 46, 77–89 (2017).

Liu, J.; Luo, X.; Wang, J.; Xiao, T.; Chen, D.; Sheng, G.; Yin, M.; Lippold, H.; Wang, C.; Chen, Y.
Thallium contamination in arable soils and vegetables around a steel plant – A newly-found significant source of Tl pollution in South China
Environmental Pollution 224, 445–453 (2017).

Liu, J.; Wang, J.; Chen, Y.; Lippold, H.; Xiao, T.; Li, H.; Shen, C. C.; Xie, L.; Xie, X.; Yang, H.
Geochemical transfer and preliminary health risk assessment of thallium in a riverine system in the Pearl River Basin, South China
Journal of Geochemical Exploration 176, 64–75 (2017).

Martin, N. P.; März, J.; Volkringer, C.; Henry, N.; Hennig, C.; Ikeda-Ohno, A.; Loiseau, T.
Synthesis of coordination polymers of tetravalent actinides (U and Np) with phthalate or mellitate ligand in aqueous medium
Inorganic Chemistry 56, 2902–2913 (2017).

Mastromarino, S.; Seibert, A.; Hashem, E.; Ciccioli, A.; Prieur, D.; Scheinost, A.; Stohr, S.; Lajarge, P.; Boshoven, J.; Robba, D.; Ernstberger, M.; Bottomley, D.; Manara, D.
Assessment of solid/liquid equilibria in the (U, Zr)O_{2+x} system
Journal of Nuclear Materials 494, 368–379 (2017).

Matys, S.; Lederer, F.; Schönberger, N.; Braun, R.; Lehmann, F.; Flemming, K.; Bachmann, S.; Curtis, S.; Macgillivray, R.; Pollmann, K.
Phage display – a new tool for the recovery of valuable metals from primary and secondary resources
Solid State Phenomena 262, 443–446 (2017).

Mayer, M.; Steiner, A. M.; Röder, F.; Formanek, P. ; König, T.; Fery, A.
Aqueous Gold Overgrowth of Silver Nanoparticles: Merging the Plasmonic Properties of Silver with the Functionality of Gold
Angewandte Chemie – International Edition 56, 15866–15870 (2017).

Merk, B.; Devan, K.; Bachchan, A.; Paul, D.; Puthiyavinayagam, P.; Srinivasan, G.
Can enhanced feedback effects and improved breeding coincide in a metal fueled, sodium cooled fast reactor?
Annals of Nuclear Energy 105, 205–218 (2017).

Merk, B.; Litskevich, D.; Whittle, K. R.; Bankhead, M.; Taylor, R.; Mathers, D.
On a Long Term Strategy for the Success of Nuclear Power
Energies 10, 867 (2017).

Mesilov, V. V.; Galakhov, V. R.; Gubkin, A. F.; Sherstobitova, E. A.; Zakharova, G. S.; Uimin, M. A.; Yermakov, A. E.; Kvashnina, K. O.; Smirnov, D. A.
X-Ray Diffraction and X-Ray Spectroscopy Studies of Cobalt-Doped Anatase TiO_2:Co Nanopowders
Journal of Physical Chemistry C 121, 24235–24244 (2017).

Moll, H.; Cherkouk, A.; Bok, F.; Bernhard, G.
Plutonium interaction studies with the Mont Terri Opalinus Clay isolate *Sporomusa sp.* MT-2.99: changes in the plutonium speciation by solvent extractions
Environmental Science and Pollution Research 24, 13497–13508 (2017).

Philipp, T.; Amann-Hildenbrand, A.; Laurich, B.; Desbois, G.; Littke, R.; Urai, J. L.
The effect of microstructural heterogeneity on pore size distribution and permeability in Opalinus Clay (Mont Terri, CH): insights from an integrated study of laboratory fluid flow and pore morphology from BIB-SEM images
Geological Society Special Publication 454 (2017).

Pidchenko, I.; Kvashnina, K. O.; Yokosawa, T.; Finck, N.; Schild, D.; Polly, R.; Bohnert, E.; Rossberg, A.; Göttlicher, J.; Dardenne, K.; Rothe, J.; Schäfer, T.; Geckeis, H.; Vitova, T.
Uranium Redox Transformations after U(VI) Coprecipitation with Magnetite Nanoparticles
Environmental Science & Technology 51, 2217–2225 (2017).

Rachamin, R.; Kliem, S.
Validation of the DYN3D-Serpent code system for SFR cores using selected BFS experiments. Part I: Serpent calculations.
Annals of Nuclear Energy 102, 158-167 (2017).

Roberts, H. E.; Morris, K.; Law, G. T. W.; Mosselmans, J. F. W.; Bots, P.; Kvashnina, K.; Shaw, S.
Uranium(V) incorporation mechanisms and stability in Fe(II)/Fe(III) iron (oxyhydr)oxides
Environmental Science & Technology Letters 4, 421–426 (2017).

Sachs, S.; Geipel, G.; Bok, F.; Oertel, J.; Fahmy, K.
Calorimetrically determined U(VI) toxicity in *Brassica napus* correlates with oxidoreductase activity and U(VI) speciation
Environmental Science & Technology 51, 10843–10849 (2017).

Safdari, M.; Phuyal, D.; Philippe, B.; Svensson, P. H.; Butorin, S. M.; Kvashnina, K. O.; Rensmo, H.; Gardner, L. K. J. M.
Impact of Synthetic Route on Structural and Physical Properties of Butyl-1,4-Diammonium Lead Iodide Semiconductors
Journal of Materials Chemistry A 23, 11730 (2017).

Schöne, S.; Radoske, T.; März, J.; Stumpf, T.; Patzschke, M.; Ikeda-Ohno, A.
[$UO_2Cl_2(phen)_2$], a Simple Uranium(VI) Compound with a Significantly Bent Uranyl Unit (phen = 1,10-phenanthroline)
Chemistry – A European Journal 23, 13574–13578 (2017).

Schymura, S.; Fricke, T.; Hildebrand, H.; Franke, K.
Elucidating the role of dissolution in CeO_2 nanoparticle plant uptake by smart radiolabeling
Angewandte Chemie – International Edition 56, 7411–7414 (2017).

Schymura, S.; Fricke, T.; Hildebrand, H.; Franke, K.
Aufklärung der Rolle von CeO_2-Nanopartikel-Auflösung bei der Aufnahme in die Pflanze mittels intelligenter Radiomarkierung
Angewandte Chemie 129, 7518–7522 (2017).

Smith, A. L.; Colineau, E.; Griveau, J. C.; Kauric, G.; Martin, P.; Scheinost, A. C.; Cheetham, A. K.; Konings, R. J. M.
A new look at the structural and magnetic properties of potassium neptunate K_2NpO_4 combining XRD, XANES spectroscopy and low temperature heat capacity
Inorganic Chemistry 56, 5839–5850 (2017).

Stockmann, M.; Schikora, J.; Becker, D. A.; Flügge, J.; Noseck, U.; Brendler, V.
Smart Kd-values, their uncertainties and sensitivities - Applying a new approach for realistic distribution coefficients in geochemical modeling of complex systems
Chemosphere 187, 277–285 (2017).

Tamain, C.; Dumas, T.; Hennig, C.; Guilbaud, P.
Coordination of Tetravalent Actinides (An=Th^{IV}, U^{IV}, Np^{IV}, Pu^{IV}) with DOTA: From Dimers to Hexamers
Chemistry – A European Journal 23, 6864–6875 (2017).

Tiquio, M. G. J.; Hurel, C.; Marmier, N.; Taneez, M.; Andral, B.; Jordan, N.; Francour, P.
Sediment-bound trace metals in Golfe-Juan Bay, northwestern Mediterranean: Distribution, availability and toxicity
Marine Pollution Bulletin 118, 427–436 (2017).

Trigub, A. L.; Tagirov, B. R.; Kvashnina, K. O.; Chareev, D. A.; Nickolsky, M. S.; Shiryaev, A. A.; Baranova, N. N.; Mokhov, E. V. K. A. V.
X-ray spectroscopic study of the chemical state of “invisible” Au in synthetic minerals in the Fe-As-S system
American Mineralogist 102, 1057–1065 (2017).

Trigub, A. L.; Tagirov, B. R.; Kvashnina, K. O.; Lafuerza, S.; Filmonova, O. N.; Nickolsky, M. S.
Experimental determination of gold speciation in sulfide-rich hydrothermal fluids from reduced to oxidized
Chemical Geology 471, 52–64 (2017).

Tullborg, E. L.; Suksi, J.; Geipel, G.; Krall, L.; Auqué, L.; Gimeno, M.; Puigdomenech, I.
The occurrences of $Ca_2UO_2(CO_3)_3$ in Fe(II) containing deep groundwater at Forsmark, eastern Sweden
Procedia Earth and Planetary Science 17, 440–443 (2017).

Tymen, S.; Scheinost, A. C.; Friebe, C.; Schubert, U. S.
In-situ XAFS characterization of PtPd nanoparticles synthesized by galvanic replacement
Advances in Nanoparticles 6, 75–91 (2017).

Tyrpekl, V.; Najii, M.; Holzhäuser, M.; Freis, D.; Prieur, D.; Martin, P.; Cremer, B.; Murray-Farthing, M.; Cologna, M.
On the Role of the Electrical Field in Spark Plasma Sintering of UO_{2+x}
Scientific Reports, 46625 (2017).

Vogel, M., Fischer, S., Maffert, A., Hübner, R., Scheinost, A. C., Franzen, C., Steudtner, R.
Biotransformation and detoxification of selenite by microbial biogenesis of selenium-sulfur nanoparticles
Journal of Hazardous Materials 344, 749–757 (2017).

Vogel, M.; Matys, S.; Lehmann, F.; Drobot, B.; Günther, T.; Pollmann, K.; Raff, J.
Use of specific metal binding of self-assembling S-layer proteins for metal bioremediation and recycling
Solid State Phenomena 262, 389–393 (2017).

Wilke, C.; Barkleit, A.; Stumpf, T.; Ikeda-Ohno, A.
Speciation of the trivalent f-elements Eu(III) and Cm(III) in digestive media
Journal of Inorganic Biochemistry 175, 248–258 (2017).

Willms, T.; Kryk, H.; Oertel, J.; Lu, X.; Hampel, U.
Reactivity of t-butyl hydroperoxide and t-butyl peroxide towards reactor materials measured by a microcalorimetric method at 30 °C
Journal of Thermal Analysis and Calorimetry 128, 319–333 (2017).

Wyżga, P.; Bobnar, M.; Hennig, C.; Leithe-Jasper, A.; Mori, T.; Gumeniuk, R.
Thermoelectric Properties of Natural Chalcopyrite from Zacatecas, Mexico
Zeitschrift für Anorganische und Allgemeine Chemie 643, 858–863 (2017).

Xiao, B.; Schmidt, M.
Incorporation of Europium(III) into Scheelite-Related Host Matrices ABO4 (A = Ca^{2+}, Sr^{2+}, Ba^{2+}; B = W^{6+}, Mo^{6+}): Role of A- and B- Sites on the Dopant Site-Distribution and Photoluminescence
Inorganic Chemistry 56, 14948–14959 (2017).

❍ ORAL PRESENTATIONS

Invited Lectures

Barkleit, A.; Wilke, C.
Chemical speciation of trivalent lanthanides and actinides in body fluids
2nd International Conference on Pollutant Toxic Ions and Molecules, PTIM2017, November 06–09, 2017, Caparica, Portugal (2017).

Barkleit, A.; Wilke, C.
Speziation trivalenter Actinide/Lanthanide im Verdauungssystem
2. Workshop - Helmholtz Cross Program Activity, Querschnittsthema Strahlenforschung "Transportprozesse in Mensch und Umwelt", October 24–25, 2017, Darmstadt, Germany (2017).

Barthen, R.; Karimzadeh, L.; Kulenkampff, J.; Gründig, M.; Lehmann, F.; Mansel, A.; Lippmann-Pipke, J.
Mining with Microbes
Guest lecture at the lecture series "Radioecology", June 01, 2017, Dresden, Germany (2017).

Baumann, N.
Uranium mining, resulting ecological problems and references to spectroscopic methods
Invited presentation, March 03, 2017, Sriracha, Thailand (2017).

Huittinen, N.
Spectroscopic investigations of actinide incorporation in $LnPO_4$ ceramic solid solutions
ThUL School 2017, October 16–20, 2017, Jülich, Germany (2017).

Ikeda-Ohno, A.
Fate of Plutonium Released from Nuclear Weapons Tests in Australia
Advanced Science Research Center Seminar, Japan Atomic Energy Agency, July 18, 2017, Tokai, Ibaraki, Japan (2017).

Ikeda-Ohno, A.
The fate of Pu released from nuclear test events into the environment
Guest lecture at the lecture series "Radioecology", May 18, 2017, TU Dresden, Germany (2017).

Karimzadeh, L.; Kulenkampff, J.; Schymura, S.; Eichelbaum, S.; Lippmann-Pipke, J.
Our strategic approach: Reactive transport modelling based on parameters obtained from batch and GeoPET column experiments: example from leaching of a fractured drill core
7th Reactive Transport PhD Workshop, February 23, 2017, Leipzig, Germany (2017).

Krawczyk-Bärsch, E.; Gerber, U.; Müller, K.; Moll, H.; Rossberg, A.; Steudtner, R.; Merroun, M. L.
Characterization of U(VI) sequestration by *Acidovorax facilis* – a spectroscopic and microscopic approach
16. Remediation Colloquium Jena, October 05–06, 2017, Jena, Germany (2017).

Kvashnina, K.; Walker, H.; Magnani, N.; Lander, G.; Caciuffo, R.
High energy resolution X-ray spectroscopy studies of U intermetallics at the U $M_{4,5}$ edges
International Conference on Strongly Correlated Electron Systems, SCES 2017, July 16–21, 2017, Prague, Czech Republic (2017).

März, J.
Tetravalent actinide complexes with N,O-donor ligands: Synthesis and characterisation
Gruppenseminar, December 08, 2017, Hannover, Germany (2017).

Patzschke, M.
Bond analysis of actinide complexes in real space
UCT und IOCB Seminar Prag, March 31, 2017, Prague, Czech Republic (2017).

Patzschke, M.
Computational Spectroscopy
ThUL School 2017, October 16–20, 2017, Jülich, Germany (2017).

Patzschke, M.
How To Analyze The Electronic Density - An Introduction To Some Useful Tools
CSC Spring School in Theoretical Chemistry, March 17, 2017, Helsinki, Finnland (2017).

Patzschke, M.
Orca for computational actinide chemistry
ThUL School 2017, October 16–20, 2017, Jülich, Germany (2017).

Patzschke, M.
Quantum Chemistry Workshop – Using Orca & Gabedit
CSC Spring School in Theoretical Chemistry, March 13–17, 2017, Helsinki, Finland (2017).

Patzschke, M.
Visualising Your Results – An Introduction to VMD
CSC Spring School in Theoretical Chemistry, March 17, 2017, Helsinki, Finnland (2017).

Patzschke, M.
Where do the Actinides go? And why we should care…
X. MMQC Mariapfarr, March 06–10, 2017, Mariapfarr, Austria (2017).

Raff, J.
Properties and application perspectives of S-layer protein self-assembly
18. Wörlitzer Workshop "Selbstorganisierende Schichtstrukturen, June 19–20, 2017, Wörlitz, Germany (2017).

Raff, J.
Radionuklide in der Biosphäre - molekulare Wechselwirkung mit Mikroorganismen
2. Workshop - Helmholtz Cross Program Activity, Querschnittsthema Strahlenforschung "Transportprozesse in Mensch und Umwelt", October 24–25, 2017, Darmstadt, Germany (2017).

Röder, F.; Lubk, A.; Houdellier, F.; Denneulin, T.; Snoeck, E.; Hÿtch, M. J.
A new degree of freedom for electron holography
PICO 2017 – Forth Conference on Frontiers of Aberration Corrected Electron Microscopy, April 30–May 04, 2017, Kasteel Valsbroek, The Netherlands (2017).

Sachs, S.; Fahmy, K.; Oertel, J.; Geipel, G.; Bok, F.
Radionuclides in living organisms – Calorimetric determination of the radionuclide toxicity
2. Workshop - Helmholtz Cross Program Activity, Querschnittsthema Strahlenforschung "Transportprozesse in Mensch und Umwelt", October 24–25, 2017, Darmstadt, Germany (2017).

Schäfer, S.; Gerber, U.; Krawczyk-Bärsch, E.; Merroun, M. L.
Biomineralization of uranium(VI) by fungi - alternative for remediation approaches?
16. Remediation Colloquium Jena, October 05–06, 2017, Jena, Germany (2017).

Scheinost, A. C.; Kvashnina, K.; Hennig, C.; Exner, J.; Rossberg, A.; Schmidt, M.; Stumpf, T.
ROBL-II: A dedicated actinide beamline for X-ray spectroscopy and scattering techniques
AnXAS 2017: 8th Workshop on Speciation, Techniques, and Facilities for Radioactive Materials at Synchrotron Light Sources, April 10–13, 2017, Oxford, United Kingdom (2017).

Tsushima, S.
Fragment Molecular Orbital Calculations for Studying Lanthanide-Protein Interaction
Institute Colloquium at Institute of Innovative Research, Tokyo Institute of Technology, January 27, 2017, Tokyo, Japan (2017).

Yalcintas, E.; Scheinost, A. C.; Gaona, X.; Altmaier, M.; Geckeis, H.
Technetium interaction with Fe(II)-minerals analysed by spectroscopy and thermodynamics
Goldschmidt 2017, August 13–18, 2017, Paris, France (2017).

Other Lectures

Albright, L.; Wilhelm, P.; Jevremovic, T.
ASTEC model development for the severe accident progression in a generic AP1000-LIKE
IAEA Technical Meeting on the Status and Evaluation of Severe Accident Simulation Codes for Water Cooled Reactors (I3-TM-54660), October 09–12, 2017, Vienna, Austria (2017).

Bader, M.
Bioassociation of uranium onto an extremely halophilic microorganism relevant in nuclear waste repositories in rock salt
Kompetenzzentrum Ost für Kerntechnik, December 07, 2017, Dresden, Germany (2017).

Bader, M.; Swanson, J.; Drobot, B.; Steudtner, R.; Reed, D. T.; Stumpf, T.; Cherkouk, A.
Comparison of two repository relevant archaea and their multistage bioassociation of uranium investigated with luminescence spectroscopy
ABC Salt V Actinide and Brine Chemistry in a Salt Repository Workshop (V), March 26–28, 2017, Ruidoso, U.S.A. (2017).

Bader, M.; Swanson, J.; Foerstendorf, H.; Müller, K.; Cherkouk, A.
Bioassociation of uranium onto extreme halophilic microorganisms relevant in nuclear waste repositories in rock salt
6th International Symposium on Biosorption and Biodegradation/Bioremediation – BioBio 2017, June 25–29, 2017, Prague, Czech Republik (2017).

Balinski, A.; Bauer, A.; Schmeide, K.; Mansel, A.; Jäschke, A.; Glasneck, F.; Kersting, B.; Krause, J.; Atanasova, P.; Scharf, C.
"SE-FLECX"-Project: Development of new extractants for Rare Earths
The 21st International Solvent Extraction Conference, November 05–09, 2017, Miyazaki, Japan (2017).

Barkleit, A.; Wilke, C.
Speciation of trivalent actinides and lanthanides in digestive media
International Conference on Environmental Radioactivity ENVIRA 2017, May 29–June 02, 2017, Vilnius, Lithuania (2017).

Barkleit, A.; Wilke, C.
Speziation trivalenter f-Elemente in den Biofluiden des Verdauungssystems
GDCh-Wissenschaftsforum Chemie 2017, September 10–14, 2017, Berlin, Germany (2017).

Bauer, A.; Jäschke, A.; Schmeide, K.
Untersuchungen zum Komplexierungs- und Extraktionsverhalten des Calix[4]arens FG74 gegenüber Uran(VI) und Thorium(IV)
Projekttreffen SE-FLECX, November 21, 2017, Montabaur, Germany (2017).

Besold, J.; Biswas, A.; Suess, E.; Scheinost, A. C.; Rossberg, A.; Mikutta, C.; Kretzschmar, R.; Gustafsson, J. P.; Planer-Friedrich, B.
Monothioarsenate transformation kinetics determines arsenic mobility in sulfidic and organic-rich systems
Goldschmidt 2017, August 13–18, 2017, Paris, France (2017).

Bilodid, Y.; Fridman, E.
Serpent-DYN3D solution of the X2 benchmark: fresh core at HZP
7th International Serpent User Group Meeting, November 06–09, 2017, Gainesville, FL, U.S.A. (2017).

Bilodid, Y.; Fridman, E.
Serpent solution of X2 benchmark: fresh core at HZP conditions
The 27th Symposium of AER on VVER Reactor Physics and Reactor Safety, October 17–20, 2017, Munich, Germany (2017).

Bilodid, Y.; Fridman, E.; Kotlyar, D.; Shwageraus, E.
Explicit decay heat calculation in the nodal diffusion code DYN3D
M&C 2017 – International Conference on Mathematics & Computational Methods Applied to Nuclear Science & Engineering 2017, April 16–20, 2017, Jeju, Korea (2017).

Bok, F.; Moog, H. C.; Altmaier, M.; Voigt, W.; Thoenen, T.
THEREDA – Thermodynamic Reference Database for the Nuclear Waste Disposal in Germany
21. European Conference on Thermophysical Properties, September 03–08, 2017, Graz, Austria (2017).

Bok, F.; Richter, A.; Brendler, V.
Building a reference database for thermodynamic sorption modelling
254th ACS National Meeting, August 20–24, 2017, Washington, DC, U.S.A. (2017).

Brinkmann, H.; Moll, H.
Interaction of uranium(VI) with cellulose degradation products
TD-315 Joint BN, GD, HT, MA Meeting 2017, February 06–07, 2017, St. Ursanne, Switzerland (2017).

Brinkmann, H.; Moll, H.
Speciation of uranium(VI) in the presence of cellulose degradation products
MIND Project Annual Meeting 2017, May 03–05, 2017, Prague, Czech Republic (2017).

Brinkmann, H.; Moll, H.; Patzschke, M.; Rossberg, A.; Stumpf, T.
Structural elucidation of U(VI)-isosaccharinic acid complexes under acidic conditions: spectroscopic and theoretical investigations
Goldschmidt 2017, August 13–18, 2017, Paris, France (2017).

Brunner, E.; März, J.
Struktur-Wirkungsbeziehungen zwischen f-Elementen und organischen Ligandsystemen
3. Projektstatusgespräch zur BMBF-geförderten Nuklearen Sicherheitsforschung, April 27–28, 2017, Dresden, Germany (2017).

Buchholz, S.; Klein-Heßling, W.; Bonfigli, G.; Kaczmarkiewicz, N.; Neukam, N.; Schäfer, F.; Wagner, T.
The code system AC2 for the simulation of advanced reactors within the frame of the German EASY project
17th International Topical Meeting on Nuclear Reactor Thermal Hydraulics (NURETH-17), September 03–08, 2017, Xi'an, China (2017).

Buchholz, S.; Schaffrath, A.; Bonfigli, G.; Kaczmarkiewicz, N.; Neukam, N.; Schäfer, F.; Wagner, T.
Evidence of design basis accidents mitigation solely with passive safety systems within the frame of the German EASY project
17th International Topical Meeting on Nuclear Reactor Thermal Hydraulics (NURETH-17), September 03–08, 2017, Xi'an, China (2017).

Fischer, S.; Jain, R.; Tsushima, S.; Jordan, N.
Fate of biological selenium(0) nanoparticles at elevated temperature
Goldschmidt 2017, August 13–18, 2017, Paris, France (2017).

Fricke, T.; Schymura, S.; Neugebauer, M.; Hildebrand, H.; Franke, K.
NanoSuppe – Verhalten von synthetischen Nanopartikeln im Wirkungspfad Abwasser-Klärschlamm – Pflanze am Beispiel TiO_2, CeO_2, MWCNT und Quantum Dots
NanoCare Clustertreffen 2017, May 04–05, 2017, Karlsruhe, Germany (2017).

Fridman, E.; Aufiero, M.
Nuclear data uncertainty quantification for the FREYA fast critical experiments
7th International Serpent User Group Meeting, November 06–09, 2017, Gainesville, FL, U.S.A. (2017).

Froehlich, D. R.; Kremeleva, A.; Rossberg, A.; Skerencak-Frech, A.; Koke, C.; Krueger, S.; Panak, P. J.
A combined EXAFS spectroscopic and quantum chemical study on the complex formation of Americium(III) with formate
AnXAS 2017 – 8th Workshop on Speciation, Techniques, and Facilities for Radioactive Materials at Synchrotron Light Sources, April 11–13, 2017, Oxford, United Kingdom (2017).

Gencheva, R.; Grudev, P.; Stefanova, A.; Jobst, M.; Wilhelm, P.
VVER-1000 RPV lower head model related to late in-vessel phenomena in case of hypothetical severe accident
The 27th Symposium of AER on VVER Reactor Physics and Reactor Safety, October 17–20, 2017, Munich, Germany (2017).

Gerber, U.; Krawczyk-Bärsch, E.; Arnold, T.; Scheinost, A. C.
Microbial reduction of uranium by anaerobic microorganisms isolated from a former uranium mine
BioRemid 2017 – International Meeting on New Strategies in Bioremediation Processes, March 09–10, 2017, Granada, Spain (2017).

Gerber, U.; Schäfer, S.; Krawczyk-Bärsch, E.
Interactions of natural occurring microorganisms with uranium(VI)
Universidad Tenica Federico Santa Maria, July 27, 2017, Valparaiso, Chile (2017).

Grahn, A.; Gommlich, A.; Kliem, S.
Simulation of a Main Steamline Break scenario using the 3D neutron kinetic core model Dyn3D coupled with the CFD software Trio U
M&C 2017 – International Conference on Mathematics & Computational Methods Applied to Nuclear Science & Engineering 2017, April 16–20, 2017, Jeju, Korea (2017).

Hennig, C.; Weiss, S.; Ikeda-Ohno, A.; Gumeniuk, R.; Scheinost, A. C.
XAFS and XRD studies on tetravalent actinides in zirconia- and zircon-based ceramics
AnXAS 2017 – 8th Workshop on Speciation, Techniques, and Facilities for Radioactive Materials at Synchrotron Light Sources, April 11–13, 2017, Oxford, United Kingdom (2017).

Hotchkis, M.; Child, D.; Johansen, M. P.; Collins, R. N.; Howell, N.; Howard, D. L.; Ikeda-Ohno, A.
Markers from Australia's nuclear legacy in marine wildlife
ANSTO User Meeting, November 22–24, 2017, National Centre for Synchrotron Science, Melbourne, Australia (2017).

Ikeda-Ohno, A.
Research on the chemistry of f-elements at HZDR – A general overview of the division Chemistry of the f-Elements
Internal colloquium, October 05, 2017, CEA-Marcoule, France (2017).

Ikeda-Ohno, A.; Mokhber-Shahin, L.; Howard, D. L.; Collins, R. N.; Payne, T. E.; Johansen, M. P.
Fate of Plutonium Released from a Former Nuclear Weapons Test in Australia
Actinides 2017, July 09–14, 2017, Sendai, Japan (2017).

Jäschke, A.
Calix[4]aren-based Ligands as Extracting Agents for f-Elements
FENABIUM-Projekttreffen, December 04, 2017, Dresden, Germany (2017).

Johansen, M. P.; Caffrey, E. A.; Child, D. P.; Collins, R. N.; Harrison, J. J.; Hotchkis, M. A. C.; Howard, D. L.; Howell, N.; Payne, T. E.; Mokhber Shahin, L.; Ikeda-Ohno, A.; Thiruvoth, S.
Methods for investigating Australia's former nuclear test sites
Annual Congress of the Royal Australian Chemical Institute (RACI) 2017, July 23–28, 2017, Melbourne, Australia (2017).

Jones, J. E.; Adam, C.; Kaden, P.; Martin, L. R.; Geist, A.; Natrajan, L. S.; Sharrad, C. A.
Towards a simplified TALSPEAK process using DTPA-amino acid conjugates
41st Annual Actinide Separations Conference, May 23–25, 2017, Lemont, IL, U.S.A. (2017).

Jones, J. E.; Langford, M. H.; Geist, A.; Panak, P. J.; Kaden, P.; Adam, C.; Adam, N.; Sharrad, C. A.; Martin, L.; Natrajan, L. S.
Modified DTPA ligand systems for simplified trivalent actinide-lanthanide separations based on the TALSPEAK process
253rd ACS National Meeting, April 02–06, 2017, San Francisco, CA, U.S.A. (2017).

Jordan, N.; Huittinen, N.; Lösch, H.; Barkleit, A.; Bok, F.; Heller, A.; Brendler, V.
Development of a Thermodynamic Database for Europium
Goldschmidt 2017, August 13–18, 2017, Paris, France (2017).

Kliem, S.
AER Working Group D on VVER Safety Analysis – Report of the 2017 Meeting
The 27th Symposium of AER on VVER Reactor Physics and Reactor Safety, October 17–20, 2017, Munich, Germany (2017).

Kliem, S.; Hampel, U.; Hurtado, A.; Kästner, W.; Kratzsch, A.; Schlösser, D.; Jansen, S.
Das Kompetenzzentrum Ost für Kerntechnik
3. Projektstatusgespräch zur BMBF-geförderten Nuklearen Sicherheitsforschung, April 27–28, 2017, Dresden, Germany (2017).

Kliem, S.; Tromm, W.; Reinecke, E. A.
Overview on Helmholtz Reactor Safety Research
2nd Sino-German Symposium on Fundamentals of Advanced Nuclear Safety Technology, September 12–15, 2017, Karlsruhe, Germany (2017).

Kloditz, R.; Radoske, T.; Patzschke, M.; Stumpf, T.
Bonding analysis of tetravalent actinide complexes with N-/O-donor ligands
ThUL School 2017, October 16–20, 2017, Jülich, Germany (2017).

Kloditz, R.; Radoske, T.; Patzschke, M.; Stumpf, T.
Bonding analysis of tetravalent actinide complexes with salen
FENABIUM-Projekttreffen, December 04, 2017, Dresden, Germany (2017).

Kloditz, R.; Radoske, T.; Schöne, S.; Patzschke, M.; Stumpf, T.
Real-space bonding analysis of tetravalent actinide complexes with N-donor ligands
Actinides 2017, July 09–14, 2017, Sendai, Japan (2017).

Konheiser, J.; Müller, S. E.; Seidl, M.
Investigations of the Effects of the Variation of Fuel Assembly Positions in a core of a PWR
17. AAA Workshop, December 04, 2017, Garching, Germany (2017).

Krawczyk-Bärsch, E.; Gerber, U.; Steudtner, R.
Bioremediation of uranium contaminated sites by *Acidovorax facilis* – a microscopic and spectroscopic study
BioRemid 2017 – International Meeting on New Strategies in Bioremediation Processes, March 09–10, 2017, Granada, Spain (2017).

Krawczyk-Bärsch, E.; Gerber, U.; Steudtner, R.; Müller, K.; Moll, H.; Rossberg, A.; Merroun, M. L.
Spectroscopic and microscopic approach of U(VI) sorption on *Acidovorax facilis* for remediation purpose
Goldschmidt 2017, August 13–18, 2017, Paris, France (2017).

Kulenkampff, J.; Barthen, R.; Gründig, M.; Karimzadeh, L.; Lippold, H.; Schymura, S.; Lippmann-Pipke, J.
Spatiotemporal quantitative imaging of leaching processes with positron emission tomography (PET), improving process understanding and modelling performance
GeoBremen 2017 – The System Earth and its Materials – from Seafloor to Summit, Joint Meeting of DGGV and DMG, September 24–29, 2017, Bremen, Germany (2017).

Kulenkampff, J.; Gründig, M.; Lippmann-Pipke, J.
Non-destructive tomographic monitoring of transport processes in barrier material (Opalinus clay) with PET
9th International Conference on Porous Media & Annual Meeting, May 08–11, 2017, Rotterdam, The Netherlands (2017).

Kulenkampff, J.; Karimzadeh, L.; Schymura, S.; Barthen, R.; Gründig, M.; Lippold, H.; Lippman-Pipke, J.
Visualizing concentration distributions in macroscopic samples in the course of geochemical processes
9th International Conference on Porous Media & Annual Meeting, May 08–11, 2017, Rotterdam, The Netherlands (2017).

Kvashnina, K. O.; Rossberg, A.; Exner, J.; Scheinost, A. C.
High-energy resolution X-ray spectroscopy studies of electron-electron interactions in actinide and lanthanide systems
Migration 2017 – 16th International Conference on the Chemistry and Migration Behaviour of Actinides and Fission Products in the Geosphere, September 10–15, 2017, Barcelona, Spain (2017).

Lippold, H.
Radiotracer exchange studies for gaining direct insight into the equilibrium characteristics of elementary processes determining humic-bound metal transport
GeoBremen 2017 – The System Earth and its Materials – from Seafloor to Summit, Joint Meeting of DGGV and DMG, September 24–29, 2017, Bremen, Germany (2017).

März, J.; Schöne, S.; Radoske, T.; Patzschke, M.; Stumpf, T.; Ikeda-Ohno, A.
Coordination Chemistry of Uranium (U(IV) and -(VI)) with Bidentate N-donor Ligands, 2,2’-Bipyridine and 1,10-Phenanthroline
Actinides 2017, July 09–14, 2017, Sendai, Japan (2017).

Mansel, A.; Franke, K.
Production and purification of no-carrier-added ^{89}Zr at the Leipzig cyclotron for extraction studies with a calix[4]arene
5th International Nuclear Chemistry Congress - INCC, August 27–September 02, 2017, Gothenburg, Sweden (2017).

Marques Fernandes, M.; Scheinost, A. C.; Baeyens, B.
Influence of Fe^{II} on the retention mechanisms of NpO_2^+ by montmorillonite
AnXAS 2017 – 8th Workshop on Speciation, Techniques, and Facilities for Radioactive Materials at Synchrotron Light Sources, April 11–13, 2017, Oxford, United Kingdom (2017).

Marques Fernandes, M.; Scheinost, A. C.; Baeyens, B.
Sorption of U and Eu on illite: influence of accessory minerals
Goldschmidt 2017, August 13–18, 2017, Paris, France (2017).

Marques, M. M.; Scheinost, A. C.; Baeyens, B.
Sorption of NpO_2^+ on montmorillonite: influence of ferrous iron
Goldschmidt 2017, August 13–18, 2017, Paris, France (2017).

Martin, N. P.; März, J.; Volkringer, C.; Henry, N.; Hennig, C.; Ikeda-Ohno, A.; Loiseau, T.
Coordination polymers of tetravalent uranium and neptunium with aromatic polycarboxylate ligands
Migration 2017 – 16th International Conference on the Chemistry and Migration Behaviour of Actinides and Fission Products in the Geosphere, September 10–15, 2017, Barcelona, Spain (2017).

Matschiavelli, N.; Kluge, S.; Cherkouk, A.
Bentonite – geotechnical barrier and source for microbial life
PETRUS-ANNETTE PhD Conference, June 23–30, 2017, Lisbon, Portugal (2017).

Matschiavelli, N.; Steglich, J.; Kluge, S.; Cherkouk, A.
Bentonite - geotechnical barrier and source for microbial life
Goldschmidt 2017, August 13–18, 2017, Paris, France (2017).

Matys, S.; Lakatos, M.; Raff, J.; Vogel, M.; Pollmann, K.
S-layer proteins for optical bio-sensing purposes
XXVI International Materials Research Congress, August 20–25, 2017, Cancun, Mexico

Matys, S.; Lakatos, M.; Raff, J.; Vogel, M.; Pollmann, K.
S-layer proteins for optical bio-sensing purposes
Workshop DNA Mitteldeutschland, September 14, 2017, Dresden, Germany (2017).

Matys, S.; Lederer, F.; Schönberger, N.; Braun, R.; Lehmann, F.; Flemming, K.; Bachmann, S.; Curtis, S.; Macgillivray, R.; Pollmann, K.
Phage display – a new tool for the recovery of valuable metals from primary and secondary resources
22. International Biohydrometallurgy Symposium, September 24–27, 2017, Freiberg, Germany (2017).

Matys, S.; Lederer, F.; Schönberger, N.; Braun, R.; Vogel, M.; Raff, J.; Jain, R.; Schrader, S.; Pollmann, K.
Concepts for the development of new materials for biosorption processes
16ème édition du congrès de la Société Française de Génie des Procédés, July 11–13, 2017, Nancy, France (2017).

Merchel, S.; Le Bras, L.; Gurlit, S.; Rugel, G.; Scharf, A.; Opel, T.; Wetterich, S.
Tackling challenges in AMS sample preparation
DPG Frühjahrstagung des Arbeitskreises Atome, Moleküle, Quantenoptik und Plasmen (AMOP), March 06–10, 2017, Mainz, Germany (2017).

Moll, H.; Sachs, S.; Geipel, G.
Canola cell (*Brassica napus*) responses to europium(III) exposure: a spectroscopic study
Goldschmidt 2017, August 13–18, 2017, Paris, France (2017).

Moog, H. C.; Altmaier, M.; Bok, F.; Brendler, V.; Gaona, X.; Marquardt, C.; Montoya, V.; Richter, A.; Scharge, T.; Thoenen, T.; Voigt, W.; Yalçintaş, E.
THEREDA – Thermodynamic Reference Database
ENTRIA Conference, September 26–28, 2017, Braunschweig, Germany (2017).

Moog, H. C.; Altmaier, M.; Brendler, V.; Bok, F.; Gaona, X.; Marquardt, C.; Richter, A.; Scharge, T.; Thoenen, T.; Voigt, W.
Recent and present activities in THEREDA
Actinide Brine Chemistry (ABC-Salt V Workshop 2017), March 26–28, 2017, Ruidoso, U.S.A. (2017).

Müller, K.; Simon, B.; Bok, F.; Rossberg, A.
Spectroscopic identification of Np(V) sorption complexes on birnessite
Goldschmidt 2017, August 13–18, 2017, Paris, France (2017).

Müller, S. E.
Biasing in MC transport calculations
Mu2e Software and Simulation Meeting, June 21, 2017, Batavia, U.S.A. (2017).

Müller, S. E.
The FLUKA Monte Carlo simulation package and its applications at the HZDR
VKTA KS-Klausurberatung, August 08–09, 2017, Lohmen, Germany (2017).

Müller, S. E.
The use of FLUKA in the Mu2e experiment
Mu2e Software and Simulation Meeting, June 07, 2017, Batavia, U.S.A. (2017).

Müller, S. E.; Ferrari, A.; Konheiser, J.
Shielding and activation studies for the MYRRHA research reactor
16th International Symposium on Reactor Dosimetry, May 07–12, 2017, Santa Fe, NM, U.S.A. (2017).

Müller, S. E.; Konheiser, J.; Naumann, B.; Ferrari, A.; Magin, A.
Source term and activation analysis for the new cyclotron for medical applications at HZDR with MCNP6 and FLUKA
DPG Spring Meeting 2017, March 27–31, 2017, Münster, Germany (2017).

Nikitin, E.; Fridman, E.
Modeling of Phenix EOL experiments with Serpent-DYN3D
7th International Serpent User Group Meeting, November 06–09, 2017, Gainesville, FL, U.S.A. (2017).

Patzschke, M.
Untersuchungen zur katalytischen Aktivität von Au(III) Verbindungen
Organisch-Chemisches Kolloquium, December 12, 2017, Dresden, Germany (2017).

Payne, T. E.; Kinsela, A. S.; Ikeda-Ohno, A.; Vazquez-Campos, X.; Waite, T. D.; Harrison, J. J.; Bligh, M. W.; Johansen, M. P.; Thiruvoth, S.; Wilsher, K. L.
Impact of dynamic geochemical conditions on plutonium and americium mobility at a legacy trench disposal site
Migration 2017 – 16th International Conference on the Chemistry and Migration Behaviour of Actinides and Fission Products in the Geosphere, September 10–15, 2017, Barcelona, Spain (2017).

Philipp, T.; Wolter, J. M.; Schmeide, K.; Stumpf, T.
Wechselwirkungen zwischen U(VI) und Ca-Bentonit sowie Cm(III) und CSH-Phasen unter dem Einfluss alkalischer und hochsalinarer Porenwässer
5. Workshop des BMWi-Verbundvorhabens “Geochemische Radionuklidrückhaltung an Zementalterationsphasen (GRaZ)“, November 15, 2017, Potsdam, Germany (2017).

Qiu, C.; Schmidt, M.; Eng, P.; Hennig, C.
Formation of Zr(IV)-nanoparticles on Muscovite (001): effect of background electrolyte
Goldschmidt 2017, August 13–18, 2017, Paris, France (2017).

Radoske, T.
Charaterization of actinide(IV) complexes with imine type ligands
FENABIUM Projekttreffen, May 10, 2017, Leipzig, Germany (2017).

Radoske, T.; Adam, C.; Schöne, S.; Patzschke, M.; März, J.; Kaden, P.
NMR investigations of paramagnetic effects in metal-organic complexes of trivalent and tetravalent actinides with soft-donor ligands
Actinides 2017, July 09–14, 2017, Sendai, Japan (2017).

Radoske, T.; März, J.; Kaden, P.; Walter, O.; Weigand, J. J.; Stumpf, T.; Ikeda-Ohno, A.
Interaction of Tetravalent Actinides (An(IV)) with Mixed N/O-Donor Imine Type Ligands
Actinides 2017, July 09–14, 2017, Sendai, Japan (2017).

Raff, J.; Liu, J.; Falke, S.; Drobot, B.; Oberthuer, D.; Kikhney, A.; Guenther, T.; Fahmy, K.; Svergun, D.; Betzel, C.
Influence of bivalent metal ions on the self-assembly of S-layer proteins from Lysinibacillus sphaericus JG-B53
XXVI International Materials Research Congress (IMRC 2017), August 20–25, 2017, Cancún, México (2017).

Schmeide, K.; Rossberg, A.; Weiss, S.; Brendler, V.; Scheinost, A. C.
Oxidation state and local structure of technetium reacted with siderite
Goldschmidt 2017, August 13–18, 2017, Paris, France (2017).

Schmeide, K.; Rossberg, A.; Weiss, S.; Brendler, V.; Scheinost, A. C.
Technetium retention by siderite under anoxic conditions
GeoBremen 2017 – The System Earth and its Materials – from Seafloor to Summit, Joint Meeting of DGGV and DMG, September 24–29, 2017, Bremen, Germany (2017).

Schnaars, K.; März, J.; Hennersdorf, F.; Harting, D.; Acker, M.; Wenzel, M.; Ikeda-Ohno, A.; Stumpf, T.; Gloe, K.; Weigand, J. J.
4-Phosphorylpyrazolones as receptor molecules for f-block elements
Actinides 2017, July 09–14, 2017, Sendai, Japan (2017).

Schöne, S.; März, J.; Kaden, P.
Synthesis and characterization of tetravalent actinide complexes with benzamidinates
FENABIUM Projekttreffen, May 10, 2017, Leipzig, Germany (2017).

Schöne, S.; März, J.; Kaden, P.
Synthesis and characterization of tetravalent actinide complexes with amidinates and guanidinates
FENABIUM Projekttreffen, December 4, 2017, Dresden, Germany (2017).

Schöne, S.; März, J.; Kaden, P.; Weigand, J. J.; Roesky, P. W.; Stumpf, T.; Ikeda-Ohno, A.
Synthesis and characterization of the first chiral benzamidinate complexes of tetravalent actinides (An(IV))
Actinides 2017, July 09–14, 2017, Sendai, Japan (2017).

Schöne, S.; Radoske, T.; März, J.; Stumpf, T.; Ikeda-Ohno, A.
Synthesis and structural characterization of mixed iron-uranium compounds with bidentate N-donor ligands
Migration 2017 – 16th International Conference on the Chemistry and Migration Behaviour of Actinides and Fission Products in the Geosphere, September 10–15, 2017, Barcelona, Spain (2017).

Schymura, S.; Fricke, T.; Hildebrand, H.; Steudtner, R.; Hübner, R.; Mansel, A.; Franke, K.
Investigation of the environmental impact of nanoparticles using smart radiolabeling
13th Cycleur – European Network of Cyclotron Research Centers – Workshop, November 23–24, 2017, Lisbon, Portugal (2017).

Sporn, M.; Neukam, N.; Schuster, C.; Hurtado, A.; Hampel, U.; Schäfer, F.
ATHLET model development for the passive pressure pulse transmitter as part of the passive safety systems of a nuclear reactor within the frame of the German EASY project
17th International Topical Meeting on Nuclear Reactor Thermal Hydraulics (NURETH-17), September 03–08, 2017, Xi'an, China (2017).

Steudtner, R.; Müller, K.; Schmeide, K.; Brendler, V.
The uranium citric acid system and its sorption onto hematite
GDCh-Wissenschaftsforum Chemie 2017, September 10–14, 2017, Berlin, Germany (2017).

Stockmann, M.; Britz, S.; Flügge, J.; Fricke, J.; Becker, D.; Noseck, U.; Brendler, V.
Smart Kd-values as realistic distribution coefficients
Goldschmidt 2017, August 13–18, 2017, Paris, France (2017).

Swanson, J.; Cherkouk, A.; Bader, M.; Reed, D.
The influence of microorganisms on subsurface, salt-based nuclear waste repositories
Goldschmidt 2017, August 13–18, 2017, Paris, France (2017).

Takao, K.; Tsushima, S.
Photochemical Reduction of Non-fluorescent Tris(carbonato)uranyl(VI) Complex
The 67th Conference of Japan Society of Coordination Chemistry, September 16–18, 2017, Sapporo, Japan (2017).

Tsushima, S.; Mochizuki, Y.; Komeiji, Y.; Okuwaki, K.; Abe, T.; Mori, H.; Tanaka, S.
Theoretical study on Calmodulin binding with Ca(II) and Eu(III) ions
The 78th Japan Society of Applied Physics Meeting, September 05–08, 2017, Fukuoka, Japan (2017).

Tsushima, S.; Mochizuki, Y.; Komeiji, Y.; Takao, K.
Computational study on the interaction between Eu(III) and calmodulin
Atomic Energy Society of Japan 2017 Fall Meeting, September 13–15, 2017, Sapporo, Japan (2017).

Tsushima, S.; Samsonov, S.; Drobot, B.; Raff, J.; Komeiji, Y.; Mochizuki, Y.
Site-specific binding affinity of Eu(III) towards Ca-binding protein calmodulin: A combined spectroscopic and theoretical study
Actinides 2017, July 09–14, 2017, Sendai, Japan (2017).

Volkringer, C.; Martin, N. P.; März, J.; Hennig, C.; Ikeda-Ohno, A.; Loiseau, T.
Coordination chemistry of tetravalent neptunium with aromatic polycarboxylate ligands
Actinides 2017, July 13–14, 2017, Sendai, Japan (2017).

Wilhelm, P.; Jobst, M.
Core degradation analysis for a generic German PWR with the severe accident code ATHLET-CD
IAEA Technical Meeting on the Status and Evaluation of Severe Accident Simulation Codes for Water Cooled Reactors (I3-TM-54660), October 09–12, 2017, Vienna, Austria (2017).

Wollenberg, A.; Günther, A.; Raff, J.; Stumpf, T.
Comparative studies of two fungi and their molecular interactions with uranium(VI) and europium(III)
Migration 2017 – 16th International Conference on the Chemistry and Migration Behaviour of Actinides and Fission Products in the Geosphere, September 10–15, 2017, Barcelona, Spain (2017).

Wolter, J. M.; Philipp, T.; Lippold, H.; Schmeide, K.; Stumpf, T.
Rückhaltung von U(VI) und Eu(III) an Ca-Bentonit und CSH-Phasen unter hoch salinaren und alkalischen Bedingungen
4. Workshop des BMWi-Verbundvorhabens "Geochemische Radionuklidrückhaltung an Zementalterationsphasen (GRaZ)", April 05–06, 2017, Mainz, Germany (2017).

Xiao, B., Schmidt, M.
Incorporation of Europium(III) into Scheelite-Related Host Matrices ABO_4 ($A = Ca^{2+}, Sr^{2+}, Ba^{2+}$; $B = W^{6+}, Mo^{6+}$): Role of A- and B- Sites on the Dopant Site-Distribution and Photoluminescence
GeoBremen 2017 – The System Earth and its Materials – from Seafloor to Summit, Joint Meeting of DGGV and DMG, September 24–29, 2017, Bremen, Germany (2017).

In addition, more than 30 posters were presented at international conferences and workshops.

❍ APPOINTMENTS

Brendler, V.

Appointment as honorary professor for Radiochemistry
October 2017, University of Applied Sciences, Dresden, Germany.

Tsushima, S.

Appointment as adjunct professor
June 2017, Tokyo Institute of Technology, Tokyo, Japan.

❍ THESES

DOCTORAL THESES

(Technische Universität Dresden, 2017, except where noted)

Hellebrandt, S.

Grenzflächenreaktionen von Actiniden an Muskovit

Hilger, I.

Influence of microstructure features on the irradiation behaviour of ODS Fe14Cr alloys

Hoffmann, A.

Entwicklung von Modellen zur anlagentechnischen Simulation von solarthermischen Kraftwerksanlagen mit Direktverdampfung
RWTH Aachen, 2017.

Holt, L.

Improvement and Validation of a Computer Model for the Thermo-mechanical Fuel Rod Behaviour during Reactivity Transients in Nuclear Reactors
Technische Universität München, Munich, 2017.

Litskevich, D.

Development of transport solutions for zooming in DYN3D
RWTH Aachen, 2017.

Schott, J.

Untersuchung der Komplexbildung im An(III)/ Ln(III)-Borat-System

Wagner, A.

Long-term irradiation effects on reactor pressure vessel steels
Martin-Luther-Universität Halle-Wittenberg, 2017.

MASTER THESES

(Technische Universität Dresden, 2017, except where noted)

Knöppel, J.

Spektroskopische und kalorimetrische Untersuchungen zur Metallbindung und Strukturänderung der MIIA-Domäne des Proteins VIC_001052

Nucke, L.

Role of local membrane protein hydration for the stability of the PIB -type ATPase CopA from *Legionella pneumophila*

Ritter, E.

Influence of Temperature and Sulfate on the U(VI) Speciation in the Aquatic System

Schernikau, M.

Further development of fc-LIF for the study of interaction of Eu(III) and U(VI) with single oxide phases

Zimmermann, T.

Einfluss der Speziation auf die Fluoreszenzeigenschaften von U(IV) im Sulfat-System
University of Applied Sciences, Dresden, Germany.

BACHELOR THESES

Schäfer, S.

Interaktion aerober und anaerober Mikroorganismen mit Uran im Flutungswasser der ehemaligen Uranerzmine Königstein

❍ JOINT MEETING OF CZECH AND GERMAN BIOPHYSICISTS

Structural Transitions of Biomolecules in Theory and Experiment

Monastery “Kloster Hünfeld”, Germany, February 23 – 25, 2017

The section "Molecular Biophysics" of the German Biophysical Society held its biannual meeting at the Kloster Hünfeld near Fulda with a focus on Czech German research contacts. The programme was organized as a joint meeting by the Division of Biophysics of the Institute of Resource Ecology Helmholtz-Zentrums Dresden – Rossendorf (Dr. Jana Oertel and Prof. Karim Fahmy, head of the section) in cooperation with Prof. Martin Hof (J. Heyrovsky Institute of Physical Chemistry, Prague). The general topic was "Structural Changes of Biomolecule in Experiment and Theory", addressing scientists and young investigators from the fields of molecular biology, electrophysiology of ion channels as well as microscopy, spectroscopy, folding and molecular dynamics of proteins. A total of 38 talks was given – 14 from Czech Rep., 23 from Germany and one from U.S.A.. Among these were 12 female presenters. Total participants were 62 (26 women). Contributions were grouped in nine sessions and an extensive poster session (sponsors: Zeiss, Asylum Research, TA-Instruments).

In addition to traditional topics, new developments were presented and discussed concerning infrared and THz-Spectroscopy and "ab initio vibrational analysis" from which new impulses are expected in the future. Likewise, the meeting included for the first time talks on DNA-nanotechnology and its potential for single molecule experiments. The conference revealed a strong common interest of internationally highly visible Czech and German research groups in membrane protein biophysics and a large complementarity of methods and an interest in using HZDR facilities by Czech researchers.

(by: K. Fahmy)

List of invited speakers:

Amaro, M.
Impact of GM1 nanodomains in the oligomerisation of membrane bound Aß monomers

Bednar, D.
FireProt: Computational Design of Thermostable Proteins

Böckmann, R.
GPCR dimerization and activation studied in sequential multiscale simulations

Coskun, U.
Calcium directly regulates phosphatidylinositol 4,5-bisphosphate headgroup conformation and recognition

Cwiklik, L.
Tear Film Lipid Layer: a molecular-level view

Fitter, J.
Proteins in crowded environments

Hauser, K.
Biomolecular dynamics studied with residue-specific resolution

Havenith, M.
THz Spectroscopy and Solvation Science

Hof, M.
Use of fuorescence spectroscopy in Synthetic Biology

Hub, J.
Detecting protein structures, ensembles, and dynamics in SAXS/WAXS data: combining MD simulations with Bayesian inference

Huber, T.
Novel chemical biology methods to study GPCRs one molecule at a time

Jungwirth, P.
Cell Penetration and Membrane Fusion: Two Sides of the Same Coin

Keller, A.
On the stability and degradation of DNA origami nanostrauctures in urea and guanidinium chloride

Keller, S.
Polymer-Bounded Nanodiscs for Membrane Biophysics

Lazar, J.
No Need to FRET: Observing Membrane Protein Structure and Function by Polarization Fluorescence Microscopy

Obsil, T.
The 14-3-3 protein-dependent regulation of neutral trehalase Nth1

Schlierf, M.
Watching Membrane Protein Folding in singulo

Schneider, B.
Interactions between interferon-gamma and extracellular portions of its two receptors R1 and R2

Schröder, I.
K^+ channel selectivity filter gating correlates with site-specific ion occupation obtained from the same experiment

Seidel, R.
Single-molecule insight into target recognition by CRISPR-Cas systems

Sychrová, H.
Yeast as a tool to study cell membrane transporters

Uetrecht, Ch.
Lipid glue in clathrin adaptor assembly and new opportunities at XFELs

Vachá, R.
Anomalous Interactions of Amyloids with Surfaces

Zayats, V.
Modulation of human ORAI1 channel: modeling and simulations

4TH INTERNATIONAL WORKSHOP ON ODS MATERIALS

HZDR, Dresden, Germany, June 26–28, 2017

Oxide Dispersion Strengthened (ODS) Fe-Cr alloys, or Nanostructured Ferritic Alloys (NFA), are promising candidates for application as structural materials in extreme environments, *i.e.* at high temperature and intense particle irradiation characteristic for both fission and fusion based future nuclear energy systems. The main argument for ODS steels is a promising combination of properties including favourable resistance against corrosion, creep and irradiation-induced swelling as well as irradiation damage tolerance and the possibility to design reduced-activation variants. The standard fabrication route of ODS steels is based on powder metallurgy and includes gas atomization of a pre-alloy, mechanical alloying, consolidation *e.g.* by hot extrusion and thermal/mechanical treatment. Details of the individual steps of the powder metallurgical route are not yet well understood with the consequence of limited reproducibility of the quality of the end product in terms of inhomogeneity, anisotropy and mechanical properties.

The International Workshop on ODS Material organized by HZDR in Dresden for the fourth time provides a regular platform to discuss recent progress in the understanding and optimization of ODS alloys using different methods of fabrication, characterization and modelling and serves to strengthen collaboration within the ODS community.

The focus of this year's workshop was on fabrication methods and their effect on the microstructure with a strong emphasis on alternative production routes aimed at upscaling the ODS production to industrial scale and making it more economically attractive. Moreover, the correlation of the microstructure with the mechanical properties was addressed as well as the effects of thermal treatment and irradiation.

The workshop included oral and poster presentations of 24 participants from 8 countries representing 13 research institutions and offered generous time for group discussions on key issues. (by: C. Heintze)

List of invited speakers:

Bergner, F.
Oxide dispersion in melt-spun Fe-Cr alloys

Binghuang, D.
The effect of the initial microstructure in terms of sink strength on the ion-irradiation-induced hardening of ODS alloys studied by nanoindentation

Bogachev, A.
NRC "Kurchatov Institute" - ITEP, Moscow, Russia
Effect of heavy ion irradiation on the microstructure of oxide dispersion strengthened steels

Chauhan, A.
Karlsruhe Institute of Technology, Karlsruhe, Germany
High-temperature fatigue and creep-fatigue interaction in a tempered martensitic 9Cr-ODS steel

Das, A.
Effect of microstructure on fracture behaviour of hot extruded ferritic ODS steels

Dawson, K.
University of Liverpool, U.K.
Restructuring nano-features in deformed and recrystallised oxide dispersion strengthened steels

Franke, P.
Karlsruhe Institute of Technology, Karlsruhe, Germany
Preparation of stainless ODS steels by internal oxidation

Giroux, P.-F.
CEA, Sacley, France
Study of nanostructured metal matrix composite material elaboration by additive manufacturing for nuclear components

Hilger, I.
Influence of microstructure features on the irradiation behaviour of ODS Fe14Cr alloys

Onorbe, E.
CIEMAT, Madrid, Spain
The evolution of internal strains in a 14Cr alloy strengthened by oxide dispersion

Sarma, M.
Magnetically induced cavitation for the dispersion of nanoparticles in liquid metals

Vallinayagam, M.
Structure and energetics of Y-Ti-O nanoclusters in bcc Fe

Vogel, K.
Dislocation movement in a 14Cr ODS steel studied by in situ Transmission Electron Microscopy

Wang, X.
Influence of foreign atoms on the diffusion of oxygen in bcc Fe

Wilms, M.
Fraunhofer Institut für Lasertechnik ILT, Aachen, Germany
Laser additive manufacturing as an alternative near net shaped fabrication method for the production of ODS materials

❍ TAM-USER-MEETING FOR CALORIMETRY

HZDR, Dresden, Germany, October 11, 2017

List of speakers:

Braissant, O.
Unispital Basel, Switzerland
Combination of Tunable Diode Laser Spectrometry (TDLAS) and Isothermal microcalorimetry for life sciences and biotechnology applications

Fahmy, K.
Helmholtz-Zentrum Dresden-Rossendorf, Germany
The metrics of calorimetry: uranium toxicity measured in plant cells

Heil, M.
Fraunhofer-Institut für Chemische Technologie, Pfinztal, Germany
Investigation of chemical stabilization by heat flow calorimetry and pseudo-isoconversional method

Hupatz, H.
Freie Universität Berlin, Germany
Thermodynamic analysis of multivalent supramolecular complexes

Maskow, Th.
Helmholtz Centre for Environmental Research, Leipzig, Germany
How to measure and quantify calorimetrically the energetic efficiency of the biological photosynthesis?

Ortmann, Ch.
TA Instruments, Eschborn, Germany
TAM IV – Charge and discharge cycles of Li-batteries

Pannen, H.
TA Instruments, Eschborn, Germany
Welcome and short introduction of TA Instruments

Suurkuusk, M.
TA Instruments, Sollentuna, Sweden
Microcalorimetry and Material Characterisation

Walter, D.
Justus-Liebig-Universität Gießen, Germany
Toxicity of aluminium and aluminium compounds – Determination by in vitro assays

Willms, Th.
Helmholtz-Zentrum Dresden-Rossendorf, Germany
Reactivity of t-butyl hydroperoxide and t-butyl peroxide towards reactor materials measured by a microcalorimetric method at 30 °C.

❍ SYMPOSIUM IN HONOR OF THE RETIREMENT OF DR. GERHARD GEIPEL

HZDR, Dresden, Germany, November 03, 2017

List of speakers:

Kumke, Michael
University of Potsdam, Germany
Ultra-Kurzzeitspektroskopie von Uranyl-Komplexen

Maret, Wolfgang
King's College London, U.K.
De re metallica: Ein kurzer wissenschaftlicher Abriss von Agricola bis zur Zinkbiologie

Panak, Petra
Universität Heidelberg, Germany
Wechselwirkung von trivalenten Actiniden und Lanthaniden mit humanen Blutserumproteinen

Walther, Clemens
Justus-Liebig Universität, Hanover, Germany
Quasi non-destructive Analysis of Single Actinide-Particles by Secondary Neutral Mass Spectrometry

Winde, Frank
School of Basic Sciences, North-West University Vaal Campus, South Africa
Gesundheitsgefährdung durch Uran? Zwei Fallstudien aus Südafrika

❍ AWARDS

Theses Awards

Drobot, B.
Entwicklung und Validierung mathematischer Methoden zur Auswertung spektroskopischer Daten der Uranyl(VI)–Hydrolyse
PhD Award, The German Chemical Society (GDCh), Nuclear Chemistry Division (2017).
&
PhD Award, HZDR (2017).

Poster Award

Kloditz, R.
Analysis of the covalent bond character of tetravalent actinide complexes with N- and O-donor ligands
Poster price, The German Chemical Society (GDCh), Nuclear Chemistry Division (2017).

❍ SEMINARS (TALKS OF VISITORS)

Montavon, Gilles
SUBATECH, Nantes, France
POLLUSOLS, a new research program at SUBATECH
January 30, 2017

Creff, Gaelle
Universite de Nice Sophia Antipolis, Nice, France
Actinides speciation in relation with biological processes
February 08, 2017

Banwart, Steven A.
University of Leeds, United Kingdom
Role of biota in the weathering of rock and minerals
February 10, 2017

Viebach, Marco
Technische Univeristät, Dresden, Germany
Minimal Model for Considering Fuel Assembly Kinematics in DYN3D Noise Analysis
March 15, 2017

Kaila, Ville
Technische Universität München, Germany
Molecular mechanisms of coupled proton-electron transfer reactions in biology
April 03, 2017

Zöllner, Dana
Technische Universität München, Germany
Nano, Micro, Macro: About moving boundaries and total conservation
April 26, 2017

Guilbaud, Philippe
CEA Marcoule, France
The Actinide Ligand Interaction Laboratory (LILA): Basic Research for Actinides in the ATALANTE facility, CEA, France
May 03, 2017

Husar, Richard
CEA Marcoule, France
A New Multi-spectroscopic Electrochemistry Approach in CEA-Marcoule
May 03, 2017

Maiwald, Martin
Universität Heidelberg, Germany
Complexation of neptunium(V) with inorganic and organic ligands in aqueous solution as a function of temperature
June 16, 2017

Rund, Martin
COMTES FHT Dobrany, Czechia
Fracture toughness of additive fabricated titanium alloys
July 04, 2017

Schäfer, Thorsten
Friedrich-Schiller-Universität Jena, Germany
BioGeoWissenschaften: Vergangene und zukünftige Ausrichtung des Lehrstuhls für Angewandte Geologie an der Friedrich-Schiller-Universität (FSU) Jena
August 07, 2017

Natrajan, Louise
Centre for Radiochemistry Research, School of Chemistry, The University of Manchester, U.K.
Investigating the Redox Chemistry of the Early Actinides Through a Combination of NMR and Luminescence Spectroscopy
August 08, 2017

Steppert, Michael
Leibniz Universität Hannover, Germany
Update on the ESI-Orbitrap mass spectrometer: redesign of the ion source region and its implications for measurements in aquatic systems and first MS/MS-data on molybdenum species in strongly acidic media
September 28, 2017

Geist, Andreas
Karlsruhe Institut of Technology, Germany
Why we created hydrophilic BT(B)P ligands – and basic science's non-negligible role therein
October 05, 2017

Schierz, Ariette
Assessment of Contaminant Fate in Aquatic Ecosystems – Two Examples: 1) A Legacy Hg Impacted Site and 2) Risk Assessment of Emerging Contaminants
November 17, 2017

Kalmykov, Stepan N.
Lomonosov Moscow State University, Russia
Pu migration- from molecular to landscape level
December 11, 2017

Drobot, Björn
Max Planck Institute of Molecular Cell Biology and Genetics Dresden, Germany
Coacervate compartments for ribozyme activity (with some thermodynamics and spectroscopy)
December 18, 2017

SESSIONS (CO)ORGANIZED BY IRE

16th International Clay Conference

Granada, Spain, July 17–21, 2017.

Merroun, M. L.; Cherkouk, A.; Romero Gonzalez, M. E.
Session OM-06:
Biogeochemical processes at the microbe/clay interface and their synergy radionuclide/organic interactions

Goldschmidt 2017

Paris, France, August 13–18, 2017.

Scheinost, A.; Waite, D.; Guillon, E.; Dror, I; Morris K.; Pearce, C.; do Sameiro Marques Fernandes, M.
Session 13f:
Redox Dynamics and their Influence on the Fate, Reactivity and Transport of Radio-Contaminants and Other Trace Elements

Cherkouk, A.; Lloyd, J.
Session 13n:
Biogeochemical Processes and Radioactive Waste Disposal

XXVI. International Materials Research Congress (IMRC 2017)

Cancún, Mexico, August 20–25, 2017.

Keller, A.; Raff, J.; Bergkvist, M.; Samano, E. C.
Session C.4:
Materials and Interfaces Based on Biomolecular Self-Assembly

GeoBremen 2017 – The System Earth and its Materials – from Seafloor to Summit

Bremen, Germany, September 24–29, 2017.

Stumpf, T.
Session 4.1: Geo-radiochemistry

Bilateral meeting

PSI *Villigen, Switzerland*	Institute of Resource Ecology (IRE) *HZDR, Dresden, Germany*

PSI, Villigen, Switzerland, September 4–5, 2017.

❍ TEACHING ACTIVITIES

(Winter term: WT; Summer term: ST)

Lectures

Bok, F.
Friedrich-Schiller-Universität, Jena
ST 2017
Geochemische Modellierung mit Geochemist's Workbench®

Brendler, V.
Dresden University of Applied Sciences,
ST 2017
Radiochemistry

Fahmy, K.
Technische Universität Dresden,
WT 2016/17
Biophysical methods
ST 2017
Biological thermodynamics

Huittinen, N.
Technische Universität Dresden,
ST 2017
Radioecology

Lippold, H.
Universität Leipzig,
ST 2017
Radioanalytik
Entstehung und Eigenschaften ionisierender Strahlung

Raff, J.
Dresden University of Applied Sciences,
WT 2016/17, WT 2017/2018
Mikrobiologie

Technische Universität Dresden,
WT 2017/2018
Mikrobielle Laugung

Schmidt, M.
Technische Universität Dresden,
WT 2017/18
Chemistry of the *f*-elements

Stumpf, T.
Technische Universität Dresden,
ST 2017
Radiochemistry

Courses

- The laboratory course "Radiochemistry" was provided from August 21–25 and from August 28– September 01, 2017, as a part of a module of the chemistry master degree program at the Technische Universität Dresden.

Advisers:

Bachran, M.
Bauer, A.
Brinkmann, H.
Drozdowski, J.
Eibl, M.
Dr. Huittinen, N.
Dr. Jordan, N.
Dr. Kaden, P.
Kloditz, R.
Lösch, H.
Molodtsov, K.
Dr. Müller, K.
Dr. Patzschke, M.
Philipp, T.
Radoske, T.
Dr. Schmidt, M.
Schönberger, N.
Schöne, S.
Schrader, S.
Weiss, S.
Wollenberg, A.
Wolter, J.

- The IRE provided the experiment "Alpha spectrometric isotope dilution analysis of uranium" of the laboratory course "Instrumental Analysis" held by the Institute for Analytical Chemistry, Technische Universität Dresden.

Advisers:

WT 2016/17	*WT 2017/18*
Molodtsov, K.	Eibl, M.
Philipp, T.	Kloditz, R.
Weiss, S.	Nucke, L.
Wollenberg, A.	Radoske, Th.
Wolter, J.	Schöne, S.
	Weiss, S.

- Biophysics course of the Dresden-International-Graduate School.

Advisers:

WT 2016/17 & WT 2017/18
Prof. Dr. Fahmy, K.
Dr. Oertel, J.
Philipp, J.

Further Activities

Attendees of the Institute of Resource Ecology at the 16th International Conference on the Chemistry and Migration Behaviour of Actinides and Fission Products in the Geosphere (Migration 2017), September 10 – 15, 2017, Barcelona, Spain.

PERSONNEL

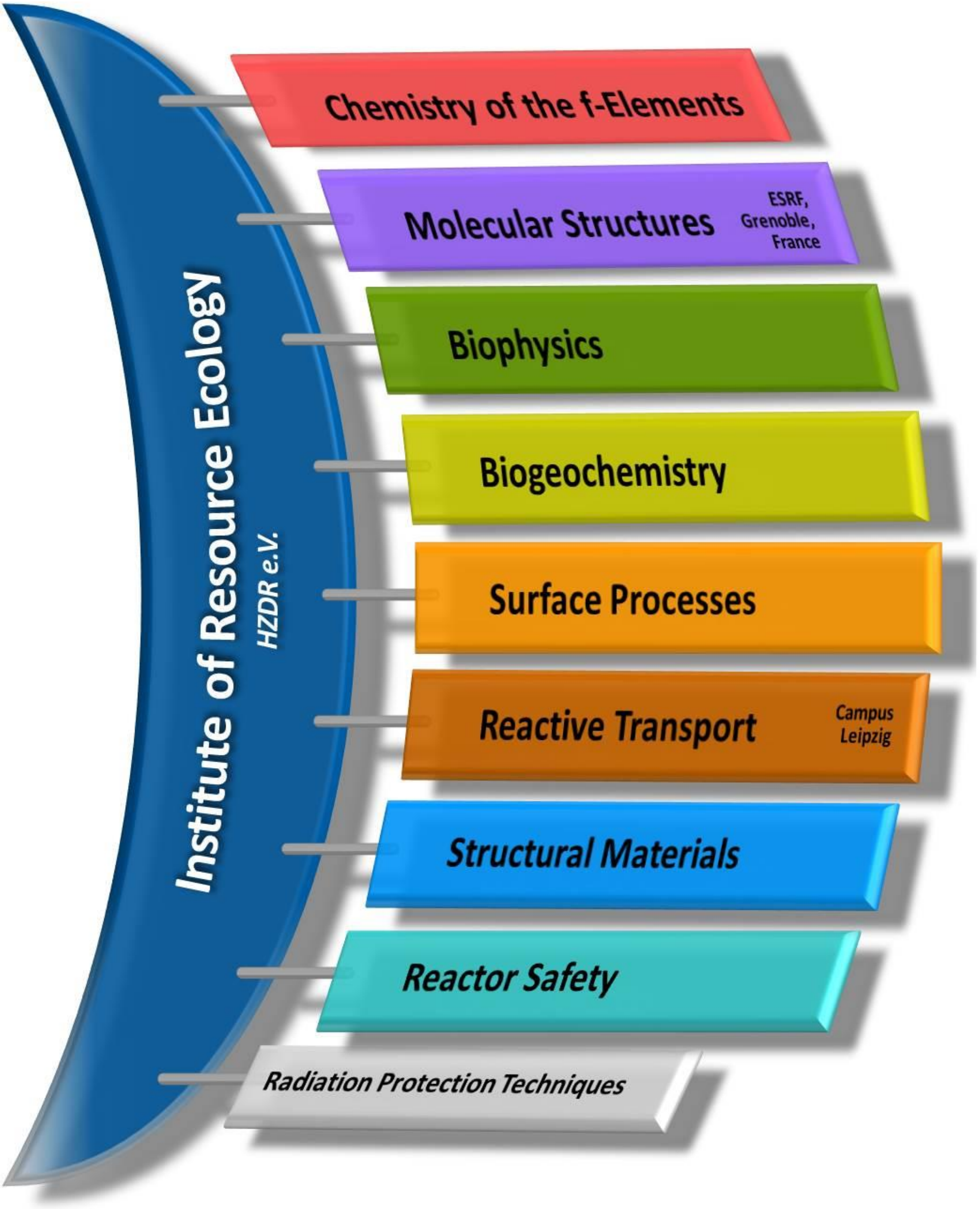
Institute of Resource Ecology
HZDR e.V.
Chemistry of the f-Elements
Molecular Structures
ESRF,
Grenoble,
France
Biophysics
Biogeochemistry
Surface Processes
Reactive Transport
Campus
Leipzig
Structural Materials
Reactor Safety
Radiation Protection Techniques

Prof. Dr. Thorsten Stumpf (HEAD OF INSTITUTE)

ADMINISTRATION:
Office Dresden: Gorzitze, Jana; Kovacs, Jenny; Kurde, Kerstin; Lauke, Regina
Office ESRF: Glückert, Marion
Office Leipzig: Gerstner, Katrin
Sysad (IT): Berndt, Ronny

PROJECT COORDINATION:
Office Dresden: Dr. Arnold, Thuro

RADIATION PROTECTION:
Dr. Steudtner, Robin; Bösel, Melanie; Falkenberg, Dirk; Henke, Steffen;
Nebe, Katrin; Rumpel, Annette

*: PhD student; as of 2017/12/31

BIOGEOCHEMISTRY

Dr. Geipel, Gerhard / Dr. Raff, Johannes

Brinkmann, Hannes*
Drozdowski, Jennifer*
Fichtner, Andreas*
(SUBATECH/HZDR)
Flemming, Katrin
Gerber, Ulrike*
Dr. Günther, Alix
Heller, Sylvia
Dr. Krawczyk-Bärsch, Evelyn
Dr. Moll, Henry
Dr. Sachs, Susanne
Seibt, Jana
Dr. Vogel, Manja
Wollenberg, Anne*

HZDR Young Investigator Group
Dr. Cherkouk, Andrea
Bachran, Madlen*
Bader, Miriam*
Kluge, Sindy
Dr. Matschiavelli, Nicole

BIOPHYSICS

Prof. Dr. Fahmy, Karim

Iric, Katarina* (HZDR/TUD)
Nucke, Lisa*
Dr. Oertel, Jana
Philipp, Jenny
Dr. Tsushima, Satoru
Subramania, Madhumalar*

CHEMISTRY OF THE F-ELEMENTS

Dr. Ikeda-Ohno, Atsushi

Dr. Barkleit, Astrid
Dr. Husar, Richard
Dr. Kaden, Peter
Kloditz, Roger*
Dr. März, Juliane
Dr. Patzschke, Michael
Radoske, Thomas*
Schöne, Sebastian*
Wilke, Claudia*

SURFACE PROCESSES

Prof. Dr. Brendler, Vinzenz / Dr. Müller, Katharina

Bauer, Anne*
Dr. Bok, Frank
Chlupka, Aline
Eckardt, Carola
Eibl, Manuel*
Fischer, Sarah*
Dr. Foerstendorf, Harald
Gürtler, Sylvia
Gurlit, Sabrina
Heim, Karsten
Dr. Huittinen, Nina
Dr. Jäschke, Astrid
Dr. Jordan, Norbert
Lehmann, Susanne*
Lösch, Henry*
Dr. Mayordomo H., Natalia
Müller, Christa
Neubert, Heidrun
Pfützner, Birke
Philipp, Thimo*
Dr. Richter, Anke
Rodriguez Hernandez, Diana M.
Dr. Schmeide, Katja
Shams Aladin Azzam, Salim
Dr. Stockmann, Madlen
Weiss, Stephan
Wolter, Jan-Martin*

HGF Young Investigator Group
Dr. Schmidt, Moritz
Dr. Hellebrandt, Stefan*
Hellebrandt, Sophia*
Molodtsov, Konrad*
Dr. Qiu, Canrong
Dr. Xiao, Bin

STRUCTURAL MATERIALS

Dr. Altstadt, Eberhard / Dr. Heintze, Cornelia

Dr. Bergner, Frank
Das, Aniruddh*
Hilger, Isabell*
Houska, Mario
Dr. Müller, Gudrun
Pietzsch, Jens
Richter, Henry
Röder, Falk
Roßner, Michaela
Rott, Sonja
Skorupa, Ulrich
Dr. Ulbricht, Andreas
Dr. Viehrig, Hans-Werner
Dr. Vogel, Karin
Webersinke, Wolfgang
Weiß, Rainer

MOLECULAR STRUCTURES

ESRF,
Grenoble

Dr. habil. Scheinost, Andreas C.

Dr. Baumann, Nils
Exner, Jörg
Dr. Hennig, Christoph
Dr. Kvashnina, Kristina O.
Naudet, Damien
Dr. Prieur, Damien
Dr. Rossberg, André

REACTIVE TRANSPORT

Campus
Leipzig

Dr. habil. Fischer, Cornelius / Dr. Lippmann-Pipke, Johanna

Barthen, Robert*
Dr. Franke, Karsten
Gründig, Marion
Gruhne, Stefan
Dr. Hildebrand, Heike
Dr. Karimzadeh, Lotfallah
Dr. Kulenkampff, Johannes
Dr. Lippold, Holger
Lösel, Dagmar
Dr. Mansel, Alexander
Schößler, Claudia
Dr. Schymura, Stefan

REACTOR SAFETY

Dr. Kliem, Sören / Dr. Wilhelm, Polina

Dr. Bilodid, Yurii
Di Nora, Vincenzo Anthonio*
Dr. Fridman, Emil
Gommlich, André
Dr. Grahn, Alexander
Hoffmann, Alexander*
Jobst, Matthias
Konheiser, Jörg
Kozmenkov, Yaroslav
Dr. Müller, Stefan
Nikitin, Evgeny*
Pescador, Eduard Diaz*
Dr. Rachamin, Reuven
Dr. Schäfer, Frank
Sporn, Michael

GUEST SCIENTISTS

Albright, Lucas Iain	*University of Utah, Salt Lake City, U.S.A.*
Baier, Silvio	*Technische Universität Dresden, Germany*
Bilodid, Ievgen	*Scientific-technical Centre for Nuclear and Radiation Safety of the Ukraine, Kiew, Ukraine*
Diaz Pescador, Eduard	*Technische Universität Dresden, Germany*
Dufaye, Maxime	*Université de Lille, France*
Formánek, Petr	*Leibnitz-Institut für Polymerforschung Dresden e.V., Germany*
Fricke, Thomas	*Vita 34 AG, Leipzig, Germany*
Ieremenko, Maksym	*Scientific-technical Centre for Nuclear and Radiation Safety of the Ukraine, Kiew, Ukraine*
Khassenov, Azamat	*Ulsan National Institute of Science & Technology (UNIST), South Korea*
Knuutinen, Jenna Janina	*University of Helsinki, Finnland*
Martin, Nicolas	*Université de Lille, France*
Martyanov, Dmitry	*Joint Institute for Power and Nuclear Research Sosny (Belarus) Minsk, Belarus*
Natrajan, Louise	*University of Manchester, U.K.*
Ovdiienko, Iurii	*Scientific-technical Centre for Nuclear and Radiation Safety of the Ukraine, Kiew, Ukraine*
Rudziankou, Ivanton	*Joint Institute for Power and Nuclear Research Sosny (Belarus) Minsk, Belarus*
Rund, Martin	*COMTES FHT Dobrany, Czech Republic*
Rydlewicz, Wojciech	*University of Cambridge, U.K.*
Sinclair, Jacqueline	*University of West of Scotland, Paisley, U.K.*
Usheva, Krystsina	*Research Institute für Nuclear Problems of Belarusian State University, Minsk, Belarus*
Vivas Méndez, Javier	*Centro Nacional de Investigationes Metalúrgicas (CENIM) Madrid, Spain*
Volkringer, Christophe	*Université de Lille, France*

MASTER/DIPLOMA/BACHELOR

Galanzew, Jurij
Knöppel, Julius
Schäfer, Sebastian
Schernikau, Martin
Vincon, Ilka
Zimmermann, Thomas

GRADUATE ASSISTANTS, STUDENT ASSISTANTS, TRAINEES

Becker, Alexander
Demnitz, Maximilian
Eckert, Louisa
Fankhänel, Tobias
Felsner, Bodo
Fischer, Evelin
Häußler, Ellen
Hilpmann, Stephan
Hohlfeld, Lutz
Jessat, Jenny
Jimenez, Susana
Lemke, Frederik
Pischel, Felix
Sprenger, Una
Werner, Julia
Winkler, Christian
Wülfing, Dominique
Zimmermann, Veit

ACKNOWLEDGEMENTS

The Institute of Resource Ecology is one of the eight institutes of the Helmholtz-Zentrum Dresden–Rossendorf e.V. (HZDR). As registered, non-profit institution, the HZDR is supported by the authorities of the Federal Government and the Free State of Saxony. In addition to the basic funding, the financial support of the projects listed below by the given organizations and companies is greatfully acknowledged.

FUNDING ORGANIZATION / COMPANY	**PROJECT TITLE**	**CONTRACT NO. (if applicable)**
Commission of the European Communities (EU)	BioMOre – An Alternative Mining Concept - Raw Materials Commitment	*H2020-642456*
	Cebama – Cement-based materials, properties, evolution, barrier functions	*H2020-662147*
	CONCERT – European Joint Programme for the Integration of Radiation Protection Research	*H2020-662287*
	ESFR-SMART – European SFR – Safety Measures Assessment and Research Tools	*H2020-754501*
	INSIDER	*H2020-755554*
	IVMR – In-Vessel Melt Retention Severe Accident Management Strategy for Existing and Future NPPs	*H2020-662157*
	MIND – Microbiology in Nuclear Waste Disposal	*H2020-661880*
	M4F	*H2020-755039*
	McSAFE – High-Performance Monte Carlo Methods for Safety Demonstration	*H2020-755097*
	NetFlot	*KIC RM 15062*
	SOTERIA	*H2020-661913*
Bundesministerium für Wirtschaft und Energie (BMWi) & Bundesministerium für Bildung und Forschung (BMBF)	BioNEWS – Wachstumskern BioSAM – Verbundprojekt 03 BioNEWS; TP 3.7: Langzeitstabile Zellen zum Aufbau und zur Regenerierung von Sensor- und Aktorsystemen für den Nachweis und die Bindung strategisch relevanter Metalle (insbesondere Seltene Erden)	*03WKCL03F*
	BioVeStRa Untersuchungen des Potentials biologischer Verfahren zur Strahlenschutzvorsorge bei Radionuklidbelastungen	*02S9276A*
	ECOMETALS – Innovative umweltschonende Prozesse für die Gewinnung strategischer und seltener Metalle aus primären und sekundären Ressourcen; TP HZDR: Rohstoffcharakterisierung, mikrobiologische Mobilisierung von Metallen	*033RF001A*
	EDUKEM – Entwicklung und Durchführung experimenteller Methoden zur verbesserten Modellierbarkeit uranhaltiger salinarer Lösungen	*02E11334B*
	FENABIUM – Struktur-Wirkungsbeziehungen zwischen f-Elementen und organischen Ligandsystemen mit Naturstoff-basierten Bindungsfunktionen in Hinblick auf eine mögliche Mobilisierung in der Umwelt	*02NUK046B*
	GRaZ – Verbundprojekt Geochemische Radionuklidrückhaltung an Zementalterationsphasen	*02E11415B*
	NanoSuppe	*03X0144A*
	NuWaMa – Ausbau einer Deutsch-Tschechischen Koopration auf dem Gebiet der Nuklearen Endlagerforschung	*01DS16008*
	r4 – SE-FLECX – Selektive Flüssig-Flüssig-Extraktion von Lanthaniden & Actiniden durch präorganisierte Calixarene	*033R132A*
	r4 – SEM^2 – Seltene-Erden-Metallurgie – fortgeschrittene Methoden für die optimierte Gewinnung und Aufbereitung am Beispiel von Ionenadsorptionstonen	*033R127D*

FUNDING ORGANIZATION / COMPANY	**PROJECT TITLE**	**CONTRACT NO. (if applicable)**
	ThermAc – Verbundprojekt Aufklärung von Thermodynamik und Speziation von Actiniden bei höheren Temperaturen in Kombination von Schätzmethoden, spektroskopischen und quantenmechanischen Methoden, Teilprojekt B	*02NUK039B*
	TransAqua – Verbundprojekt Transfer von Radionukliden in aquatischen Ökosystemen Teil A: Untersuchungen zu den Wechselwirkungen zwischen unter Tage lebenden Mikroorganismen mit Uran Teil B: Spektroskopische Bestimmung der Bindungsform (Speziation) trivalenter Actinide/Lanthanide in Biofluiden des menschlichen Gastrointestinaltraktes und im Blut	*02NUK030F*
	TRANS-LARA – Verbundprojekt Transport- und Transferverhalten langlebiger Radionuklide entlang der kausalen Kette Grundwasser-Boden-Oberfläche-Pflanze unter Berücksichtigung langfristiger klimatischer Veränderungen, Teilprojekt B	*02NUK051B*
	UMB – Verbundprojekt Umwandlungsmechanismen in Bentonitbarrieren, Teilprojekt B	*02E11344B*
	VESPA II – Verbundprojekt Verhalten langlebiger Spalt- und Aktivierungsprodukte im Nahfeld eines Endlagers und Möglichkeiten ihrer Rückhaltung	*02E11607B*
	WTZ Russland – Transientenanalysen für schnelle Reaktoren	*1501462*
Gesellschaft für Anlagen- und Reaktorsicherheit gGmbH (GRS)	Diffusionsexperimente	
	DYN3D Codetraining	
	THEREDA III	
Helmholtz-Gemeinschaft Deutscher Forschungszentren e.V. (HGF)	HGF-Nachwuchsgruppe Dr. Schmidt	*VH-NG-942*
	Flüchtlingsinitiative	*SO-FI-0004*
	Exzellenznetzwerk-Phase 2 "Physics of Life - The Dynamic Organization of Living Matter"	*ExNet-0029-Phase2-3*
PreussenElektra GmbH (bis 01.07.2016 : E.ON Kernkraft GmbH)	Lokale Leistungsänderung	
	Nachkühlkettenberechnung	
	Uncertainty	
STFC Daresbury	DYN3D Codetraining	
TU Dresden	Holzchemie	
TÜV NORD	Prüfung geologischer Fragen	*M.ASS.06.015.01.F70*
TÜV SÜD	Datenbibliotheken für WWER-1000-Reaktoren	*3611R01504*
	Gemischte Reaktorkerne	*3617R01520*
UJV Rez, a.s.	DYN3D für UJV Wartung 2016/2017	
	DYN3D für UJV Wartung 2017/2018	

INDEX OF AUTHORS

HZDR

HELMHOLTZ
ZENTRUM DRESDEN
ROSSENDORF

Institute of Resource Ecology
Bautzner Landstrasse 400
01328 Dresden/Germany
Phone +49 351 260-3210
Fax +49 351 260-3553
Email contact.resourceecology@hzdr.de
http://www.hzdr.de

Member of the Helmholtz Association